CORA Cork Open Research Archive
Cartlann Taighde Oscailte Chorcaí

Title	Development of electromagnetic vibration energy harvesters as powering solution for IoT based applications
Authors	Paul, Kankana
Publication date	2022-09-20
Original Citation	Paul, K. 2022. Development of electromagnetic vibration energy harvesters as powering solution for IoT based applications. PhD Thesis, University College Cork.
Type of publication	Doctoral thesis
Rights	© 2022, Kankana Paul. - https://creativecommons.org/licenses/by-nc-nd/4.0/
Download date	2026-11-02 10:29:10
Item downloaded from	https://hdl.handle.net/10468/14473



UCC
University College Cork, Ireland
Coláiste na hOllscoile Corcaigh

Ollscoil na hÉireann, Corcaigh

National University of Ireland, Cork



Development of Electromagnetic Vibration Energy Harvesters as powering solution for IoT based applications

Thesis presented by

Kankana Paul, M.Tech

For the degree of

Doctor of Philosophy

University College Cork

Department of Electrical and Electronic Engineering

[Tyndall National Institute]

Supervisor: Saibal Roy

Co-supervisor: Andreas Amann, Peter Kennedy

Head of the Department: William P. Marnane

SEPTEMBER 2022

Declaration

This dissertation is the result of the work carried out in Micropower Systems and Nano magnetics (within Micro and Nano Systems Centre) Group at Tyndall National Institute from November 2017 to July 2022.

This is to certify that the work I am submitting is my own and has not been submitted for another degree, either at University College Cork or elsewhere. All external references and sources are clearly acknowledged and identified within the contents.

Kankana Paul
Tyndall National Institute,
University College Cork,
September 2022

Abstract

The drive towards building pervasive intelligence encompassing urban as well as rural environments has paved the way for the Internet of Things (IoT), which has reshaped our regular lifestyle alleviating the dependence on wired communication systems since its inception. The inexorable advancement in low to ultra-low power electronics have steered the rapid growth of the IoT platform expanding into several application fields. With the ongoing implementation of 5G (Fifth generation) and the emergence of 6G (Sixth generation) wireless technology on the horizon, the explosive growth of IoT connected devices reinforces the requirement of a robust and reliable power solution for the deployed wireless communication platforms. Utilizing distributed clean energy sources, especially the ubiquitous mechanical energy available in environment through dedicated transducers in the form of vibration energy harvesters (VEHs) to power the IoT-based wireless sensor platforms is a sought after alternatives to batteries in the forthcoming IoT applications.

The potential of the resonant/linear VEHs have been limited owing to the narrow operable frequency bandwidth as well as due to the lack of intelligent device designs that aids to yield large electrical power from the provided mechanical energy. In this thesis, a concertina shaped linear VEH spring architecture has been exploited to instigate large amplitudes of oscillation, which aids to yield a high power density ($455.6\mu W/cm^3g^2$) at resonance from a relatively small device footprint. From the application perspective, this concertina-VEH has been utilized to power the electronics interface and enhance the performance of a NFC (Near Field Communication) based wireless sensor platform which offers the benefits of low power consumption and on call data acquisition through this short range NFC based communication protocol. Such a robust autonomous wireless sensing platform offers the potential to be used in a large number of IoT based applications.

Despite of the large deliverable power obtained from the resonant VEH, the energy extraction drops dramatically as the excitation frequency deviates from the resonance condition, which is inevitable owing to the random nature of vibrations. A novel broadband VEH with tapered spring geometry has been developed as a part of this thesis to address this issue. Nonlinear restoring forces arising from the stretched springs enables the VEH to generate large power over a considerably wide bandwidth (45Hz of hysteresis width that is the difference of the jump down and jump up frequency with 1g excitation amplitude) of operable frequencies. Suitable power management strategies have been proposed to enhance the energy extraction capabilities. The nonlinear VEH has been successfully used to harness mechanical energy from

the broadband vibrations of a car; the extracted energy is fed to a wireless sensor platform that reports on ambient temperature and humidity. This self-powered sensing system opens up the scope for exploiting this technology for monitoring food and medicinal quality during transportation while the VEH extracts mechanical energy from the transporting vehicle and perpetually powers the wireless sensor node.

Multiple nonlinearities arising from the stretching of the VEH spring as well as from the interaction of repulsive magnets have been introduced into the energy harvester, which gives rise to coexisting multiple energy branches. Not all of these energy states are achieved through the typical excitation frequency routine, some of these energy states are rather hidden. Experimentally a route to achieve these hidden energy branches have been explored in this work. Suitable frequency routines have been designed to achieve and sustain these higher energy states. A useful graphical representation has been introduced in the form of 'eye diagrams' that essentially estimates the transaction of energy from mechanical to electrical domain, and provides deep insight of the dynamical features of each energy branches, based on time resolved measurements of acceleration and voltage. A mathematical model has been developed to investigate the intricate complexities of the nonlinear system, which supports the experimental findings.

One of the major impediments in miniaturizing high-efficiency macroscale VEHs into MEMS (Micro-Electro-Mechanical-System) scale is the lack of matured technology for the CMOS (Complementary-Metal-Oxide-Semiconductor) compatible integration of magnets and the adverse effect of scaling on the permanent hard magnets. A part of the presented work investigates the effect of patterning continuous thin films of magnets into micromagnet array. With detailed analytical framework and exhaustive finite element analysis, the shape, size and distribution of these micromagnets have been optimized to maximize the stray magnetic field emanating from each edge of these magnets. Novel MEMS device topologies comprising of linear/nonlinear MEMS springs, micromagnet arrays and copper microcoil have been proposed which systematically maximizes the electromagnetic interaction between the micromagnets and the integrated coil that in turn translates into large deliverable power.

In addition to the developed device prototypes and demonstrations, this thesis further provides a firm roadmap that highlights the potential routes for enhancing the energy harvesting capabilities through highly integrated MEMS scale VEHs as well as for improving system level integration to establish these VEHs as a reliable and sustainable alternative of batteries in IoT applications.

List of Publications

List of Journal Publications:

1. **K. Paul**, D. Mallick and S. Roy, "Performance improvement of MEMS Electromagnetic Vibration Energy Harvester using optimized patterns of micromagnet array," in *IEEE Magnetics Letters*, vol. 12, pp. 1-5, 2021.

2. **K. Paul**, A. Amann, S. Roy, "Tapered nonlinear vibration energy harvester for powering Internet of Things", Applied Energy, vol. 283, pp. 116267, 2019.

3. D. Mallick, **K. Paul**, T. Maity, and S. Roy, "Magnetic performances and switching behavior of Co-rich CoPtP micro-magnets for applications in magnetic MEMS," *Journal of Applied Physics*, vol. 125, no. 2, pp. 023902, 2019.

4. S. Roy, D. Mallick, and **K. Paul**, "MEMS-Based Vibrational Energy Harvesting and Conversion Employing Micro-/Nano-Magnetics," *IEEE Transactions on Magnetics*, vol. 55, no. 7, pp. 1-15, 2019.

5. **K. Paul**, A. Amann, S. Roy, "Exploration of high energy branches in a novel electromagnetic vibration energy harvester combining multiple nonlinearity"- Submitted to Physical Review Applied, Under review.

6. **K. Paul**, D. R. Gawade, R. B.V.B. Simorangkir, B. O'Flynn, J. L. Buckley, A. Amann, S. Roy, "A Concertina-Shapes Vibration Energy Harvester-Assisted NFC Sensor With Improved Wireless Communication Range", *IEEE Internet of Things Journal, pp. 1-13, 2022.*

List of Conference Publications:

1. **K. Paul**, A. Amann, S.Roy, "Design optimization of tapered wideband nonlinear electromagnetic vibration energy harvesters for powering IoT", *2021 IEEE International Conference on Magnetics (INTERMAG 2021), pp. 1-2.*

2. B. Zaghari, A. Weddell, **K. Paul**, S. Roy, S. Beeby, "Nonlinear time-periodic variable reluactance energy harvester for smart bearings in aircraft jet engines", *2020 10th European Nonlinear Dynamics Conference (ENOC), Lyon, France.*

3. **K. Paul**, D. Mallick and S. Roy, "Improved Performances of Wideband MEMS Electromagnetic Vibration Energy Harvesters using Patterned Micro-magnet Arrays," *2019 19th International Conference on Micro and Nanotechnology for Power Generation and Energy Conversion Applications (PowerMEMS)*, 2019, pp. 1-6.

4. D. Mallick, **K.Paul**, S. Roy, "Design optimization of Fully Integrated, MEMS Electromagnetic Enegry Harvesting Devices using Patterned Micro-magnet Arrays", 2018 IEEE 18th International Conference on Nanotechnology (IEEE NANO), Cork, Ireland, 2018, pp. 1-3.

List of Awards

1. Finalist Awardee of Tyndall National Institute's Research Publication of the Year competition, Ireland, 2020.
2. Winner of International Society of Electrochemistry (ISE) Annual Regional student Poster Competition, Ireland, 2019 sponsored by Analog Devices.
3. Winner of Poster presentation Competition in Noise In Physical Systems (NIPS) Summer School, Italy, 2019.
4. Winner of Tyndall National Institute Postgraduate Student Poster Competition, Ireland 2019, sponsored by Intel.
5. Travel grant for IEEE Magnetics Society Summer School, USA, 2019.

Acknowledgements

This work is supported in part by the Platform Research Grant from "CONNECT"- a strategic Research Centre on "Communication and Future Network-Sustainable IoT" funded by the Science Foundation Ireland (SFI), and is co-funded through the European Regional Development Fund under Grant 13/RC/2077_P2; in part by the EU Horizon 2020 Research and Innovation Programme through Project "Enables" under Grant 730957.

Throughout this interdisciplinary PhD dissertation work, I did get the opportunity to collaborate with people from diverse fields, which has shaped my research mind-set and helped me grow as an early stage researcher. Firstly, I would like to thank Prof. Saibal Roy, my PhD supervisor for giving me this opportunity to work on such an emerging research topic of green energy harvesting. He has always been a great source of inspiration who believes in taking up challenges and pushing the boundaries of innovation. His advice, encouragement and enthusiasm has helped me a lot to frame this work. I would sincerely express my deepest gratitude to Dr. Andreas Amann, my co-supervisor, who is an excellent researcher and a very patient teacher. He walked me through complex mathematical problems during the weekly meetings and consistently advised on strengthening the fundamentals while driving for perfection. The discussions with him has been perhaps the best learning experience during my PhD and I cannot thank him enough for his efforts, motivation and unfailing support. I would also like to thank Prof. Peter Kennedy, my co-supervisor and Dr. Philip Murphy, my monitor, for the valuable advice and support throughout this research work. I would also sincerely thank Mike Hayes, who has been a great source of motivation in this journey. A special thanks to Dr. Anirban Bhattacharyya, my M.Tech supervisor and an insightful teacher who inspired me to pursue a research career in the field of MEMS, CMOS processing and microelectronics.

This work involves many experiments and I am very thankful to the incredible research staff and laboratory staff in Tyndall who have helped me with thorough training and useful advice from time to time. Therefore, I am gratefully acknowledging the efforts of Finbarr Waldron, Tony Compagno, Dermot Houston, Paul Tassie, Dan O'Connell, Joe O'Brien, Vince Lodge, Michael Schmidt, Donal O'Sullivan, Declan Casey, Fiona Barry, Matteo Menolotto and many others.

During my PhD life, we experienced the unprecedented situation in form of Covid-19 that has tested the limits of human resilience. In such a difficult time, staying far away from home became increasingly difficult. Thanks to my supervisor, co-supervisors, and my Tyndall family

who have always been there for me, even in such a critical time. Heartfelt thanks to Fatima Gunning, Orla Slattery, Cian O'Mathuna, and Mary Kent for consistently keeping in touch during this difficult phase. PhD is a rollercoaster ride, there are ups and downs. Friends have played a great part in overcoming the obstacles of my PhD life, weekend dinners and long coffee breaks have been rewarding breathing zones. Many thanks to Debarati Di, Swatchith, Dinesh, Sanjeev, Liudmila, Archisman, Sutapa, Suvoprasad Da, Subha Da, Tandra Di, Shree, Samvit, Vanessa, Steve, Sini and all of my wonderful office colleagues for making my stay in Cork feel like home. I owe a big thanks to my best friend Sohini, who despite of the geographical distance has always been there for me. Very special thanks to my groupmates Tuhin Da, Pranay Da and Dhiman Da, who have always motivated me and guided me to excel. I thank my partner Aritra for his support and compassion, which has always motivated me to do better.

My family, my grandparents and my parents are my greatest strength; they have given me unconditional love and unfailing support during my PhD. They made great sacrifices so that I could scale dizzy heights and chase my dreams. I express my deepest gratitude to them for having faith in me and for pushing me to achieve my goals; you mean the world to me.

Thank you
Kankana Paul

To My family and my teachers

Table of contents

Declaration ..... **i**

Abstract ..... **ii**

List of Publications ..... **iv**

List of Awards ..... **v**

Acknowledgements ..... **vi**

Table of contents ..... **ix**

List of figures ..... **xiii**

List of tables ..... **xxii**

Chapter 1: Introduction **23**

1.1 Introduction 23

1.2 Moore and More Than Moore 24

1.3 Internet of Things (IoT), the vision of a smart future 28

1.4 Wireless Sensor Nodes and the need of sustainable power source: 32

1.5 Renewable sources of energy for Wireless Sensor Network: 37

1.5.1 Solar Energy as a renewable energy source: 38

1.5.2 Thermal Energy as a renewable energy source: 41

1.5.3 RF Energy as a renewable energy source: 43

1.5.4 Mechanical energy from ambient vibrations as a renewable energy source: 46

1.6 Vibration energy harvesters- transduction principles: 49

1.7 Limitations of the linear EM generators: 59

1.8 Challenges in miniaturization of the EM-VEHs: 60

1.9 Motivation of this thesis: 61

1.10 Thesis outline: 62

1.11 References 63

Chapter 2: Theoretical background and Literature review on Electromagnetic Vibration Energy Harvesters 69

2.1 Introduction.....69

2.2 Theoretical background of Resonant/Linear Electromagnetic Vibration Energy Harvesters.....70

2.3 Resonant Electromagnetic Vibration Energy Harvesters.....75

2.4 Theoretical background of Nonlinear Electromagnetic Vibration Energy Harvesters… 84

2.5 Nonlinear Wideband Electromagnetic Vibration Energy Harvesters: 88

2.6 Micro-scale Vibration Energy Harvesters:.....100

2.7 Power management strategies for efficient power delivery 108

2.8 Conclusion: 113

2.9 References:.....**Error! Bookmark not defined.**

Chapter 3: A Meso-scale Vibration Energy Harvester for Improved Wireless Communication- A Feasibility Study..... 120

3.1 Introduction.....120

3.2 The technology gap and a potential solution .....**Error! Bookmark not defined.**

3.3 Design and fabrication of the Concertina VEH: 122

3.4 Experimental Characterization of the VEH and Discussions: 129

3.5 Design and fabrication of the NFC based sensor node: 131

3.6 Feasibility experiment of battery-less and VEH assisted NFC sensor node platform:… 134

3.7 Comparison with the state-of-the-art VEHs and envisaged IoT application: 137

3.8 Conclusion: 140

3.9 References:.....141

Chapter 4: Tapered Nonlinear Vibration Energy Harvester for Powering Internet of Things 144

4.1 Introduction....144
4.2 Technology gap and a potential solution....144
4.3 Modelling, parameter selection and fabrication of the EMVEH:....146
4.3.1 Design and fabrication of the EMVEH: 146
4.3.2 Dynamical analysis:....152
4.4 Experimental methods, results and discussion:....153
4.4.1 Spring stiffness measurements:....153
4.4.2 Open circuit condition: 154
4.4.3 Load performance:....157
4.5 Demonstration of complete Energy Harvesting solution: 162
4.5.1 Variation of Maximum Power Point for Nonlinear EM-VEH: 162
4.5.2 Powering of a wireless sensor node: 166
4.6 Conclusion:....171
4.7 Reference: 172
Chapter 5: Time resolved Eye Diagrams to exploit Hidden High Energy Branches in a Nonlinear Wideband Vibration Energy Harvester 174
5.1 Introduction....174
5.2 The knowledge gap and a potential solution....174
5.3 Frequency response: Hidden energy branch 176
5.4 Eye diagrams 180
5.5 Reduced order model:....182
5.6 Experimental methods, results and discussions: 185
5.7 Conclusion 192
5.8 References....192
Chapter 6: Design optimization of MEMS EM-VEH using Patterned Magnet Array . 194
6.1 Introduction....194

6.2 Challenge with integrating conventional bulky Permanent Magnets: 194
6.3 Patterned array of Micromagnets:.....197
6.4 Design optimization using patterned array of magnets 202
6.5 MEMS linear and nonlinear VEH with optimized patterned micromagnets 206
6.5.1 Introduction to the problem and a potential route to overcome the challenge…. 207
6.5.2 Finite element analysis (FEA) and optimization of magnetic flux density.....209
6.5.3 Design strategy 214
6.5.4 Results and Discussion 218
6.6 Conclusion 224
6.7 References.....224
Chapter 7: Conclusions and Future Work 227
7.1 Introduction.....227
7.2 Summary of the work.....228
7.3 Existing pertinent challenges and potential solutions 231
7.4 Future work, a continuation of the work in this dissertation 234
7.5 Final remarks 238
7.6 References.....239

List of figures

Figure 1.1: Evolution of advanced electronics since the invention of vacuum tube [3, 4, 6-12].

Figure 1.2: Portrays the evolution of 5nm by TSMC over the past 50 years [16].

Figure 1.3: The depiction of the different eras in the technical evolution of Moore's law [19].

Figure 1.4: The key stakeholders of Internet of Things market.

Figure 1.5: An overall view of the concept of Smart City [35].

Figure 1.6: Prediction of the extent of the IoT connected devices up to year 2025 [43].

Figure 1.7: The basic architecture of a Wireless Sensor Network for the Internet of Things.

Figure 1.8: (a) Average values of CO_2 emission over a cradle-to-gate assessment period for different batteries, (b) Emission of toxic pollutant for per kg battery production [63].

Figure 1.9: Comparison of the power consumption of different popularly used RF communication technologies [66].

Figure 1.10: Overview of the power requirements of different IoT devices [69].

Figure 1.11: Battery life comparison of commercial batteries [72].

Figure 1.12: Power consumption of (A) ICT based electronic devices and (B) IoT based portable electronic devices [73].

Figure 1.13: Schematic of the working principle of a solar cell [74].

Figure 1.14: (a) The Secchi disk for manual water clarity measurement, (b) The solar powered autonomous system for water clarity measurement [81].

Figure 1.15: (a) Schematic of typical thermoelectric generator is shown and the zoomed inset shows the connection between the p-type and n-type material. (b) Model of Multi-Mission Radioisotope Thermoelectric Generator has been shown. (c) A recently developed wearable TEG device taped to the chest of a user is shown [83-85].

Figure 1.16: Schematic of a RF energy harvester system [92].

Figure 1.17: (a) Flexible NFC based ECG patch for biomedical applications [93], (b) Schematic representation of the NFC based smart mask for real-time CO_2 detection [95].

Figure 1.18: (a) Schematic of an inertial generator representing basic working principle [99] (b) Different transduction mechanism use for harvesting energy from vibrations.

Figure 1.19: Vibration data for 'Human climbing up stairs' from the Real Vibrations repository have been shown, on the left panel the time domain signal and on the right the Fourier Transformed frequency domain signal have been shown.

Figure 1.20: (a) Batch fabricated electret-free Silicon based electrostatic generator, (b) MEMS Electrostatic VEH with finger-teeth interdigited comb like capacitor structure, (c) Thin Electrostatic sheet based generator for wireless oral health management [103-105].

Figure 1.21: (a) Trapezoidal PZT film based Piezoelectric VEH, (b) Omnidirectional Piezoelectric VEH for ultra-low frequency vibrations [107, 108].

Figure 1.22: (a) Sliding surface triboelectric generator with linear gratings for performance enhancement, (b) 3D printed triboelectric energy harvester for harnessing wind energy, (c) Teflon tape and cosmetic fixing powder based triboelectric VEH [111-113].

Figure 1.23: Illustration of Faraday's law that governs the electromagnetic transduction in EM-VEHs.

Figure 1.24: (a) Rotational Electromagnetic VEH for harnessing human induced vibrations, (b) Twist driving and ratchet-clutch based human vibration driven Electromagnetic VEH, (c) Anchorless self-powered system for powering trackside electronic devices, (d) Electromagnetic VEH for scavenging energy from vehicular suspensions, (e) 3D printed VEH for harnessing energy from the airflow of HVAC duct [114-118].

Figure 2.1: The Basic block diagram of a Single degree of freedom system.

Figure 2.2: Plot to shown the effect of the damping parameters (a) on amplitude of displacement and phase, (b) of the same of a SDOF system.

Figure 2.3: Electrical representation of Electromagnetic generator.

Figure 2.4: (a) Plot to show the effect of damping, and (b) external forcing on the average power.

Figure2.5:(a) Electromagnetic generator prototype developed by Jones et al. [4], (b) Electromagnetic microcantilever based generator demonstrated by Beeby et al. [5], (c) Macroscale electrically tuneable electromagnetic energy harvester (Perpetuum Ltd.), (d) and the corresponding variation of output power with varying load capacitance demonstrated by Zhu et al. [6], (e) Schematic representation of frequency tuning strategy developed by Zhu et al. [7], (f) Schematic representation of frequency tuning through multiple cantilevers of varying length developed by Sari et al. [8], (g) and the corresponding power output over wide bandwidth by increasing the length of adjacent cantilevers by 3μm.

Figure 2.6: (a) MEMS scale multi-frequency energy harvester chip and the MEMS device assembled with the magnet [12], (b) Schematic representation of 2DOF energy harvester [13], (c) Cross-section view of high figure of merit energy harvester with primary, secondary mass and coils [14], (d) Assembled 2DOF vibration energy harvester for tramway application [15], (e) 3DOF MEMS energy harvester with ferrofluid as lubricant [16].

Figure 2.7: (a) Tubular electromagnetic energy harvester with radially and axially magnetized permanent magnets, and coils [21], (b) Electromagnetic energy harvester with (1) coil array, (2) coil holder, (3) magnet array, (4) magnet casing, (5) in planar moving springs, (6) device housing [23].

Figure 2.8: (a) Liquid spring based electromagnetic vibration energy harvester, (top) the equilibrium configuration in the absence of external force, and (bottom) the situation when the magnet is displaced from the equilibrium due to external force [25], (b) In planar electromagnetic generator with ferrofluid as lubricant (top), arrangement of magnets in the array along with ferrofluid (bottom) [26].

Figure 2.9: Plots to show the different (a) restoring force and (b) potential energy profile.

Figure 2.10: (a) Dynamic response of a monostable nonlinear oscillator for different amplitudes of excitation. (b) Dynamic response of a monostable nonlinear oscillator for different damping conditions for fixed amplitudes of excitation.

Figure 2.11: (a) Schematic of nonlinear electromagnetic generator based on magnetic levitation [41]. (b)Human vest with energy harvester and associated electronics [42]. (c) Schematic of magnetic spring based microscale energy harvester with flexible coil [33], and (d) shows the RMS output voltage obtained from the energy harvester.

Figure 2.12: (a) Schematic of dual-Halbach array based magnetic spring assisted electromagnetic generator [32], (b) shows the Halbach array of magnets, (c) shows the springs, magnets and the series connected coils, (d) and (e) shows the mounted magnet assembly and the fabricated device respectively.

Figure 2.13: (a) Schematic of MEMS electromagnetic vibration energy harvester [30] with tuneable nonlinearity through topological variations as shown with springs A, B and C, (b) dynamic response of the different devices employing these springs. (c) Schematic representation of the stretching based spring included in energy harvesting device [28], and (d) comparison of the dynamic response with a linear counterpart.

Figure 2.14: (a) Schematic of nonlinear electromagnetic vibration energy harvester [29], and the (b) variation of spring force for different nonlinear springs.

Figure 2.15: Two different auxetic structures developed by [46] is shown in (a) and (b). (c) Shows the schematic of the piezoelectric vibration energy harvester along with the auxetic patches. The dynamic nonlinear response of the piezoelectric transducer is shown in (d) and (e).

Figure 2.16: (a) M shaped bistable piezoelectric and electromagnetic vibration energy harvester configuration [48]. (b) Schematic and (c) image of the fabricated bistable vibration energy harvester with multiple permanent magnets [37]. (d) Image of the fabricated bistable vibration energy harvester [39] and the corresponding (e) tuneable potential energy, restoring force profile.

Figure 2.17: Schematic and cross-sectional view of the goblet like bistable electromagnetic vibration energy harvester are shown in (a) and (b) respectively [49]. The bistable potential energy profile and the enveloped surface of the device are shown in (a) and (b) respectively.

Figure 2.18: The (a) tri-stable and (b) quad-stable potential energy profile of the magnetic levitation based energy harvester [50]. (c) Schematic of synergetic poly-stable piezoelectric energy harvester brick [51]. (d) Schematic of the proposed hybrid electromagnetic and triboelectric energy harvester is shown along with the image of the fabricated prototype of the electromagnetic-triboelectric harvester [53]. The SEM images at the bottom are of the PTFE nanostructure and Al-nanograss structure.

Figure 2.19: Image of (a) spiral Si-spring with mounted magnet, copper coil in PDMS mold and fully assembled MEMS device by [56]. (b) Image of in-plane moving MEMS VEH with four bar link type MEMS spring [57]. (c) Image of different components of frequency tuneable MEMS VEH by [63]. (d) Double layer microfabricated copper coil used by [64] for implementing MEMS VEH.

Figure 2.20: (a) Schematic representation of in-plane MEMS VEH with large-mass, small-mass spring structure and patterned layer of coils [66]. (b) Schematic illustration of the MEMS VEH with Silicon spring and flexible stack of coils [67].

Figure 2.21: (a) SEM image of the wafer with the silicon spring and the embedded NdFeB/Ta magnets (left) and the spiral coils developed by [70]. (b) SEM image of the in-plane moving MEMS spring with electroplated magnet array and coil layer underneath (left) as shown in the schematic (right) proposed by [71]. (c) Two MEMS VEH with patterned magnets and coils developed by [72]. (d) Top and bottom side of the parylene diaphragm based MEMS energy harvester with micromagnets comprising of wax bonded NdFeB powders fabricated by [73].

Figure 2.22: (a) Image to compare the dimension of the MEMS VEH and a coil, along with further zoomed in view of the energy harvester prototype [75]. (b) 3D schematic of the silicon based 3D solenoidal coil for MEMS VEH [76], the SEM image of the fabricated solenoidal coil is shown in (c) along with the vertical cross-section along the B-B` plane. (d) Schematic of the MEMS energy harvester with closed magnetic circuit developed by [77].

Figure 2.23: Basic voltage multiplier architecture [85].

Figure 2.24: The system architecture of hybrid harvester interface using synergistic energy extraction strategy [88].

Figure 2.25: Schematic of the power management circuit used for the hybrid energy harvester [89].

Figure 2.26: Schematic of the hybrid energy harvester interface [90].

Figure 2.27: Schematic of the power management circuit used with MEMS scale harvester [91].

Figure 2.28: Schematic of the designed power management circuit [92].

Figure 3.1: Schematic of the conceived Electromagnetic vibration energy harvester. The red arrow indicates the out-of-plane motion of the VEH.

Figure 3.2: The design of Concertina springs with (a) single stage on the outer side, (b) single stage on the inner side, (c) double stage spring in series. All have been shown along with the displacement profile for an applied force F. (d) The comparison of the spring force vs displacement characteristics for the designed springs.

Figure 3.3: The electromagnetic interaction between the coil and the magnet assembly and the corresponding variation of magnetic field lines have been shown in (a) for no displacement, (b) for 0.7 mm displacement, (c) for 1 mm displacement and (d) for 2.5 mm displacement of the magnets from the equilibrium position. (e) The variation of magnetic flux linkage and the induced voltage for different displacement of the magnet.

Figure 3.4: The first three modes of oscillation of the concertina spring structure: (a) at 78 Hz, (b) at 156 Hz, and (c) 247 Hz. The out-of-plane and torsional modes of vibrations have been portrayed.

Figure 3.5: Schematic of the experimental setup for the electrodynamic characterization of the developed linear concertina-VEH.

Figure 3.6: (a) The variation of load voltage and power delivered across the load with respect to the variation of the resistive load for the developed linear VEH with concertina springs that is shown at the inset. (b) The variation of the power delivered across the optimized resistive load as the frequency of excitation is varied. The Inset shows the level of powered delivered to the load as a function of the amplitude of acceleration.

Figure 3.7: (a) The functional block diagram of the NFC sensor hardware. (b) The developed NFC sensor hardware [24].

Figure 3.8: (a) The functional block diagram of the NFC sensor hardware when assisted with the developed concertina VEH. (b) The developed NFC sensor hardware along with the AC-DC rectification stage integrated to facilitate the rectification of incoming AC voltage from the VEH.

Figure 3.9: (a) The experimental set-up of employing the developed VEH to support the NFC sensor hardware. The VEH is placed on the shaker under the cover. (b) The variation of the rectified voltage

across the load capacitor for different amplitudes of excitation of the VEH. The inset shows the fast charging cycle of the load capacitor used in this experiment.

Figure 3.10: The variation of the power delivered by the VEH across the optimized load has been shown in (a) Demonstrates the communication range the NFC hardware provides as a function of the amplitude of excitation of the VEH. (b) The blue points show the power consumption of the NFC sensor hardware when the amplitude of excitation for the VEH changes from 0.2g to 0.6g.

Figure 4.1: Tapered FR4 spring architecture with spring arms having (a) 1 (b) 0.75 (c) 0.5 (d) 0.17 taper ratio and the variation of their (e) nonlinear restoring force, (f) principal stress distribution along the length of the beam is shown.

Figure 4.2: Detailed schematic of the prototypes P1 and P2.

Figure 4.3: (a) Schematic of the prototype P1, (b) Schematic and direction of magnetization in the coil-magnet assembly of P1.

Figure 4.4: Finite element analysis of the spring structures depicting different modes of P1 (a) and P2 (b). The variation of the spring force with the amplitude of displacement corresponding to mode-1 and the variation of spring torque with angle of rotation corresponding to mode-2, 3 have been shown. Experimentally obtained force-displacement corresponding to Mode-1 is shown (in orange).

Figure 4.5: The Instron test set-up for the measurement of force-displacement relationship of the FR4 spring structure.

Figure 4.6: (a) The open circuit voltage measurement of the prototype P1. (b) The open circuit voltage measurement of the prototype P2. Time domain signal at the inset that portrays the peculiar sharp peak of the open circuit voltage at 2g. The simulated results are shown in (c) and (d) for the prototype P1 and P2 respectively.

Figure 4.7: Variation of the load power at optimum load resistance with frequency for the prototype (a) P1 and (b) P2. The simulated results are shown in (c) and (d) for P1 and P2 respectively.

Figure 4.8: Variation of the load power with load resistance at 0.5g acceleration for P1 (left) and P2 (right).

Figure 4.9: Comparison plot of the variation of hysteresis width of P1 and P2 with external excitation amplitude.

Figure 4.10: System architecture for powering a target load through ambient Vibrational Energy Harvesting.

Figure 4.11: Variation of Load power with respect to load voltage at different level of external acceleration for P1 (a) and P2 (c). Variation of Load power with respect to load voltage at different values of excitation frequency for P1 (b) and P2 (d).

Figure 4.12: Variation of the DC voltage corresponding to the maximum power point with (a) frequency variation (b) amplitude of external force variation for P1 and P2 as obtained from Fig. 9. The adjacent flow chart (c) depicts a suitable Perturb and Observe strategy.

Figure 4.13: Overview of the energy harvesting system powering the Cypress IoT kit, (a) Logged data in the PC through wireless communication established by the BLE USB bridge (b) Logged data in the smart phone through CYPRESS BLE Beacon app when the motherboard is configured as a stand-alone wireless sensor node and it communicates through wireless bluetooth connectivity.

Figure 4.14: (a) Output voltage of the vibration energy harvester, full bridge rectifier and the charge pump circuit connected across the harvester in grey, blue and red respectively. (b) Output voltage of the charge pump circuit attached across the harvester and the current consumption of the motherboard associated with the IoT kit.

Figure 4.15: Depiction of the energy harvesting system with the target sensor node, (a) logging sensor data in laptop through the BLE USB bridge, (b) logging data directly in smart phone through bluetooth connectivity. (c) Illustration of the operable range of frequency and acceleration where the wireless sensor node could be powered by P2.

Figure 4.16: (a) Time trace of the vibration experienced in the rear part of a car recorded with data logger (Slamstick), the inset shows the frequency range over which substantial mechanical energy was found to be distributed in the car. (b) Shows the experimental set-up consisting of the rectifier, sensor node, the energy harvester unit and a slamstick (vibration data logger) to record the vibrations from the car. (c) Illustrates the number of data packets received over a small snippet of time and (d) shows the path that the car traversed around Tyndall National Institute.

Figure 5.1: Schematic view (top) and cross-section view (bottom) of the VEH. White arrows indicate the polarity of the magnets. The fabricated VEH prototype is shown at the inset.

Figure 5.2: Schematic view of the experimental set-up for concurrent experimental measurement of the load voltage and the amplitude of excitation fed to the VEH to construct the eyes.

Figure 5.3: Variation of load power with (a) conventional up and down sweep and (b) designed frequency sweep of the drive for 0.8g excitation. The top and bottom inset of (a) are the time traces of the VEH's response on up and down sweep respectively. The inset of (b) shows the time trace of the VEH's response corresponding to large power output.

Figure 5.4: (a) Shows the extent of the energy branches EB1, EB2 and EB3 for 0.8g drive amplitude. The branch EB3 is achieved through the designed frequency routine. (b) Shows the mapping of energy branches EB1, EB2 and EB3 on the acceleration-frequency plane.

Figure 5.5: (a) Plot of a nonlinear displacement and velocity as a function of time. The point *A* and *B* represents the local maxima, and *C* represents the local minima of the displacement function. (b) The electromagnetic interaction between the fixed and the moving repulsive set of magnets.

Figure 5.6: (a) Shows the dynamic response of the system using the ROM with traditional frequency sweeps, (b) shows the response with the special frequency routine to achieve the hidden high-energy state.

Figure 5.7: The eyes corresponding to the electromagnetically transduced energy for discrete values of *d* (=1mm, 2.5mm, 7mm) are shown.

Figure 5.8: With d=2.5mm, the eyes corresponding to electrical energy dissipating through involved damping are shown in (a)-(e). The eyes representing mechanical energy injection into the VEH are shown in (f)-(j). The colours of these eyes correspond to the different energy branches depicted in Fig.2(a) and Fig.3.

Figure 5.9: Variation of the deliverable power of the VEH as a function of the frequency and amplitude of the drive for d =2.5mm, (a) with conventional up and down frequency sweep and (b) with specifically designed frequency routine.

Figure 5.10: The performance comparison of the VEH topologies in terms of the extracted power across a resistive load 2kΩ for different values of interspacing between the repulsive magnets *d* (=1mm, 2.5mm, and 7mm).

Figure 6.1: The lines in figure (a) shows the magnetic field H inside and outside the material and that of figure (b) shows the magnetic induction B in and around the magnetic material. Inside material the B and H lines point in opposite direction.

Figure 6.2: FEM simulation using COMSOL to show the advantage of using micro-patterns (right) compared to a block (left) of integrated permanent magnet, minimizing the demagnetization field. Both top view (on surface of the magnets) and cross-sectional view are shown. Plots below show the variation of magnetic flux density along a line through the middle of the magnetic structures.

Figure 6.3: Variation of the average magnetic field with (a) pattern heights and (b) interspacing of the pattern elements observed at a distance of 10um above the surface of the patterned magnet structures.

Figure 6.4: Variation of average magnetic field with pattern heights observed at a distance of (a) & (b) 10 µm (c) & (d) 30 µm and (e) & (f) 50 µm above the surface of the magnetic structures for different inter-pattern gap values. The same for the continuous block of magnet is also shown in each plot as a reference. Inset show the variation of average magnetic field as a function of inter-spacing distances of the patterns with different aspect ratios (ARs).

Figure 6.5: Figure showing the design strategy to improve the electromagnetic interaction.

Figure 6.6: (a) Schematic of a simple integrated EM VEH device. Comparison of output power for various micro-pattern shapes with block height of (b) 50 µm, (c) 250 µm.

Figure 6.7 (a) shows a block of magnet (on left) and a replacement of the magnet with stripe patterns separated by a distance 'a' (on right) having out-of-plane magnetization. (b) Depicts the surface current representation of the magnets in (a). (c) And (d) shows the distribution of the vertical component of magnetic flux density on a plane that is 10μm away from the top surface of the magnet and stripe patterns respectively.

Figure 6.8: (a) Comparison of the z-component of magnetic flux density for different shapes of magnets having equal volume to that of a thin film of 10μm thickness. Plots of average magnetic flux density as a function of the total magnetic volume on a plane of observation 10μm away from the top of the array of magnets having (b)cuboid, (c)cylinder, (d)stripe-shaped elements are shown. (e) Shows schematic of the square (left) and rectangular copper coil (right) used with the stripe patterned magnets.

Figure 6.9: Proposed topologies for the MEMS EM-VEH.

Figure 6.10: Fundamental modes of oscillation of the designed (a) Linear (b) Nonlinear MEMS spring structures.

Figure 6.11: Four nonlinear spring architecture with varying nonlinear spring stiffness coefficient is presented where the stretchable springs are arranged in a way that facilitates stretching in the same direction as the central paddle moves in-plane.

Figure 6.12: (a) Variation of power density and obtainable half-power bandwidth with respect to the nonlinear spring stiffness of the different nonlinear spring architecture with mechanical damping fixed at 0.001 using topology 4 with rectangular coil. (b) Shows the variation of load power density of spring-c with frequency.

Figure 7.1: Vision of fully integrated MEMS VEH device with high normalized power density.

Figure 7.2: Nonlinear wideband flexible MEMS scale VEH comprising of flexible MEMS spring, embedded bonded magnets and high-density microcoil.

Figure 7.3: Process flow for the fabrication of MEMS spring master mold that would be used to fabricate PDMS springs.

Figure 7.4: Process flow for the fabrication and specific magnetization of bonded micromagnets.

List of tables

Table 1.1- Key parameters of Vibration Characteristics from ambient sources that are available from the Energy Harvesting Network vibration data repository [100].

Table 2.1- Nonlinear potential energy for different values of coefficients.

Table 3.1: Comparison of spring materials and associated properties of EMVEH springs.

Table 3.2: Comparison of wireless communication technologies.

Table 3.3: Comparison of state-of-the-art harvesters and their performance with the developed VEH and wireless powering system.

Table 4.1: Comparison of contemporary VEH devices with P1 and P2.

Table 5.1: Different parameters of the VEH.

Table-5.2: Parameters and their values used in the ROM.

Table-5.3: Efficiency of energy transaction from mechanical to electrical domain through different energy branches.

Table 6.1- Different parameters for the proposed topology.

Table 6.2. Structural details of the MEMS spring structures.

Table 6.3. Value of the EM coupling obtained from FEM analysis with different topologies of EM-VEH.

Table 6.4- Performance comparison of EM-VEHs.

Chapter 1: Introduction

1.1 Introduction

The first firm step of mankind towards the modern age and low power electronics was taken by the British Engineer John A. Fleming, who invented the vacuum tube in 1904/1905 [1, 2] that was soon widely used in radio, radar, early electronic computers and televisions. This was followed by the fascinating inventions of Bipolar Junction Transistor (BJT) [3] and Metal Oxide Semiconductor Field Effect Transistor (MOSFET) [4] leading to the development of Complementary Metal Oxide Semiconductor (CMOS) Transistor, which is the building block of the modern day Integrated Circuits (ICs). Gordon E. Moore, the Director, Research and Development Laboratories of Fairchild Camera and Instrument Corp. observed a significant trend and in 1965 he extrapolated that the demand of functions per chip and hence the number of components per chip in the semiconductor industry will get doubled in every 18 months [5], which would result in 65,000 components per integrated circuit chips by 1975. He also concluded that the inverse proportionality between the 'cost per component' and the 'number of components' will consequently reduce the cost of electronics chips over the years. Known as the 'Moore's law', over nearly the past 60 years, this prediction has been a reliable barometer of success for the globally leading semiconductor industries, driving them to push the boundaries of innovation. The increasing demand of faster, smaller and cheaper electronics has also driven the advancement of low power electronics towards exploring the potential of non-classical CMOS devices such as FinFET, Stacked Nanosheet FET, Carbon Nanotube transistor etc. that empowered the development of modern age computer microprocessors. On the other hand, alternatives for the CMOS based electronics such as Spintronic devices, molecular electronics, single electron transistors, quantum information processing etc. have drawn growing interest owing to the potential that they offer in scaling down the device size as well as the power consumption, while increasing the complexity and computational capabilities. These rapid advances in the domain of power-efficient electronic solutions have steered the development of 'Internet of Things' (IoT), a network of web-enabled miniaturized electronic devices that collects, acts on the physical environmental data and efficiently transfers these vital data from edge to the cloud. The following section is dedicated for the discussion of the advancements in electronics and eventually IoT that creates a perfect synergy between the physical world and the digital world.

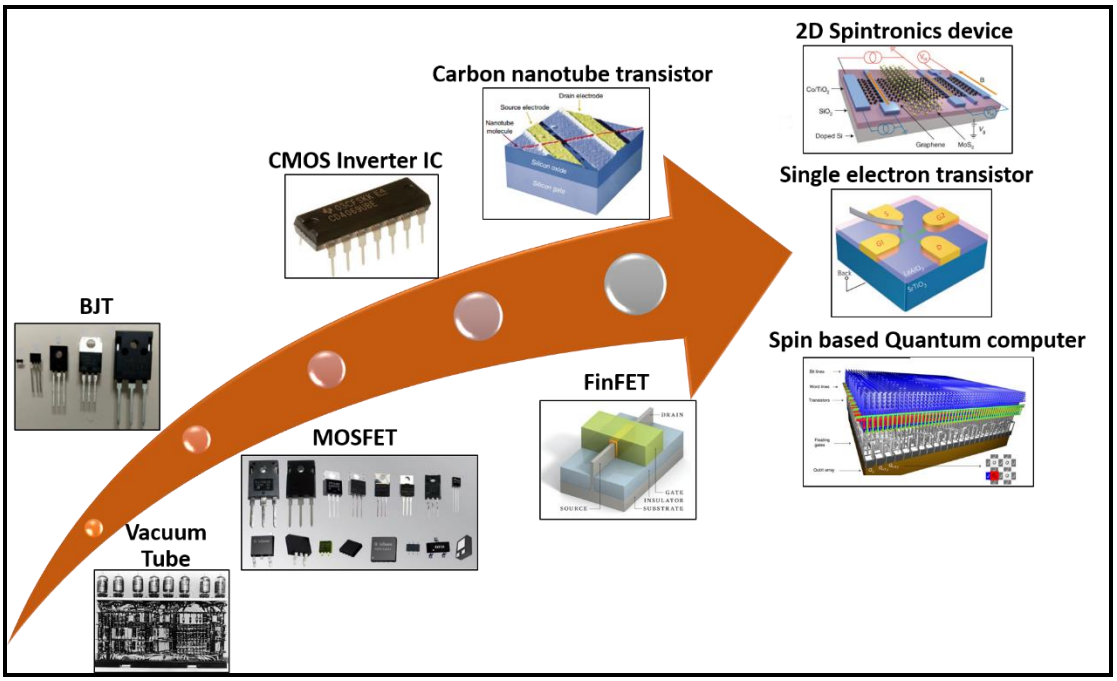


Figure 1.1: Evolution of advanced electronics since the invention of vacuum tube [3, 4, 6-12].

1.2 Moore and More Than Moore

This section presents a brief discussion on the evolution of advanced electronics over the years and highlights the key trends of this development which prepares the ground for the era of advanced electronic functionalities and integrated artificial intelligence that constitutes this concept of the 'Internet of Things'.

Ever since Gordon Moore predicted the future of electronics and semiconductor manufacturing industry following the trend of doubling the functionality and transistor density in an IC chip every 18 months, this law has become a key metric of success for the Semiconductor Manufacturing industry. Fig. 1.1 has been assembled to show the continued success of semiconductor industry in this direction by highlighting the key technologies along the way. CMOS technology has enabled packing ICs with millions of transistors while scaling down feature size (e.g. gate length or channel length, thickness of the gate insulator, distance between the closest interconnects etc.), keeping the technology trend abreast with Moore's law. Increasing complexities and the impetus towards scaling down the 'feature size' less than 100nm has led to the development of 3D transistors like FinFET [8], Gate-All-Around-FET (GAAFET) that offers key benefits like faster switching speed, lower power consumption while working based on the fundamental principle of a MOS transistor. Short Channel Effect is one of the key hindrances when downscaling the FETs to sub-10nm range, which has also been

addressed through the development of Carbon Nanotube FETs [9, 13] that offer further ease in scaling down the device footprint, high degree of electrostatic control over the gate and is a potential alternative of Silicon for small-scale electronic applications.

Leading commercial chip manufacturers have improved the performance of the produced chips in terms of footprint, speed of operation as well as cost-effectiveness. Initially the processing undertaken to produce the target chip would bear the title of the dimension of the smallest element in the chip, for example the length of a transistor gate or the half-pitch, which represents the distance between two elements on a chip [14]. However, lately the key industrial process technologies derive their name from the architecture or the generation of the design used for implementation. For examples, Intel offers the 14nm technology going beyond its 22nm node process, exploiting Intel's 2nd generation 3D tri-gate transistors to manufacture chips with increased functionalities as well as reduced power consumption [15]. TSMC (Taiwan Semiconductor Manufacturing Company Limited) is the global leader in the semiconductor manufacturing industry. Their unwavering effort towards keeping Moore's law alive also includes using Extreme Ultraviolet Lithography (EUV) in their processing for ultra-high precision chip manufacturing and improving the packing density of transistors in each chip. Fig. 1.2 depicts the evolution of the 5nm process technology [16] using EUV at TSMC over the past half-century, starting from the 3µm ancestors. TSMC now aims for commercializing N3 (3nm) and N2 (2nm) node process technology in the near future for empowering smart IoT applications [17].

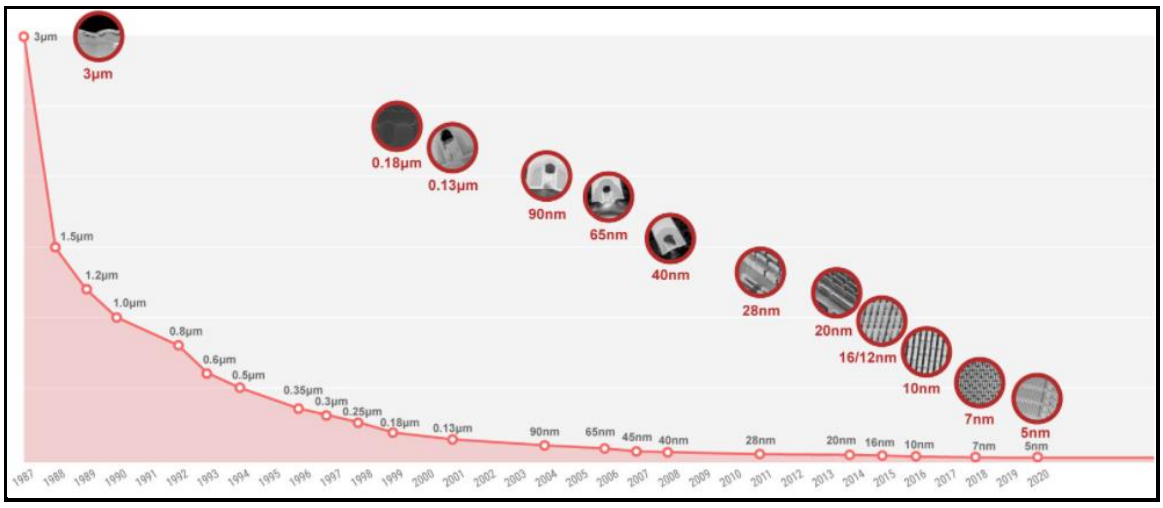


Figure 1.2: Portrays the evolution of 5nm by TSMC over the past 50 years [16].

The International Technology Roadmap for Semiconductors (ITRS), which has now become the International Roadmap for Devices and Systems (IRDS), has been a reliable guide for the semiconductor foundries and researchers, as well as for governments to guide the advancement of faster, smaller and cost-effective semiconductor device fabrication over a '15-year horizon'. The key drivers behind their projection of the 'More Moore' [18] scenario are 'High performance computing', 'Mobile computing', 'Autonomous sensing and computing' which will be achieved through novel 3D integration along with memory, non-volatile memory, logic technologies etc. to continue following the scaling indicated in Moore's law, while enhancing the device functionalities at a reduced power level and in a cost-effective way. The capability of electronic devices to facilitate autonomous sensing and computing is the key enabler of the 'Internet of Things' (IoT) that bridges the gap between the physical world and the digital world through seamless wireless communication between the deployed wireless nodes which collect data through the embedded sensors and transfers this data from the edge to the cloud.

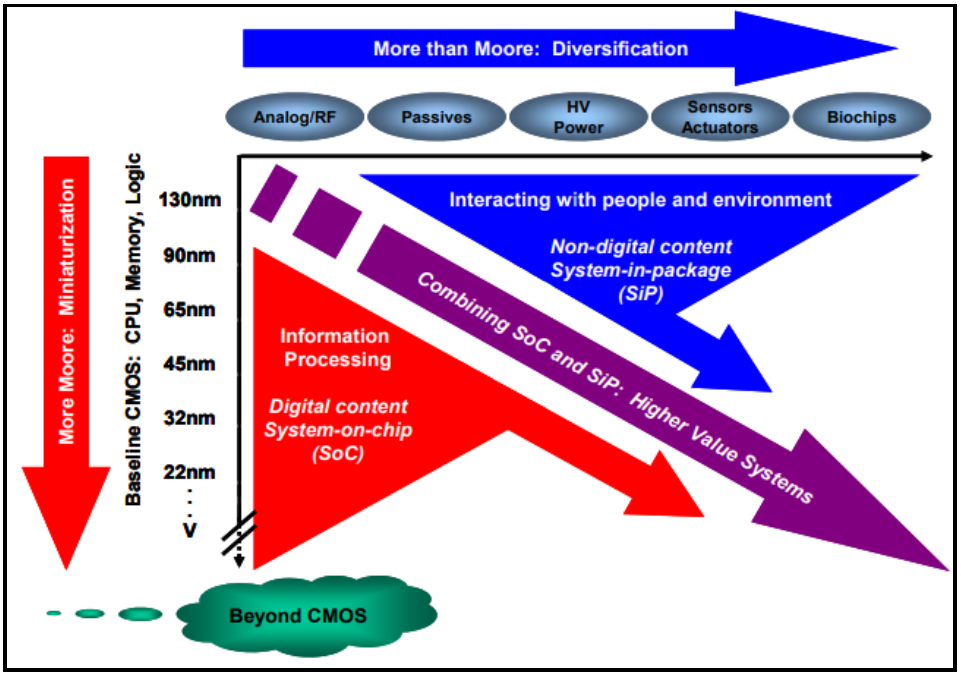


Figure 1.3: The depiction of the different eras in the technical evolution of Moore's law depicted by IRDS (International Roadmap for Devices and Systems) [19].

From the perspective of real-world applications, the power consumption of these nodes should be very low. In this context, the 'More Moore' projection [18] from IRDS anticipates

(Fig. 1.3) the development and integration of Spin-Transfer-Torque Magnetic RAM (STT-MRAM) that would empower the low power IoT-based applications. Despite the exponential pace of technology development, the drive for further scaling down the minimum feature size of the transistors and associated electronics in IC chips is becoming increasingly challenging as the sizes of these components approach the length scale of atoms and molecules (Sub-5nm range). At this length scale, the fundamental operation of the electronics changes and Quantum effects starts to play out which poses a great limitation in controlling the motion of the carriers flowing through the channels. Considering this path of scaling following Moore's law, it is predicted that in the year 2036, 'Moore's law and Quantum Physics will converge' as it won't be possible to implement transistors having a minimum feature size as small as that of an electron [20]. Moreover, the smaller the implemented device, the faster will be the flow of electrons through it, which in turns gives rise to heating issues that are undesirable for ICs. These fundamental limitations restrain the future growth of semiconductor foundries in creating highly integrated ICs with advanced functionalities. Emerging alternative CMOS technologies, or in other words 'Beyond CMOS' [21] technologies like Spintronics, Quantum Computing, Neuromorphic Engineering, Molecular Electronics etc. have paved the path for faster and highly integrated electronics platforms while addressing the heating issue arising in earlier generation electronics. The capability of performing large numbers of computations simultaneously offers the characteristics of 'parallelism' to the quantum computers [22] as well as to the neuromorphic computational devices, which dramatically increases the operational speed of these devices. The laws of Quantum physics such as Quantum Entanglement and Quantum Superposition are powerful tools [23] that are exploited to design and implement robust algorithms for solving complex and intricate computational problems, bringing a paradigm shift in the world of computation. Similarly, another alternative research interest is to mimic the distributed neural networks of the human brain in an electronics platform to implement a neuromorphic computational system [24], which enhances the speed and performance of the devices by orders of magnitude compared to the classical electronic devices, while minimizing the energy consumption of such platforms. On this positive curve of improvement, there is also a perpetual drive towards coupling Quantum phenomena with neuromorphic algorithm for implementing 'Quantum Neuromorphic Computing' devices [25]. The key performance metrics and parameters like the speed of operation in terms of the delay, the size of the device in terms of the minimum dimension that can be implemented and the cost of the implemented device often decides the fate of a technology. The maximum possible delay allowed in a classical Si-based CMOS platform is typically 1μs, which is dramatically reduced

down to 1fs (10^{-15}s) with Quantum computers [26]. Furthermore, the operational energy reduces down from 4 X 10^{-18}J per operation to 10^{-21}J per operation for Quantum systems, which illustrates the potential of this emerging technology in allowing further scaling down the electronics while increasing the efficiency of the electronics platforms in meeting the predictions of Moore.

The 'More than Moore' [19] era is empowered by cutting edge technologies that do not essentially follow Moore's law of scaling and miniaturization, but rather offer additional non-digital functionalities for translating board level systems to Systems on Chip (SoC) and Systems in Package (SiP). The additional functionalities are implemented at the system level through complex embedded software, which allows sensing, data communication, actuation, energy transaction, power management etc. in such integrated platforms. Hence, from the application point of view, embedded software and artificially intelligent networks have become intrinsic components of these complex systems, making them 'smart'. Thus the combined development in integrated electronics heralded the era of 'Internet of Things (IoT)' [27] which has essentially changed the way we measure, evaluate and communicate data from the edge to the cloud, while bridging the gap between the physical world and the digital world. In the near future, IoT is going to become an integral fabric of our society, extending its applications in diverse fields from healthcare [28], transportation [29, 30], disaster management [31], security [32], and surveillance [33] to food quality monitoring, industrial monitoring, agriculture etc.

1.3 Internet of Things (IoT), the vision of a smart future

The drive towards providing fast and uninterrupted services to the consumer through automated systems has played a pivotal role in directing the research innovations and emergence of cutting-edge commercial products. The exponential advancements in low power and embedded electronics has led to the 'Internet of Things' which connects objects/devices/sensors to the internet that communicates and exchanges data among each other as well as with the end user, forming a responsive network of 'things'. As a first stepping stone towards 'connecting things', in 1982, a group of students of Carnegie Mellon University connected a coke vending machine to the central computer network of university to ensure the availability of cold beverages in their institute [34]. Later in 1999, Kevin Ashton, while explaining the potential of Radio-frequency-identification (RFID) devices, coined the term 'Internet of Things' (IoT) [27] to promote the applicability of connecting the physical world and 'things' such as sensors, devices, systems to the internet for enhanced accessibility of the information in the form of

data. Ever since its inception, the exponential growth of the 'IoT' market is trying to build an ecosystem of digitally controlled devices embedded with diverse functionalities along with artificial intelligence (AI) and cloud based solutions. Leveraging such IoT based platforms depends largely on the identification and interdisciplinary interaction between the stakeholders in this ecosystem. Some of the key stakeholders (Fig. 1.4) in this front would be – 1) the cutting edge engineering in terms of device design, fabrication and system integration, 2) IT and Data science for integrating these devices with cloud based solutions, enabling human-free operation through advanced functionalities, 3) Finance, 4) Product management and 5) Product Operation for ensuring a positive economic return, promoting and leveraging the advancements of the devices and systems at a commercial product scale, 6) End users or consumers who will be finally using the product, while practically evaluating the efficacy of the system in providing the required service/information.

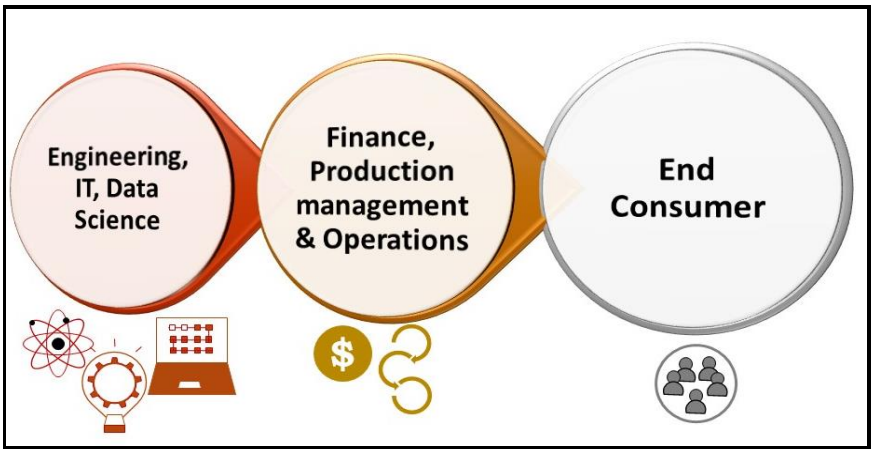


Figure 1.4: The key stakeholders of Internet of Things market.

The working principle of IoT can be explained through the basic framework of the system design, which can be divided into- 1) Perception layer, 2) Network layer and 3) Application layer. Highly efficient wireless sensors extract or sense vital data from the physical world; similarly, actuators are used to further act on the sensed data and intervene in the physical world (e.g. switching systems between off and on states, controlling humidity/temperature/ pressure of particular environments, etc.) which builds the Perception layer. This key responsibility of this layer is to convert the physical reality into digital data. The Network layer is comprised of IoT Gateways and Routers that convert process and transport the vital data from the edge devices to the cloud. Based on the application scenario, these gateways can provide additional data conditioning, pre-processing and computational functionalities. All this data storage, analysis and management is the key function of the cloud,

which forms the final Application layer of the IoT architecture. Depending on the complexity of data collection, transmission and processing, the IoT architecture can comprise more intricate layers, however functionally the above-mentioned layers define the basic working principle of any IoT driven system.

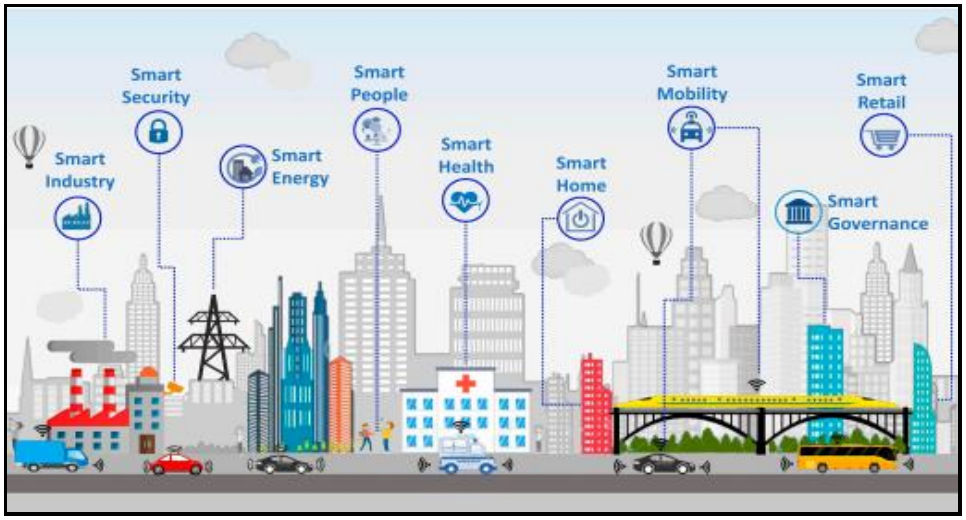


Figure 1.5: An overall view of the concept of Smart City [35].

The booming IoT market is aiding the materialization of the vision of a 'Smart City' [35], that will facilitate the regular lifestyle of humans with tailored fast service both in rural and urban areas (as depicted in Fig. 1.5). The dramatic advancements in Information and Communication Technologies (ICT) has prepared the ground for materializing the vision of ubiquitous sensing and computing of very large volumes of real-time data for Smart City. The embedded state-of-the-art sensors and actuators would communicate large-scale data at an unparalleled pace and accuracy, empowered with machine learning and artificial intelligence, these sensors would create a robust wireless network enabling a responsive and smart environment. As shown in Fig 1.5, the diverse application area of these IoT based platforms includes security and surveillance systems [36], wearable devices [37], transportation systems [38], smart farming [39], environmental monitoring systems [40], retail service [41], etc. The surge in the demand for IoT connected devices in urban and rural life steers the anticipation of over 30 billion IoT based connections to be all around us by 2027 [42] with a Compound Annual Growth Rate (CAGR) of 13%. IoT Analytics (Fig. 1.6) have predicted a slightly lower value of 27 billion IoT connections by the year 2025 [43]. It is to be noted that, depending on the analysis and the impact of Covid-19-induced chip shortage; these projections may vary considering the dynamic nature of the market. Irrespective of this fact, such an expanding

market for IoT would have a potential impact on the global economy resulting in an economic return on the scale of $3.9 trillion to $11.1 trillion per year by 2025 [44].

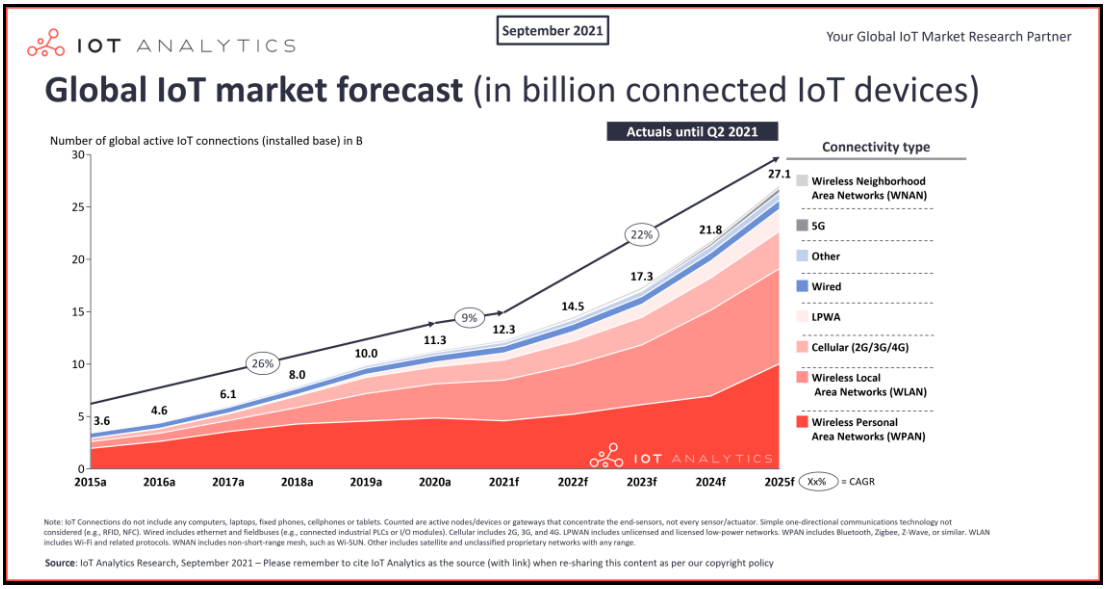


Figure 1.6: Prediction of the extent of the IoT connected devices up to year 2025 [43].

The explosive growth of the utilization of connected wireless devices has given rise to a paradigm shift in the industrial world, grounding the concept of 'Industrial Internet of Things' (IIoT) which aims to improve industrial operations and productivity as well as the industrial economy. Instead focussing on individual users, the IIoT pivots overall industrial transformation by implementing Machine to Machine (M2M) connections empowered by machine learning, enabling a human interference free, autonomous production line/supply chain that is more cost and time effective and more economically sustainable. These advancements have accelerated the fourth industrial revolution, also known as Industry 4.0 [45] that would cast a remarkable positive impact on the overall socioeconomic balance. Irrespective of the target application area, the most significant components of the IoT framework are the wireless sensors, which are deployed at the edge of the architecture allowing them to interact closely with the physical world to sense, collect/transmit significant volumes of data. Hence, in the following section, a comprehensive discussion on the architecture, functionalities and required power source for these wireless sensors is presented.

1.4 Wireless Sensor Nodes and the need of sustainable power source

Wireless Sensor Nodes are the integral components of IoT; billions of these deployed sensor nodes together form a Wireless Sensor Network (WSN) through which they extract data from real world environment and exchange data seamlessly among each other, and further communicate this data to the end user. Functionally, wireless sensor nodes are comprised of four major components dedicated for-1) Sensing, 2) Computing, 3) Communicating, 4) Energy Supply, Storage and Power Management, as shown in Fig 1.7. The sensors, being the edge devices, are perhaps the indispensable components of the WSN that are responsible for measuring a physical quantity, or variation of physical parameters and for converting this information into equivalent electrical/electronic signals that can be processed by microcontrollers/computers. Popularly used types of sensor include mechanical sensor (pressure sensor), motion and position sensor (accelerometer, gyroscope), temperature and humidity sensor, chemical and biochemical sensor (gas sensor, smoke sensor). Following the data acquisition stage, the data needs to be processed and conditioned through high volume computations, which are executed by the embedded microcontroller units (MCUs). Typically, the MCUs are composed of processor, memory and I/O peripherals. The binary data reaches the processor unit through the I/O peripherals; upon receiving this data, the processor performs arithmetic/logical operations and in some cases communicates specific commands to other embedded components. Next, the information is stored in pre-programmed volatile or non-volatile memory and finally the required data is communicated through the I/O interface. For a large chunk of IoT applications, commercial PIC microcontrollers [46], AVR series microcontrollers [47], MSP430 microcontrollers [48], PSoC microcontrollers [49] etc. are used, and for dedicated ultra-low-power applications, state-of-the-art microcontrollers are developed with tailored characteristics (e.g. high volume of edge computing) and power requirements [50, 51]. Following the data processing and storage, the next critical function of the WSN is the communication of the data at the prescribed rate wirelessly around a required radius of distance from the sensor node, which is performed by the transceivers, that comes with the functionalities of transmitting and receiving the processed information. Wireless media like RF transceiver, Infrared, Laser are often used for the data communication, with a predominance of RF technologies like NFC [52], WLAN [53], Bluetooth [54], Zigbee [55], LoRaWAN [56], RFID [57], SIGFOX [58] etc. that cover a wide range of data transmission rates, communication ranges, and transmission power. Depending on the target application area, the compatible communication technology is chosen.

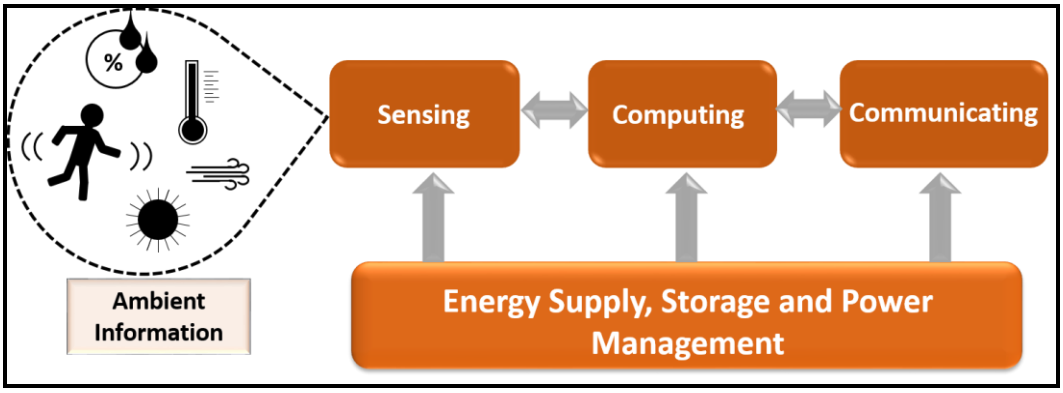


Figure 1.7: The basic architecture of a Wireless Sensor Network for the Internet of Things.

The energy storage unit of the WSN supplies the required power to the sensors, microcontroller, radio transceiver and other associated components such ADC (Analog to Digital converter), DAC (Digital to Analog Converter), I/O peripherals etc. Commercial batteries are a popular choice as the energy storage and power source of the WSNs. Broadly the batteries can be categorized as- 1) Primary battery (Zinc-Carbon, Alkaline, Lithium cell batteries) that are commercially available in wide range of sizes and have limited lifetime (not rechargeable), 2) Secondary battery (Lithium-Sulphur, Lithium-ion, Lead-Acid batteries, etc.) which withstand a large number of charge/discharge cycles, making it an attractive choice for portable electronic devices like laptop, mobile phone, etc., 3) Fuel cell battery (that are majorly used in fuel cell vehicles), 4) Flow battery (Vanadium based redox batteries that uses chemical reactions for generating the energy) and 5) Supercapacitor (comprises electrolyte and two electrodes separated by an insulating material) that offers the unique benefit of fast charging and high lifetime, making it a potential candidate for a wide range of IoT based applications.

Despite the advantages and commercial availability of high capacity batteries, the widespread deployment of WSNs is highly restrained due to critical limitations of these batteries. Firstly, the lifetime of these batteries, although they have been improved significantly over the past decade, is still finite [59-61] and hence needs to be replaced over a specific time interval, which poses a great challenge in terms of the fit-and-forget (once deployed, in principle, the WSN should not need any maintenance) type operation of the WSN. With the rapid advancement of low-power electronics, the sensors and microcontrollers of WSNs are provided with multiple additional functionalities, which come together with heavy computational load that potentially would deplete the charge from the battery faster, requiring frequent replacement, increasing the cost of maintenance. Secondly, the increasing production

of batteries are in turn increasing the demand of the raw materials [62] of these batteries such as Lead, Lithium, Cobalt, Zinc etc. which not only perturbs the socio-economic balance around the mining industry but are also harmful for the environment, particularly the tremendous environmental hazard they are likely to produce during their disposal at the end of their lifecycle.

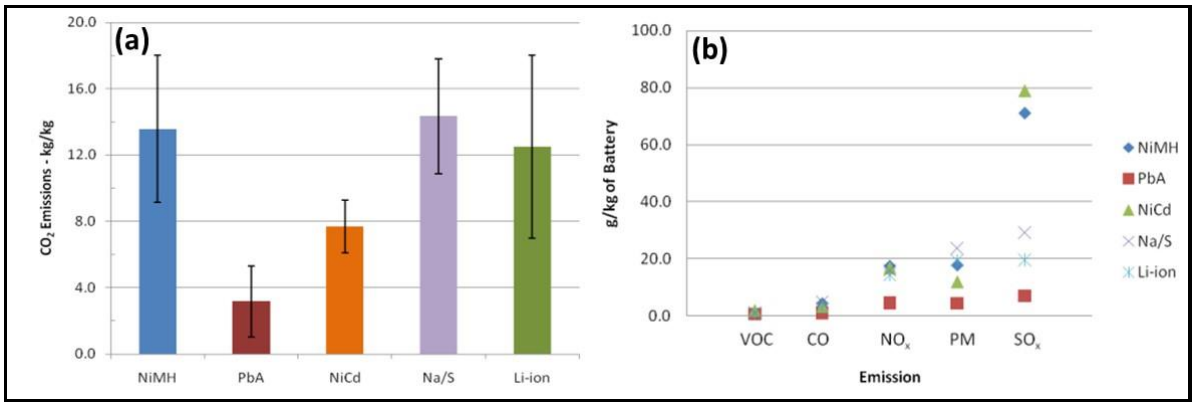


Figure 1.8: (a) Average values of CO_2 emission over a cradle-to-gate assessment period for different batteries, (b) Emission of toxic pollutant for per kg battery production [63].

Fig. 1.8(a) shows the average value of the harmful CO_2 emission over a cradle-to-gate assessment (lifecycle of the product from resource extraction to the factory) period per kg for the production of various batteries and Fig. 1.8(b) shows the emission of other toxic pollutants such as volatile organic compounds, carbon-monoxide, various oxides of sulphur and nitrogen along with fine particulate matter [63]. Hence, considering public health and safety as well as environmental wellbeing, the replacement of batteries with a carbon-neutral/green-energy source is of utmost urgency. Thirdly, the limited lifetime and the need of frequent replacement of the batteries is a key constraint in the ubiquitous deployment of wireless sensor nodes at inaccessible locations such as deserts [64], forests [65] or in high-risk environments such as radioactive zones, mines, etc. where the rough terrain and cluttered environment makes it extremely difficult for a human to perform periodic system maintenance activities. Furthermore, the bulky volume of the battery restraints efficient system miniaturization down to the MEMS scale, in fact occupies significant volume in the WSN system compared with other components; this is undesirable, especially for wearable IoT based applications.

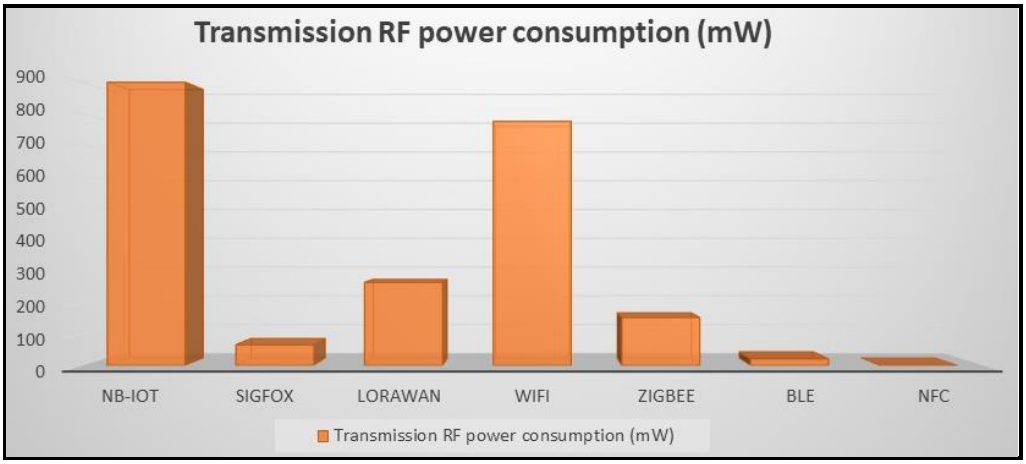


Figure 1.9: Comparison of the power consumption of different popularly used RF communication technologies [66].

Fig. 1.9 depicts the average power consumption during data transmission of the widely used RF communication technologies [66] such as NB-IoT (NarrowBand Internet of Things), SigFox (a French global network provider), LoRaWAN (Long Range Wide Area Network), WiFi (Wireless Fidelity), ZigBee, BLE (Bluetooth Low Energy), and NFC (Near Field Communication). The power consumption of NB-IoT is significantly large owing to the large communication range (10000m) that this technology offers, and the power requirement dramatically reduces from 900mW for NB-IoT to 0.198mW for NFC primarily driven by the lower range of communication (0.07m). The WSN draws power from the installed battery during the active, sleep and idle mode of operation; hence, the power demand depends on the distribution of these modes over the cycle of operation. Experimentally the current consumption during the transmission/reception cycle has been shown in [67], which peaks at 25.4mA for LoRaWAN, and 393µA for Bluetooth IoT system, while both the system operates with a typical 3-3.3V DC supply from battery. Along with experimental evidence [68] have demonstrated that the radio broadcaster of an IoT device extracts 75% of the energy that is fed to the system, whereas the microcontroller takes only ~25% energy for the processing, computation and transfer of the acquired data. Fig. 1.10 here extracted from [69] shows the typical power consumption range of different IoT controlled devices and sensors. The power demand largely depends on the functionalities of the sensor node as well as on the chosen wireless communication protocol.



Figure 1.10: Overview of the power requirements of different IoT devices extracted from [69].

Together with several rural, urban, and industrial applications, WSN finds its place in niche and critical application area such as earthquake detection and notification [70], flood detection [71] etc. where the unpredictable nature of the occurrence of these events calls for extremely accurate measurements throughout a year. Now this in turn would require a high efficiency sustainable power supply as the energy depleting batteries may ruin the chance of picking up the critical signals for the disaster management. The commercial alkaline batteries dissipate the stored power very quickly, for example with an average current of 5mA; the battery would have only 700mAh as shown in Fig. 1.11. [72]. Hence, to promote the uninhibited growth of IoT devices for materializing 'Smart City', the WSNs need to be autonomous, self-powered, capable of producing power on-the-go. Scavenging clean energy from ambient sources has therefore become an attractive alternative of energy limited bulky batteries to perpetually power the wireless sensor nodes efficiently and sustainably, thereby offering a carbon-neutral/green power source in the ever-expanding field of IoT.

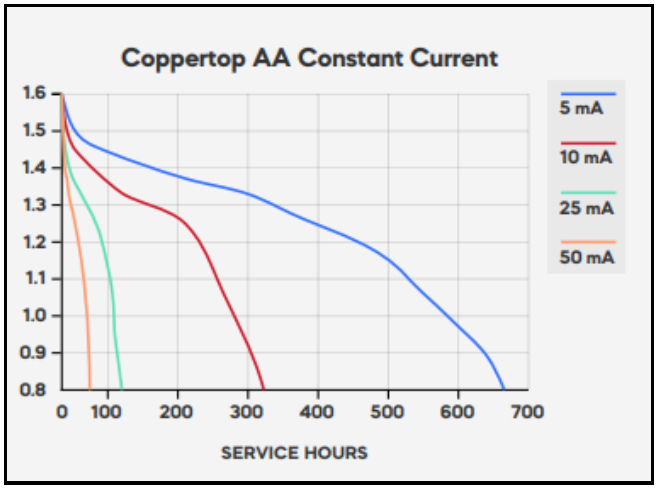


Figure 1.11: Battery life comparison of commercial batteries [72].

1.5 Renewable sources of energy for Wireless Sensor Network

Rapid technological advancements in the design of microsystems and wireless platforms has opened up the avenue of emerging applications of WSNs including in-situ health monitoring, structural health monitoring, smart agriculture, food safety/security, autonomous transport etc. It is anticipated that "78 million batteries will be dumped every day by 2025" [73] which prepares the ground for the development of sustainable power source that reliably replaces battery, majorly outpacing them in energy density and service time. With the rapid advances in low power electronics, the portable electronic devices, data logger and transmitters, MEMS sensors together with ultra-low-power microcontrollers have significantly reduced the overall power requirement of typical WSNs as shown in Fig.1.12. Hence, the low power electronic devices, which demands low power ranging from hundreds of Nanowatts to Hundreds of Microwatt, matches well with the deliverable power of the renewable energy sources.

Harvesting energy from omnipresent ambient vibrations has captivated significant research attention over the past decade as a potential solution to address the powering issue of various IoT based platforms. This section presents an introduction to different available ambient energy sources and further through a detailed discussion points out the efficacy and present challenges of using the omnipresent vibrational energy to solve the continuous powering issue of WSNs.

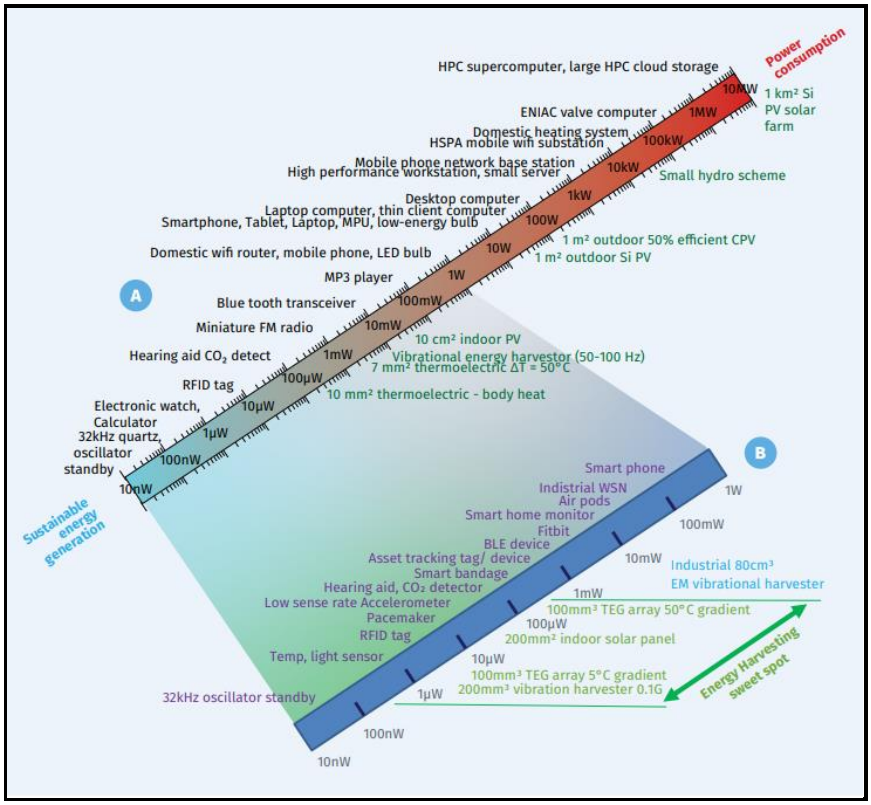


Figure 1.12: Power consumption of (A) ICT based electronic devices and (B) IoT based portable electronic devices [73].

1.5.1 Solar Energy as a renewable energy source

Solar energy is inexhaustible and it is a form of clean energy that can be scavenged to meet the power requirements of IoT systems. The photovoltaic (PV) cells, which are typically optoelectronic devices composed of p-n semiconductor layers, absorbs large collection of incoming photons from the sunlight, and directly converts it into electricity through the flow of electrons and holes in the semiconductor device (Fig. 1.13). One of the important key performance indicator of a PV cell is the maximum efficiency of the PV cells in converting the incident photons to usable electrical energy can be represented as-

$$\eta_{max} = \frac{P_{max} \times 100\%}{P_{inc}} \tag{1.1}$$

Where, P_{max} is the maximum electrical power that can be extracted from the PV cell, P_{inc} is the solar power incident on the cell (which is the product of the area of the PV cell and the incident solar radiation flux). Therefore, larger the active area (area where the solar energy is absorbed), higher will be the available electrical power from the PV cell. A significant fraction of the incident solar energy is reflected from the surface of the cell, and the rest gets absorbed

into the material, a part of which again is lost in the semiconductor in the form of dissipated heat (due to the hole-electron recombination). Hence, for optimal power extraction the use of high-quality anti-reflection (AR) coatings or alternatively micro/nano-structured surface are used to minimize the loss due to surface reflection and the recombination loss is addressed by including a passivation layer (Silicon-dioxide or Silicon-nitride) on the PV cells that inhibits the rate of charge recombination. Broadly, the PV cells are classified based on the constituent type of semiconductor material- monocrystalline cell, polycrystalline cell, and thin-film cell.

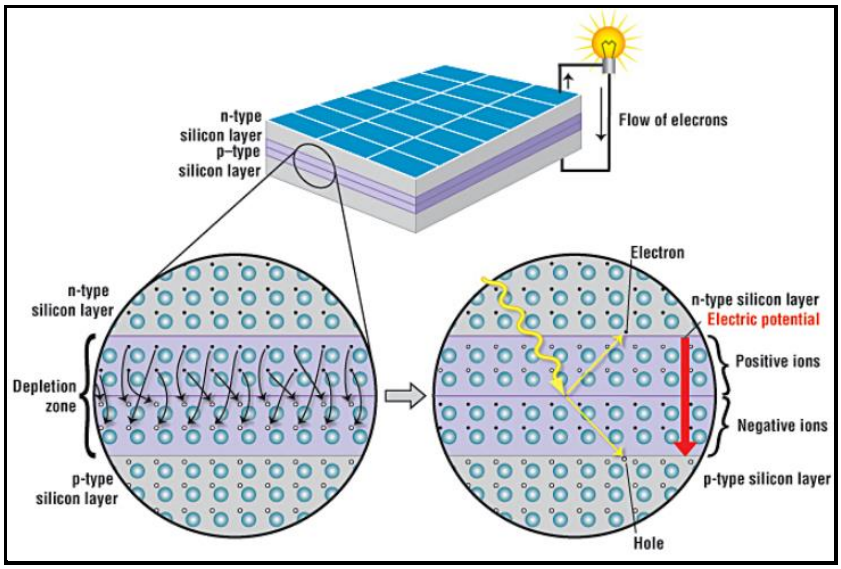


Figure 1.13: Schematic of the working principle of a solar cell [74].

Typically, the monocrystalline PV cells demonstrated average efficiency of 15%-20% when subjected to strong incident energy [75], which has been improved to 26.7% in a Silicon monocrystalline cell by Kaneka Corporation [76] that yields a power density of 26.7mW/cm^2. Recently, a detailed experimental roadmap has been presented to realize a 31% efficiency in thin crystalline-silicon PV cell [77]. However, by virtue of being an indirect bandgap material, silicon crystals are weak solar energy absorbers, which results in reduced solar energy conversion efficiency for indoor conditions where the sunlight irradiance reduces (outdoor irradiance 100-1000W/cm^2, indoor irradiance 1-10W/cm^2 [78]). Considering the wide range of IoT based indoor applications, development of high power density PV cells that are capable of harnessing significant energy from indoor conditions is extremely important. Thin-film PV cells (for example, GaAs) although offer larger power densities of 16.6μW/cm^2 and 92.2μW/cm^2 for 200lx and 1000lx indoor illumination settings [79], but the fabrication cost of growing epitaxial layers hinders the widespread use of these PV cells in urban, rural indoor and outdoor applications. Apart from these, multi-junction PV cells, perovskite cells and more

recently organic PV cells have been developed to enhance the efficiency of solar energy extraction from these photoelectronic devices.

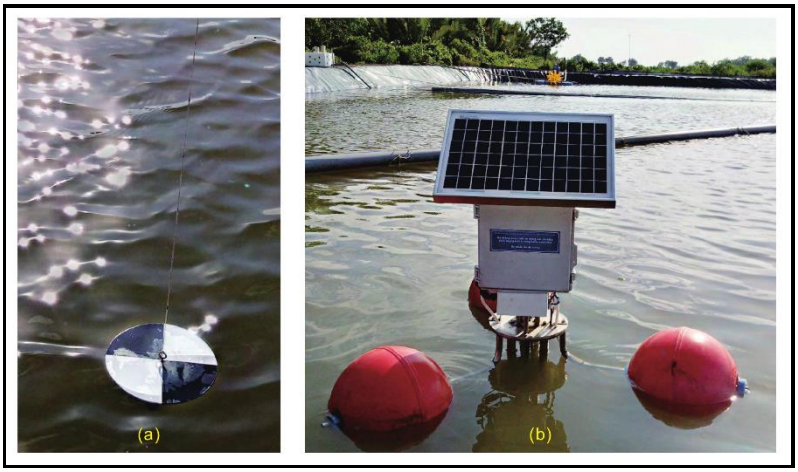


Figure 1.14: (a) The Secchi disk for manual water clarity measurement, (b) The solar powered autonomous system for water clarity measurement [81].

The abundance of solar energy in open fields has made solar energy based IoT system a potential candidate for implementing 'smart irrigation'. Recently, [80] developed an autonomous solar powered IoT system that monitors the soil moisture, humidity, temperature of a farm and based on the requirements, this system controls the irrigation pumps to improve the quality of the crops. On the other hand, for the perpetual monitoring of water quality, [81] have developed a self-powered IoT system deployed in buoys that harnessed required electrical power from solar energy and measures the clarity of water, replacing the manual Secchi disk measurements (Fig. 1.14). The omnipresence, lack of harmful emission (as in the case of fossil fuels), and the ease of integration with electronic systems are the key advantages offered by PV technology in the context of IoT applications. However, the prominent drawback of this technology are-

- Solar energy is not steadily available throughout the day, the intensity and span of availability largely depends on the geographical location, time of the day and of course the weather conditions. Hence, additional energy storage element (rechargeable batteries, supercapacitors etc.) would be an essential requirement for perpetually powering a WSN through solar power.
- For indoor IoT applications (such as building condition monitoring, smart office etc.), the irradiance reduces dramatically by three to four orders of magnitude which poses a

great challenge in the implementation of high conversion efficiency PV technology for WSNs.

1.5.2 Thermal Energy as a renewable energy source

Thermal energy is a ubiquitous renewable energy source that can be captured and converted into electrical power through dedicated thermoelectric generators (TEGs) which are solid-state devices comprising of p-type and n-type legs (large array) that are connected electrically in series but thermally in parallel, forming a TEG module. When these TEGs are subjected to a temperature gradient on both ends of the semiconductor pillar, then the majority charge carriers from the semiconductors starts flowing. This drives the negative charge carriers from the n-type leg to the p-type leg, which results in a current flow from the cold to the hot side of the TEG, conversely for the p-type material the current flows from the hot side to the cold side (Fig. 1.15). On externally connecting this device, a current proportional to the temperature gradient flows through the external circuit, which could be harvested as useful electrical energy across a suitable load. This effect of a potential difference build-up arising from the diffusion of charge carriers which migrates from the hot to the cold side in the presence of a temperature gradient across the device, is called Seebeck effect [82], after the name of the German scientist Thomas Johann Seebeck who invented this phenomenon.

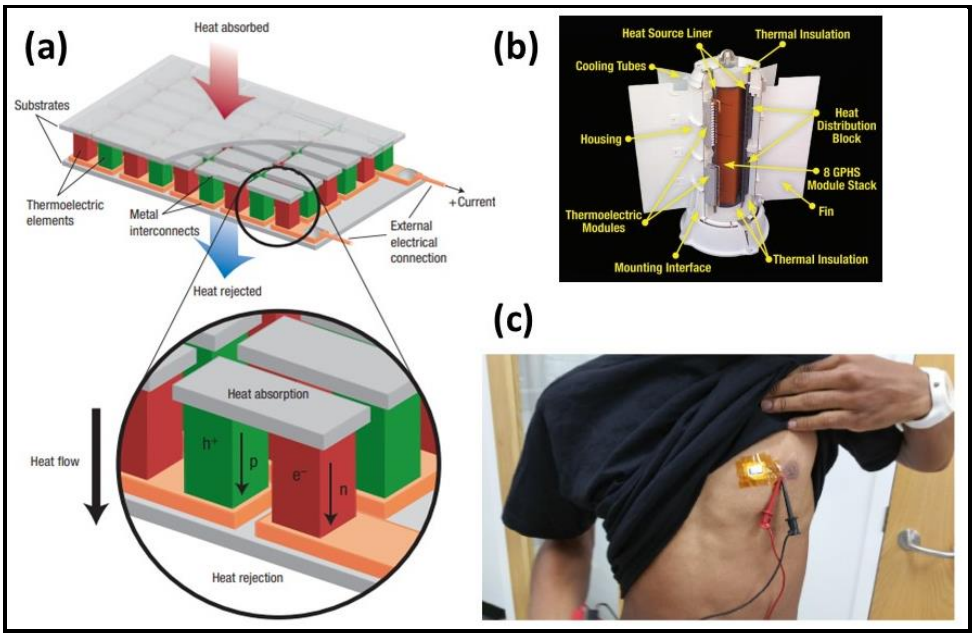


Figure 1.15: (a) Schematic of typical thermoelectric generator is shown and the zoomed inset shows the connection between the p-type and n-type material. (b) Model of Multi-Mission Radioisotope Thermoelectric Generator has been shown. (c) A recently developed wearable TEG device taped to the chest of a user is shown [83-85].

The p-type and n-type materials have positive and negative Seebeck coefficients ($S = -\frac{\Delta V}{\Delta T}$ in the unit of Volt/Kelvin) respectively, which is a measure of the thermoelectric voltage that is induced across these semiconductor materials when subjected to a temperature gradient. The figure of merit of a TEG is defined as-

$$zT = \frac{S^2\, G\, T}{\kappa} \tag{1.2}$$

where, S is the Seebeck coefficient of the material, T is the temperature gradient that the TEG is subjected to, G is the electrical conductance and κ is the thermal conductance of the respective material. Hence, high electrical conductance, low thermal conductance, large seebeck coefficient are the key parameters that pivots the material selection for constructing a high efficiency TEG. However, these material properties are interconnected, making it difficult to tailor and optimize one parameter without affecting the other parameters, for maximizing zT. Bismuth Telluride (Bi_2Te_3) have been popularly chosen as the thermoelectric material for research as well as for industrial applications, however, the low zT value (~1) of this material has obstacled the efficiency of the TEGs and restricted its application. Other materials like Silicon Germanium (SiGe) alloys and Lead Telluride (PbTe) offers higher temperature of operation (up to 900K) owing to the large melting point. PbTe have been well used in NASA spacecraft [84] for implementing large efficiency TEGs operating at high temperatures (Fig. 1.15). There also has been significant research interest devoted towards the development of low-dimensional nanostructured thermoelectric materials by introducing complex boundaries and interfaces into the material [86]; however, the intricate processing of these materials burdens the cost of the TEGs, reducing their commercial applicability. Controlled flow of electrons and phonons through the superlattices of the Bi_2Te_3/Sb_2Te_3 thin films have yielded a high zT value of ~2.4 [87] at room temperatures. Further, improved carrier mobility in n-type SnSe crystals have experimentally demonstrated a high zT value of ~2.8 [88] at 773K temperature.

The thermoelectric effect has been well used in these energy harvesters that are small, light-weight, doesn't cause any noise and can work for long hours even under harsh environment and most importantly gives out very little noise and emission. The TEGs find wide range of applications in automobile industry, naval industry and aerospace applications, ease of scalability makes it an attractive candidate for harvesting waste heat from human body through different wearable TEGs such as- [89] developed a thermoelectric polymer coated fabric for harvesting body temperatures which could become a reliable power source for IoT

systems, [85] realized a TEG powered wearable health and environment monitoring system (Fig. 1.15). Despite of these advancements, the widespread production and use of TEGs at commercial scale is still a matter of concern due to the low efficiencies of the thermoelectric materials, and the lack of large operational temperatures (apart from industrial environments) which favours high zT values, have restricted the usage of thermoelectric devices.

1.5.3 RF Energy as a renewable energy source

Radio Frequency (RF) energy is also present in our surrounding as well as in dedicate sources, which can be harnessed and converted into electrical power to provide an alternative of batteries in IoT based application. In recent years, with the rapid advancements of electronics, especially the popularity of mobile electronic devices and the omnipresence of digital television signal (Ultra-High-Frequency, UHF, 300-3000MHz), mobiles phones (900-950MHz) with 2G, 3G, 4G connectivity, WiFi signals (2400-2483.5MHz), that are rich in RF energy have pivoted an upsurge of interest to exploit RF energy for energy harvesting as well as for information processing and transmission. RF energy, that is spread over the frequency span of 3kHz-300GHz, is transferred and coupled majorly in three forms- 1) RF energy transfer and harvesting, which is a far field technology that allows the antenna in the energy harvesting system to harvest RF energy transmitted by a distant source and to subsequently convert this harnessed energy in electrical power, 2) Inductive coupling, that is a near field technology, encompassing the electromagnetic interaction between two coils tuned to matched resonances allowing wireless electrical power transfer through coupling, 3) Magnetic resonance, that is again a near field technology but contrastingly in this case the energy generation and transfer between the two coils is facilitated through the evanescent mode coupling between the two coils.

RF energy harvesting systems can be broken into the primary components as shown in Fig. 1.16. Antenna is the essential frontend component of the RF energy harvesting system, which is responsible for receiving and transmitting the electromagnetic waves [90]. Following this antenna, an impedance matching circuit is the next component, which matches the impedance between the antenna and the follow up circuitry to maximize the power transfer. Next, the alternating signal obtained from the matching circuit is rectified, if required, then amplified to a fixed DC voltage which could be used to power the load electronics (wireless sensor nodes in case of IoT based applications). Considering air to be a predominant medium of transmission between the transmitting antenna and the receiving antenna, the efficiency of the RF energy harvesting can be expressed as [91],

$$\eta_{air} = G_t \left(\frac{\lambda}{4\,\pi\,r}\right)^2 \tag{1.3}$$

Where, G_t is the gain of the transmission antenna, λ *is* the wavelength of transmitted RF signal, r is the distance of the point of observation from the transmitting antenna or the range of communication. Hence, the routes for maximizing this efficiency are increasing the gain of the receiving antenna by enlarging the geometrical footprint of the antenna, which is unrealistic for majority of IoT based applications that utilizes miniaturized system components for majority of the applications. Reducing the range of communication and the wavelength of transmission, both of these parameters depend on the requirements of the target application.

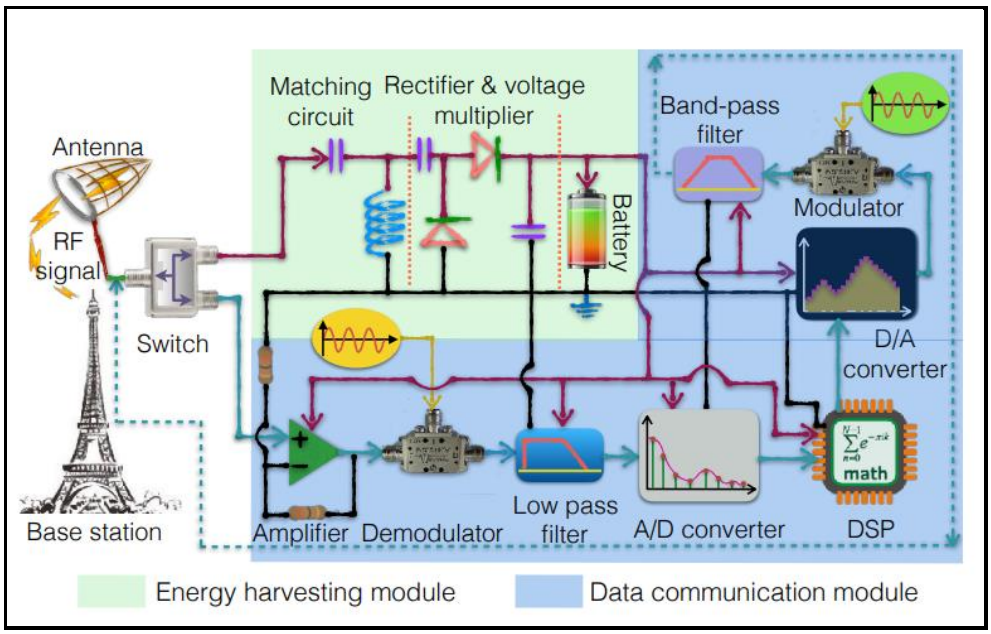


Figure 1.16: Schematic of a RF energy harvester system [92]

Over the past decade, Radio Frequency Identification (RFID) technology has been greatly exploited in asset tracking, contactless payment, security, logistics, access control, authentication etc. that majorly encompasses near field communications operating at 13.56MHz band. The installation of NFC technology in smartphones have boosted the development of this communication technology owing to its inherent low power requirement and on-call data acquisition facility (with smartphone as the reader, the installation cost for the reader infrastructure reduces substantially). By virtue of being a short-range communication protocol, the efficiency of the NFC system depends on the type of reader, size of the NFC antenna, inductive coupling between the reader and the antenna, the impedance matching between the transmitting and receiving end etc. The low cost, small footprint and ease of integration of NFC based systems have opened wide range of urban, rural, industrial and

healthcare applications. An NFC communication based wearable flexible ECG sensor patch has been developed by [93] that monitors and communicates bio-signals acquired from the ECG to a smartphone, establishing a robust bio-medical health monitoring system (Fig. 1.17). A battery less continuous physiological monitoring system with NFC sensors integrated on human body (temperature sensor node, strain sensor node, gyroscope), near field relay on the clothing that connects the wireless readers directly to the sensor nodes [94] and established distant (~1m) wireless power as well as data transfer around a human body while establishing a real-time physiological observation that could be exploited in athletics, clinical diagnostics etc. In a very recent work, a flexible battery-less NFC sensor based CO_2 monitoring system in medical grade facemask (FFP2) has been developed (Fig.1.17) that reduces the health risk of rebreathing CO_2 while wearing facemask to reduce spreading the novel coronavirus [95].

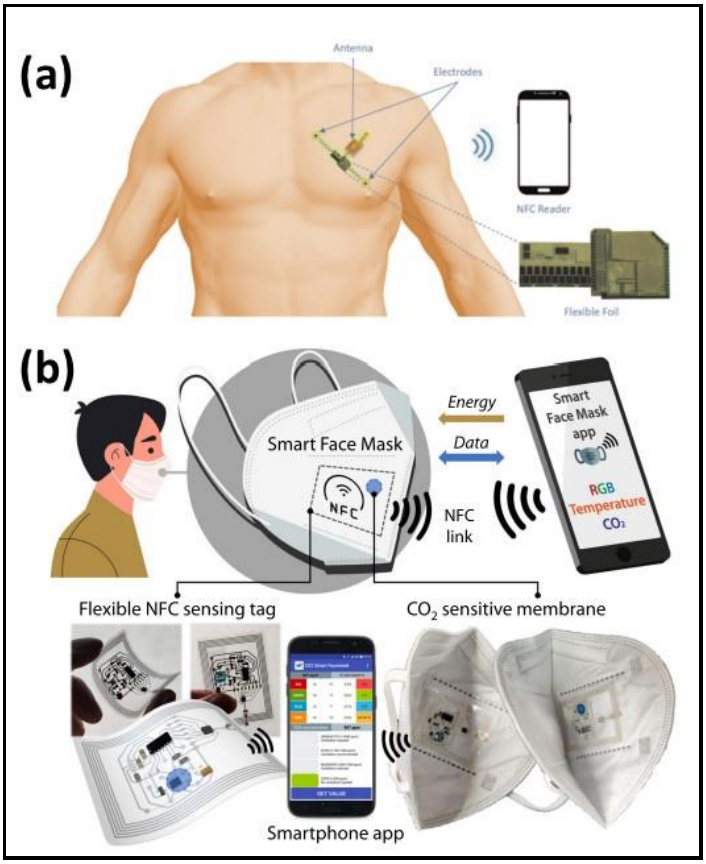


Figure 1.17: (a) Flexible NFC based ECG patch for biomedical applications [93], (b) Schematic representation of the NFC based smart mask for real-time CO_2 detection [95].

Although, the RF energy harvesting system offers distinct advantages and there is a growing interest in exploiting this technology for IoT, however, the low power density [96-98] and the large dependence of the efficiency on the transceiver performance poses a great

challenge in wide applicability of these harvesters for powering sensor nodes in IoT environment.

1.5.4 Mechanical energy from ambient vibrations as a renewable energy source

The drive towards the implementation of a sustainable power source as a replacement of batteries for WSNs have steered the growing interest in utilizing ambient mechanical energy available from surrounding vibrations through suitable transducers to obtain the required electrical energy. The ubiquity of vibrations in rural, semi-urban, urban places and in industrial environment makes it an attractive candidate among the other clean energy sources. The availability and characteristics of vibrations, although cannot be predicted, but is mostly available all through a day spread over ambient sources like vehicles (bus, truck, train, car, tram, airplane etc.), roadway, operational machines (pump, motor, air conditioning system, washing machine etc.), and most importantly the human body (running, walking, climbing up stairs, pace of heart etc.). Hence, through a suitably designed transducer, ample mechanical energy could be scavenged from these vibrational sources, otherwise unused.

Broadly, these transducers comprise of a spring structure that exhibits motions using the desired degrees of freedom, mass of the system, which often acts as the central load for majority of the transducers, dampers including mechanical damping, parasitic damping, electrical damping etc. On external excitation, the spring architecture of these transducers start to oscillate with respect to the position of equilibrium. Depending on the transducing mechanism used, the energy extracted from the external vibration is converted into electrical energy, which is obtained across a suitable load. As shown in Fig.1.18 (a), these transducers can be represented through the key functional components, and the power outcome over a period of oscillation from such a device can be represented as [99]-

$$P = \frac{2\, Y_0\, Z_0\, \omega^3\, m}{\pi} \tag{1.4}$$

Where, m is the proof mass, ω is the frequency and Y_0 is the amplitude of excitation, Z_0 is the maximum internal displacement. In principle, the mass of this system exhibits motion and performs work against the damping forces present in the system utilizing the inertia, which is where these system derives the name 'inertial generator'. On the other hand, considering the energy harvesting capability of these devices, from the application point of view they are often called Vibration Energy Harvesters (VEHs). The ambient mechanical energy is converted into electrical energy primarily using the following transductions mechanisms- PiezoElectric (PE),

Electrostatic (ES), Electromagnetic (EM) and Triboelectric (TE). The principle of operation along with some example cases have been discussed for each of the transduction mechanism in the next section.

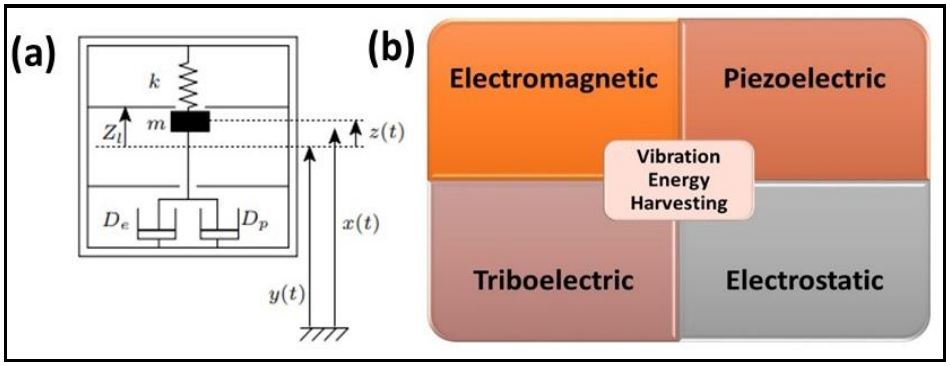


Figure 1.18: (a) Schematic of an inertial generator representing basic working principle [99] (b)Different transduction mechanism use for harvesting energy from vibrations.

The efficiency of these VEHs depends on large set of parameters; however, the selection of device for target application influences the device performance greatly. The design and implementation of a complete autonomous wireless sensor platform solution demands for high efficiency VEHs to power the electronics associated with the sensor node, as well as thorough understanding of the vibration environment where the sensor is deployed.

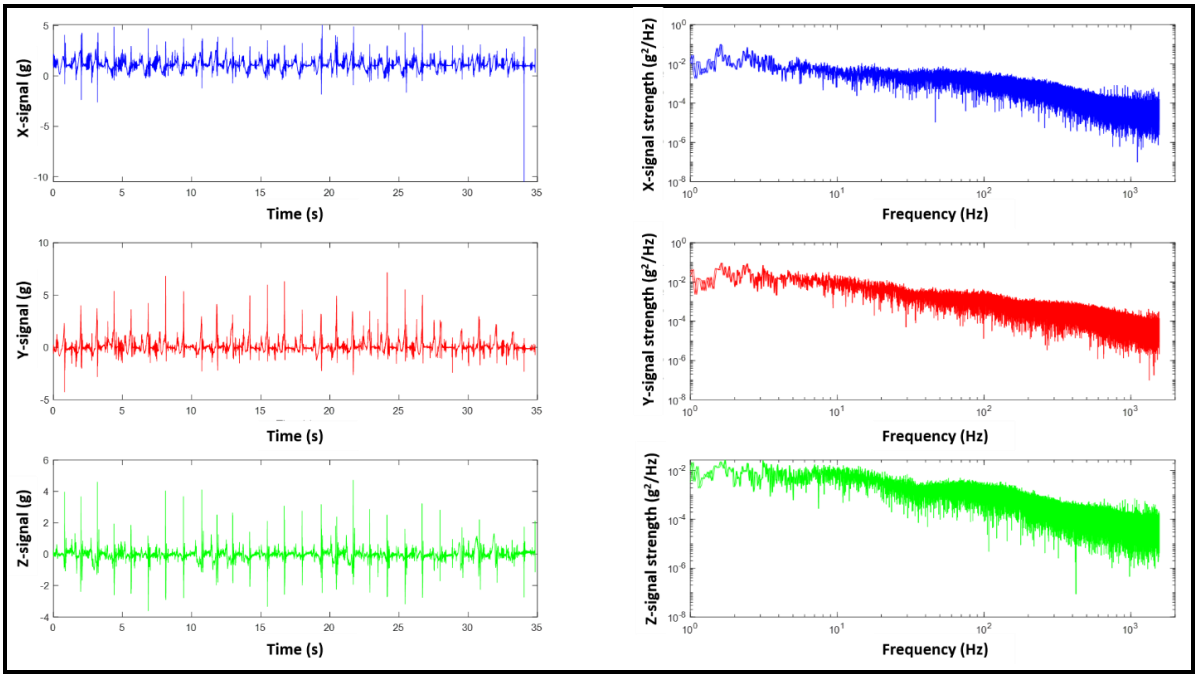


Figure 1.19: Vibration data for 'Human climbing up stairs' from the Real Vibrations repository [101] have been shown, on the left panel the time domain signal and on the right the Fourier Transformed frequency domain signal have been shown.

Although the vibration spectral characteristics are considerably unique for each vibration source. However, studying the data extracted from different vibration sources provides a solid ground to know the peak acceleration, dominant frequencies, broadband or narrowband nature of the vibrations.

EPSRC funded network Energy Harvesting [100] and Real Vibrations from NIPS lab [101] offers rich vibrations data repository comprising of vibration data from –

1) Automobiles & Public Transportation - Car/Van, Bus, Train, Minimetro, Airplane etc.
2) Bridges- Chicago North Bridge, Clifton Suspension Bridge etc.
3) Machinery- Motor, Generator, Drill Press, Lathe.
4) Human Motion- walking on ground, going down stairs etc.
5) Animal Motion- Cat, Dog walking etc.
6) Musical Instruments- Electric Bass, Acoustic Guitar etc.
7) Public Places- Supermarket Cart, Escalator, Elevator etc.

As an example of vibrational characteristics, Fig. 1.19 shows the motion of a human while climbing up stairs [102], the left panel shows the time domain signal data that has been extracted from the Real Vibrations repository [101] and the right hand side panel shows the signal strength for different directions- blue, red and green colour for x, y and z-direction. Since human motion mostly offers low frequency vibrations, majority of the mechanical energy is distributed over the low frequency domain (<100Hz).

The table 1.1 below summarizes the key characteristics of few of the vibration spectra from the repository of Energy Harvesting Network [100]. The vibrational spectra offered by each of these sources have different dominant frequencies, and the peak acceleration values differs in the X, Y and Z-axis. Such widely distributed vibrations offers a great scope for utilizing and harnessing this energy through suitable VEHs.

Table 1.1- Key parameters of Vibration Characteristics from ambient sources that are available from the Energy Harvesting Network vibration data repository [100].

Vibration Source	X − axis		Y − axis		Z − axis	
	f_{peak}	g_{peak}	f_{peak}	g_{peak}	f_{peak}	g_{peak}
Ford Focus Engine	35Hz	1946.7mg	35Hz	1022mg	35Hz	1490.7mg
VW Transporter Van- Dashboard	23Hz	349.1mg	23Hz	137.6mg	23Hz	318.1mg
VW Transporter Van- Driver's seat (underneath driver)	33Hz	220.1mg	33Hz	74.5mg	33Hz	26.2mg
VW Transporter Van- Steering Wheel	29Hz	315.4mg	29Hz	316.3mg	29Hz	258.7mg
VW Transporter Van- Engine Block	264Hz	1457.9mg	264Hz	1683.8mg	264Hz	1277.8mg
VW Transporter Van- Top of Engine	192Hz	4193.3mg	192Hz	1575.1mg	192Hz	2090.8mg
Clifton suspension bridge - location 04	160Hz	0.7mg	160Hz	3.2mg	160Hz	1.3mg
Chest Freezer	9Hz	12.5mg	9Hz	8.5mg	9Hz	9.9mg
Combination Boiler	100Hz	23.4mg	100Hz	19.3mg	100Hz	19.1mg
Domestic Washing machine	11Hz	113.9mg	11Hz	49mg	11Hz	238.3mg
Human head	19Hz	45.7mg	19Hz	77.1mg	19Hz	16mg
Human motion- lower leg	19Hz	1097.3mg	19Hz	697.4mg	19Hz	682.9mg
Human motion - Chest	19Hz	55.1mg	19Hz	155.5mg	19Hz	77.5mg
Human motion- Wrist	19Hz	79.4mg	19Hz	50.5mg	19Hz	36.6mg
Ward-Leonard Generator Set 1	200Hz	1356.3mg	200Hz	1229.6mg	200Hz	1568.8mg
Water pump motor	211Hz	535.2mg	211Hz	388.9mg	211Hz	705mg

1.6 Vibration energy harvesters- transduction principles

The **Electrostatic (ES)** transduction mechanism exploits relative displacements where two or more electrically charged components move performing work against the electrical forces, which can be harvested in the form of varying potential. Electrostatic transducers are of capacitive type; it works through the movement of two plates relative to each other with a dielectric between them that forms a variable capacitor. We can define capacitance C as,

$$C = \frac{Q}{V} \tag{1.5}$$

Where Q is the charge on the plates and V is the voltage on the moveable plates. We know that for a parallel plate capacitor this capacitance can be given as,

$$C = \frac{\epsilon_0 \, \epsilon_r \, A}{d_s} \tag{1.6}$$

Where ϵ_0 and ϵ_r represents the dielectric permittivity of free space and the relative dielectric permittivity of the material between the plates respectively, A is the area of each of the plates and d_s is the distance between the plates. This kind of electrostatic generator employs variable capacitor or in other words *'varactor'* that consists of two sets of electrodes, one of them is fixed while the other one is attached to the moving mass that receives the external excitation, the mechanical energy is harvested and extracted as the work done against the electrostatic force between the mobile plates.

These systems are very attractive owing to their high sensitivity, and the compatibility with silicon based micro-machined fabrication process, which makes these devices suitable for miniaturization. Basset et al. [103] batch-fabricated an electret-free silicon based generator that exhibits in-plane motion, offering a total volume of 1cm^2 ×1mm, which successfully harvested 61nW power with an acceleration amplitude of 0.25g and at the excitation frequency of 250Hz (matched with the resonance frequency), once the device is precharged at 6V (Fig. 1.20(a)). Though the produced power may seem quite low, but considering the factors like size and operating voltage, this presented structure is capable of working at a really low frequency compared with similar footprint devices, which proves the potential of this MEMS scale device. Lu et al. developed a high-efficiency MEMS ES-VEH [104] comprising interdigitated finger-teeth comb like structure for the capacitor to reduce mechanical damping, and a cavity holding small ball that aids in frequency up-conversion (Fig. 1.20(b)). This device operates at ultra-low frequency (1-20Hz), and converts 450nJ energy per cycle of oscillations, which makes it an attractive VEH device for wearable applications (in IoT for remote healthcare and diagnostics).

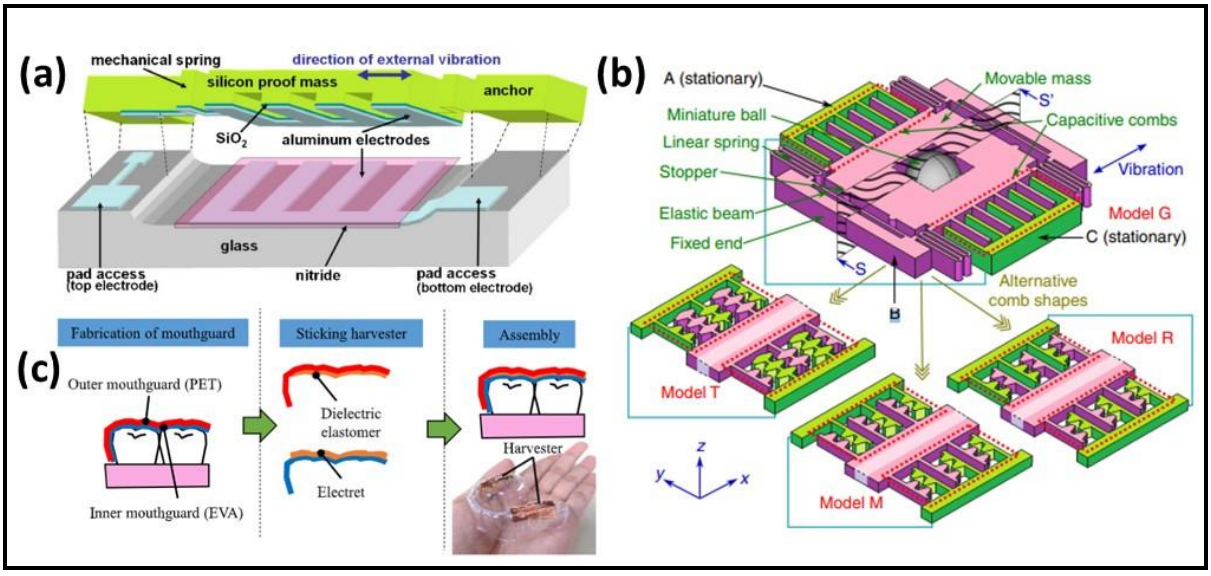


Figure 1.20: (a) Batch fabricated electret-free Silicon based electrostatic generator, (b) MEMS Electrostatic VEH with finger-teeth interdigitated comb like capacitor structure, (c) Thin Electrostatic sheet based generator for wireless oral health management [103-105].

Ichikawa et al. recently developed a thin sheet ES-VEH that are embedded on inside a dental mouth guard and has the capability of generating 2.5μW power from a small force equivalent of biting (Fig. 1.20(c)) which opens up the scope for development of wireless oral health management [105]. Recently inorganic insulator material SiO_2/Si_3N_4 films has been employed as the electret material [106] such as its corrugated surface is at a varying distance from the electrode which varies linearly with the displacement of the proof mass. This device topology generated 495μW under sinusoidal vibration at 1.2 kHz due to the capacitance change induced in the architecture. This device was mounted inside of tire treads and at a speed of 60km/h it generated 60μW output power from the impacts which makes it suitable for powering the tire sensors, enabling the implementation of 'intelligent automobiles'.

The electrostatic energy harvesters also known as capacitive energy harvesters have good fabrication compatibility with integrated circuit (IC) fabrication process, which aids in miniaturization of the device, however, offer low power density and requires external DC bias or pre-charged electrets membrane that brings additional constraints in the implementation of these VEHs.

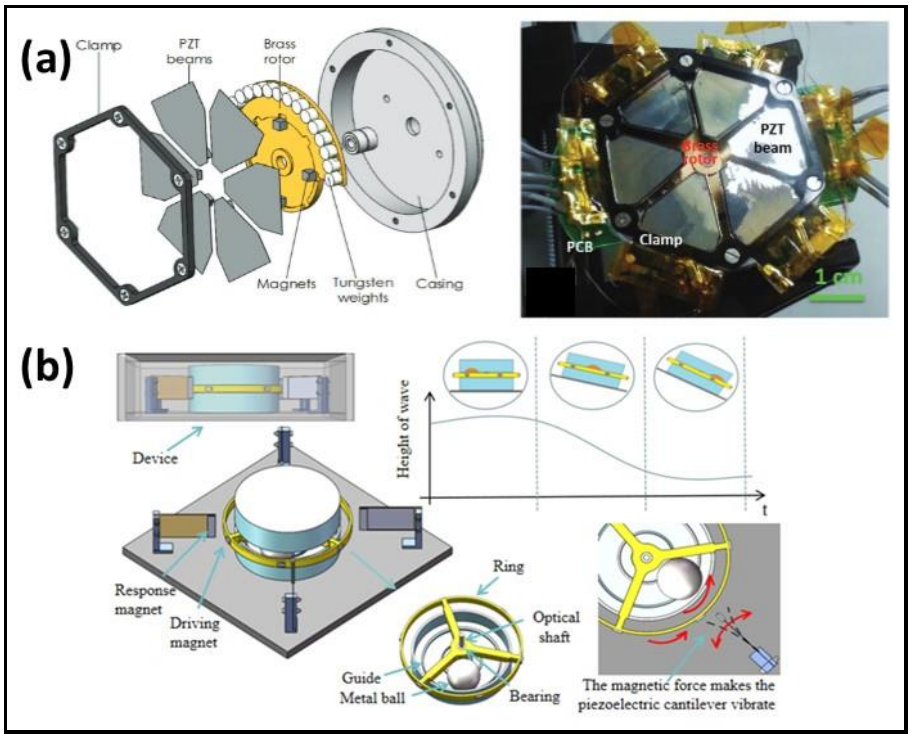


Figure 1.21: (a) Trapezoidal PZT film based Piezoelectric VEH, (b) Omnidirectional Piezoelectric VEH for ultra-low frequency vibrations [107, 108].

In **Piezoelectric (PE) transduction** mechanism electric polarization proportional to the strain appears at the boundaries of a strained piezoelectric material, which can be exploited in the form of a voltage across an electric load. In this type of transduction mechanism, a piezoelectric material converts the induced strain that it experiences from external vibration into electrical energy. Common example of this type of material are Quartz, Lead Zirconate Titanate (PZT), Aluminium Nitride, Gallium Arsenide and polymer material PolyVinyliDeneFluoride (PVDF). The piezoelectric transducer helps to convert mechanical strain into electrical energy, which is called the direct piezoelectric effect (represented by the first constitutive relation below).

On the other hand, these crystalline materials undergoes deformation when electric field is applied on it. This is known as the converse effect (represented by the second constitutive relation below). The direct effect can be used as an energy transducer and the converse effect can be used as an actuator. The electromechanical behaviour of these materials can be modelled with the help of two linear constitutive relations –

$$\{S\} = [s^E]\{T\} + [d]^T \{E\} \quad (1.7)$$

$$\{D\} = [d]\{T\} + [\epsilon^T]\{E\} \quad (1.8)$$

here, {D} stands for the electric displacement vector, {T} symbolizes the stress, {S} represents the strain vector and {E} is the electric field vector, $[s^E]$ is the compliance matrix calculated at constant electric field, $[d]$ represents the matrix with the piezoelectric coefficients, $[\epsilon^T]$ is the matrix for dielectric constant calculated at constant stress. Most popularly used piezoelectric generator structures are cantilever type, cymbal type, stack type or shell type. Out of these, the cantilever beam type generator is widely used because of its simple structure and ease of producing high strain for a given input force.

Roundy et al. designed a two-layer piezoelectric cantilever beam with a mass placed at its free end. Subjected to an external acceleration of 2.5m/s^2 at 120Hz, this device generated 250μW of power per cubic-centimetre [109]. Yeo et al. developed a wearable (wrist worn) PE-VEH comprising six bimorphs of trapezoidal shaped thick {001} oriented thick PZT films (Fig. 1.21(a)) on Nickel substrate and demonstrated a large power density of 2886μW/cm^{2}g^2 when subjected to a fixed excitation of 0.15g [107]. Harnessing mechanical energy from low frequency vibrations has always been a challenge for the energy harvesting research community. Recently, an omnidirectional PE VEH has been proposed and developed that extracts mechanical energy from ultra-low frequency vibration of water waves, and offers 6.32mW power while being excited at 0.9Hz [108]. A ball in the VEH architecture has been used to perceive all the incoming vibrations from different direction and to scale the frequency up by inducing magnetic interaction for the ease of operation (Fig. 1.21(b)). Lately, the potential of new materials is also being investigated to enhance the efficiency of the PE VEHs. In this context, Lee et al. proposed novel PE-VEHs exploiting mechanical metamaterials or phononics [110] crystals that aids in wave localization, which in turn improves the energy density of these device and offers tailored performance depending on the material selection and device design.

The primary benefits of the PE energy harvesters are the ease in scaling of the device, simple and matured fabrication technology in both macro and MEMS scale, and simple integration technique, which makes it a cost-effective approach as well. Unlike the ES energy harvesters, the PE harvesters do not require external DC biasing or precharged electrets, which reduces additional system constraints from these VEH. However, the piezoelectric material, by virtue of being ceramic in nature, are generally brittle and which poses great challenge in deploying these devices in harsh vibration environment and for long operational hours. Moreover, these materials suffer from electric fatigue, which is a reduced rate of switching

polarization arising from material inhomogeneity or appearance of microcracks, limiting the performance of these devices. In addition, the large impedance of these devices limits the applicability of PE generator in real-world vibration energy harvesting scenario.

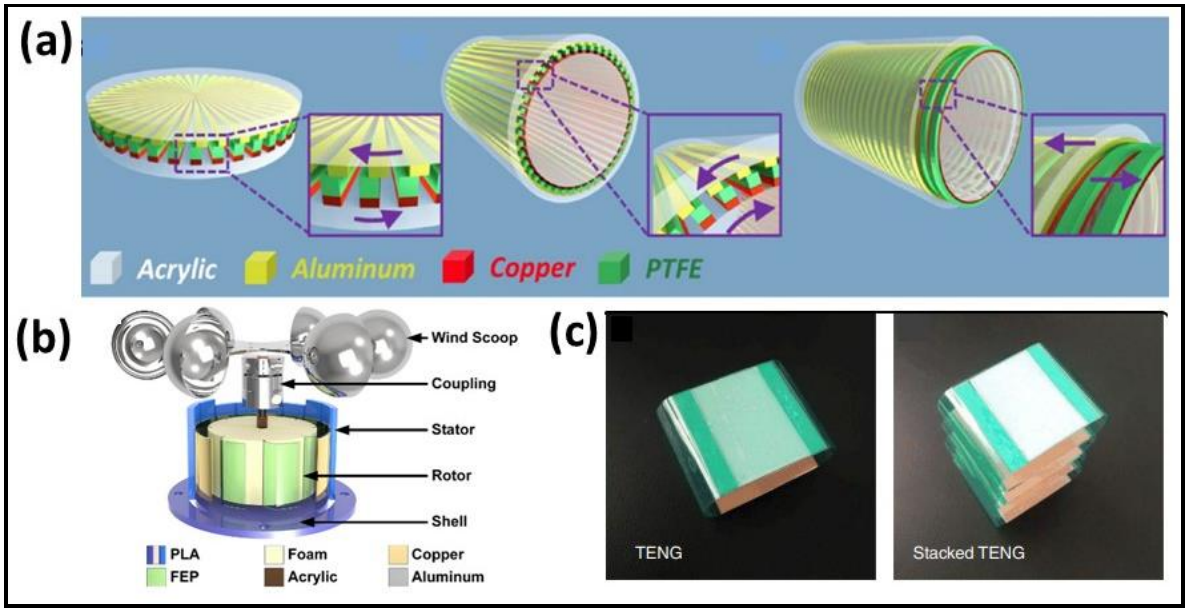


Figure 1.22: (a) Sliding surface triboelectric generator with linear gratings for performance enhancement, (b) 3D printed triboelectric energy harvester for harnessing wind energy, (c) Teflon tape and cosmetic fixing powder based triboelectric VEH [111-113].

The **Triboelectric (TE)** VEHs transduce the mechanical energy from friction or contact between two different triboelectric materials, this mechanism is a combination of contact electrification and electrostatic induction. This effect relies on the principle of generating charge on the surface of two different materials after contact that induce electric potential between mobile conductive electrodes and this induced potential drives the flow of mobile charge and current between the electrodes. The triboelectric generators offer cost-effectiveness, high conversion efficiency, and they are simple to fabricate, which makes them an attractive choice as an alternative source of energy. TE nanogenerators can be broadly classified into vertical contact type, lateral sliding type. Apart from this single electrode mode and freestanding triboelectric layer mode generators has also been reported. In the vertical contact separation mode, the motion of the charged surfaces in this generator would be ideally perpendicular to each other.

The lateral sliding mode exploits the developed triboelectric charge from the relative sliding motion between the two dielectric surfaces when it comes in contact with each other.

Zhu et al. [111] explored this lateral sliding electrification among two materials- Al and PTFE that are of course triboelectric in nature and acts as the sliding surface (Fig. 1.22(a)). The e-beam evaporator has been used for this work to deposit aluminium film (on acrylic substrate), which here worked as both the triboelectric layer and the electrode material. Linear gratings on the sliding surface increased the charge accumulation, which resulted in enhanced current generation when the surfaces are slid at a constant velocity of 10m/s.

Owing to the ease of fabrication and integration of the fabricated device, the TE generators find versatile applications in IoT platforms. Li et al. presented a TE-VEH for smart agriculture that power wireless sensor platform enabling it to report the ambient temperature, humidity and level of illumination [112]. The mechanical energy is extracted from ambient wind by designing lightweight 3D printed stator with thin copper electrodes, foam based flywheel with thin FEP (Fluorinated Ethylene Propylene) layer and aluminium based wind scoop platform (Fig. 1.22(b)). With a minimum wind speed of 3.3m/s, the TE-VEH starts working and offers a peak power of 2.8mW, which is adequate level of electrical energy required to power wireless sensor platforms. In real world environment, this device has been used to successfully power soil thermometer, as well as 300 LED light that are used to lighting plants in dark. A number of strategies have been undertaken over the last decade to enhance the performance of TE generator by selecting and micro/nano-patterning the material surface. A surprising and cost effective solution has been proposed by Xia et al, who developed TE generator with Teflon tape and cosmetic face powder, utilizing their triboelectric properties (Fig. 1.22(c)). The large power density (570.96μW/cm^2) offered by this device enables it to be used to power bicycle speed sensor while harvesting mechanical energy from the vibrations of the bicycle [113].

The TE generators have gained popularity in the field of energy harvesting for the ease of fabrication, integration and as a cost-effective solution for replacing batteries. However, the efficiency of the device greatly depends on the material selection, also the durability of these devices are still questionable considering created friction and consequent erosion during large number of operation cycles. Moreover, these devices offer large open circuit voltage and instantaneous peak output power. However, generated average power density is quite less compared to other mechanisms, which requires suitable electronic interface with these devices to condition the extracted power, rather than providing power directly to the WSN. These drawbacks limits the application fields for the TE generator.

For the **Electromagnetic (EM)** transduction mechanism, the variation of magnetic flux through a coil takes place due to the motion of a permanent magnet nearby, hence causing an electric current to flow. Compared to piezoelectric and electrostatic energy harvesters, electromagnetic energy harvesters are capable of delivering higher level of power into a low impedance load and the internal resistance of the electromagnetic energy harvesters is relatively low, leading to larger output current. For electromagnetic vibrational energy harvesters (EM-VEH) the basic working principle is Faraday's law of electromagnetic induction in which the relative motion between magnet and coil induces voltage into the latter (Fig. 1.23). This induced voltage is proportional to the rate of change of magnetic flux passing through the coil and can be represented as-

$$V = -N\frac{d\emptyset}{dt} = -N\frac{d\emptyset}{dx}\frac{dx}{dt} = -N\,v\,\frac{dB_{effective}}{dx}\sum_{i=1}^{N}A_i \tag{1.9}$$

Where, N is the number of turns of the coil, $\emptyset$ is the total magnetic flux linkage, v is the velocity of the relative motion between the coil and the magnet, $\frac{dB_{effective}}{dx}$ is the gradient of magnetic flux density and A_i is the area of each individual turn of the coil.

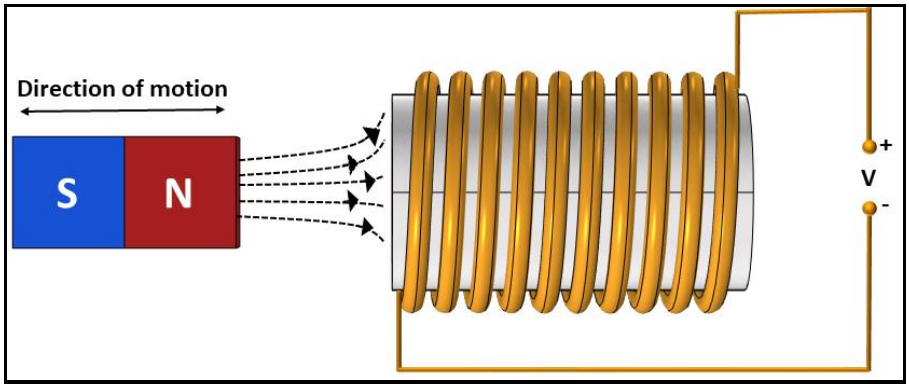


Figure 1.23: Illustration of Faraday's law that governs the electromagnetic transduction in EM-VEHs.

The structural longevity of the EM VEHs have enabled the use of these VEH in wide range of real-world applications, one such area is extracting mechanical energy from human body motion during walking, running, swimming etc. to sustainably power wireless sensor platforms that would monitor different health parameters and bio-signals from the body. However, the ultra-low frequency vibrations obtained from human motion makes it increasingly difficult to harness significant mechanical energy. Liu et al. developed an EM-VEH that exploits the rotational dynamics of human motion [114] and harnesses electrical energy through four embedded coils, which electromagnetically interacts with disk shaped

rotor (Fig. 1.24(a)). They demonstrated the capability of the device in generating a large output power of 10.4mW from vibrations of handshaking offering 8Hz excitation signal. Similar efforts have been devoted towards realizing a rotational EM-VEH through 'twist driving' and 'ratchet clutch' [115] composed of a maximum of eight magnets arranged around the perimeter of the ratchet and four vertical coils are arranged to interact with these magnets (Fig. 1.24(b)). When a human steps on this device, compressive force is applied on the ratchet which then reach up to 3700rpm revolution generating a peak output power of 32.2mW.

Utilizing the robustness of EM-VEHs, [116] have developed an anchorless mounted energy harvesting system in railroad to implement a self-powered wireless network by powering track-side electrical devices around railway tracks (Fig. 1.24(c)). The mechanical energy emanating from the shock absorbers of vehicles have also been harnessed through a four phased electromagnetic generator system [117] that has a magnet assembly along with spacers arranged in a way that produces radially outward magnetic field, which induces voltage across the copper coils in the shock absorber (Fig. 1.24(d)). Scavenging energy from vehicle suspension, the presented harvester generated 2-8W electrical energy from the suspension velocity of 0.25ms-0.5m/s. There also has been significant research interest towards extracting mechanical energy from flow-induced motion, for example water flow, airflow etc. In a recent work, EM-VEHs are fabricated through 3D printing with the motivation of extracting mechanical energy from wind flow (Fig. 1.24(e)) of an HVAC exhaust duct [118]. The 3D printed technology of course reduces down the cost of fabrication, moreover, allows tailoring the design parameters easily. The optimized EM-VEH generates 0.305W, yielding 6.59% energy conversion efficiency and lights up four LED lights with the harvested power.

The key merits and demerits of all the above-mentioned transduction mechanism have been summarized in Table 1.2. Although the macro scale implementation of electromagnetic transduction based energy harvesting device is part of a matured technology, however, the miniaturization of these devices is still a challenge owing to the unfavourable scaling of electromagnetic forces and lack of efficient CMOS integrable magnetic material.

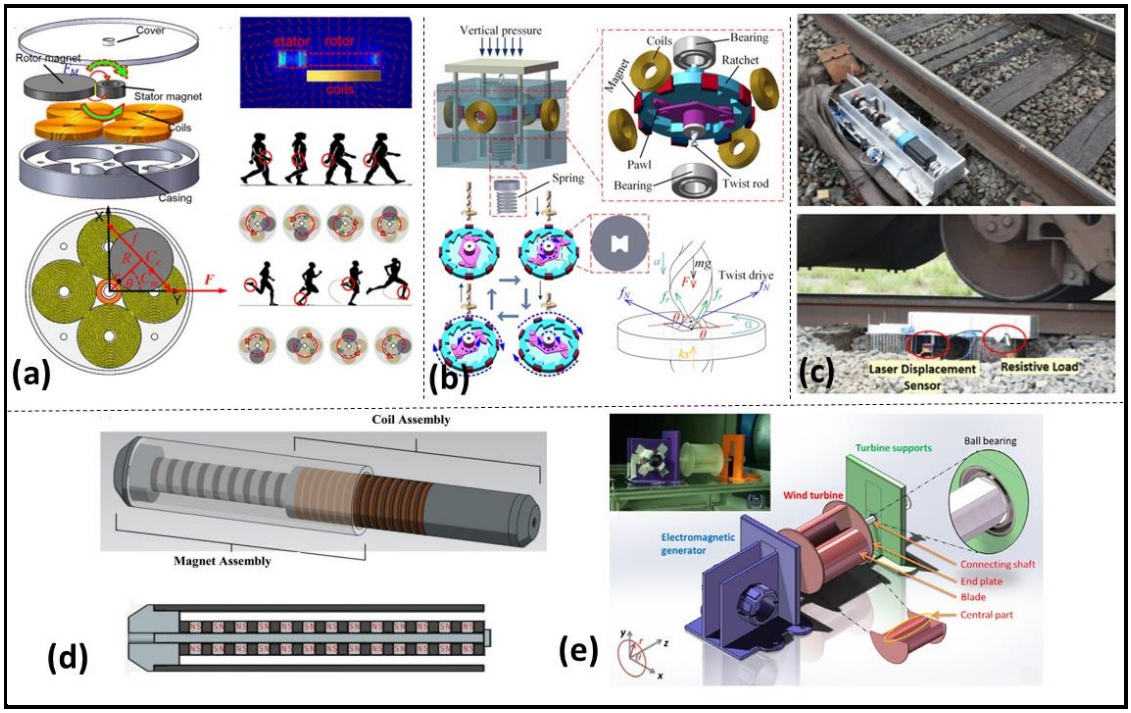


Figure 1.24: (a) Rotational Electromagnetic VEH for harnessing human induced vibrations, (b) Twist driving and ratchet-clutch based human vibration driven Electromagnetic VEH, (c) Anchorless self-powered system for powering trackside electronic devices, (d) Electromagnetic VEH for scavenging energy from vehicular suspensions, (e) 3D printed VEH for harnessing energy from the airflow of HVAC duct [114-118].

On the other hand, EM generators comprising typically of spring, coil, magnets, are easy to implement. These VEH do not require any external DC biasing or electrets for operation. Owing to the low internal resistance of these VEH, it offers low-to moderate output voltage but high output current resulting in high output power. Additionally, since the materials used for the construction of these VEH are not brittle which significantly improves the reliability and longevity, so these EM-VEHs can be used in harsh vibration environment. Owing to these benefits, the electromagnetic transduction mechanism has been chosen for the implementation of energy harvesting devices in this work.

Table 1.2- Comparison of different mechanical energy transduction mechanism

Transduction mechanism	Merit	Demerit
Electrostatic	• High sensitivity, and the compatibility with silicon based micro-machined fabrication process • Suitable for miniaturization.	• Low power density. • Requires external DC bias or pre-charged electrets membrane. • Additional constraints in the implementation of these devices.

Piezoelectric	• Offers ease in scaling of the device. • Simple and matured fabrication and integration technology in both macro and MEMS scale. • No requirement of external DC biasing or precharged electrets.	• Brittle nature of ceramic piezoelectric material poses great challenge in deploying these devices in harsh vibration environment and for long operational hours. • Piezoelectric materials suffer from electric fatigue • Large impedance of these devices limits the applicability of PE generator in real-world vibration energy harvesting scenario.
Triboelectric	• Ease of fabrication, integration. • A cost-effective alternative of batteries.	• Large dependence of device efficiency on the material selection. • Less durable devices owing to the friction and consequent erosion during large number of operation cycles. • Large open circuit voltage and instantaneous peak output power but average delivered power is low, requires additional power conditioning interface.
Electromagnetic	• Easy implementation of spring, mass, damper based energy harvesting device. • No requirement of any external DC biasing or electrets for operation. • High output current resulting in high output power. • High reliability and longevity of devices, suitable for the use in harsh vibration environment.	• Not easy to scale down. • Non-traditional magnetic material development and integration techniques used, such as sintering, powder bonding, that in turn increases the cost of fabrication. • Electromagnetic flux linkage scales down dramatically with volume hindering efficient device miniaturization..

1.7 Limitations of the linear EM generators

A breadth of studies has been undertaken to shed light on the intricate electromechanical dynamics of these VEHs to provide experimental evidence of the predicted benefits. Most of the VEHs presently available in the market are linear resonant oscillators whose oscillating amplitude enhances significantly, when external vibrations are applied to it at resonant frequency. So these systems offer high Q-factor. However, lack of intelligent spring design limits the large amplitude of oscillations, which is particularly valuable for the EM transducers. Moreover, the linear oscillators are insensitive to the vibrations that fall outside the narrow resonance band. Hence, these VEH requires a resonance frequency tuning mechanism or a wider operable frequency bandwidth to make it capable of extracting energy effectively as the

ambient vibrations have their energy distributed over a wide frequency spectrum with significant predominance of low frequency components (<100Hz). There are a number of techniques through which the resonance frequency of the oscillator is tuned, the easiest of which is by altering the mass, length or thickness of the vibrating body. However, in operational condition it is very challenging to alter these parameters. In case of widening the bandwidth there is a trade-off between the system bandwidth and the Q-factor. Wider bandwidth unfortunately lowers the Q-factor, hence degrading the output performance. Due to these limitations, in recent years' lot of research work is focused on the implementation of nonlinear systems (bi-stable or multi-stable potential instead of mono-stable potential) in order to increase the vibration energy harvester's frequency bandwidth. The nonlinear-VEHs outperforms the resonant ones by enhancing the interaction between the external excitation and the VEH unit over a wider range of frequency and amplitude of vibrations, thereby enabling it to scavenge energy robustly from a wider spectrum. The deliberate inclusion of cubic-stiffness nonlinearities exhibiting mono-stable potential characteristics in compact spring architecture or/and magnetic repulsion based bi-stable nonlinearity manifesting high energy inter-well oscillations through the repulsive magnets placed appropriately- has been quite popular techniques of incorporating nonlinearity through intelligent design strategies that has resulted in enhanced output performance.

1.8 Challenges in miniaturization of the EM-VEHs

The present cutting-edge technologies have created the drive for miniaturized and highly integrated electronics. Finding compact designs and implementing those in MEMS scale is of paramount importance nowadays. The electromagnetic forces scale down dramatically with volume, which is a major hindrance in miniaturization of these electromagnetic transduction based VEHs. Moreover, the shape-dependent 'Demagnetizing Field' degrades the magnetic performance of the bulky permanent magnets. The effect of scaling and demagnetizing field could potentially be addressed by manipulating the aspect ratio and micro-patterning of the magnetic structures. Therefore, a key challenge is CMOS compatible integration of patterned permanent magnets with high energy-product. In addition to this, the scaling down of the structures responsible for mechanical movement results in shifting the frequency up which is not desirable as most of the vibrational energy is spread over the lower frequency regime. Another critical aspect of implementation of MEMS scale electromagnetic vibration energy

harvester is the increased value of coil loss in microscale and risks of electrical shorting in compact multilayer coil topologies.

1.9 Motivation of this thesis

The work presented in this thesis is a part of the project "Electromagnetic Vibration Energy Harvester for Powering IoT" which is supported by 'CONNECT' strategic research centre funded by Science Foundation Ireland and EU Horizon 2020 Research and Innovation Programme 'EnABLES'. The work aims to address the pertinent powering issue of the ubiquitous wireless sensor nodes, a vital part of the IoT architecture. Out of the renewable energy sources, the mechanical energy extracted from ambient vibrations have become very popular because of its availability in our surrounding and the ease it offers in the extraction of energy through the popular transduction mechanism. The inefficiency of the linear resonant VEHs in converting the real world non-stationary and broadband ambient vibrations has paved the way for the development of wideband VEH by purposeful incorporation of nonlinearities in the harvester units to widen its usable bandwidth and enhance its output performance. Furthermore, there is an increasing demand of efficient miniaturized energy harvesting system, which would potentially offer the ease of device integration for critical application areas.

- This work aims for the development of high efficiency linear EM VEHs that is capable of extracting substantial mechanical energy from low to moderate level of excitation (<0.5g) while keeping the dominant frequency of vibration low (<100Hz).
- Further, this work aims to develop wideband electromagnetic vibration energy harvester for harvesting energy over ultra-wide range (~50Hz) of frequencies with improved power density.
- Wideband VEH to be implemented by tailoring the spring design (that exhibits large amplitude of oscillations) and assimilating different forms of nonlinearity (geometrically induced stretching effect, effect of magnetic repulsion).
- MEMS scale VEH devices will be developed as a part of this work, while identifying and mitigating pertinent issues of miniaturization.
- Moreover, it aims to address the challenges of enhancement of the electromagnetic coupling and hence the power while reducing the size by employing efficient magnet configurations and interactions.

- The motivation of this work will be driven towards demonstration of energy harvesting capabilities of the developed devices by integrating them with target wireless sensor platforms.
- This interdisciplinary research not only targets to develop robust and reliable power source for next generation ICT and IoT but also enables to investigate the role of relatively unexplored complex dynamics to increase the operational bandwidth and power-density in the meso and MEMS-scale.

1.10 Thesis outline

- Chapter 2- This chapter presents a detailed overview of the state-of-the-art vibration energy harvesters that majorly exploits electromagnetic transduction to harness ambient mechanical energy. The theoretical background along with the key dynamic features of linear and nonlinear generators have been discussed. Operable frequency broadening strategies have been discussed both in the context of macroscale and microscale energy harvesters along with suitable interface electronics.
- Chapter 3- This chapter discusses the development of a meso-scale vibration energy harvester that aims to improve the efficiency of wireless communication. The feasibility of powering a near field communication based wireless sensor node through the developed resonant vibration energy harvester has been studied.
- Chapter 4- The design, fabrication and characterization of a wideband nonlinear vibration energy harvester has been presented in this chapter. The efficiency of the developed energy harvester in powering wireless sensor platform has been demonstrated in a real-world application scenario.
- Chapter 5- A wideband vibration energy harvester comprising multiple nonlinear restoring forces has been presented in this chapter. The nonlinear forces arises from the stretchable spring design as well as the involved repulsive magnetic interaction, this instigates complex dynamical behaviours and introduces multistability in the system. A novel theoretical model along with a useful graphical tool have been introduced to analyse the energy transaction through each of the energy branches, which is exploited to estimate the efficiency of the energy harvesting system.
- Chapter 6- The pertinent challenges of MEMS (Micro-Electro-Mechanical-Systems) scale vibration energy harvesters. Pattering of magnets and optimization of the shape, size and distribution of magnets elements in arrays have been presented in this chapter

as an alternative to the continuous thin film of magnets. Furthermore, compact device topologies have been proposed which strengthens the electromagnetic interaction, which in turns enhance the deliverable power from the miniaturized energy harvesting devices.

- Chapter 7- This chapter summarizes the novel findings that are presented in this thesis. Discussions have been extended on the existing challenges in realizing fully integrated high-efficiency vibration energy harvesters, potential solutions have been identified in this context. A firm roadmap has been presented to implement a reliable low-frequency wideband fully integrated MEMS vibration energy harvester offering large power density as a continuation of the work presented in this dissertation.

1.11 References

[1] J. A. Fleming, "Improvements in instruments for detecting and measuring alternating electric currents," *GB patent*, vol. 190424850, 1904.

[2] J. A. Fleming, "On the conversion of electric oscillations into continuous currents by means of a vacuum valve," *Proceedings of the Royal Society of London*, vol. 74, no. 497, pp. 476-487, 1905.

[3] L.A.P. Santos, “An Overview on Bipolar Junction Transistor as a Sensor for X-ray Beams Used in Medical Diagnosis”, *Sensors*, vol. 22, no. 5, pp. 1923, 2022, https://doi.org/10.3390/s22051923.

[4] "Popular MOSFETs frequently used in Power Electronics Designs", https://components101.com/articles/popular-mosfets-frequently-used-in-power-electronics-designs.

[5] G. E. Moore, "Cramming more components onto integrated circuits," ed: McGraw-Hill New York, 1965.

[6] “701 Vacuum tubes”, IBM, https://www.ibm.com/ibm/history/exhibits/701/701_141510.html

[7] "CD4069UBE CD4069 CMOS Hex Inverter Breadboard-Friendly IC DIP-14." https://www.walmart.com/ip/CD4069UBE-CD4069-CMOS-Hex-Inverter-Breadboard-Friendly-IC-DIP-14/221862415.

[8] C. Hu. "How the Father of FinFETs Helped Save Moore’s Law." https://spectrum.ieee.org/how-the-father-of-finfets-helped-save-moores-law.

[9] C. Dekker, "How we made the carbon nanotube transistor," *Nature Electronics*, vol. 1, no. 9, pp. 518-518, 2018/09/01 2018, doi: 10.1038/s41928-018-0134-9.

[10] X. Lin, W. Yang, K. L. Wang, and W. Zhao, "Two-dimensional spintronics for low-power electronics," *Nature Electronics*, vol. 2, no. 7, pp. 274-283, 2019/07/01 2019, doi: 10.1038/s41928-019-0273-7.

[11] G. Cheng *et al.*, "Sketched oxide single-electron transistor," *Nature Nanotechnology*, vol. 6, no. 6, pp. 343-347, 2011/06/01 2011, doi: 10.1038/nnano.2011.56.

[12] M. Veldhorst, H. G. J. Eenink, C. H. Yang, and A. S. Dzurak, "Silicon CMOS architecture for a spin-based quantum computer," *Nature Communications*, vol. 8, no. 1, p. 1766, 2017/12/15 2017, doi: 10.1038/s41467-017-01905-6.

[13] Z. Chen, D. Farmer, S. Xu, R. Gordon, P. Avouris, and J. Appenzeller, "Externally assembled gate-all-around carbon nanotube field-effect transistor," *IEEE electron device letters*, vol. 29, no. 2, pp. 183-185, 2008.

[14] "Technology Node." https://en.wikichip.org/wiki/technology_node.

[15] "Intel® 14 nm Technology." https://www.intel.com/content/www/us/en/silicon-innovations/intel-14nm-technology.html.

[16] "5nm Technology, TSMC." https://www.tsmc.com/english/dedicatedFoundry/technology/logic/l_5nm.

[17] "Future R&D Plans , TSMC." https://www.tsmc.com/english/dedicatedFoundry/technology/future_rd.
[18] "INTERNATIONAL ROADMAP FOR DEVICES AND SYSTEMS™, 2021 UPDATE, MORE MOORE." [Online]. Available: https://irds.ieee.org/images/files/pdf/2021/2021IRDS_MM.pdf.
[19] "INTERNATIONAL ROADMAP FOR DEVICES AND SYSTEMS™ 2021 UPDATE,MORE THAN MOORE,WHITEPAPER."[Online].Available:https://irds.ieee.org/images/files/pdf/2021/2021IRDS_MtM.pdf.
[20] J. R. Powell, "The quantum limit to Moore's law," *Proceedings of the IEEE,* vol. 96, no. 8, pp. 1247-1248, 2008.
[21] "INTERNATIONAL ROADMAP FOR DEVICES AND SUSTEMS-2021 UPDATE, BEYOND CMOS." [Online]. Available: https://irds.ieee.org/images/files/pdf/2021/2021IRDS_BC.pdf.
[22] M. N. Leuenberger and D. Loss, "Quantum computing in molecular magnets," *Nature,* vol. 410, no. 6830, pp. 789-793, 2001.
[23] R. Penrose, "Quantum computation, entanglement and state reduction," *Philosophical Transactions of the Royal Society of London. Series A: Mathematical, Physical and Engineering Sciences,* vol. 356, no. 1743, pp. 1927-1939, 1998.
[24] S. Furber, "Large-scale neuromorphic computing systems," *Journal of Neural Engineering,* vol. 13, no. 5, p. 051001, 2016/08/16 2016, doi: 10.1088/1741-2560/13/5/051001.
[25] D. Marković and J. Grollier, "Quantum neuromorphic computing," *Applied Physics Letters,* vol. 117, no. 15, p. 150501, 2020/10/12 2020, doi: 10.1063/5.0020014.
[26] J. A. Hutchby, G. I. Bourianoff, V. V. Zhirnov, and J. E. Brewer, "Extending the road beyond CMOS," *IEEE circuits and devices magazine,* vol. 18, no. 2, pp. 28-41, 2002.
[27] K. Ashton, "That 'internet of things' thing," *RFID journal,* vol. 22, no. 7, pp. 97-114, 2009.
[28] M. Shojaee, S. Nasresfahani, M. K. Dordane, and M. H. Sheikhi, "Fully integrated wearable humidity sensor based on hydrothermally synthesized partially reduced graphene oxide," *Sensors and Actuators A: Physical,* vol. 279, pp. 448-456, 2018/08/15/ 2018, doi: https://doi.org/10.1016/j.sna.2018.06.052.
[29] F. Zantalis, G. Koulouras, S. Karabetsos, and D. Kandris, "A review of machine learning and IoT in smart transportation," *Future Internet,* vol. 11, no. 4, p. 94, 2019.
[30] A. R. Sfar, Y. Challal, P. Moyal, and E. Natalizio, "A game theoretic approach for privacy preserving model in IoT-based transportation," *IEEE Transactions on Intelligent Transportation Systems,* vol. 20, no. 12, pp. 4405-4414, 2019.
[31] S. A. Shah, D. Z. Seker, S. Hameed, and D. Draheim, "The rising role of big data analytics and IoT in disaster management: recent advances, taxonomy and prospects," *IEEE Access,* vol. 7, pp. 54595-54614, 2019.
[32] S. Marksteiner, V. J. E. Jiménez, H. Valiant, and H. Zeiner, "An overview of wireless IoT protocol security in the smart home domain," *2017 Internet of Things Business Models, Users, and Networks,* pp. 1-8, 2017.
[33] A. K. Gupta and R. Johari, "IOT based electrical device surveillance and control system," in *2019 4th international conference on internet of things: Smart innovation and usages (IoT-SIU)*, 2019: IEEE, pp. 1-5.
[34] J. Teicher. "The little-known story of the first IoT device." https://www.ibm.com/blogs/industries/little-known-story-first-iot-device/.
[35] B. N. Silva *et al.*, "Urban planning and smart city decision management empowered by real-time data processing using big data analytics," *Sensors,* vol. 18, no. 9, p. 2994, 2018.
[36] S. Sruthy and S. N. George, "WiFi enabled home security surveillance system using Raspberry Pi and IoT module," in *2017 IEEE International Conference on Signal Processing, Informatics, Communication and Energy Systems (SPICES)*, 2017: IEEE, pp. 1-6.
[37] T. N. Gia *et al.*, "Energy efficient wearable sensor node for IoT-based fall detection systems," *Microprocessors and Microsystems,* vol. 56, pp. 34-46, 2018.
[38] M. Derawi, Y. Dalveren, and F. A. Cheikh, "Internet-of-Things-Based Smart Transportation Systems for Safer Roads," in *2020 IEEE 6th World Forum on Internet of Things (WF-IoT)*, 2020: IEEE, pp. 1-4.
[39] H. M. Jawad, R. Nordin, S. K. Gharghan, A. M. Jawad, and M. Ismail, "Energy-efficient wireless sensor networks for precision agriculture: A review," *Sensors,* vol. 17, no. 8, p. 1781, 2017.
[40] M. Alvarez-Campana, G. López, E. Vázquez, and V. A. Villagrá, "Smart CEI Moncloa: An IoT-based platform for people flow and environmental monitoring on a smart university campus," *State-of-the-Art Sensors Technology in Spain 2017,* vol. 17, no. 2856, p. 1, 2018.
[41] S. G. Dacko, "Enabling smart retail settings via mobile augmented reality shopping apps," *Technological Forecasting and Social Change,* vol. 124, pp. 243-256, 2017/11/01/ 2017, doi: https://doi.org/10.1016/j.techfore.2016.09.032.
[42] "IoT connections outlook." https://www.ericsson.com/en/reports-and-papers/mobility report/dataforecasts/iot-connections-outlook.

[43] S. Sinha. "State of IoT 2021: Number of connected IoT devices growing 9% to 12.3 billion globally, cellular IoT now surpassing 2 billion." IOT ANALYTICS. https://iot-analytics.com/number-connected-iot-devices/.
[44] J. Manyika *et al.*, *The Internet of Things: Mapping the value beyond the hype*. McKinsey Global Institute New York, NY, USA, 2015.
[45] "What is Industry 4.0?" https://www.ibm.com/topics/industry-4-0.
[46] "8-bit PIC® MCUs." https://www.microchip.com/en-us/products/microcontrollers-and-microprocessors/8-bit-mcus/pic-mcus.
[47] "8-bit AVR® MCUs." https://www.microchip.com/en-us/products/microcontrollers-and-microprocessors/8-bit-mcus/avr-mcus.
[48] "MSP430 microcontrollers." https://www.ti.com/microcontrollers-mcus-processors/microcontrollers/msp430-microcontrollers/overview.html.
[49] "32-bit PSoC™ 6 Arm® Cortex®-M4 / M0+" https://www.infineon.com/cms/en/product/microcontroller/32-bit-psoc-arm-cortex-microcontroller/psoc-6-32-bit-arm-cortex-m4-mcu/.
[50] R. Dekimpe and D. Bol, "ECG Arrhythmia Classification on an Ultra-Low-Power Microcontroller," *IEEE Transactions on Biomedical Circuits and Systems*, vol. 16, no. 3, pp. 456-466, 2022, doi: 10.1109/TBCAS.2022.3182159.
[51] K. Kozalakis *et al.*, "Wide-Range Light Harvesting Module for Autonomous Sensor Nodes," *IEEE Access*, vol. 10, pp. 32180-32189, 2022, doi: 10.1109/ACCESS.2022.3161486.
[52] A. Lazaro, R. Villarino, and D. Girbau, "A survey of NFC sensors based on energy harvesting for IoT applications," *Sensors*, vol. 18, no. 11, p. 3746, 2018.
[53] M. M. Islam, N. Funabiki, R. W. Sudibyo, K. I. Munene, and W.-C. Kao, "A dynamic access-point transmission power minimization method using PI feedback control in elastic WLAN system for IoT applications," *Internet of Things*, vol. 8, p. 100089, 2019.
[54] M. Collotta, G. Pau, T. Talty, and O. K. Tonguz, "Bluetooth 5: A concrete step forward toward the IoT," *IEEE Communications Magazine*, vol. 56, no. 7, pp. 125-131, 2018.
[55] E. D. N. Ndih and S. Cherkaoui, "On enhancing technology coexistence in the IoT era: ZigBee and 802.11 case," *Ieee Access*, vol. 4, pp. 1835-1844, 2016.
[56] J. Haxhibeqiri, E. De Poorter, I. Moerman, and J. Hoebeke, "A survey of LoRaWAN for IoT: From technology to application," *Sensors*, vol. 18, no. 11, p. 3995, 2018.
[57] X. Jia, Q. Feng, T. Fan, and Q. Lei, "RFID technology and its applications in Internet of Things (IoT)," in *2012 2nd international conference on consumer electronics, communications and networks (CECNet)*, 2012: IEEE, pp. 1282-1285.
[58] B. Vejlgaard, M. Lauridsen, H. Nguyen, I. Z. Kovács, P. Mogensen, and M. Sorensen, "Coverage and capacity analysis of sigfox, lora, gprs, and nb-iot," in *2017 IEEE 85th vehicular technology conference (VTC Spring)*, 2017: IEEE, pp. 1-5.
[59] Y. Kim, Y. Park, M. Kim, J. Lee, K. J. Kim, and J. W. Choi, "Corrosion as the origin of limited lifetime of vanadium oxide-based aqueous zinc ion batteries," *Nature Communications*, vol. 13, no. 1, p. 2371, 2022/05/02 2022, doi: 10.1038/s41467-022-29987-x.
[60] S. Abada, M. Petit, A. Lecocq, G. Marlair, V. Sauvant-Moynot, and F. Huet, "Combined experimental and modeling approaches of the thermal runaway of fresh and aged lithium-ion batteries," *Journal of Power Sources*, vol. 399, pp. 264-273, 2018/09/30/ 2018, doi: https://doi.org/10.1016/j.jpowsour.2018.07.094.
[61] C. P. Grey and D. S. Hall, "Prospects for lithium-ion batteries and beyond—a 2030 vision," *Nature Communications*, vol. 11, no. 1, p. 6279, 2020/12/08 2020, doi: 10.1038/s41467-020-19991-4.
[62] A. R. Dehghani-Sanij, E. Tharumalingam, M. B. Dusseault, and R. Fraser, "Study of energy storage systems and environmental challenges of batteries," *Renewable and Sustainable Energy Reviews*, vol. 104, pp. 192-208, 2019/04/01/ 2019, doi: https://doi.org/10.1016/j.rser.2019.01.023.
[63] J.L.Sullivan and L.Gaines, "A review of battery life cycle analysis: state of knowledge and critical needs," 2010, doi: 10.2172/1000659.
[64] A. H. Dehwah, M. Mousa, and C. G. Claudel, "Lessons learned on solar powered wireless sensor network deployments in urban, desert environments," *Ad Hoc Networks*, vol. 28, pp. 52-67, 2015/05/01/ 2015, doi: https://doi.org/10.1016/j.adhoc.2015.01.013.
[65] A. Farinha, R. Zufferey, P. Zheng, S. F. Armanini, and M. Kovac, "Unmanned Aerial Sensor Placement for Cluttered Environments," *IEEE Robotics and Automation Letters*, vol. 5, no. 4, pp. 6623-6630, 2020, doi: 10.1109/LRA.2020.3015459.
[66] K.Paul *et al.*, "A Concertina Shaped Vibration Energy Harvester Assisted NFC Sensor With Improved Wireless Communication Range," *IEEE Internet of Things Journal*.

[67] J. C. Rodriguez, V. Nico, and J. Punch, "A Vibration Energy Harvester and Power Management Solution for Battery-Free Operation of Wireless Sensor Nodes," *Sensors*, vol. 19, no. 17, 2019, doi: 10.3390/s19173776.
[68] W. Trappe, R. Howard, and R. S. Moore, "Low-Energy Security: Limits and Opportunities in the Internet of Things," *IEEE Security & Privacy*, vol. 13, no. 1, pp. 14-21, 2015, doi: 10.1109/MSP.2015.7.
[69] M. K. Mishu *et al.*, "Prospective efficient ambient energy harvesting sources for iot-equipped sensor applications," *Electronics*, vol. 9, no. 9, p. 1345, 2020.
[70] J. Won, J. Park, J.-W. Park, and I.-H. Kim, "BLESeis: Low-Cost IoT Sensor for Smart Earthquake Detection and Notification," *Sensors*, vol. 20, no. 10, 2020, doi: 10.3390/s20102963.
[71] V. Babu and V. Rajan, "Flood and Earthquake Detection and Rescue Using IoT Technology," in *2019 International Conference on Communication and Electronics Systems (ICCES)*, 17-19 July 2019 2019, pp. 1256-1260, doi: 10.1109/ICCES45898.2019.9002406.
[72] X. IoT. "Practical Power Solutions For Wireless IoT." https://www.mouser.com/pdfDocs/Xidas_WP.pdf.
[73] "EnABLES European Infrastructure Powering the Internet of Things Research Infrastructure Position Paper." [Online].Available:https://www.enables-project.eu/wpcontent/uploads/2021/02/EnABLES_ResearchInfrastructure_PositionPaper.pdf.
[74] "How a Solar Cell Works." https://www.acs.org/content/acs/en/education/resources/highschool/chemmatters/past-issues/archive-2013-2014/how-a-solar-cell-works.html.
[75] J.F.Randall, "On the use of photovoltaic ambient energy sources for powering indoor electronic devices," Ecole Polytechnique Federale de Lausanne, Switzerland, 2003. [Online]. Available: https://infoscience.epfl.ch/record/87589?ln=en
[76] M. A. Green, Y. Hishikawa, E. D. Dunlop, D. H. Levi, J. Hohl-Ebinger, and A. W. Y. Ho-Baillie, "Solar cell efficiency tables (version 51)," *Progress in Photovoltaics: Research and Applications*, vol. 26, no. 1, pp. 3-12, 2018, doi: https://doi.org/10.1002/pip.2978.
[77] S. Bhattacharya and S. John, "Beyond 30% Conversion Efficiency in Silicon Solar Cells: A Numerical Demonstration," *Scientific Reports*, vol. 9, no. 1, p. 12482, 2019/08/28 2019, doi: 10.1038/s41598-019-48981-w.
[78] J. Randall and J. Jacot, "The performance and modelling of 8 photovoltaic materials under variable light intensity and spectra," in *World Renewable Energy Congress VII & Expo*, 2002, no. CONF.
[79] I. Mathews, P. J. King, F. Stafford, and R. Frizzell, "Performance of III–V Solar Cells as Indoor Light Energy Harvesters," *IEEE Journal of Photovoltaics*, vol. 6, no. 1, pp. 230-235, 2016, doi: 10.1109/JPHOTOV.2015.2487825.
[80] A. R. Al-Ali, A. Al Nabulsi, S. Mukhopadhyay, M. S. Awal, S. Fernandes, and K. Ailabouni, "IoT-solar energy powered smart farm irrigation system," *Journal of Electronic Science and Technology*, vol. 17, no. 4, p. 100017, 2019/12/01/ 2019, doi: https://doi.org/10.1016/j.jnlest.2020.100017.
[81] T. N. Pham *et al.*, "Development of a Solar-Powered IoT-Based Instrument for Automatic Measurement of Water Clarity," *Sensors*, vol. 20, no. 7, 2020, doi: 10.3390/s20072051.
[82] E. Velmre, "Thomas Johann Seebeck (1770-1831)," *Thomas Johann Seebeck (1770-1831)*. Article vol. 13, no. 4, pp. 276-282, 2007. [Online]. Available: https://ucc.idm.oclc.org/login?URL=https://search.ebscohost.com/login.aspx?direct=true&db=a9h&AN=27961660&site=ehost-live.
[83] G. J. Snyder and E. S. Toberer, "Complex thermoelectric materials," *Nature Materials*, vol. 7, no. 2, pp. 105-114, 2008/02/01 2008, doi: 10.1038/nmat2090.
[84] F. Ritz and C. E. Peterson, "Multi-mission radioisotope thermoelectric generator (MMRTG) program overview," in *2004 IEEE aerospace conference proceedings (IEEE Cat. No. 04TH8720)*, 2004, vol. 5: IEEE, pp. 2950-2957.
[85] M. Hyland, H. Hunter, J. Liu, E. Veety, and D. Vashaee, "Wearable thermoelectric generators for human body heat harvesting," *Applied Energy*, vol. 182, pp. 518-524, 2016/11/15/ 2016, doi: https://doi.org/10.1016/j.apenergy.2016.08.150.
[86] J.-F. Li, W.-S. Liu, L.-D. Zhao, and M. Zhou, "High-performance nanostructured thermoelectric materials," *NPG Asia Materials*, vol. 2, no. 4, pp. 152-158, 2010/10/01 2010, doi: 10.1038/asiamat.2010.138.
[87] R. Venkatasubramanian, E. Siivola, T. Colpitts, and B. O'Quinn, "Thin-film thermoelectric devices with high room-temperature figures of merit," *Nature*, vol. 413, no. 6856, pp. 597-602, 2001/10/01 2001, doi: 10.1038/35098012.
[88] C. Chang *et al.*, "3D charge and 2D phonon transports leading to high out-of-plane ZT in n-type SnSe crystals," *Science*, vol. 360, no. 6390, pp. 778-783, 2018, doi: doi:10.1126/science.aaq1479.

[89] Y. Du *et al.*, "Thermoelectric Fabrics: Toward Power Generating Clothing," *Scientific Reports*, vol. 5, no. 1, p. 6411, 2015/03/23 2015, doi: 10.1038/srep06411.
[90] L.-G. Tran, H.-K. Cha, and W.-T. Park, "RF power harvesting: a review on designing methodologies and applications," *Micro and Nano Systems Letters*, vol. 5, no. 1, p. 14, 2017/02/28 2017, doi: 10.1186/s40486-017-0051-0.
[91] M. Cansiz, D. Altinel, and G. K. Kurt, "Efficiency in RF energy harvesting systems: A comprehensive review," *Energy*, vol. 174, pp. 292-309, 2019/05/01/ 2019, doi: https://doi.org/10.1016/j.energy.2019.02.100.
[92] Y. Luo, L. Pu, G. Wang, and Y. Zhao, "RF Energy Harvesting Wireless Communications: RF Environment, Device Hardware and Practical Issues," *Sensors*, vol. 19, no. 13, 2019, doi: 10.3390/s19133010.
[93] M. Zulqarnain *et al.*, "A flexible ECG patch compatible with NFC RF communication," *npj Flexible Electronics*, vol. 4, no. 1, p. 13, 2020/07/15 2020, doi: 10.1038/s41528-020-0077-x.
[94] R. Lin *et al.*, "Wireless battery-free body sensor networks using near-field-enabled clothing," *Nature Communications*, vol. 11, no. 1, p. 444, 2020/01/23 2020, doi: 10.1038/s41467-020-14311-2.
[95] P. Escobedo *et al.*, "Smart facemask for wireless CO2 monitoring," *Nature Communications*, vol. 13, no. 1, pp. 1-12, 2022.
[96] A. M. Zungeru, L.-M. Ang, S. Prabaharan, and K. P. Seng, "Radio frequency energy harvesting and management for wireless sensor networks," *Green mobile devices and networks: Energy optimization and scavenging techniques*, no. 13, pp. 341-368, 2012.
[97] A. S. Thangarajan *et al.*, "Static: Low Frequency Energy Harvesting and Power Transfer for the Internet of Things," (in English), *Frontiers in Signal Processing*, Original Research vol. 1, 2022-January-19 2022, doi: 10.3389/frsip.2021.763299.
[98] M. Piñuela, P. D. Mitcheson, and S. Lucyszyn, "Ambient RF Energy Harvesting in Urban and Semi-Urban Environments," *IEEE Transactions on Microwave Theory and Techniques*, vol. 61, no. 7, pp. 2715-2726, 2013, doi: 10.1109/TMTT.2013.2262687.
[99] P. D. Mitcheson, E. K. Reilly, T. Toh, P. K. Wright, and E. M. Yeatman, "Performance limits of the three MEMS inertial energy generator transduction types," *Journal of Micromechanics and Microengineering*, vol. 17, no. 9, p. S211, 2007.
[100] "Vibration data openly available from University of Southampton, UK." Vibration data openly available from University of Southampton, UK; http://eh-network.org/data/.
[101] "Real Vibrations." https://realvibrations.nipslab.org/.
[102] "Human climbing up stairs." Real Vibration. https://realvibrations.nipslab.org/node/1089.
[103] P. Basset, D. Galayko, A. M. Paracha, F. Marty, A. Dudka, and T. Bourouina, "A batch-fabricated and electret-free silicon electrostatic vibration energy harvester," *Journal of Micromechanics and Microengineering*, vol. 19, no. 11, p. 115025, 2009/10/12 2009, doi: 10.1088/0960-1317/19/11/115025.
[104] Y. Lu, F. Marty, D. Galayko, J.-M. Laheurte, and P. Basset, "A power supply module for autonomous portable electronics: ultralow-frequency MEMS electrostatic kinetic energy harvester with a comb structure reducing air damping," *Microsystems & Nanoengineering*, vol. 4, no. 1, p. 28, 2018/09/24 2018, doi: 10.1038/s41378-018-0025-2.
[105] K. Ichikawa and W. Hijikata, "Energy harvesting from biting force with thin sheet harvester based on electret and dielectric elastomer," *Nano Energy*, vol. 99, p. 107357, 2022/08/01/ 2022, doi: https://doi.org/10.1016/j.nanoen.2022.107357.
[106] Y. Naito and K. Uenishi, "Electrostatic MEMS Vibration Energy Harvesters inside of Tire Treads," *Sensors*, vol. 19, no. 4, 2019, doi: 10.3390/s19040890.
[107] H. G. Yeo, T. Xue, S. Roundy, X. Ma, C. Rahn, and S. Trolier-McKinstry, "Strongly (001) Oriented Bimorph PZT Film on Metal Foils Grown by rf-Sputtering for Wrist-Worn Piezoelectric Energy Harvesters," *Advanced Functional Materials*, https://doi.org/10.1002/adfm.201801327 vol. 28, no. 36, p. 1801327, 2018/09/01 2018, doi: https://doi.org/10.1002/adfm.201801327.
[108] G. Shi *et al.*, "A piezoelectric vibration energy harvester for multi-directional and ultra-low frequency waves with magnetic coupling driven by rotating balls," *Applied Energy*, vol. 310, p. 118511, 2022/03/15/ 2022, doi: https://doi.org/10.1016/j.apenergy.2021.118511.
[109] S. Roundy, P. Wright, and J. M. Rabaey, "A Study of Low Level Vibrations as a Power Source for Wireless Sensor Nodes," *Computer Communications*, vol. 26, pp. 1131-1144, 07/01 2003, doi: 10.1016/S0140-3664(02)00248-7.
[110] G. Lee, D. Lee, J. Park, Y. Jang, M. Kim, and J. Rho, "Piezoelectric energy harvesting using mechanical metamaterials and phononic crystals," *Communications Physics*, vol. 5, no. 1, p. 94, 2022/04/19 2022, doi: 10.1038/s42005-022-00869-4.
[111] G. Zhu *et al.*, "Linear-Grating Triboelectric Generator Based on Sliding Electrification," *Nano Letters*, vol. 13, no. 5, pp. 2282-2289, 2013/05/08 2013, doi: 10.1021/nl4008985.

[112] X. Li *et al.*, "Breeze-driven triboelectric nanogenerator for wind energy harvesting and application in smart agriculture," *Applied Energy*, vol. 306, p. 117977, 2022/01/15/ 2022, doi: https://doi.org/10.1016/j.apenergy.2021.117977.
[113] K. Xia *et al.*, "A triboelectric nanogenerator based on cosmetic fixing powder for mechanical energy harvesting," *Microsystems & Nanoengineering*, vol. 5, no. 1, p. 26, 2019/07/01 2019, doi: 10.1038/s41378-019-0066-1.
[114] H. Liu *et al.*, "A non-resonant rotational electromagnetic energy harvester for low-frequency and irregular human motion," *Applied Physics Letters*, vol. 113, no. 20, p. 203901, 2018/11/12 2018, doi: 10.1063/1.5053945.
[115] Y. Zhang, A. Luo, Y. Wang, X. Dai, Y. Lu, and F. Wang, "Rotational electromagnetic energy harvester for human motion application at low frequency," *Applied Physics Letters*, vol. 116, no. 5, p. 053902, 2020/02/03 2020, doi: 10.1063/1.5142575.
[116] T. Lin, Y. Pan, S. Chen, and L. Zuo, "Modeling and field testing of an electromagnetic energy harvester for rail tracks with anchorless mounting," *Applied Energy*, vol. 213, pp. 219-226, 2018/03/01/ 2018, doi: https://doi.org/10.1016/j.apenergy.2018.01.032.
[117] L. Zuo, B. Scully, J. Shestani, and Y. Zhou, "Design and characterization of an electromagnetic energy harvester for vehicle suspensions," *Smart Materials and Structures*, vol. 19, no. 4, p. 045003, 2010/02/25 2010, doi: 10.1088/0964-1726/19/4/045003.
[118] N. Han, D. Zhao, J. U. Schluter, E. S. Goh, H. Zhao, and X. Jin, "Performance evaluation of 3D printed miniature electromagnetic energy harvesters driven by air flow," *Applied Energy*, vol. 178, pp. 672-680, 2016/09/15/ 2016, doi: https://doi.org/10.1016/j.apenergy.2016.06.103.

Chapter 2: Theoretical background and Literature review on Electromagnetic Vibration Energy Harvesters

2.1 Introduction

As described in chapter-1, this era of IoT demands for the development of robust communication system between the deployed wirelessly connected sensor platforms. However, one of the major impediment in the pervasive deployment of wireless sensor nodes for building a resilient self-powered network is in finding a reliable and sustainable power source as a replacement of the energy-limited batteries for perpetual operation of the IoT devices. The omnipresence of mechanical energy in the form of vibrations in the rural/urban domestic and industrial environment offers the unique opportunity of harnessing these vibrations and converting it into usable electrical energy to power these deployable sensor nodes. Electromagnetic-Vibration Energy Harvesters (EM-VEHs) have emerged over the years as an attractive alternative of batteries for these sensor platforms. There has been significant research interest driven towards utilizing this type of electromagnetic transducers with improved device design and topologies, material selection and development, efficient power management etc. However, the key constraint in the widespread usage and viability of these VEHs are-

- While majority of the commercial EM-VEH devices are composed of narrowband linear oscillators but with the limited bandwidth, they lose their practical applicability considering the broadband nature of ambient vibrations.
- The omnipresent vibrations have their mechanical energy distributed over a wide-range of frequencies, which calls for frequency tuning mechanism or intrinsically wideband EM-VEHs to harness the mechanical energy efficiently.
- Although, the macro-scale electromagnetic-generators outpaces the contemporary VEHs, however, the performance of the MEMS (Micro-Electro-Mechanical-System)-scale EM-VEHs deteriorates drastically, owing to the weak EM-interaction and EM-coupling between the magnet-coil assembly, also the small displacements of the MEMS spring structures.

Hence, the following section presents a detailed review of EM-VEHs both in macro and in micro-scale discussing and addressing these challenges.

2.2 Theoretical background of Resonant/Linear Electromagnetic Vibration Energy Harvesters

As mentioned previously, the electromagnetic vibration energy harvesters can be simply represented by second order mass damper and spring system where $x(t)$ is the displacement of the generator mass m, $y(t)$ is the displacement of the harvester housing due to external excitation of the form $y(t) = Y_0\, e^{i\omega t}$ and $z(t)$ is the relative displacement of the mass (where, $z(t) = x(t) - y(t)$). The dynamics of the system can be then expressed by the following equation,

$$\boldsymbol{m\ddot{z}(t) + c\dot{z}(t) + kz(t) = -m\ddot{y}(t)} \tag{2.1}$$

Where, k is the stiffness constant of the spring and c is the total damping coefficient of the system ($c = c_m + c_e$ = sum of the mechanical and electrical damping). We define $F_0 = m\omega^2 Y_0$, and let us consider the trial solution of the form $z(t) = Z_0\, e^{i\omega t}$ and if we consider both the real and imaginary part of the equation (2.1) above then it can be written as,

$$\boldsymbol{\left(-m\omega^2 Z_0 + i\omega c Z_0 + kZ_0\right)e^{i\omega t} = F_0\, e^{i\omega t}} \tag{2.2}$$

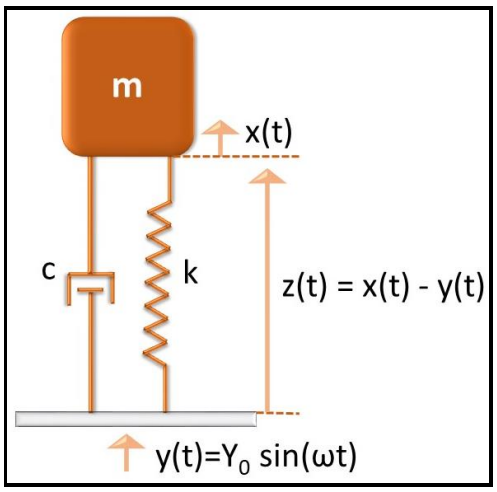


Figure 2.1: The Basic block diagram of a Single degree of freedom system.

Hence, the amplitude of displacement and the associated phase angle can be represented as,

$$\boldsymbol{|Z_0| = \frac{F_0}{\sqrt{(k-m\omega^2)^2+(\omega c)^2}} \quad and \quad \theta = tan^{-1}\left(\frac{-\omega c}{k-m\omega^2}\right)} \tag{2.3}$$

Hence, the relative displacement $z(t)$ can be represented as,

$$z(t) = \frac{F_0}{\sqrt{(k-m\omega^2)^2+(\omega c)^2}} \tan^{-1}\left(\frac{-\omega c}{k-m\omega^2}\right) e^{i\omega t}$$

$$= \frac{F_0}{\sqrt{(k-m\omega^2)^2+(\omega c)^2}}\, sin(\omega t - \theta) \tag{2.4}$$

The displacement of the mass maximizes when the frequency of external excitation $\omega \left(= \sqrt{\frac{k}{m}}\right)$ matches with the natural frequency of oscillation of the mass ω_n, i.e. the resonance takes place for $\omega = \omega_n$, resulting in the maximum displacement, $|Z_0|_{\max} = \frac{mY_0\omega_n}{c}$. The mechanical damping ratio of the resonant system is expressed as, $\rho_m = \frac{c_m}{2m\omega_n}$, and the open circuit quality factor (Q_{OC}) can also be expressed in terms of the damping ratio $Q_{OC} = \frac{1}{2\rho_m}$. This mechanical damping arises from various sources such as the frictional loss between moving surface or the loss due to the structural material itself. Through the dampers (both mechanical and electrical), the acquired energy is dissipated from the dynamic system. On the other hand, the damping present in the system also broadens the response at the cost of reduced amplitude. As shown above, the mechanical damping coefficient of the system (ρ_m) is inversely proportional to the quality factor Q_{OC}, so as evident from Fig.2.2(a), lower the damping, sharper are the peaks and higher is the amplitude of the peak whereas higher damping also flattens or broadens the response. Therefore, there is always a trade-off between the obtainable peak amplitude of the response and the bandwidth of the same.

The Electromagnetic transducer works according to Faraday's law, the relative displacement between the coil and the magnet induces electromotive force into the coil which is proportional to the rate of change of magnetic flux passing through the coil,

$$V = -N\frac{d\emptyset}{dt} = -N\frac{d\emptyset}{dz}\frac{dz}{dt} = -N\,v\,\frac{dB_{effective}}{dz}\sum_{i=1}^{N} A_i \tag{2.5}$$

Where, N is the number of turns of the coil, $\emptyset$ is the total magnetic flux linkage, v is the velocity of the relative motion between the coil and the magnet, $\frac{dB_{effective}}{dz}$ is the gradient of magnetic flux density and A_i is the area of each individual turn of the coil. The spatial gradient of magnetic flux can be treated as a constant if the amplitude of relative movement is small enough. Now when the load is connected with the coil, current flowing through it restricts the movement of the harvester unit or rather damps its motion electrically. Therefore, in this context the electrical damping associated with the system needs to be investigated thoroughly to understand its effect on the response of the system. So the equation representing the system will be modified,

$$m\ddot{z}(t) + c\dot{z}(t) + kz(t) = -m\ddot{y}(t) - F_{em} \tag{2.6}$$

Where, F_{em} is the electromagnetic force acting on the system. In electrical domain, the electromagnetic transducer can be expressed in terms of series connected R_c, R_L and L which are the resistance of the coil, resistance of the load and the inductance of the coil respectively.

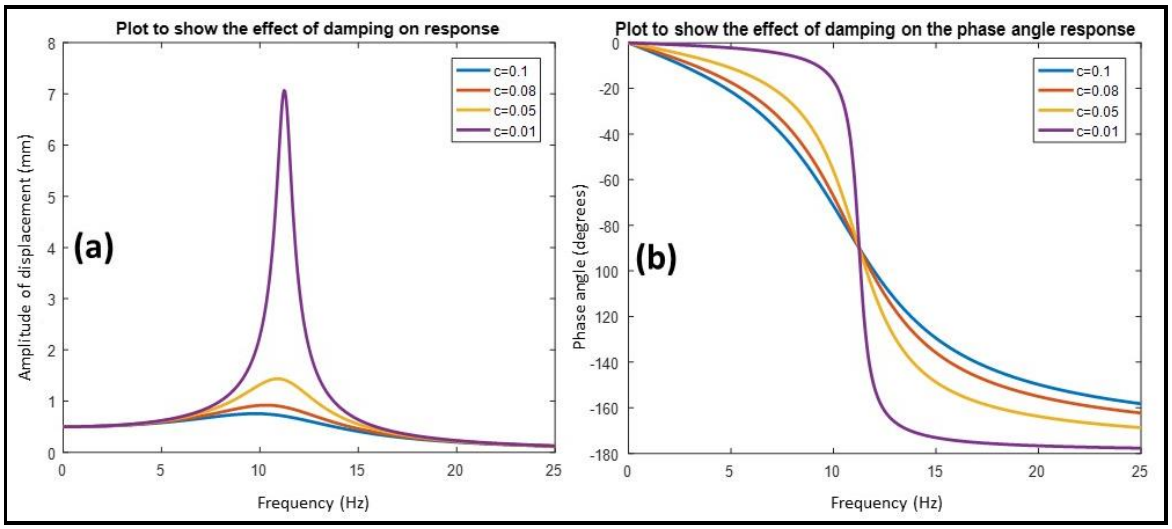


Figure 2.2: Plot to shown the effect of the damping parameters (a) on amplitude of displacement and phase, (b) of the same of a SDOF system.

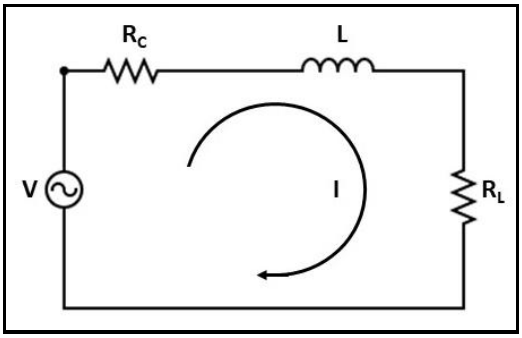


Figure 2.3: Electrical representation of Electromagnetic generator.

The induced voltage V in this case can be considered as the voltage source as shown in Fig.2.3. Applying Kirchhoff's voltage law in the shown closed circuit loop we get,

$$\boldsymbol{V_{load} = I\,R_L = V - I(R_c + j\omega L)} \tag{2.7}$$

Now, considering that the current flowing through the coil is I. The electromagnetic force can be then expressed as,

$$F_{em} = I\,N\,\frac{d\varphi}{dz} = \frac{N\,V}{R_c+R_L+j\omega L}\,\frac{d\varphi}{dz}$$

$$= \frac{N\left(N\,\frac{d\varphi}{dt}\right)}{R_c+R_L+j\omega L}\,\frac{d\varphi}{dz}$$

$$= \frac{1}{R_c+R_L+j\omega L} N \frac{d\varphi}{dz} \left(N \frac{d\varphi}{dz} \frac{dz}{dt}\right)$$

$$= \frac{1}{R_c+R_L+j\omega L} \left(N \frac{d\varphi}{dz}\right)^2 \left(\frac{dz}{dt}\right)$$

$$= \boldsymbol{c_{em}}\left(\frac{\boldsymbol{dz}}{\boldsymbol{dt}}\right) \tag{2.8}$$

Where, c_{em} is the electromagnetic damping coefficient associated with the system, R_c is the coil resistance, R_L is the load resistance and L is the inductance of the coil. Now as these vibrations based energy harvesters operate at mostly low frequencies, so the effect of the inductance on c_{em} can be neglected as compared to R_c and R_L. Finally, the damping coefficient and the corresponding force can be expressed in the following form,

$$\boldsymbol{c_{em}} = \frac{\boldsymbol{1}}{\boldsymbol{R_c+R_L}} \left(\boldsymbol{N} \frac{\boldsymbol{d\varphi}}{\boldsymbol{dz}}\right)^{\boldsymbol{2}} \quad \boldsymbol{\&} \quad \boldsymbol{F_{em}} = \frac{\boldsymbol{1}}{\boldsymbol{R_c+R_L}} \left(\boldsymbol{N} \frac{\boldsymbol{d\varphi}}{\boldsymbol{dz}}\right)^{\boldsymbol{2}} \frac{\boldsymbol{dz}}{\boldsymbol{dt}} \tag{2.9}$$

Therefore, the average electrical power dissipated through this electromagnetic damper can be given as,

$$P_e = \frac{1}{T}\int_0^T \mathrm{F_{em}} \frac{dz}{dt} dt$$

$$= \frac{1}{T}\int_0^T \frac{1}{R_c+R_L} \left(N \frac{d\varphi}{dz}\right)^2 \left(\frac{dz}{dt}\right)^2 dt$$

$$= \frac{1}{T} \frac{1}{R_c+R_L} \left(N \frac{d\varphi}{dz}\right)^2 \int_0^T \left(\frac{dz}{dt}\right)^2 dt$$

$$= \frac{1}{T} \frac{1}{R_c+R_L} \left(N \frac{d\varphi}{dz}\right)^2 \int_0^T \left[\frac{\mathrm{F_0}\,\omega}{\sqrt{(k-m\omega^2)^2+(\omega c)^2}} \cos(\omega t - \theta)\right]^2 \mathrm{dt}$$

$$= \frac{c_{em}\ \mathrm{m}^2\,\omega^6\,\mathrm{Y_0^2}}{2[(k-m\omega^2)^2+(\omega c)^2]}$$

$$= \frac{\boldsymbol{c_{em}\,\omega^3\,Y_0^2\left(\frac{\omega}{\omega_n}\right)^3}}{\boldsymbol{2\omega_n\left[\left(1-\left(\frac{\omega}{\omega_n}\right)^2\right)^2+\left(2\rho_T\left(\frac{\omega}{\omega_n}\right)\right)^2\right]}} \tag{2.10}$$

To calculate the total average power dissipated across both the mechanical and the electrical damper, we consider the total damping ratio $\rho_T = \frac{c}{2m\omega_n}$ and substitute this in the equation (2.10) above in the place of the electrical damping to obtain,

$$\boldsymbol{P_{avg}} = \frac{\boldsymbol{m\,\rho_T\,\omega^3\,Y_0^2\left(\frac{\omega}{\omega_n}\right)^3}}{\boldsymbol{\left[\left(1-\left(\frac{\omega}{\omega_n}\right)^2\right)^2+\left(2\rho_T\left(\frac{\omega}{\omega_n}\right)\right)^2\right]}} \tag{2.11}$$

At resonance, i.e. for $\omega = \omega_n = \sqrt{k/m}$, maximum power is dissipated across the dampers which can be represented as,

$$P_{avg_{max}} = \frac{m\,\rho_T\,\omega_n^3\,Y_0^2\left(\frac{\omega_n}{\omega_n}\right)^3}{\left[\left(1-\left(\frac{\omega_n}{\omega_n}\right)^2\right)^2+\left(2\rho_T\left(\frac{\omega_n}{\omega_n}\right)\right)^2\right]} = \frac{m^2\,\omega_n^4\,Y_0^2}{2(c_{em}+c_m)} \tag{2.12}$$

The variation of the average power with frequency of operation and the effect of different parameters is shown in the figure below.

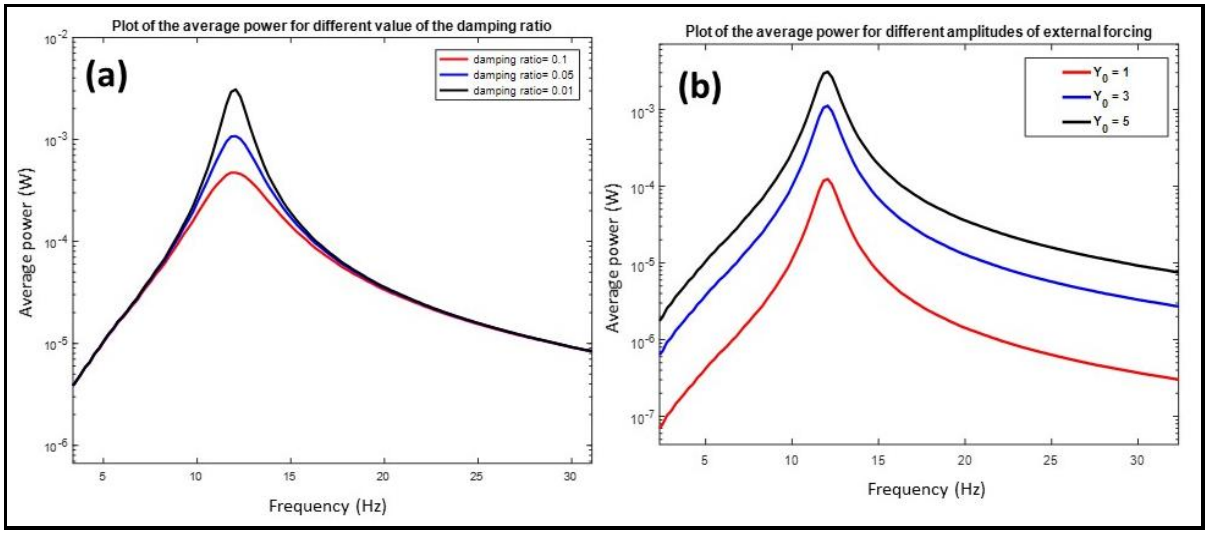


Figure 2.4: (a) Plot to show the effect of damping, and (b) external forcing on the average power.

It is noticeable from the plots (Fig.2.4) that for lower values of the damping ratio, the peak amplitude of the average power shifts to higher values without any considerable alteration in the bandwidth, which on the other hand is modified when the amplitude of external forcing changes. For a larger amplitude of the excitation, the peak shifts to higher value and the frequency response broadens slightly as well.

From the analysis above, we can derive that the linear VEHs offer maximum electrical power when operated at resonance, i.e. when the natural frequency of oscillation of the VEH matches with the frequency of the external excitation. The dynamic response demonstrates narrowband and sharp resonance peaks. Although the damping does not tailor the frequency of oscillation, but has influence on the amplitude of displacement of the oscillators and hence on the obtainable power, larger damping results in reduced power. On the other hand, higher amplitudes of external excitation translate into larger extracted power from the VEH. In the following section, a detailed survey of resonant electromagnetic generators has been presented showing the evolution of the linear devices and the state-of-the-art VEHs.

2.3 Resonant Electromagnetic Vibration Energy Harvesters

Over the past couple of decades, the surge of research in the field of mechanical energy harvesting from ambient vibrations through electromagnetic transducers underpins the simplicity of implementation of this harvester with a spring-mass-damper system [1] along with high mechanical energy extraction efficiency at resonance [2]. For the classical linear type Vibration Energy Harvesters (VEHs), the response from the harvester is maximized at resonance when the frequency of excitation equals the natural frequency of oscillation of the energy-harvesting unit. The external excitation provided to this harvester translates into relative displacement between the magnet and coil and induces an extractable voltage across terminals of the coil. Among the earliest proposed micro-generators, Williams et al. reported a $5mm \times 5mm \times 1mm$ device [3] that has the capability of extracting 1μW electrical power at 70Hz frequency, which increases to 0.1mW power for 330Hz excitation. In 1998, Amirtharajah et al. developed an electromagnetic generator with the resonance frequency of 94Hz, and the deliverable power extracted from the vibrations of human walking was estimated to be 400μW on average, which enabled the implementation of a self-powered DSP system [4]. An even lower resonant frequency device was developed by the researchers of The Chinese University of Hong Kong [5], a magnet spring arrangement comprising of a NdFeB magnet mounted on spiral copper springs. This harvester generated a power of 10μW at the input excitation frequency of 64Hz. Jones et al. developed miniaturized generators (Fig. 2.5(a)) comprising of magnets, spring and coil in such a way that on external vibration, the coil interacts with the magnetic flux which induces extractable voltage across the coil [6]. The cantilever springs were developed on etched stainless steel which held wire wound copper coils as the mass of the system, and the magnets were kept stationary on a rigid fixture, allowing the coil to cut through the magnetic flux (As shown in Fig. 2.5(a)). The fabricated generator demonstrated the capability of extracting a peak power of 3.9mW, along with an average 157μW power from vibrations of the engine block of a Volkswagen Polo car during a 1.24km journey at 25km/h average speed.

In 2007, Beeby *et al*. developed an electromagnetic microgenerator [7] with the aim of harvesting vibrational energy from an air compressor unit. They employed four sintered rare earth material NdFeB magnets bonded to the top and bottom surface of a cantilever beam and zinc coated mild steel keepers were used to aid the coupling of magnetic flux between the top and bottom magnets (Fig. 2.5(b)). Tungsten alloy blocks attached to the free end of the cantilever beam served the purpose of additional mass for increasing the vibration quality and

a coil wound from enamelled copper wire of 12µm diameter was used to extract the energy. They reported generation of 46µW power to a resistive load of 4kΩ at the resonant frequency of 52Hz from a 60mg vibration level. Output performance is improved as this device delivers 30% of the total power dissipated in the generator to electrical power across the load.

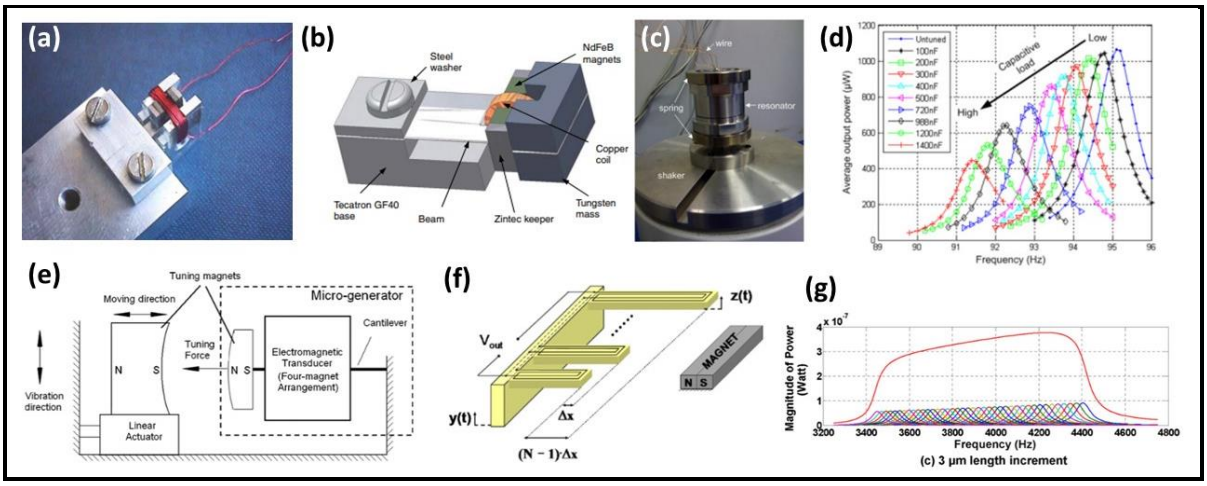


Figure 2.5: (a)Electromagnetic generator prototype developed by Jones et al. [4], (b)Electromagnetic microcantilever based generator demonstrated by Beeby et al. [7], (c) Macroscale electrically tuneable electromagnetic energy harvester (Perpetuum Ltd.), (d) and the corresponding variation of output power with varying load capacitance demonstrated by Zhu et al. [20], (e) Schematic representation of frequency tuning strategy developed by Zhu et al. [21], (f) Schematic representation of frequency tuning through multiple cantilevers of varying length developed by Sari et al. [22], (g) and the corresponding power output over wide bandwidth by increasing the length of adjacent cantilevers by 3µm.

These linear type VEHs employing high efficiency transducers have been used both in academia [8-12] and in the industry [13, 14] as a robust and reliable solution to the powering issue of wireless sensor platforms. This class of VEH offers large deliverable power at resonance, at the cost of considerably low bandwidth of operating frequencies. However, with an intelligent design strategy, frequency tuning [15] and prior knowledge of the vibration characteristics of the site of deployment [16], the VEH could be designed to trigger the resonance, which effectively results in larger power generation. Qiu *et al.* presented an electromagnetically transduced resonant VEH exploiting a Halbach assembly of magnets, which enhances the electromagnetic interaction and maximizes the output power to 90.35mW with 0.5g excitation and at a low frequency of resonance (12.65Hz) [17]. Although this device has great potential for powering a wireless sensor platform, this comes at the cost of a large footprint (volume of the device, calculated 164.27cm^3). Gao *et al.* experimentally investigated

the performance of resonant VEHs in transducing mechanical energy from wheelset/track of railways [18]. The device delivers 119mW power at 6Hz resonance for a 1.2-2mm rail track displacement, but occupies a large footprint of 1680cm^3, which limits its range of applicability. Recently Rubes *et al.* presented an autonomous wireless sensing and communication platform powered through an electromagnetic vibration energy harvester that resonates at 33Hz with harmonic excitation [19]. The energy harvesting system drives a wireless sensor node to deliver 600 samples of data per second at the cost of a considerably large volume of 124cm^3. Owing to the geometry of the linear springs, these resonant harvesters exhibit characteristically small displacements around the point of static equilibrium, which restricts large amplitudes of oscillation for a small excitation amplitude. Hence, a key challenge is to develop linear resonators within a small footprint that can facilitate large amplitudes of oscillations even for smaller excitations, while demonstrating linear spring-force variation.

Another key fundamental limitation of the resonant VEHs is the critical dependence of the device performance on the resonance frequency matching which hinders the real life application scenario for these otherwise efficient resonance VEHs. Significant research effort has been devoted towards exploring the efficiency of different frequency tuning mechanism, which tunes the frequency of the oscillator through mechanical (changing mass, spring length, spring stiffness, applying axial load etc.) [21, 23] or electrical (changing electrical load) [24] means to match with that of the external excitation to enhance mechanical energy harnessing capabilities. Zhu et al. electrically tuned the operable frequency range of a commercially available electromagnetic macroscale generator (Perpetuum ltd.) which is resonant at 95.1Hz for 10mg excitation (Fig. 2.5(c) and (d)). The capacitive load across the VEH has been varied from 0-1400nF that tuned the resonance frequency by 3.8Hz at 10mg excitation without notably compromising the obtainable output power from the device [20], which proves the potential of this approach for frequency tuning. Bidirectional frequency tuning for the EM-VEHs has been achieved [25] by tailoring inductive load and capacitive load to tune the resonant frequency of the linear VEHs to the higher and lower frequency range respectively.

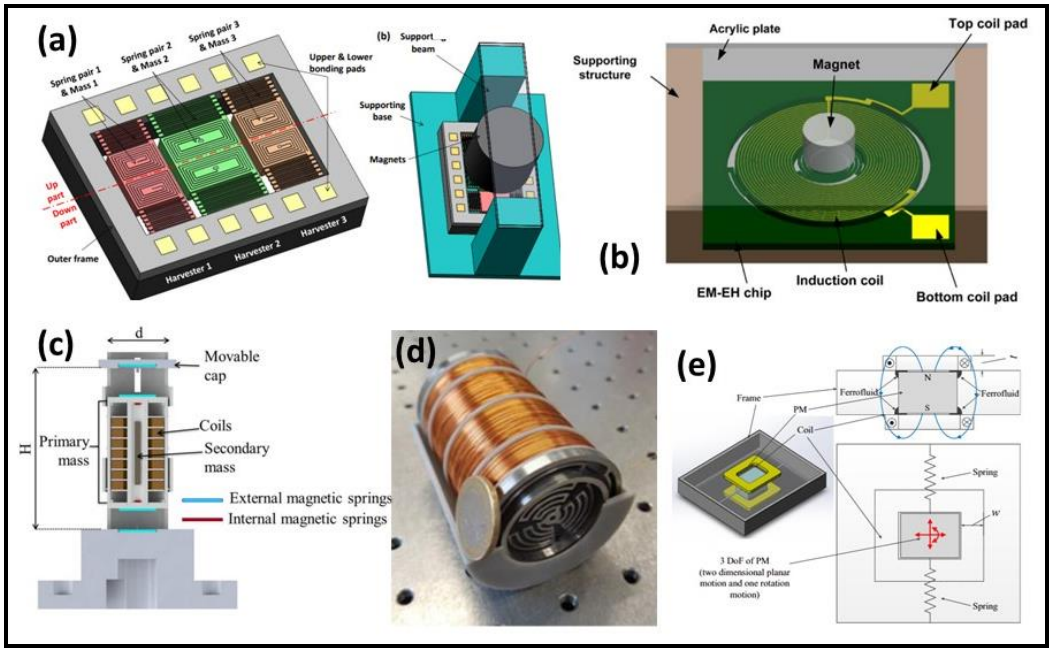


Figure 2.6: (a) MEMS scale multifrequency energy harvester chip and the MEMS device assembled with the magnet [26], (b) Schematic representation of 2DOF energy harvester [27], (c) Cross-section view of high figure of merit energy harvester with primary, secondary mass and coils [28], (d) Assembled 2DOF vibration energy harvester for tramway application [29], (e) 3DOF MEMS energy harvester with ferrofluid as lubricant [30].

Frequency tuning has been also implemented by means of introducing magnetic interaction into the energy harvesting system. The resonant frequency of a microgenerator has been tuned from 67.6Hz to 98Hz by introducing axial tensile force through external magnets placed near the electromagnetic VEH [21], which is excited at a constant acceleration of 0.59m/s^2.

Another popularly chosen route to enhance the range of operable frequencies of the EM-VEHs is to use array of electromagnetic transducers, each having different natural frequency of oscillation. In 2008, Sari *et al*. employed a series of Parylene cantilevers [22] varying in lengths, each patterned with coil that interacts with the fixed magnet in the middle of the device, allowing electric current to be generated when relative movement between the cantilevers with the coils take place. By virtue of being a polymer material, Parylene offers large deflection range for the cantilevers compared with Silicon, and it is simpler in terms of fabrication. Fig. 2.5(g) shows the predicted output from such an array of 40 cantilevers, which extends the operable frequency range up to 1 kHz with a steady 0.4μW power output. This performance enhancement was also validated through fabricated multi-cantilever array prototype.

Designing multimodal structures as well as the inclusion of multiple degrees-of-freedom have also been preferred choices of the energy harvesting research community for

improving the bandwidth of operable frequencies. Yang et al. designed [31] a low cost electromagnetic energy harvester with three permanent magnets attached to an acrylic beam and three set of bi-layer spiral copper coil under the magnets fabricated on PCB. The magnets mounted on the acrylic beam instigates multiple modes of oscillation at 369Hz, 938Hz, 1184Hz, and on external vibration, the coils experience a change of magnetic flux that results in induced voltage across the coils. This device yields 1.157μW power in sum from all the coils exhibiting the first mode of oscillation while it is excited with 14μm amplitude external force. This strategy has also been utilized in MEMS scale for the realization of a multimode VEH. A microchip scale EM-VEH has been implemented with three different micro-transducers that are fabricated on a single Silicon chip [26] and carries Al coils (Physical Vapour Deposited). The central mass for each of the transducers are suspended through folded springs that aids in exhibiting in-planar motion when excited with mechanical vibrations and cylindrical magnets are fixed on top of the silicon chip through supporting beam (Fig. 2.6 (a)). Each of the micro-transducer exhibited 3 natural modes of vibration, which sums up a total of 9 modes for the overall VEH unit that resulted in broadening the range of operable frequencies over 100-800Hz. V-shaped and open delta-shaped plate like geometry have also been implemented with optimized mass and optimal placement of these mass on the plate structure to excite adjacent multiple modes of vibration [32]. It was experimentally shown that an open delta geometry along with three mass placed at optimal locations promotes adjacent modes of vibration at 8Hz, 11.8Hz and 19.2Hz.

Multimodal energy harvesting have gained increasing research interest among the other bandwidth widening strategies owing to its simpler implementation, as it does not require any external tuning component, rather depends mostly on the design of the vibrating structures. Tao et al. presented the design, fabrication and characterization of a two-degree-of-freedom (2DOF) resonant MEMS EM-VEH system [27] comprising of a circular resonator implemented in SOI (Silicon-On-Insulator) wafer, having a larger ‘primary mass’ and smaller ‘accessory mass’ connected through a set of circular springs (Fig. 2.6(b)). Microfabricated coils on the primary mass interacts on external excitation with the magnet mounted on top through acrylic beam. The device exhibits two closely spaced modes at 326Hz and 391Hz that corresponds to the 2DOF of the structure and yields a maximum normalized power density of 2.3×10^{-7} W/cm^{3}g^2. Velocity amplification has been also exploited in 2DOF system [28] that utilizes the relative motion between larger secondary mass and smaller primary mass, the latter surrounded by the former and held within limited motion by magnetic springs as shown in Fig.2.6(c). To strengthen the electromagnetic interaction, Halbach array of magnets are used as the primary

mass to promote strong electromagnetic interaction between the magnets and the coil that is wrapped around the magnet array. The device yielded a large output power of 2.75mW for 0.4g excitation at 11.25Hz, which makes it a potential substitute of a C-type battery in low power electronics applications. An innovative 2DOF system have been presented by Perez et al. which deliver 6.5mW power on average utilizing membrane type springs (Fig. 2.6(d)) holding inner mass magnets and outer mass coils [29]. The broad operable frequency range of this device enables it to harness mechanical energy from vibrations of railway/tramway, making it an attractive alternative of batteries for on-board railway applications.

Han et al. proposed a cubic harvester [33] without any spring, aimed to convert energy from all three dimensions. They designed a cubic box with a free permanent magnet placed inside without any support of springs, thus harvesting vibrational energy from all directions. The device offered ultra-wide working bandwidth between 20Hz to 100Hz and at 26.87Hz the maximum power output is 0.75μW. Harvesting substantial mechanical energy from human motion has always been a great challenge owing to the ultra-low frequency of dominant vibrations along with the multiple degrees of freedom associated with the movement. To address this issue, Wu et al. designed a miniaturised resonant EM-VEH with a permanent magnet located in an aluminium casing held through elastic spring support as shown in Fig. 2.6(e), and two coil windings were included on the top and bottom plate of this structure to interacting with the changing magnetic flux when the magnet moves [34]. The magnet in this case is free to move inside the casing and exhibits 3DOF motion on being excited through external force. Ferrofluid has been used inside the casing to reduce the frictional loss between the magnet and the casing, which also reduces the energy dissipation arising from such friction. The capability of harnessing mechanical energy from all directions enables the device to offer wider frequency bandwidth. The primary resonant modes were experimentally found to be at 7.5Hz and 10Hz in the x-direction, 10Hz and 14Hz in the y-direction for different stiffness of the elastic spring. The VEH unit mounted on a shoe generate a high power level of up to 2.8mW from the running motion of human proving its potential in wearable application area.

Apart from bandwidth widening efforts, there is also a continuous drive towards improving the overall performance of these resonant EM VEHs, which is often executed by exploring different designs, topologies of the device, as well as by exploiting different dynamical complexities of these transducers. The cylindrical dimension of commercial batteries has often driven the research in developing similar shaped VEHs that could replace the batteries. To produce large power density from these VEH, an imperative requirement is to explore novel coil-magnet configurations that would essentially strengthen the electromagnetic

coupling and hence the obtainable output power. Large scale energy harvesting through linear energy transducers have been demonstrated by [35] that is built to harvest mechanical energy from vehicular suspensions or even long bridges (Fig. 2.7(a)). The VEH utilizes the strong magnetic field generated by arranging radially and axially magnetized permanent magnets together around an aluminium shaft. The radial and axial magnets are placed alternatively, stacked on top of each other forming a column. Two of such columns have been used in this device, separated through an intermediate layer of copper coils that yielded a large power density of $27.2 \times 10^4\,W/m^3$ from a relative velocity of 0.25m/s, which emulates typical velocity experienced in vehicle suspensions. Similar tubular linear VEHs have been developed for harnessing mechanical energy from free piston engine [36] that are widely used in electric vehicle, which opens up the scope of using these VEHs for condition monitoring of electric vehicles.

Halbach configuration of magnets is well known for its potential in dramatically improving magnetic field distribution in the preferred direction, while minimizing the fields from the opposite direction. Recently, a linear generator has been implemented with an array of coils, cubic halbach arrangement of magnets have been reported which utilizes couple of springs to instigate in-planar motion of the magnet array with respect to the coils [37] as shown in Fig. 2.7(b). In addition to the Halbach array of magnets, this work also explores the capability of magnet arrays that comprise alternately placed opposite polarized magnet elements. The alternative arrangement of cube shaped magnets were reported to offer the largest variation of magnetic flux density with respect to time. Owing to the enhanced coil magnet interaction, the VEH produced 35.5mW RMS power for an external force of amplitude $9.8m/s^2$.

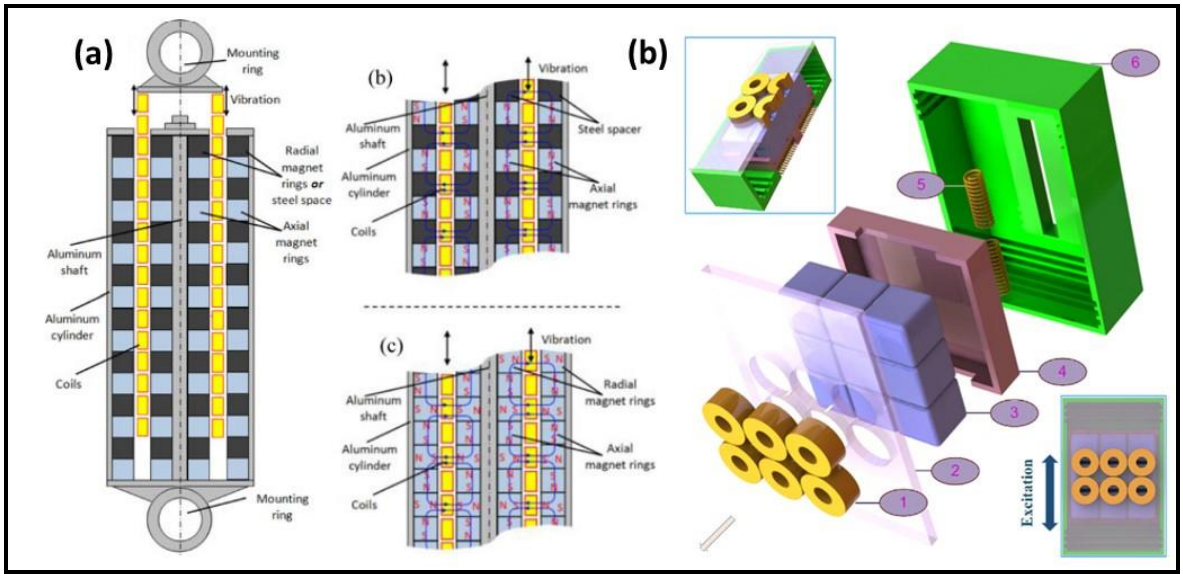


Figure 2.7: (a) Tubular electromagnetic energy harvester with radially and axially magnetized permanent magnets, and coils [35], (b) Electromagnetic energy harvester with (1) coil array, (2) coil holder, (3) magnet array, (4) magnet casing, (5) in planar moving springs, (6) device housing [37].

Along with exploring the avenues of novel and high magnetic flux density configurations, researcher in this field of vibration energy harvesting have also exploited the magnetic properties of Ferrofluids, which is a suspension of nano-scale magnetic dipoles dispersed in non-magnetic fluids that offers zero net magnetization in the absence of external magnetic fields. The externally applied magnetic fields aid in rotating the magnetic dipoles that results in net magnetic moment produced in the fluid, parallel to the direction of the external field. In the context of vibration energy scavenging, upon the application of external excitation force on ferrofluids, substantial change of magnetic flux density is achieved, which could be utilized by coils that are wrapped around the ferrofluid containers to induce significant voltage. Ferrofluids have gained interest in this field of research owing to its fluid nature, which aids the material to conform onto any shape, and could be used for inaccessible locations where practically solid permanent magnets cannot be used, especially considering small-scale devices. Bibo et al. developed a ferrofluid based (15% Fe_3O_4) vibration energy harvester, which generates larger surface waves from the sloshing motion of the fluid in resonant conditions even with low amplitude of external forces [38]. These surface waves generate time varying magnetic flux density, which is harnessed through wrapped copper coils (1000 turns and 37.5Ω resistance). The dominant modal frequencies of the ferrofluid could be tuned by varying the fluid height and the radius of the container carrying the ferrofluid. This device converted weak and low frequency excitations (~0.25g, <10Hz) into 18mV voltage and 1μW power across an optimized external load. Ferrofluids are versatile materials for energy harvesting applications

and have been well utilized for implementing liquid springs in VEHs and as a lubricant to minimize the mechanical damping arising from the motion associated with VEHs.

Wang et al. presented a low resonant frequency EM-VEH that comprise of disc shaped magnets arranged in a slotted acrylic tube that is filled with ferrofluid, and microfabricated copper coils developed on flexible material (parylene) that is wrapped around the acrylic tube [39] as shown in Fig. 2.8(a). With no external excitation, the ferrofluid places the magnet array in an equilibrium position with respect to the coils; however, on external forcing when the magnet array deflects from its position of equilibrium, the ferrofluid restores the magnets back to its position with a force that is proportional to the initial displacement of the magnet array. Hence, ferrofluid in this case works as a liquid spring for the VEH system that brings the natural frequency of oscillation down to 16Hz. Subjecting the VEH to 3g force, a maximum output power of 79nW was delivered to suitable resistive load. On the other hand, Chae et al. developed a VEH that promotes lateral motion of a magnet array inside an aluminium housing and the ferrofluid material is used between the magnet array and the casing as a lubricant [40] to reduce the mechanical damping caused by the friction of the movement of these magnets inside the casing (Fig. 2.8(b)). This work experimentally demonstrated that the over 93,600 cycles of operation, the power outcomes of the system reduces to 59.73% without using the ferrofluid, however, with the lubricant the power only depreciates 1.02% as the frictional loss is reduced.

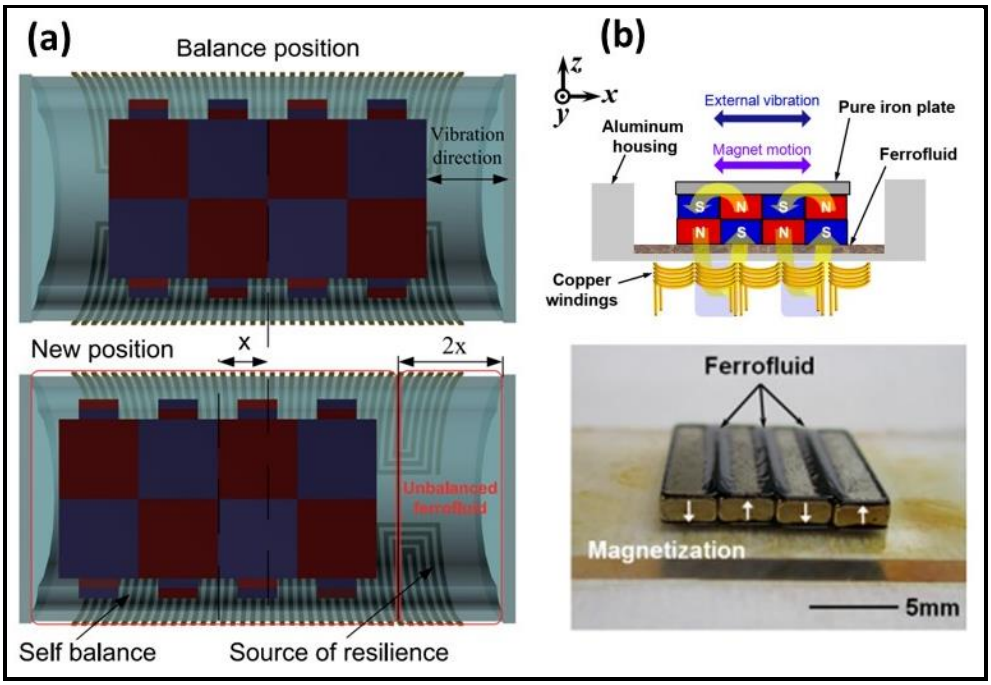


Figure 2.8: (a) Liquid spring based electromagnetic vibration energy harvester, (top) the equilibrium configuration in the absence of external force, and (bottom) the situation when the magnet is displaced from the equilibrium due to external force [39], (b) In planar electromagnetic

generator with ferrofluid as lubricant (top), arrangement of magnets in the array along with ferrofluid (bottom) [40].

2.4 Theoretical background of Nonlinear Electromagnetic Vibration Energy Harvesters

The typical linear energy harvesters that have been shown above are optimally designed to harvest energy within a narrow frequency band in the neighborhood of the natural frequency of the oscillator. Moreover, these systems are more applicable for the scenario where the vibration source has discrete frequency peaks. Majority of the ambient vibrations are random and wideband in nature; the amplitude and frequency of the source varies continuously which demands for a wideband energy scavenger to efficiently harness the mechanical energy. However, the linear harvesters can only scavenge useful energy for a relatively shorter part of the vibration spectrum, which imposes excessive constraints on their usability. To address this cardinal issue, the nonlinear oscillators could be considered instead of the linear ones.

Nonlinear harvesters can be modelled using Duffing oscillator equation (2.13), which takes into account the nonlinear forces arising in the system owing to spring modifications, magnet attraction/repulsion etc. This nonlinear restoring force enables the linear resonance to be tuned for changes in static displacement and due to this shift in resonance frequency; a relatively large amplitude response persists over a wide frequency range that in turn increases the bandwidth of operation of the system over which power can be harvested. The generalized representation of nonlinear potential energy ($U(x)$) and the associated force ($F(x)$) can be given by-

$$\boldsymbol{U(x) = \frac{1}{2}kx^2 + \frac{1}{4}k_n x^4} \tag{2.13}$$

$$\boldsymbol{F(x) = -\frac{dU}{dx} = -kx - k_n x^3} \tag{2.14}$$

$U(x)$ is called the Duffing potential energy and depending on the value of the coefficients k and k_n it can take different forms as shown in the table 2.1 below.

Table 2.1- Nonlinear potential energy for different values of coefficients

$k > 0$	Monostable
$k>0$, $k_n > 0$	Hardening type
$k > 0$, $k_n < 0$	Softening type
$k < 0$, $k_n > 0$	Bi-stable

The nature of the nonlinear potential energy relies on the coefficients k and k_n, where k is majorly responsible for the linear spring force associated with the system, whereas k_n introduces the nonlinearities into the system. Henceforward, k and k_n will be referred to as linear and nonlinear spring stiffness coefficients respectively. When the coefficient $k_n = 0$, with $k > 0$, then the equation (2.13) and (2.14) above represents a linear system where the spring force varies linearly with the displacement (x). For nonzero value of the nonlinear stiffness coefficient, $k > 0$ produces a potential energy profile with a single stable minima (at $x = 0$), hence called monostable potential energy, and $k < 0$ produces a nonlinear potential energy profile with two minima separated by a potential energy barrier (at $x = 0$), and hence called bistable potential energy.

The monostable type nonlinearity can take two forms depending on the value of k_n with $k > 0$. For $k_n > 0$, the restoring force increases with increase in displacement, which implements the monostable-hardening type nonlinearity. The nature of this spring force makes the spring 'harder' to deform, and thus it derives the name 'hardening' nonlinearity. On the other hand, for $k_n < 0$, the restoring force reduces with increasing displacement, which manifests a relatively 'soft' spring that is easy to deform, and hence derives its name as 'softening' nonlinearity. Fig. 2.9 shows the variation of linear and nonlinear forces along with the corresponding potential energies. In terms of implementation, monostable nonlinearity can be induced in the otherwise linear transducers by geometrically tailoring the springs, forcing it to stretch on the application of external force [41-44]. Monostable nonlinearity has also been included in energy harvesters by the means of magnetic interaction. The magnets are arranged in such a way that the device utilizes the magnetic force as a spring instead of using a physical spring structure, which is popularly known as magnetic levitation and has been well exploited in the field of vibration energy harvesting [45-47]. On the other hand, the bistable effect has been realized in the nonlinear systems through the introduction of beam buckling [48-50], magnetic repulsion/attraction [51-53], magnetic attraction force and ferromagnetic beam [54] etc. The details regarding the experimental implementation of various nonlinearities will be discussed in the following section along with the merits and demerits of these nonlinear systems.

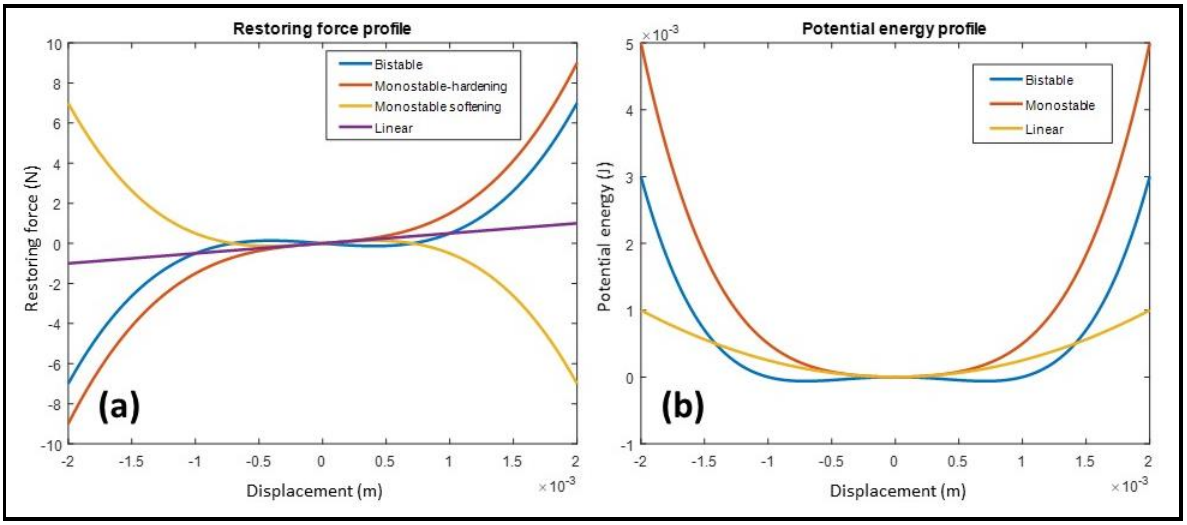


Figure 2.9: Plots to show the different (a) restoring force and (b) potential energy profile.

For the sake of simplicity, the following analysis takes into account the monostable nonlinearity included in a dynamic system through nonlinear force arising from stretching of spring. The externally applied force is considered to be harmonic in nature, of the form $F\ cos(\omega_0 t)$. The dynamical equation representing such an electromagnetic transducer can be expressed in the following form,

$$\boldsymbol{m}\,\ddot{x} + \boldsymbol{c_m}\,\dot{x} + \frac{\boldsymbol{dU}}{\boldsymbol{dx}} + \boldsymbol{\gamma I} = \boldsymbol{F\ cos(\omega_0 t)} \tag{2.15}$$

where, m is the mass of the system, c_m is the mechanical damping coefficient, $\frac{dU}{dx}$ represents the spring restoring force, $\gamma\ (= N\frac{d\emptyset}{dx})$ is the electromagnetic coupling coefficient that depends on the number of turns in the coil and on the spatial gradient of magnetic flux $\emptyset$, I is the current flowing through the electromagnetic transducer. The spring restoring force comprises of the linear term kx arising from the spring bending and the cubic nonlinear force $k_n x^3$ arising from stretching of the spring. As shown for the linear case, the electrical circuit of the electromagnetic transducer can be represented by the following equation (2.16),

$$\boldsymbol{I\,R_L = V - I(R_c + j\omega L)} \tag{2.16}$$

Where, R_L and R_C are the resistance of the load and the coil in the external conversion circuit, V is here the induced voltage which is equal to $\gamma\dot{x}$. Considering negligible contribution from the inductor L at low frequency, the equation of motion for the nonlinear electromagnetic generator can be re-written as,

$$\boldsymbol{m\ddot{x} + \left(2m\rho_m\omega + \frac{1}{R_c+R_L}\,\gamma^2\right)\dot{x} + kx + k_n x^3 = F\,cos(\omega_0 t)} \tag{2.17}$$

Where, ρ_m is the mechanical damping ratio. The contribution of mechanical and electromagnetic damping together, $c_T = c_e + c_m$ gives the total damping associated with this electromagnetic generator. From the equation (2.17) above the power dissipated across the electromagnetic damper can be expressed as,

$$\boldsymbol{P_e = \frac{1}{R_c+R_L}\,\gamma^2\,(\dot{x})^2} \tag{2.18}$$

The equation of motion has been solved numerically in MATLAB using the 4th order Runge-Kutta integration method and Fig. 2.10 shows the dynamic response of the electromagnetic transducer obtained from this solution. The unique characteristics of these nonlinear systems are its multivalued nature, at a fixed driving frequency two stable solution or in other words, two stable steady states with different output energy may co-exist for this kind of system. The system response follows the solid lines when the driving frequency is swept in the forward sense, i.e. from low to high frequency (the up sweep), on the other hand the dashed lines represent the system response when the driving frequency is swept back from high to low frequency (the down sweep). Let us consider the blue line from Fig. 2.10 (a), it is noticeable from the response that the system follows a higher energy state during the up sweep of driving frequency and stays on this higher energy state until 90Hz frequency. After this, the response suddenly drops and the energy output is very low, the frequency at which the response drops is called jump down frequency. Contrastingly, during the down sweep of driving frequency the energy outcome from the system is relatively low, and at 46Hz response jumps up and meets the previous energy state. The region between the two jumps, for a single driving frequency, there are multiple energy state that the system can achieve, which represents the multistability characteristics of such nonlinear system that is also responsible for widening the bandwidth of the nonlinear system. The region between the jump points is called hysteresis and the selection of the energy state that the system follows depends on the initial conditions and the drive frequency routine.

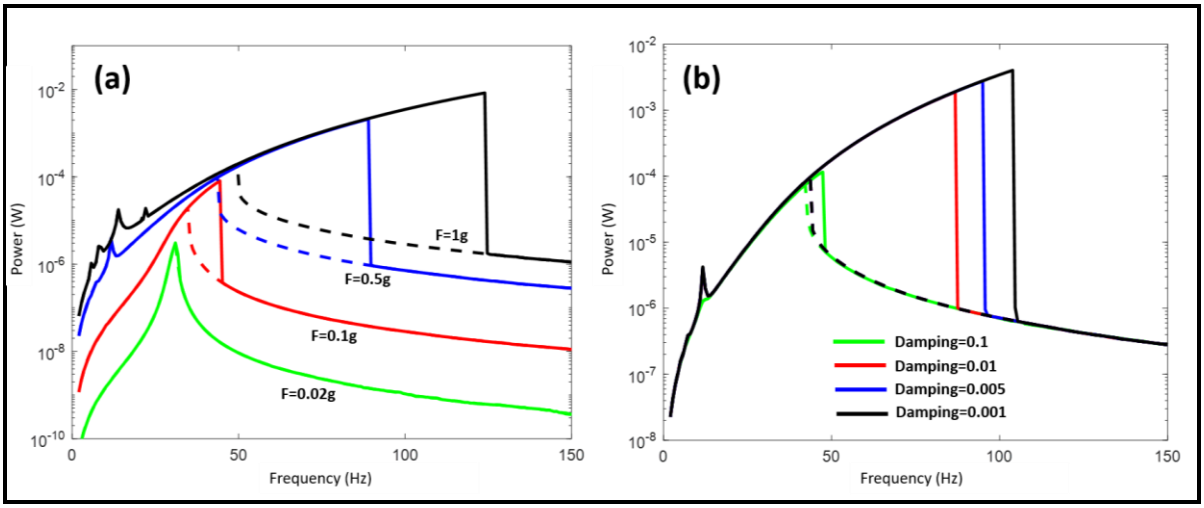


Figure 2.10: Dynamic response of a monostable nonlinear oscillator for (a) different amplitudes of excitation and (b) for different damping conditions for fixed amplitudes of excitation are obtained by solving the equation of motion (2.17).

Keeping all the parameters fixed, if the amplitude of external excitation is varied, the peak of the response moves to higher frequencies and the bandwidth of operation widens considerably as shown in Fig. 2.10(a). For very low amplitude of excitation (0.02g), the system behaviour resembles the linear ones. With increasing excitation, the nonlinear effect kicks in and the system starts to demonstrate multistable characteristics. The variation in response of this type of nonlinear system for different values of damping offered by the system is shown in Fig. 2.10(b) keeping the amplitude of the external excitation fixed (F=0.5g). It is noticeable that reducing the damping not only enhances the amplitude of the response, but it also widens the bandwidth considerably.

In the following section, a comprehensive summary of reported nonlinear electromagnetic generators has been provided with a thorough analysis of the performances, majorly emphasizing on the monostable counterpart.

2.5 Nonlinear Wideband Electromagnetic Vibration Energy Harvesters

The linear generators suffer degradation of performance as the vibration frequency moves away from the resonant frequency of the device. On the other hand, most of the ambient vibrations occur over a wide range of frequency, which is why broadening the operation frequency bandwidth to enhance the performance of these harvesters is of utmost importance. Compared to the linear techniques, the nonlinear harvesters are less sensitive to the variations arising due

to the manufacturing tolerances, can achieve power generation over a larger and continuous bandwidth, thus fruitfully improving the overall performance of the device. Nonlinear spring compliance incorporated into the spring geometry has been exploited in the field of VEHs to widen the operable bandwidth of frequencies [55], making the harvester suitable for harnessing mechanical energy from broadband vibrations.

One of the simplest nonlinear generator would be the one with monostable single-degree-of-freedom configuration, which consists of one stable equilibrium state and one oscillating mass. Levitation of a permanent magnet with the help of two opposing polarity fixed magnet is a fascinating demonstration of nonlinear stiffness strategy, which is much easier to control and manufacture, also would substantially improve the energy harvested. The use of magnetic levitation eliminates the need of a mechanical spring without compromising with the output of the harvester. In 2009, Mann et al. [56] presented a nonlinear energy harvester, which works on the principle of magnetic levitation. They formed a tube-like structure which had two magnets at its two extreme ends inserted into a Teflon tube through threaded support, this was used to repulse and eventually levitate a central magnet which induced nonlinear restoring force into the system. This nonlinear force largely depends on the distance between the end magnets and the central magnet. Two copper coils are wound on both sides, which interacts with the changing magnetic flux from the levitating magnet that exhibits motion along on tube on external vibrations. The device demonstrated the capability of exhibiting large oscillations and hence scavenging substantially large mechanical energy over a wide range of operable frequencies. Foisal et al. designed and developed magnetic spring based electromagnetic generator that harnesses mechanical energy from low frequency vibrations [45]. They used array of the conceived generators one above another and offered a 7-10Hz frequency bandwidth along with a 52.02$\mu W/cm^3$ power density.

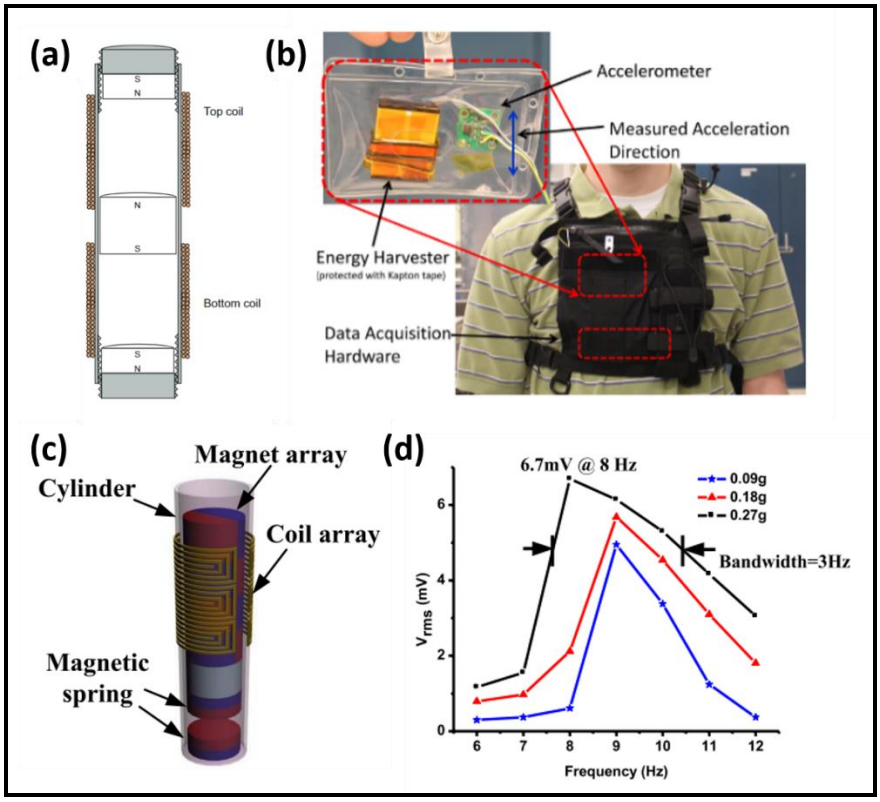


Figure 2.11: (a) Schematic of nonlinear electromagnetic generator based on magnetic levitation [56]. (b)Human vest with energy harvester and associated electronics [57]. (c) Schematic of magnetic spring based microscale energy harvester with flexible coil [47], and (d) shows the RMS output voltage obtained from the energy harvester.

Berdy et al., [57] designed and fabricated a magnetic levitation based vibration energy harvester tested on human subjects. The compact device along with the necessary circuitry was attached to the vest of the subjects. The walking motion of human generated 71µW of power, which increased to 342 µW from the running motion. Using magnetic levitation is a sough after approach specifically for low frequency applications. Zhang et al. developed a microscale electromagnetic generator that uses four radially magnetized stack of magnets levitated in a Teflon casing with end fixed magnets and wrapped around flexible coil that is microfabricated on parylene [47]. This device delivered 0.53µW power while it was excited with a low frequency vibration at 8Hz frequency and 0.27g amplitude. Additionally, the nonlinear magnetic interaction also aided in widening the operable frequency bandwidth up to 3Hz, as shown in Fig. 2.11(d). They extended their investigation into a macroscale prototype which on being placed in a backpack, delivered a large electrical power of 14.8mW from 2.68m/s slow running speed of a human.

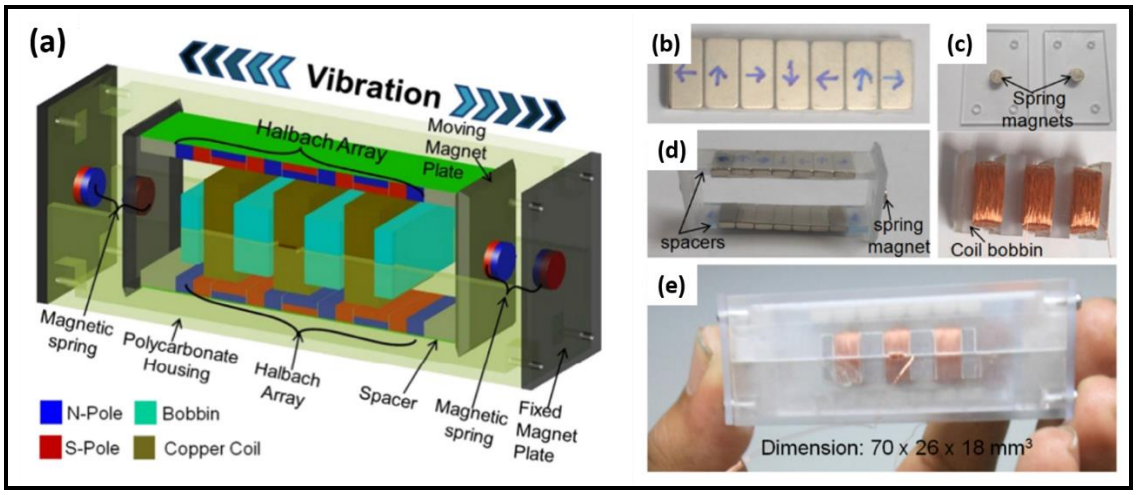


Figure 2.12: (a) Schematic of dual-Halbach array based magnetic spring assisted electromagnetic generator [46], (b) shows the Halbach array of magnets, (c) shows the springs, magnets and the series connected coils, (d) and (e) shows the mounted magnet assembly and the fabricated device respectively.

Salauddin et al. also utilized the frequency downscaling benefits offered by magnetic spring based generator architecture [46]. As shown in Fig. 2.12(a), they used two Halbach array of magnets to concentrate the magnetic flux towards the series connected coil that is fixed between this magnet assembly. The magnet array are fixed to a plate on both ends which holds repulsive set of magnets to instigate the effect of magnetic spring with the magnets fixed at the ends of the housing. When the device is externally excited with vibrations, the suspended magnet array exhibits horizontal motion with respect to the fixed coil, which promotes strong interaction between the concentrated magnetic field from the Halbach array and the fixed coils. This device delivered a large maximum power of 1093μW under 0.5g excitation, which is attributed to the intensified electromagnetic interaction. The nonlinear magnetic spring in this device aided in scaling the frequency of oscillation down to 11Hz, which makes it an attractive high performance device for low frequency applications.

Another viable route for the inclusion of nonlinear effects exhibiting monostable characteristics is to tailor spring design in such a way that forces the spring to stretch on the application of load. In 2009, Marinkovic et al. exploited the cubic nonlinear restoring force arising from displaced beams that are fixed on both ends to realize a wide bandwidth energy harvester named ‘Smart Sand’ [41]. They fabricated the spring architecture on Silicon-on-insulator with fixed support along the perimeter and tether like spring arms allowed to exhibit motion while the two ends the fixed at the rigid support. While exhibiting large deflection, this allows the spring to stretch when the deflection of the proof mass is larger than the thickness of the spring that accounts for the nonlinear restoring force in the system. With piezoelectric

transducer, the miniaturized device delivers an average power of 25μW/cm^3 within a small footprint of 0.01cm^3, while this device extends the operational frequency range between 160-400Hz.

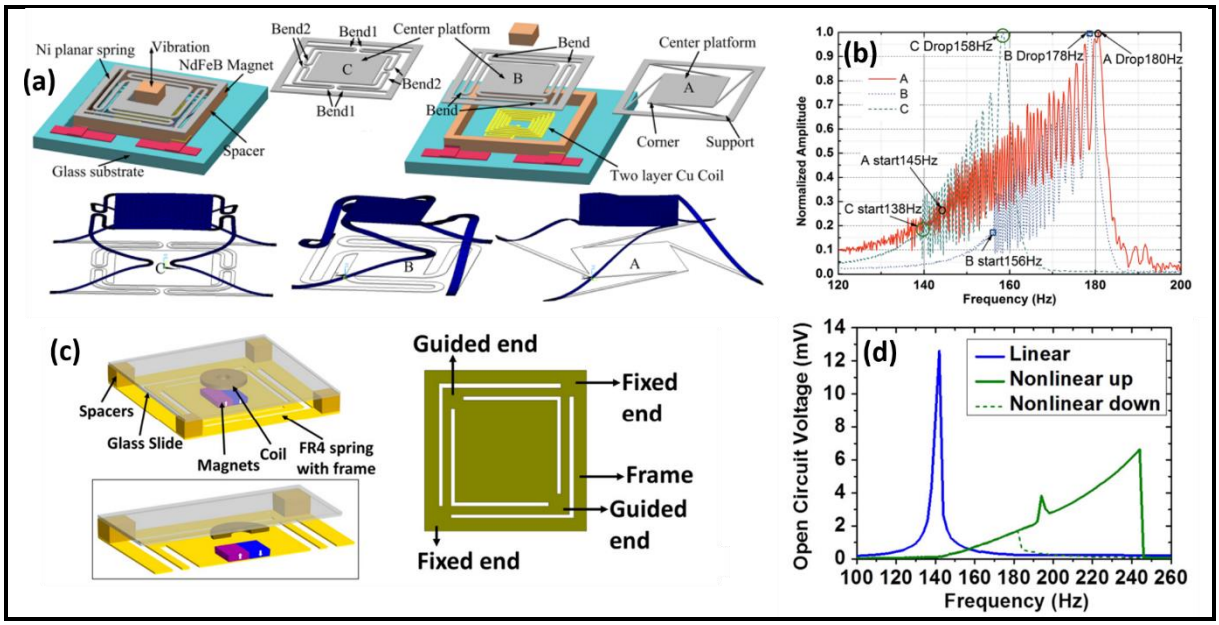


Figure 2.13: (a) Schematic of MEMS electromagnetic vibration energy harvester [44] with tuneable nonlinearity through topological variations as shown with springs A, B and C, (b) dynamic response of the different devices employing these springs. (c) Schematic representation of the stretching based spring included in energy harvesting device [42], and (d) comparison of the dynamic response with a linear counterpart.

Dai et al. utilized the stretching strain in MEMS electromagnetic vibration energy harvester to realize tuneable nonlinearity by varying the topology of the spring architecture [44] as shown in Fig. 2.13(a). A central platform that holds the proof mass is suspended through tether like thin Nickel based springs that are fixed at one end with a rigid support. When subjected to external vibration, these spring aids the proof mass to exhibit out-of-plane displacements, while the springs exhibits stretching strain. The nonlinear restoring force aided in bending the frequency response of the device and widened the operable frequency range beyond the resonance condition. With 0.8g excitation, the fabricated MEMS device offered 28Hz broad frequency bandwidth along with 70mV RMS voltage output, which shows the potential of the stretching based nonlinearity in improving the overall performance of the device.

In 2014 Mallick et al. presented a stretching-strain based nonlinear electromagnetic energy harvesting system [42] where the nonlinearity arises due to the stretching of the spring arms. A low Young's modulus material FR4 is used as the material for the fabrication of the

resonator as this low modulus of material aids in bringing the operational frequency down. As the resonator structure (fixed-guided cantilever arms) vibrates due to the external vibrations, the permanent magnet attached with it vibrates and the magnetic flux is intercepted by the coil arrangement above the magnet (shown in Fig. 2.13(c)), which induces voltage into the coil. Through analytical modelling, they highlighted that the stretching based nonlinearity, spring hardening in nature, is inversely proportional to the thickness of the springs that are used in the system, hence thinner springs would potentially induce higher degree of nonlinearity. Hence, this opens up the scope for optimizing the spring design to instigate stronger nonlinearity without compromising the mechanical stability of the overall device. For input acceleration as low as 0.05g, the response shows linear resonator characteristics with linear resonant frequency of 170Hz. The system shows non-resonant nature as the input acceleration is increased and this leads to widening of the operational bandwidth. They also designed a linear resonator of same volume as the non-linear one, and they experimentally established that the half-power bandwidth is 5 times wider in the nonlinear harvesting system compared to its linear counterpart (Fig. 2.13(d)). Recently, Aldawood et al. reported a macroscale enhanced magnetic spring based energy harvester [43]. Instead of using two fixed magnets at the top and bottom, it employed three different FR4 based circular spring architecture possessing hardening based nonlinearity that guided the motion of the top magnet (as shown in Fig. 2.14) which resulted in enhanced normalized power density of 1.35mW/cm^{3}g^2 at lower acceleration as small as 0.1g, that shows an improvement of 40 times as compared with the conventional energy harvester of similar architecture. This device further showed a 60% enhancement in the bandwidth as compared with traditional energy harvesters owing to the stretching based nonlinearity included deliberately in the structures. Despite of these benefits, the cubic-hardening stiffness based nonlinear effects strengthen only at higher amplitudes of excitation, which puts a critical limit on the viability of these nonlinear VEHs for relatively weaker vibrations that are predominantly present in bridges, air conditioning systems, trams, trains, etc. [58-61]. Additionally, depending on the nature of vibration, higher power generation through nonlinear VEHs is not always guaranteed [62]. However, by virtue of offering a wider bandwidth of operable frequencies, instead of peak power delivered for specific frequencies like linear VEHs, nonlinear VEHs are promising in providing large average power density over a broad range of frequencies [63] (random vibrations) as compared with linear VEHs.

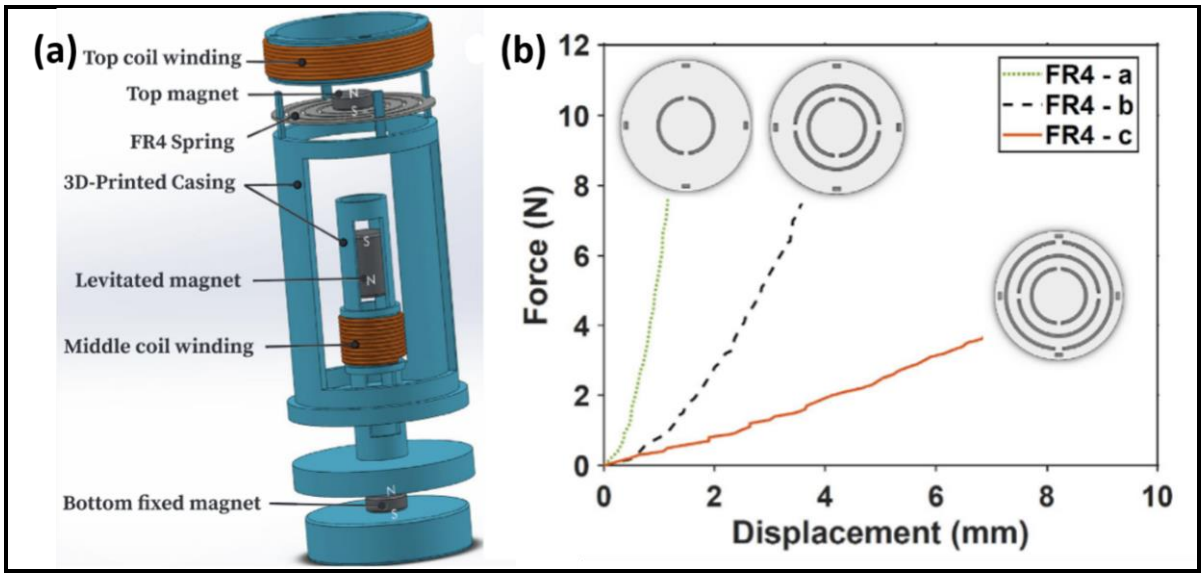


Figure 2.14: (a) Schematic of nonlinear electromagnetic vibration energy harvester [43], and the (b) variation of spring force for different nonlinear springs.

Recently, auxetic structures have drawn significant research attention owing to the unique characteristics of lateral expansion on extension or transversal contraction on compression, which exhibits negative Poisson's ratio [65-67]. As shown in Fig. 2.15(a) and (b), the compressive force on one side shown with the blue arrow deforms the structure in a way that it experiences compression in the orthogonal plane as well. Chen et al. exploited these characteristics by including auxetic structures close to the fixed end of a double clamped piezoelectric beam [68], as shown in Fig. 2.15(c), which efficiently reduced the natural frequency of oscillation of the structures and yielded larger stress compared with a simple cantilever, which in turn aided in generating larger power from the piezoelectric transducer. Fig. 2.15(d) and (e) shows the nonlinear dynamic response in terms of the RMS voltage of the piezoelectric energy harvesters that employs auxetic structures (a) and (b) respectively. The solid and dashed lines stand for the frequency up and down sweeps obtained through model, whereas the symbols represent the experimental results demonstrating strong nonlinear characteristics. These auxetic structures, although presently limited to the area of piezoelectric transducers [69], have tremendous potential of being utilized in for electromagnetic vibration energy harvesting, especially where geometrically induced spring hardening/softening nonlinearities are exploited.

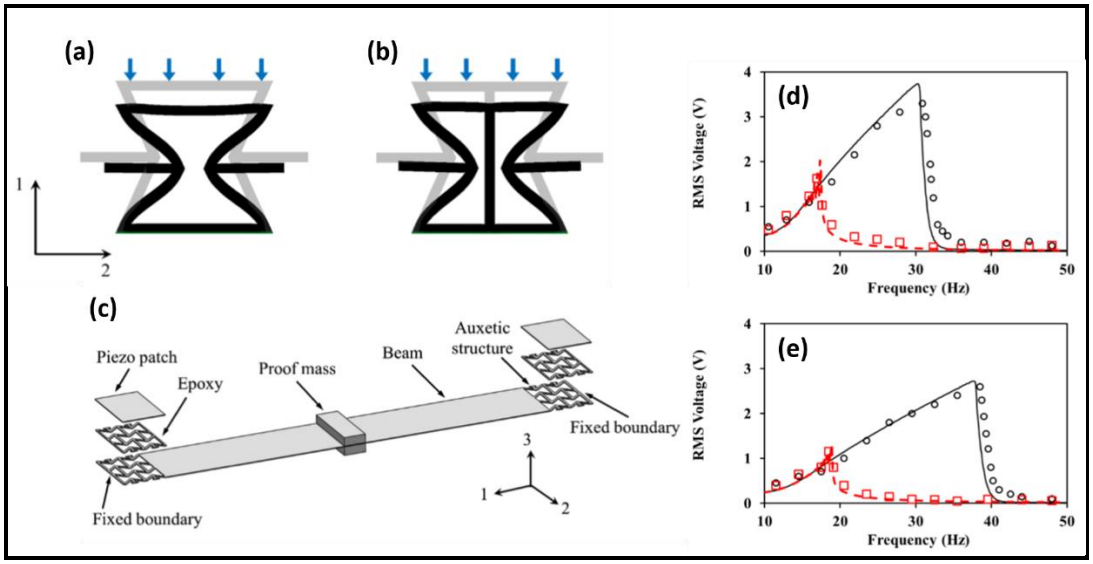


Figure 2.15: Two different auxetic structures developed by [68] is shown in (a) and (b). (c) Shows the schematic of the piezoelectric vibration energy harvester along with the auxetic patches. The dynamic nonlinear response of the piezoelectric transducer is shown in (d) and (e).

Multiple stable energy states of an energy harvester offer the freedom of choosing and achieving the desired energy state that would result in improved energy harvesting (higher power and wider bandwidth) from amplitude and acceleration varying vibration environment. The potential function of a bi-stable system has a couple of potential energy well that is separated by an energy barrier. With high excitation amplitude, the bistable system oscillates between the stable states or in other words the potential wells. The shallower the well, more frequent will be the inter-well oscillation that leads to increased effective bandwidth and amplitude of response. The different ways of incorporating bistability includes buckling in a beam with fixed ends, use of cantilever tip and external magnet close to it. In case of buckling, below a certain load the beam stays usually in the monostable state and jumps to the bistable state once buckling has occurred. Cottone et al. presented two electromagnetic vibration energy harvesters, one using the proof mass fixed to the centre of a single buckled beam and the other one using the central proof mass with doubly clamped two buckled beams [49], while one of the clamped end is tuneable to instigate the effect of buckling. The buckling height influences the shape of the bistable potential energy function. On external excitation, the central mass comprising of magnet assembly moves with respect to the stationary coil and generates power across the coil. The buckling aids in bringing non-resonant bistable characteristics into the energy harvesting system which rendered 2.5 times improved bandwidth with the bistable harvester compared with the resonant counterpart. Although the bistability implemented through buckling improves the overall device performance, however, this comes at the cost of

substantially large external excitation amplitude, which aids in escaping the potential energy barrier and realize the benefits of buckling. With the motivation of implementing beam buckling at lower excitation amplitude, Leadenham et al. developed a pre-bent M-shaped beam with clamped ends as shown in Fig. 2.16(a).

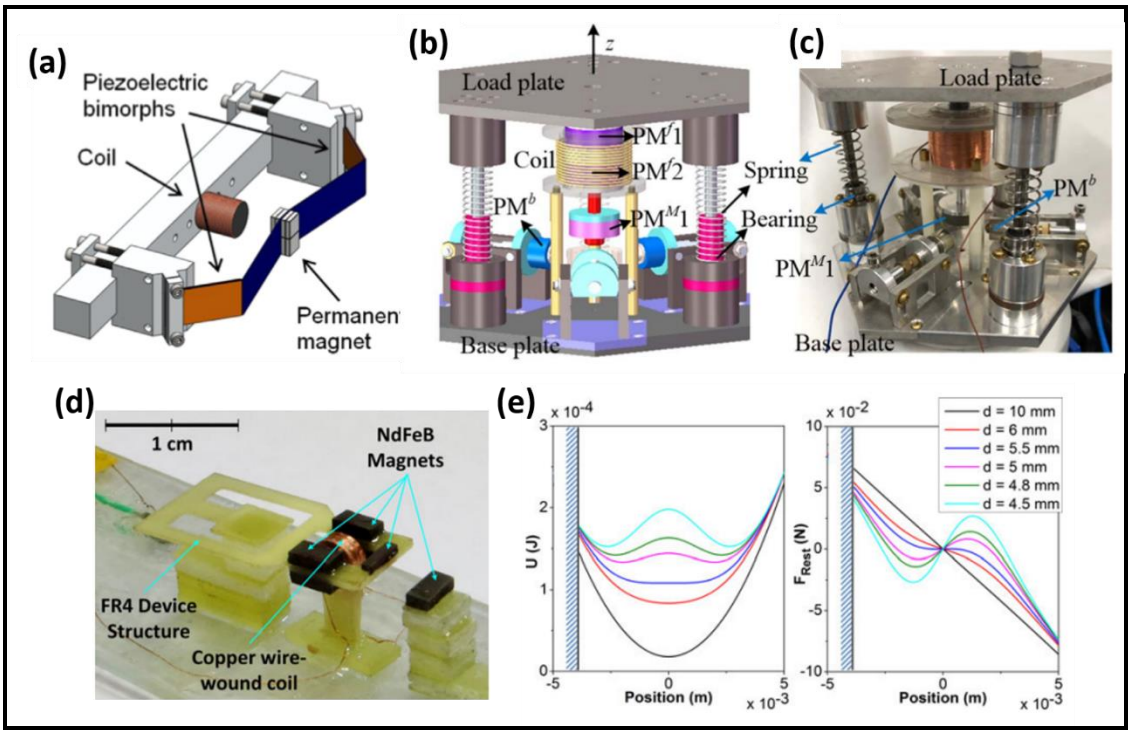


Figure 2.16: (a) M shaped bistable piezoelectric and electromagnetic vibration energy harvester configuration [70]. (b) Schematic and (c) image of the fabricated bistable vibration energy harvester with multiple permanent magnets [51]. (d) Image of the fabricated bistable vibration energy harvester [53] and the corresponding (e) tuneable potential energy, restoring force profile.

The central permanent magnet vibrates on external forcing with respect to the fixed coil aiding the electromagnetic transduction. They also included four piezoelectric patches closed to the clamped end for yielding usable energy from the large stress experienced in this part. This nonlinear system demonstrated 8900% bandwidth enhancement as compared to its linear counterpart at low base excitation of 0.07g [70].

Yan et al. developed nonlinear energy harvesting system with multiple permanent magnets, while exploiting the repulsive and attractive magnetic interaction to induce nonlinear forces into the system [51]. The energy harvesting system is designed in a way that the nature of the bistable potential energy well changes with varying relative positions of the magnets. The device exhibits intrawell and interwell oscillation dynamics and generates a large power of up to 28mW when excited with mechanical vibrations. In 2016, Podder et al. proposed a relatively simpler energy harvesting device that employs repulsive pair of magnets to induce

bistable nonlinear restoring force in a FR4 based energy harvester [53]. They used a FR4 based folded cantilever spring structure that holds a magnets assembly which moves with respect to a fixed coil as shown in Fig. 2.16(d) and a repulsive pair of magnets, one on the tip of the spring and one fixed next to the tip, accounts for the nonlinear restoring force in the device. The distance 'd' between these two repulsive pair of magnets influences the nonlinear potential energy and the restoring force (as shown in Fig. 2.16(e)). The bistable device widened the bandwidth by up to 3.4Hz at 0.4g. With higher excitation amplitude, the spring exhibited collision with the base, demonstrating further wide bandwidth of operation. In 2020, Gu et al. reported a very interesting planar multi-directional energy harvesting device that is inspired from the shape of a goblet [71] as shown in Fig. 2.17(a) and a cross-section view in Fig. 2.17(b). With in-plane excitations (along the x-y direction), the magnetic ball (NdFeB ball with 15mm diameter) oscillated within the goblet like body and the coils wound outside harnesses the changing magnetic flux and converts it into usable electrical energy through electromagnetic transduction. Experimentally they showed that with low excitation amplitude (0.1g-0.6g) the ball exhibits weak nonlinear characteristics and yields very low power, which increases when the excitation is moderate (0.6g-1g) and the motion of the ball is chaotic. However, the response of the energy harvester improves dramatically when the high amplitude excitation is applied (1.2g-1.8g, at 5Hz) as the ball then exhibits larger circular motion along the wall of the body. The high performance of this device at low frequencies makes it a logical choice for human wearable applications as it delivers high power (1.4mW) while extracting mechanical energy from human walking.

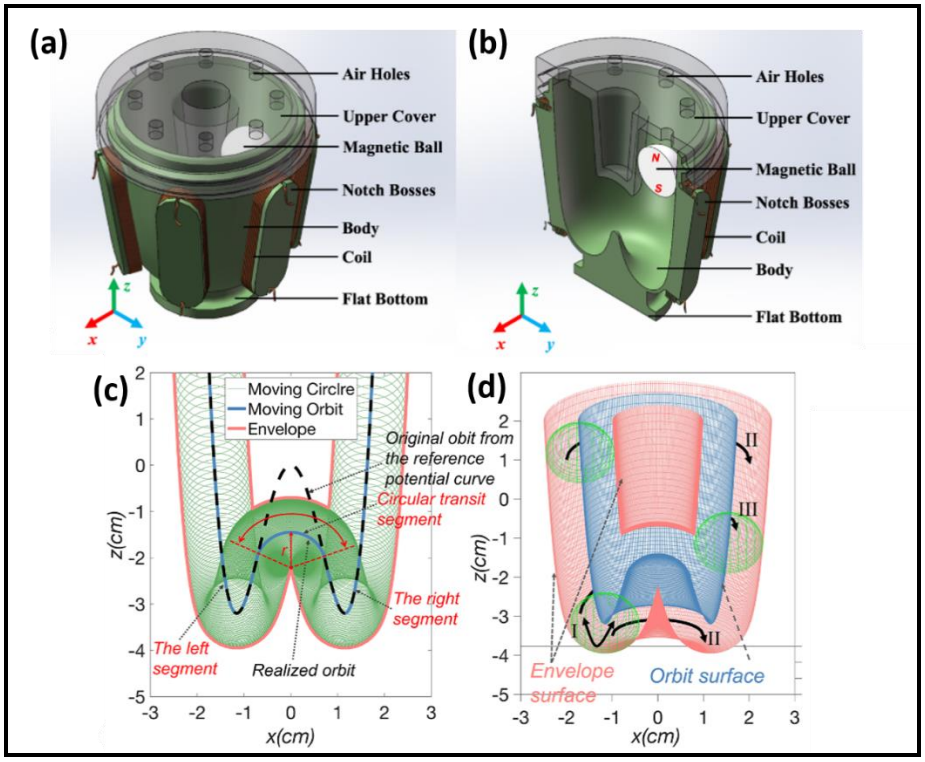


Figure 2.17: Schematic and cross-sectional view of the goblet like bistable electromagnetic vibration energy harvester are shown in (a) and (b) respectively [71]. The bistable potential energy profile and the enveloped surface of the device are shown in (a) and (b) respectively.

There are few limitations of the bistable system- the critical excitation level required to initiate the interwell oscillations, the operation regions where high energy and low energy branches co-exist and the sensitivity to initial conditions. Owing to these drawbacks, research interest nowadays has shifted to tri-stable, quad-stable and in fact poly-stable systems that promotes larger amplitudes of oscillation across the wells for smaller excitations. In order to enhance the energy extraction efficiency of this energy harvesting device, researchers have also opted for combining multiple transduction mechanism in a single device through intelligent design strategy, thereby realizing hybrid vibration energy harvesting system. Keeping the footprint low, this energy harvesting unit dramatically improves the performance as the contributions from the different transducers are added.

Through sophisticated design modifications, Gao et al. achieved tri-stable and quad-stable energy harvesting device by including external magnets with specific polarities, which interacts with the central magnets suspended through levitation [72]. Fig. 2.18(a) and (b) shows the tri-stable and quad-stable potential energy profiles. Experimentally this device demonstrated rich nonlinear characteristics while revealing phenomena like potential well escape, dynamical bifurcation, chaotic oscillation etc. In terms of the performance, the device rendered a range of 5-12Hz improvement in the operable frequency bandwidth along with a larger RMS power

output of 440.98mW. Deng et al. proposed a synergetic poly-stable energy harvester that comprises multiple piezoelectric (PVDF) cantilever with magnets at the tip, repulsive in orientation with respect to the adjacent magnets. In this system, the number of stable equilibrium states exponentially depends on the number of proof masses present in the device [73]. They further proposed an energy harvesting brick, as shown in Fig. 2.18(c) where the cantilever dynamics is highly influenced by the magnetic interactions, which improves the non-resonance performance of the device while widening the bandwidth 41 times and the power density is reported to improve by 760%. Although the energy transduction is based on the piezoelectric beams in this device, however, such design strategy could also find potential applications in wideband electromagnetic transducers.

Recently, Wang et al. developed a complex energy harvesting device combining three different mechanical energy transducers into a hybrid form, impact-driven piezoelectric generator, electromagnetic generator array and sliding-mode as well as contact-separation mode triboelectric generator in a single design of small footprint [74]. The design parameters were optimized to engineer a tuneable potential energy profile that can be varied from monostable to bi-stable, tri-stable and quad-stable shape, the large amplitude inter-well oscillations resulted in a 1-11Hz bandwidth enhancement. At an ultra-low frequency of 3Hz, with 1g force, the hybrid energy harvester renders a massive 85.9mW power. Salauddin et al. a hybrid vibration energy harvester exploiting the electromagnetic and triboelectric transduction mechanisms used to harvest power from human activities (Fig. 2.18(d)). For the electromagnetic transduction, they used set of halbach array of magnets and moving coil, which are suspended by magnetic levitation, the triboelectric counterpart transduces vibrational energy from the interaction between Al-nanograss and nano-structured PTFE layer. Under an external acceleration of 0.6g at 4.5Hz frequency across 710Ω load resistance, the prototype delivered 10.07mW power [75].

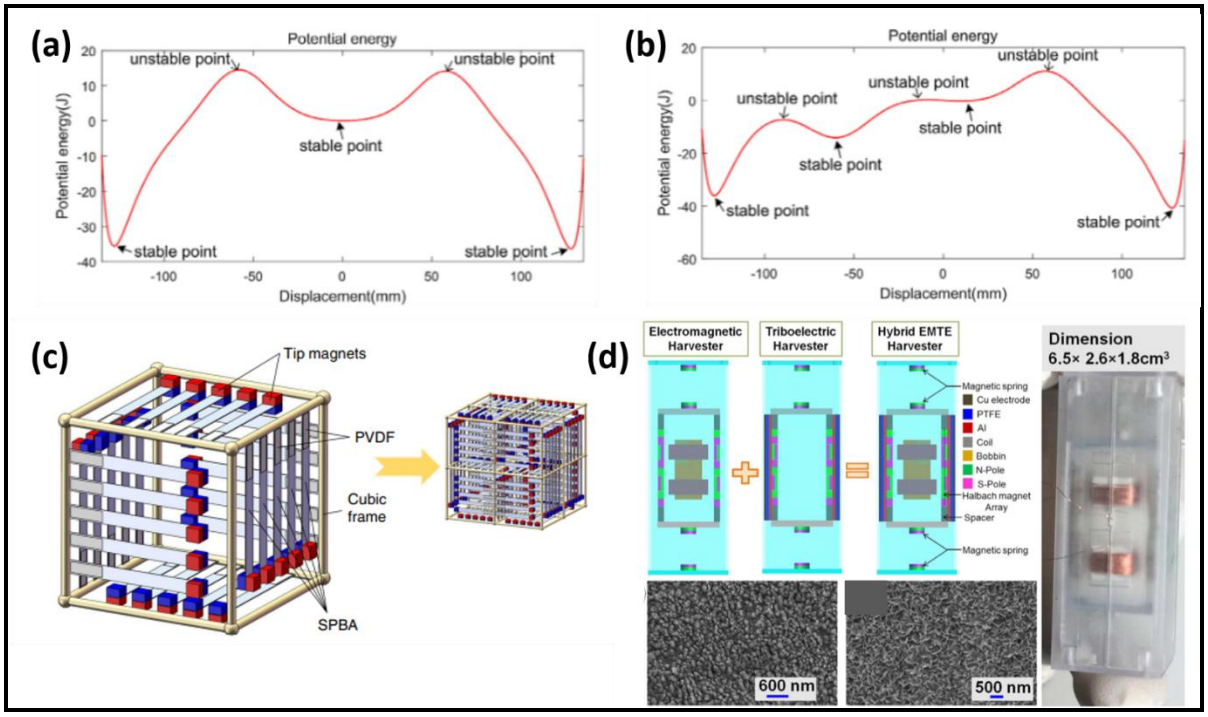


Figure 2.18: The (a) tri-stable and (b) quad-stable potential energy profile of the magnetic levitation based energy harvester [72]. (c) Schematic of synergetic poly-stable piezoelectric energy harvester brick [73]. (d) Schematic of the proposed hybrid electromagnetic and triboelectric energy harvester is shown along with the image of the fabricated prototype of the electromagnetic-triboelectric harvester [75]. The SEM images at the bottom are of the PTFE nanostructure and Al-nanograss structure.

2.6 Micro-scale Vibration Energy Harvesters

The EM transducers are characterized by low internal (coil) resistance, low output voltage and high output current [76]. While the macro/meso-scale implementation of EM VEH devices is well explored and provide better performances among all the transduction mechanisms, micro-scale implementation of such devices remains a challenge. This could be mainly attributed to two facts – increase of coil loss at the micro-scale and lack of high-performance micro-magnets required for such devices. These facts have restricted the number of reported works in this particular area considerably compared to the piezoelectric or electrostatic MEMS generators. On the brighter side, EM generators do not require complex biasing mechanisms as in the case of electrostatics. In addition, the reliability/longevity of this type of transducers is significantly better than the others, which is extremely critical for any EH based systems [77]. MEMS based EM VEH devices can be divided into three categories according to their level of integration – (1) MEMS suspension only, (2) MEMS suspension with micro-coil, (3) Fully MEMS integrated device at chip-scale.

It is quite straightforward to fabricate the mechanical suspension using standard Si MEMS processing. Park et al. presented a MEMS scale EM-VEH with batch fabricated springs

on [100] silicon wafer, bulk NdFeB magnet and wire wound miniaturized copper coil packaged in a low-cost PDMS based mold [78], as shown in Fig. 2.19(a). Resonant at 54Hz, this MEMS device with discrete coil and magnet generated 115μW power when excited with 0.57g vibrations. Often these silicon springs limits the amplitudes of oscillation <1mm, and higher amplitudes of oscillation can be achieved but at the cost of compromised structural stability. Yang et al. developed a four-bar-linkage type MEMS spring on DRIE etched silicon wafer (as shown in Fig. 2.19(b)) that offers the benefit of large amplitude of in-planar displacement [79], up to 2mm, which is challenging to achieve in MEMS scale. The central stage of the spring holds two N42 grade NdFeB magnets as proof mass, on mounting the magnets the spring is packed in a plastic casing, that is placed over two 400 turns coils that are also packaged in a separate plastic casing. On exciting this MEMS device near 76Hz, it delivered a maximum power of 2.2mW with 1.1g vibrations, making it a potential candidate for IoT applications owing to the large power generation capability.

Silicon is the most commonly used material in MEMS devices due to their suitability with CMOS compatible fabrication processes and mechanical robustness. However, due to its large elastic modulus (Y=170 GPa), the operational frequency becomes high with miniaturization in size. Hence, many researchers have exploited other polymeric materials like parylene [80] and PDMS [81] for developing the spring structure in order to reduce the frequency within the same footprint. Other than polymers, metallic and metal alloy based mechanical structures have also been explored. Yang et al. used a MP35N alloy (35% Co, 35% Ni, 20% Cr, 10% Mo) based MEMS spring for implementing a relatively robust energy harvesting device that withstands harsh operating conditions [82]. Apart from the spring constituent material, in terms of the operation this device bears resemblance to that of [79]. Subjected to 1.08g and 107.7Hz external excitation, this device generated 1.26mW power and survived a 6-foot drop proving the robustness of the device. Similarly, MEMS-scale springs have been developed with nickel [83], wet-etched copper foil [84] etc.

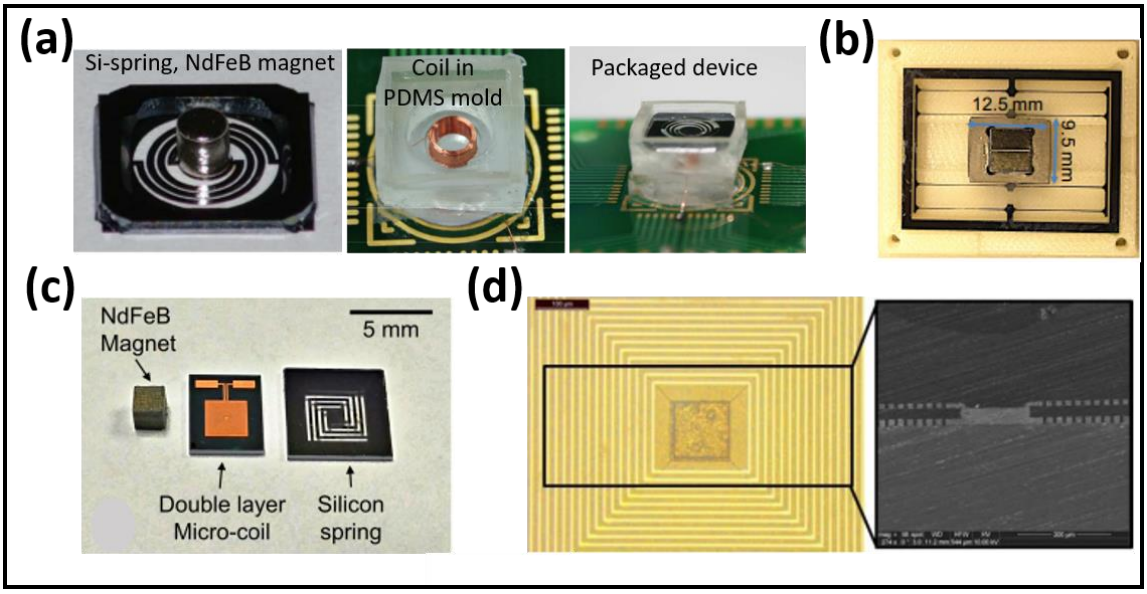


Figure 2.19: Image of (a) spiral Si-spring with mounted magnet, copper coil in PDMS mold and fully assembled MEMS device by [78]. (b) Image of in-plane moving MEMS VEH with four bar link type MEMS spring [79]. (c) Image of different components of frequency tuneable MEMS VEH by [85]. (d) Double layer microfabricated copper coil used by [86] for implementing MEMS VEH.

In other approaches, high-density copper coils along with MEMS scale silicon springs are microfabricated, one of them is either mobile, or stationary depending on the energy harvesting device topology. Podder et al. proposed a frequency tuneable MEMS electromagnetic vibrational energy harvester that comprise of bulk magnet and microfabricated coil and spring (Fig. 2.19(c)) [85]. The spiral shaped MEMS spring is fabricated on a Silicon-On-Insulator wafer with 50μm of device layer for the spring arms and bulk NdFeB 2mm cube magnet has been bonded to the central stage of the MEMS spring. To intensify the electromagnetic interaction between the coil and magnet, double layer planar electrodeposited copper coil has been microfabricated on silicon wafer, which is kept stationary in this device. To tune the natural frequency of oscillation and to instigate the effect of nonlinearity in the system, a miniaturized external magnet with opposing polarity has been used. The distance between the two magnets influences the nonlinear restoring force and by precisely manipulating the repulsive magnetic force, the stiffness of the spring structure is controlled. At a low excitation level of 0.025g, the frequency of oscillation is tuned from 188.5Hz to 223.1Hz as the distance between the repulsive pair of magnets is changed from 10mm to 5mm. Mallick et al. also used microfabricated double layer copper coil for implementing high figure of merit nonlinear MEMS energy harvester [87]. On comparing the performance of the microfabricated double layer coils (as shown in Fig. 2.19(d)) with that of the commercially available coils of similar footprint, it was concluded that the wire wound copper coils comprising of larger

number of coil turns outperforms the microfabricated coils. Liu et al. developed a MEMS harvesting chip which comprise of a large mass which holds spiral patterned coils and moves with the aid of folded springs attached to this mass (Fig. 2.20(a)) [88]. Four small mass are also fabricated on the silicon chip that holds double layer of patterned coils, are fixed to the rigid support through folded springs and are responsible for inducing nonlinear restoring force into the large mass when it exhibits in-planar motion. A bulk cylindrical magnet is fixed with an acrylic cover and placed over the large mass through a spacer. With the MEMS spring and coil, the device rendered a peak power density of 1.6×10^{-8}W/cm^3. Similar silicon chip-scale springs with microfabricated coils have been used by [26]. Recently, Li et al. developed a MEMS EM-VEH with MEMS spring and flexible stack of planar coils [89] to increase the output power by increasing the number of turns in the coil. Two sets of spiral copper wires (35μm) are electroplated on both sides of a polyimide film and 20 such layers are used together as a coil stack for the energy harvester. Silicon folded springs holds the central silicon stage and a disc shaped magnet is glued to this stage and placed over the coil stack through designed spacers as shown in Fig. 2.20(b). With 1g harmonic excitation, this MEMS device delivered 10.5μW power at 143 resonant frequency.

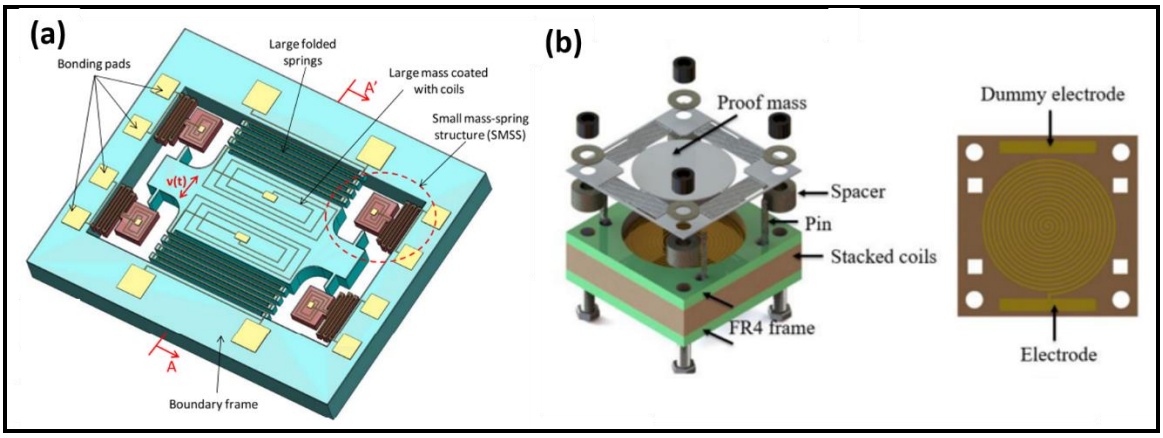


Figure 2.20: (a) Schematic representation of in-plane MEMS VEH with large-mass, small-mass spring structure and patterned layer of coils [88]. (b) Schematic illustration of the MEMS VEH with Silicon spring and flexible stack of coils [89].

As shown in the examples above, there has been significant effort towards implementing high-performance MEMS VEH, however, one the critical bottleneck in materializing this ambition is the lack of suitable miniaturized permanent hard-magnets that would enhance the performance of the energy harvesters. Along with high magnetic coercivity, remanence, the maximum energy product $(BH)_{max}$ that is defined by the largest rectangular area

from the second quadrant of BH curve is one of the key parameter that influences the performance of the magnet, especially in the context of energy harvesting through electromagnetic transduction. Rare earth based permanent hard magnets, for example bulk NdFeB offers a large energy product, $(BH)_{max}$ =450kJ/m^3 [90]. However, these performance metrics are obtained with high temperature treatment/sintered magnets, which makes them incompatible with standard CMOS fabrication flow. The problem with permanent micro-magnets for EM VEH or most MEMS applications extends beyond just high-energy product material development or process integration and relates to the lack of intelligent design strategies. When a relatively thin film/block of permanent magnet is used in a MEMS device as source of magnetic field, the stray magnetic field appears only from the edge of the magnet and a large part of the material is wasted. This is due to the presence of the demagnetization field, which acts to demagnetize the magnet in a direction that is opposite to the direction of the magnetization [91]. Hence, the magnetic flux density also diminishes due to the demagnetizing field. In a magnet of finite length, demagnetizing field arises because of the free magnetic poles at the terminating ends of the magnet. This strength of the demagnetization field is dependent on the magnetization and the physical magnet shape. A commonly used approximation is to assume that the demagnetizing field H_d is uniform and opposite in direction to the magnetization (M),

$$\boldsymbol{H_d = -DM} \tag{2.19}$$

Where, D is the demagnetization factor, which has a value between 0 and 1 depending on shape of the magnet. Also, the energy product is a shape-dependent property of a magnet and can be expressed as [91],

$$\boldsymbol{(BH) = \mu_0 D(1-D){M_S}^2} \tag{2.20}$$

Thin films with perpendicular and parallel magnetization have D≈1 and D≈0, respectively, and both correspond to vanishing energy products. Hence, uniformly magnetized thin films produce no stray field outside the magnet, except at the edges, and most of the magnetic material is wasted. Hence, when a uniformly deposited magnetic block/film is used as a flux-source, the magnetic flux intensity is greatly reduced which affect the performance of integrated magnetic transducers.

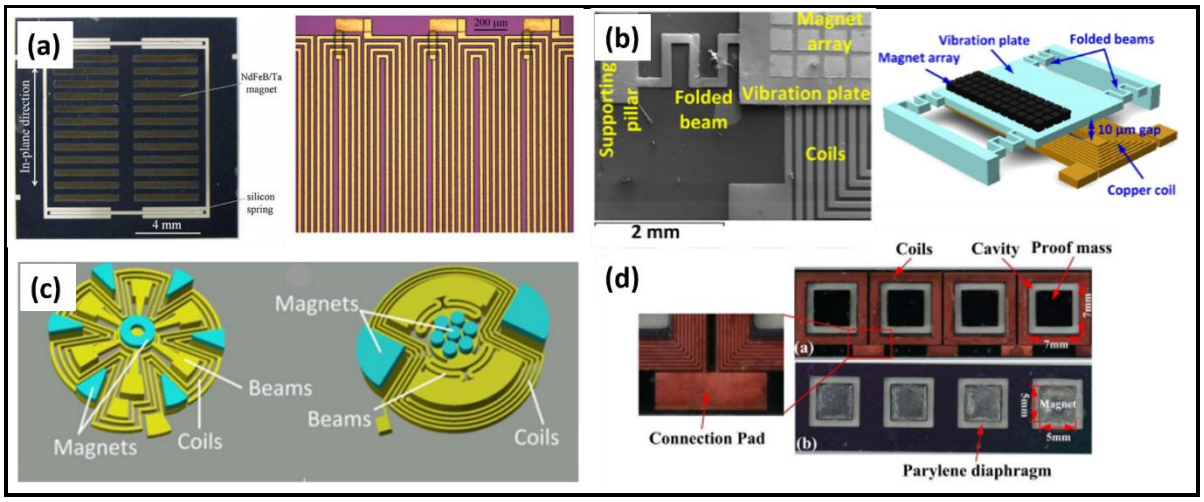


Figure 2.21: (a) SEM image of the wafer with the silicon spring and the embedded NdFeB/Ta magnets (left) and the spiral coils developed by [92]. (b) SEM image of the in-plane moving MEMS spring with electroplated magnet array and coil layer underneath (left) as shown in the schematic (right) proposed by [94]. (c) Two MEMS VEH with patterned magnets and coils developed by [95]. (d) Top and bottom side of the parylene diaphragm based MEMS energy harvester with micromagnets comprising of wax bonded NdFeB powders fabricated by [96].

To circumvent this issue, Jiang et al. developed MEMS scale VEH using a vibrator layer that comprise of high aspect ratio silicon springs exhibiting planar motion that holds sputtered NdFeB/Ta magnets filled into fabricated trenches (Fig. 2.21(a)), and a stationary layer that holds electroplated spirals series connected coils [92]. Trenches in the silicon spring are fabricated through DRIE and up to 20µm thick NdFeB/Ta magnets have been fabricated. To enhance the electromagnetic coupling, the spirals coils are fabricated on a separate silicon wafer with similar lateral dimensions as that of each of the micromagnets and placed right below the patterned magnets. These two layers of silicon are bonded together and on external vibration, resonating at 115Hz, the spring carrying the micromagnets oscillates with respect to the coils such that substantial magnetic flux change is experienced by the coil, which resulted in 1.2nW/cm^3 power density from this MEMS device. The gradual oxidation of the NdFeB/Ta micromagnets that results in magnetic flux density accounts for the low power output from the MEMS device. Tao et al. bonded NdFeB powder with bi-component epoxy resin to form micromagnets that are packed into a mold and are used as a poof mass with electroplated nickel spring [97]. Together with electroplated copper coil that is fixed to the base, this MEMS device generated 20.9µV at 365Hz resonant frequency. Han et al. [94] presented an in-plane electromagnetic energy harvester, with electroplated CoNiMnP magnets allowing full integration of the magnets in a compact device. The most attractive part of this design is the placement of the magnet array on one side of the coil, which allows a large change of magnetic

flux through the coil once it experiences the relative motion with respect to the magnets, as shown in the schematic representation of Fig. 2.21(b). These unipolar-patterned array of magnets on a moving spring structures induced voltage in the fixed rectangular planar coils and the maximum peak output power was observed to be 0.98mV at a frequency of 48Hz. In 2014, Han et al. developed a novel design to increase power output of a fully integrated MEMS VEH. They employed a batch fabrication process to develop electroplated patterned CoNiMnP magnets, that are suspended from dedicated silicon MEMS springs and interacts with the electroplated copper coils that are fabricated at the bottom layer of the magnets. Copper beams are also added to the spring layer to reduce the frequency of oscillation (down to 64Hz) while supporting the vibrating silicon spring layer. The two reported design exploited different geometry of patterned magnets, such as triangular, annular, disc shaped etc. as shown in Fig. 2.21(c) that are dimensionally optimized to enhance the electromagnetic interaction with the dedicated coils [95]. A maximum power density of 0.03μW/cm^3 was achieved with this MEMS device. Zhang et al. followed a different strategy and used vertical stack of wax-bonded NdFeB micromagnets with dual layer of electroplated copper coil (isolated by a layer of parylene and connected through a via hole) to strengthen the electromagnetic interaction and hence the mechanical energy harvesting capability through a MEMS scale device [96]. Since the coils and the magnets are fabricated on a single wafer (as shown in Fig. 2.21(d)), batch fabrication as well as vertically stacking multiple of such layer is relatively easy. The magnetic powder mixed with wax powder is packed in 300μm deep trenches that are suspended to move with respect to the coils through parylene diaphragm. This fully integrated MEMS generator yielded 0.55nW power when operated with 400Hz and 6.4g vibration. Although the batch fabrication technique that is presented in this work to form the array of harvesters is very promising in the context of CMOS compatible fabrication and system integration, however, the low performance of the micromagnets and weak electromagnetic interaction between the magnets and the coils deteriorates the overall performance of these MEMS generators and makes them incompatible for IoT based applications.

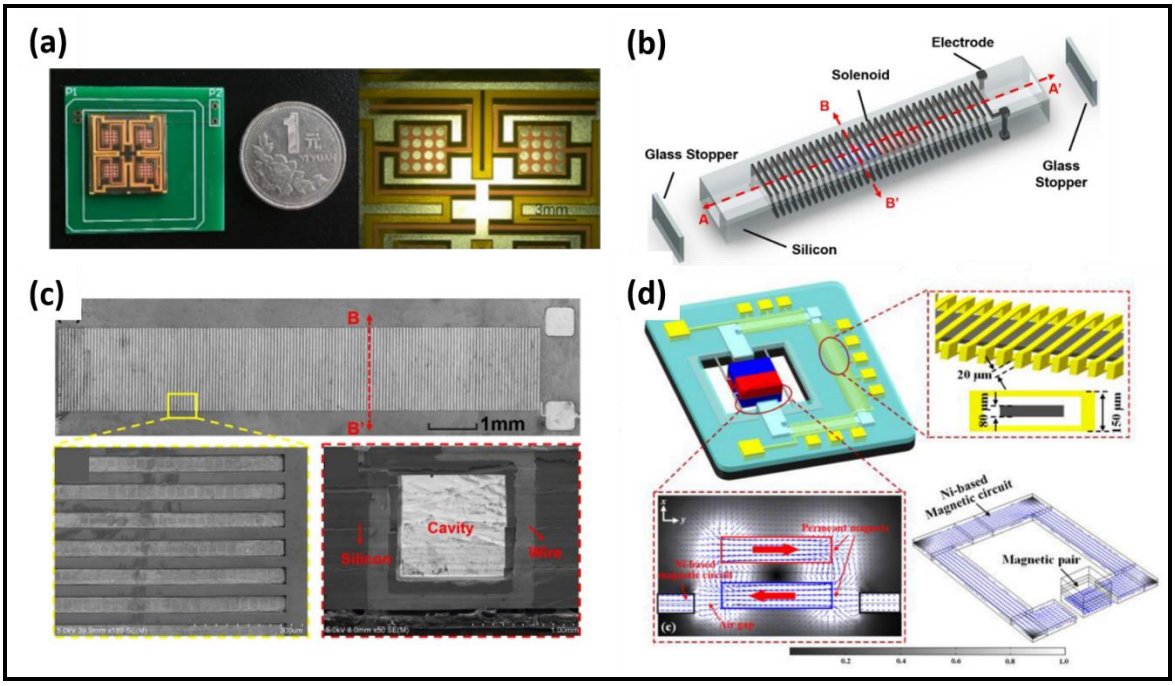


Figure 2.22: (a) Image to compare the dimension of the MEMS VEH and a coil, along with further zoomed in view of the energy harvester prototype [98]. (b) 3D schematic of the silicon based 3D solenoidal coil for MEMS VEH [99], the SEM image of the fabricated solenoidal coil is shown in (c) along with the vertical cross-section along the B-B` plane. (d) Schematic of the MEMS energy harvester with closed magnetic circuit developed by [100].

In 2018, Zhang et al. designed and developed an integrated and batch fabricated MEMS VEH that comprises of four different generator, each possessing curved vibrating beams that holds a central stage containing sixteen electroplated CoNiMnP disc shaped micromagnets with average thickness of 18μm, and electroplated copper coils around the vibrating beams (as shown in Fig. 2.22(a)) [98]. This harvester shows promising performance in the low frequency range, 10-40Hz, which is otherwise a great challenge especially for MEMS scale device where the frequency relates to the size scaling inversely. At 18Hz, this device generates 0.423mW power that is rectified (AC-DC conversion) and subsequently used to charge a supercapacitor to drive suitable wireless sensor node. To further boost the performance of these MEMS energy harvesters, in 2021, Wu et al. utilized MEMS fabrication techniques to realize 3D solenoidal coils on silicon [101]. Copper springs are fabricated and mounted on top and bottom to hold a permanent hard magnet at the centre along with aluminium weights as proof mass. On both sides of this magnet, 3D MEMS copper coils are inserted with steel sheet core to reduce the magnetic leakages that reduces the efficiency of the coils in MEMS electromagnetic transducers. The coils are fabricated on silicon by etching the coils wire grooves, through holes, two such layer are bonded together and later electroplated copper is used to fill these grooves.

Furthermore, the interaction between the soft magnetic core and the central permanent magnet induces nonlinear force into the MEMS device, which widens the frequency response. Interestingly they reported that the output power and the bandwidth is related to the offset position of the magnet with respect to the position of equilibrium. With 250μm-offset position, this device delivered 55.65μW power along with a bandwidth of 4Hz for 1g, which changes to 22.23μW power and 13Hz bandwidth when the offset is reduced to 174μm.

Recently, 3D solenoidal coils have been exploited in silicon based chip-scale electromagnetic VEH by [99]. They employed micro-casting technique to form metal solenoidal coils on silicon, and a cylindrical magnet is suspended inside the silicon channel to move on external vibrations. Four silicon wafers have been photo-lithographically patterned to fabricate the wire grooves, inlet vias, electrodes etc. and a cavity is created to build the channel for the magnets and two end stopper are used to limit the motion of the magnet (Fig. 2.22(b)). Molten $ZnAl_x$ alloy is filled into the moulds to form 150 turns of the micro-solenoid wires having 40μm wire width and 25μm gap between the adjacent turns (Fig. 2.22(c)). With a 10mm long magnet into the channel, this device yielded 309.64μW/cm^3 power density for ~5g acceleration at 24Hz frequency. Such design strategy will further optimized design parameters could become a potential route to promote wafer-level batch fabrication of the MEMS VEHs and to enhance the performance of these integrated devices. In this context, Wang et al. developed a monolithically fabricated MEMS device that uses nickel based closed magnetic circuit with copper solenoidal coil to increase the energy conversion efficiency of the generator (Fig. 2.22(d)) [100]. Nonlinear clamped-guided springs are used to suspend permanent hard magnet, which vibrates on external excitation. The high-efficiency micro-solenoid dramatically improved the output performance of the device, delivered 265.2μW power with, and enhanced bandwidth of 30Hz for 1g vibrations.

2.7 Power management strategies for efficient power delivery

The obtained output from a vibration based energy harvester is of AC characteristics. However, the practical load (wireless sensor platforms) demands for a constant DC supply. Hence, a suitable power conditioning circuit is required to extract the maximum possible output power from the harvester unit. This power conditioning section comprises of a rectifier and a power management unit, which is dedicated to extract maximum possible electric power from the harvester when it is subjected to real-world non-stationary vibrations varying in both amplitude and frequency. In terms of simplicity, the most popular rectifiers used for this purpose are the

half-wave [102] and bridge [103] rectifiers. However, the overall efficiency of these rectifiers are significantly low owing to the voltage drop across each of the diodes. In case of the harvesters, that produce significantly high power, such rectifiers are used to convert the DC signal into AC power [104]. In some improved rectifier designs, gate cross-coupled rectifiers implemented with the help of cross-connected NMOS transistors increases the conversion efficiency owing to the low drain to source voltage drop [105]. Also the active rectifiers offer relatively higher efficiency in converting the AC voltage to usable DC signal [106], but the requirement of an external battery to power up the internal circuitry makes them a less attractive choice for the cases where the harvester produces low output power (few microwatt). Another form of active rectification is the Negative Voltage Converter (NVC)—a bridge rectifier implemented with MOSFETs (and an active diode) that reduces the device voltage drop, when compared against using a diode rectifier [107]. In addition, a popular strategy is to multiply the voltage obtained from the harvester unit which is popularly done with the help of charge pump circuits [108]. The charge pump circuit delivers the power to the load by the charging and discharging of the associated capacitors, functioning as a switching regulator. This particular rectification strategy is appropriate for the low current demanding target applications.

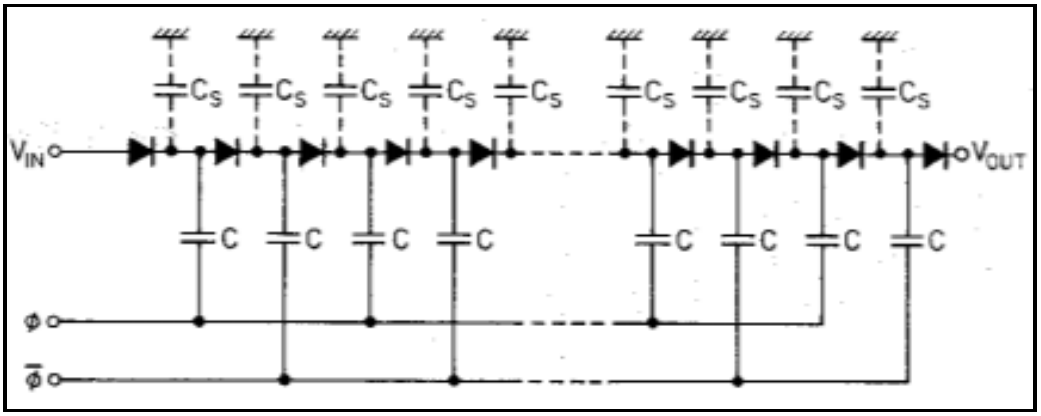


Figure 2.23: Basic voltage multiplier architecture [108].

Post voltage regulation stage, the critical task is to regulate the DC voltage to provide a stable supply to the load section, while maximizing the energy extraction. The advancements in the low power electronics had led the IC industry to develop compact Power Management Integrated Circuits (PMICs) which implements Maximum Power Point Tracking (MPPT) algorithms that aim to match the impedance observed by the harvester to that of the harvester itself. One of the algorithms is the 'Perturb and Observe' strategy which alters the input voltage until the input power is maximized. Costanzo et al. reported a power management circuit that exploits this MPPT strategy [109] by periodically tailoring the duty cycle of the oscillator that

controls the switching of the DC-DC converter and by monitoring the corresponding peak power that is obtained from the system. They optimized the selection of the sampling interval and the duty cycle of the perturbation to enhance the efficiency of the MPPT mechanism. Costanzo et al. further developed a speed driven adaptive maximum power point tracking strategy that measures the generator speed in real-time and implements dynamic adaptive control to maximize the energy conversion efficiency, even more than the P&O strategy [110]. Many other intelligent power management strategies are employed to optimize the energy extraction from the harvester.

Chamanian et al. [111] developed a hybrid suitable power management interface to synergistically extract power from electromagnetic and piezoelectric vibration energy harvester. The output of the electromagnetic harvester is rectified through an active doubler architecture (Fig. 2.24) and the energy is stored in a capacitor, which later delivers this energy to the piezoelectric energy harvester resulting in enhanced charge extraction. This produces a steady output of 1 to 3.4V.

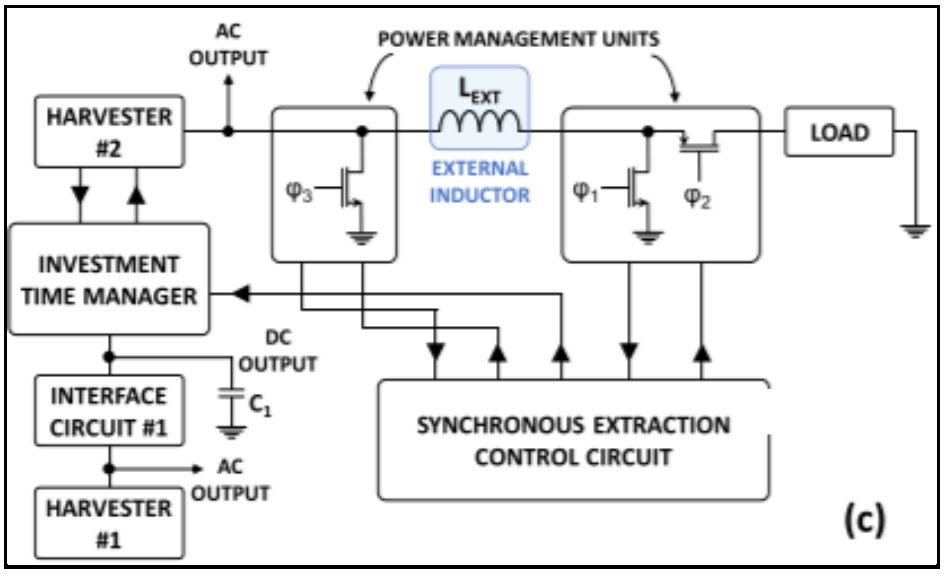


Figure 2.24: The system architecture of hybrid harvester interface using synergistic energy extraction strategy [111].

Similarly, another power management circuit used in [112] involves one of the commercially available solution LTC3588 that comprises of low-loss full wave rectifier, which stores the energy used for the low current buck converter (Fig.2.25). This low power consumption architecture allows supplying a steady DC power to the wireless sensor platform.

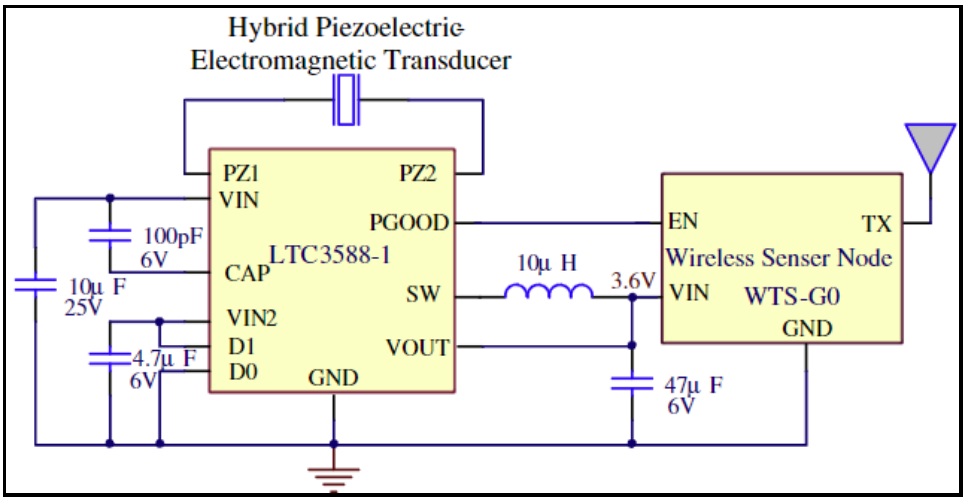


Figure 2.25: Schematic of the power management circuit used for the hybrid energy harvester [112].

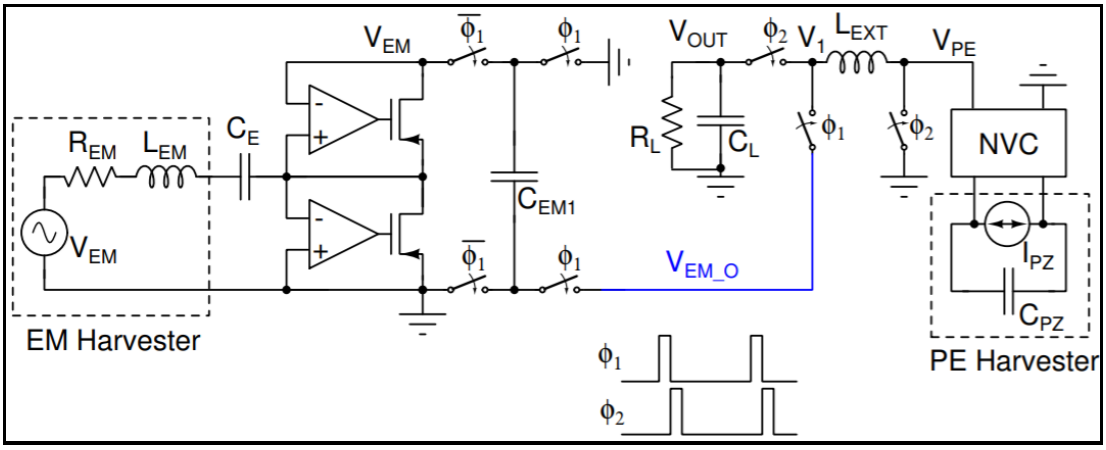


Figure 2.26: Schematic of the hybrid energy harvester interface [113].

A novel power management topology is proposed by [113]. The first part of the circuit converts the AC output of the electromagnetic energy harvester and it is stored across the capacitor C_{EM} that later transfers this energy to the associated inductor through resonance. The piezoelectric harvester employs the synchronous electric charge extraction algorithm and modifies the connection of the inductor with the NVC circuit as shown in Fig. 2.26. The designed circuit showed a peak improvement of 1.3 times in terms of the conversion efficiency, which could potentially enhance the power delivered to the load, ensuring a reliable system level operation with the wireless sensor platform. Aktakka et al. developed an efficient and integrated self-powered power management unit for a MEMS scale vibration energy harvester [114]. The bias-flip stage in the power management unit aids in increasing the energy

harvesting efficiency and the following negative voltage converter along with the active diode rectifies the AC signal obtained from the energy harvester with minimum voltage drop and the rectified energy is stored in a temporary reservoir as shown in Fig. 2.27. The trickle charger transfers this stored energy and charges the permanent reservoir up to a specific level, which is an ultra-capacitor in this case. This power management topology offered a 58-86% efficiency in converting and transferring energy from the harvester leads to the ultra-capacitor.

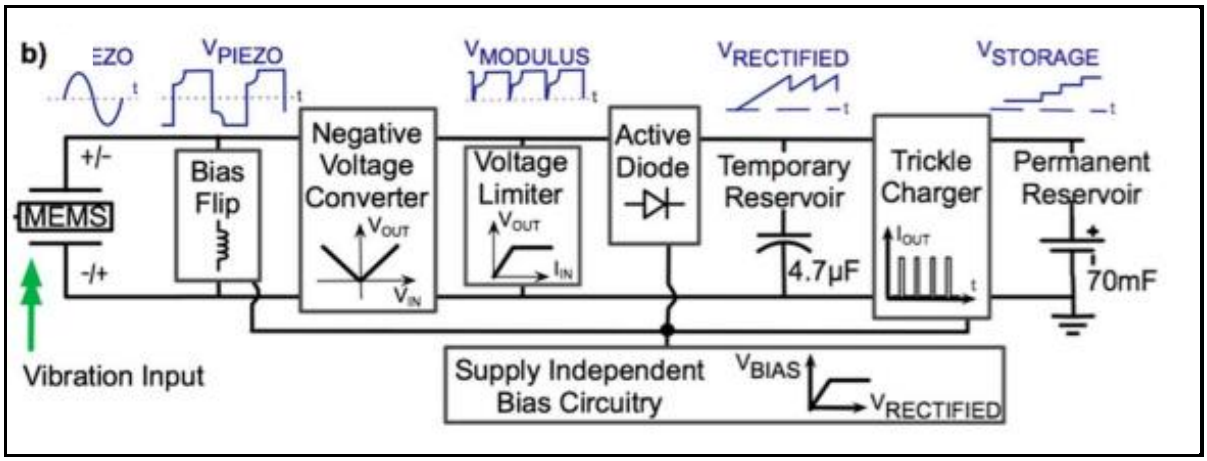


Figure 2.27: Schematic of the power management circuit used with MEMS scale harvester [114].

Recently, Yao et al. designed an autonomous power management interface electronics for nonlinear electromagnetic vibration energy harvesters [115] that aims to extract mechanical energy from the vibrations of automobile suspensions. As shown in Fig. 2.28, the interface electronics comprise of five key parts. A full bridge rectifier circuits has been employed as the first part of this circuit to rectify the AC signal of the energy harvester into DC signal, which is then conditioned through the following cascade buck-boost converter that is responsible for the DC-DC conversion. The oscillator circuit with specific switching frequency and duty cycle is responsible for generating square pulses to facilitate the switching associated with the buck-boost converter. To significantly reduce the energy loss in the power management process the wake-up circuit is used which detects the incoming energy, and activates the circuit immediately when this energy is sufficient, and shuts the circuit down when the energy flow stops. This wake-up stage also minimizes the power consumption when the circuit enters sleep mode. The overvoltage protection circuit is also added to protect the rest of circuit from further energy transfer once the energy storage unit is completely charged. They estimated the efficiency of the designed power management circuit to be 74.3% considering the harvester

extracts energy from a car that is driven at 25m/s speed. From the same group, an adaptive power management circuit is designed for piezoelectric generators that tailors the impedance to match with that of the generator to maximize the energy conversion efficiency [116]. They reported a maximum efficiency of 80% with this adaptive circuit.

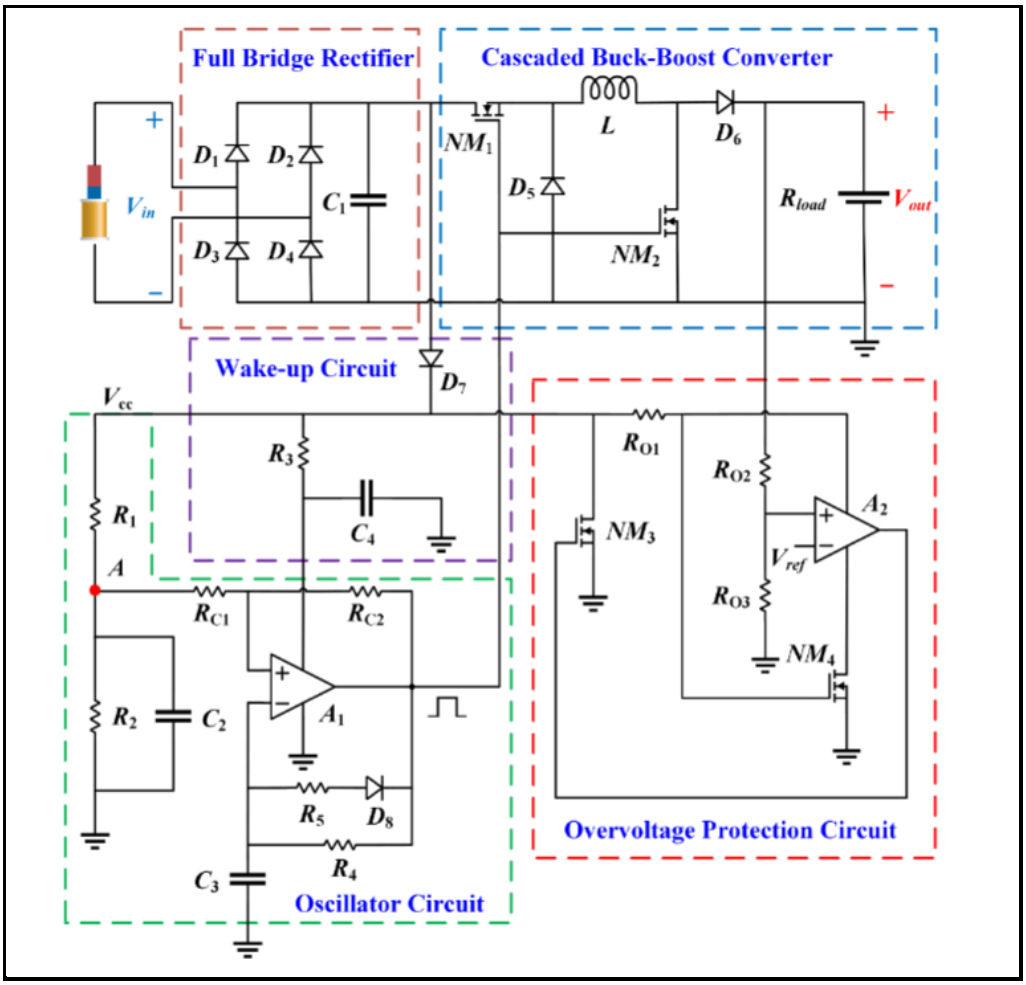


Figure 2.28: Schematic of the designed power management circuit [115].

2.8 Conclusion

This chapter provides a detailed overview of vibration energy harvesters while emphasizing on the state-of-the-art literature in the field of electromagnetic vibration energy harvesting. To gain deep insight of the dynamical features of these systems, a firm theoretical background has been prepared. Majority of the early works have developed linear or resonant vibration energy harvesters, which maximizes the amplitude of vibration and yields large power when the frequency of excitation matches with the natural frequency of oscillation of the harvester. Such harvesters are suitable for harnessing mechanical energy from sources that offers discrete frequency peaks. However, majority of the real-world vibrations have the mechanical energy

distributed over wide range of frequencies with a clear predominance of low-frequency components. This makes the development of a highly efficient wideband vibration energy harvesters an imperative requirement. A thorough literature survey has been presented in this chapter on nonlinear wideband vibration energy harvesters, along with a theoretical background to understand the sources and nature of nonlinearities induced into the energy harvesting system. While the performance of macroscale energy harvesters is promising in the context of substituting batteries for IoT based applications, but the power outcome of the microscale generators is often limited to hundreds of nanowatts, which makes them impractical for real-world applications. With a thorough literature review, the key challenges in developing a fully integrated MEMS scale electromagnetic transducer has been discussed and potential routes are highlighted to overcome these bottlenecks. Finally, from the perspective of system level integration, conditioning the obtained electrical power is as important as is the extraction of power through the energy harvester. Suitable rectifier as well as power management architecture have been discussed that could improve the performance of the energy harvesting system and enable powering a wireless sensor platform through the vibration energy harvester.

2.9 References

[1] D. Mallick, P. Constantinou, P. Podder, and S. Roy, "Multi-frequency MEMS electromagnetic energy harvesting," *Sensors and Actuators A: Physical*, vol. 264, pp. 247-259, 2017/09/01/ 2017, doi: https://doi.org/10.1016/j.sna.2017.08.002.

[2] L. Zuo, B. Scully, J. Shestani, and Y. Zhou, "Design and characterization of an electromagnetic energy harvester for vehicle suspensions," *Smart Materials and Structures*, vol. 19, no. 4, p. 045003, 2010/02/25 2010, doi: 10.1088/0964-1726/19/4/045003.

[3] C. B. Williams and R. B. Yates, "Analysis of a micro-electric generator for microsystems," *Sensors and Actuators A: Physical*, vol. 52, no. 1, pp. 8-11, 1996/03/01/ 1996.

[4] R. Amirtharajah and A. P. Chandrakasan, "Self-powered signal processing using vibration-based power generation," *IEEE journal of solid-state circuits*, vol. 33, no. 5, pp. 687-695, 1998.

[5] W. J. Li, T. C. H. Ho, G. M. H. Chan, P. H. W. Leong, and W. Hiu Yung, "Infrared signal transmission by a laser-micromachined, vibration-induced power generator," in *Proceedings of the 43rd IEEE Midwest Symposium on Circuits and Systems (Cat.No.CH37144)*, 2000, vol. 1, pp. 236-239 vol.1.

[6] P. Glynne-Jones, M. J. Tudor, S. P. Beeby, and N. M. White, "An electromagnetic, vibration-powered generator for intelligent sensor systems," *Sensors and Actuators A: Physical*, vol. 110, no. 1-3, pp. 344-349, 2004.

[7] S. P. Beeby *et al.*, "A micro electromagnetic generator for vibration energy harvesting," *Journal of Micromechanics and Microengineering*, vol. 17, no. 7, pp. 1257-1265, 2007/06/05 2007.

[8] F. M. Foong, C. K. Thein, and D. Yurchenko, "Important considerations in optimising the structural aspect of a SDOF electromagnetic vibration energy harvester," *Journal of Sound and Vibration*, vol. 482, p. 115470, 2020/09/15/ 2020, doi: https://doi.org/10.1016/j.jsv.2020.115470.

[9] L. Dhakar, H. Liu, F. E. H. Tay, and C. Lee, "A new energy harvester design for high power output at low frequencies," *Sensors and Actuators A: Physical*, vol. 199, pp. 344-352, 2013/09/01/ 2013, doi: https://doi.org/10.1016/j.sna.2013.06.009.

[10] M. Perez, S. Chesné, C. Jean-Mistral, K. Billon, R. Augez, and C. Clerc, "A two degree-of-freedom linear vibration energy harvester for tram applications," *Mechanical Systems and Signal Processing*, vol. 140, p. 106657, 2020/06/01/ 2020, doi: https://doi.org/10.1016/j.ymssp.2020.106657.

[11] R. Torah, P. Glynne-Jones, M. Tudor, T. O'Donnell, S. Roy, and S. Beeby, "Self-powered autonomous wireless sensor node using vibration energy harvesting," *Measurement Science and Technology*, vol. 19, no. 12, p. 125202, 2008/10/24 2008, doi: 10.1088/0957-0233/19/12/125202.

[12] S. Lee, B. D. Youn, and B. C. Jung, "Robust segment-type energy harvester and its application to a wireless sensor," *Smart Materials and Structures*, vol. 18, no. 9, p. 095021, 2009.
[13] "Perpetuum." https://perpetuum.com/applications/rail/.
[14] "Data Sheet, Revibe energy harvester." https://revibeenergy.com/modeld/.
[15] D. Mallick and S. Roy, "Bidirectional electrical tuning of FR4 based electromagnetic energy harvesters," *Sensors and Actuators A: Physical*, vol. 226, pp. 154-162, 2015/05/01/ 2015, doi: https://doi.org/10.1016/j.sna.2015.02.016.
[16] E. K. Reilly, F. Burghardt, R. Fain, and P. Wright, "Powering a wireless sensor node with a vibration-driven piezoelectric energy harvester," *Smart Materials and Structures*, vol. 20, no. 12, p. 125006, 2011/11/14 2011, doi: 10.1088/0964-1726/20/12/125006.
[17] J. Qiu, X. Liu, H. Chen, X. Xu, Y. Wen, and P. Li, "A Low-Frequency Resonant Electromagnetic Vibration Energy Harvester Employing the Halbach Arrays for Intelligent Wireless Sensor Networks," *IEEE Transactions on Magnetics*, vol. 51, no. 11, pp. 1-4, 2015, doi: 10.1109/TMAG.2015.2455041.
[18] M. Gao, P. Wang, Y. Cao, R. Chen, and D. Cai, "Design and Verification of a Rail-Borne Energy Harvester for Powering Wireless Sensor Networks in the Railway Industry," *IEEE Transactions on Intelligent Transportation Systems*, vol. 18, no. 6, pp. 1596-1609, 2017, doi: 10.1109/TITS.2016.2611647.
[19] O. Rubes, J. Chalupa, F. Ksica, and Z. Hadas, "Development and experimental validation of self-powered wireless vibration sensor node using vibration energy harvester," *Mechanical Systems and Signal Processing*, vol. 160, p. 107890, 2021/11/01/ 2021, doi: https://doi.org/10.1016/j.ymssp.2021.107890.
[20] D. Zhu, S. Roberts, T. Mouille, M. J. Tudor, and S. P. Beeby, "General model with experimental validation of electrical resonant frequency tuning of electromagnetic vibration energy harvesters," *Smart Materials and Structures*, vol. 21, no. 10, p. 105039, 2012.
[21] D. Zhu, S. Roberts, M. J. Tudor, and S. P. Beeby, "Design and experimental characterization of a tunable vibration-based electromagnetic micro-generator," *Sensors and Actuators A: Physical*, vol. 158, no. 2, pp. 284-293, 2010.
[22] I. Sari, T. Balkan, and H. Kulah, "An electromagnetic micro power generator for wideband environmental vibrations," *Sensors and Actuators A: Physical*, vol. 145-146, pp. 405-413, 2008/07/01/ 2008.
[23] M. Wischke, M. Masur, F. Goldschmidtboeing, and P. Woias, "Electromagnetic vibration harvester with piezoelectrically tunable resonance frequency," *Journal of Micromechanics and Microengineering*, vol. 20, no. 3, p. 035025, 2010.
[24] A. Cammarano, S. G. Burrow, D. A. W. Barton, A. Carrella, and L. R. Clare, "Tuning a resonant energy harvester using a generalized electrical load," *Smart Materials and Structures*, vol. 19, no. 5, p. 055003, 2010/03/23 2010.
[25] D. Mallick and S. Roy, "Bidirectional electrical tuning of FR4 based electromagnetic energy harvesters," *Sensors and Actuators A: Physical*, vol. 226, pp. 154-162, 2015/05/01/ 2015.
[26] H. Liu, T. Chen, L. Sun, and C. Lee, "An electromagnetic MEMS energy harvester array with multiple vibration modes," *Micromachines*, vol. 6, no. 8, pp. 984-992, 2015.
[27] K. Tao *et al.*, "A novel two-degree-of-freedom MEMS electromagnetic vibration energy harvester," *Journal of Micromechanics and Microengineering*, vol. 26, no. 3, p. 035020, 2016/02/11 2016.
[28] V. Nico, E. Boco, R. Frizzell, and J. Punch, "A high figure of merit vibrational energy harvester for low frequency applications," *Applied Physics Letters*, vol. 108, no. 1, p. 013902, 2016.
[29] M. Perez, S. Chesné, C. Jean-Mistral, K. Billon, R. Augez, and C. Clerc, "A two degree-of-freedom linear vibration energy harvester for tram applications," *Mechanical Systems and Signal Processing*, vol. 140, p. 106657, 2020/06/01/ 2020.
[30] S. Wu, P. C. K. Luk, C. Li, X. Zhao, Z. Jiao, and Y. Shang, "An electromagnetic wearable 3-DoF resonance human body motion energy harvester using ferrofluid as a lubricant," *Applied Energy*, vol. 197, pp. 364-374, 2017/07/01/ 2017.
[31] B. Yang *et al.*, "Electromagnetic energy harvesting from vibrations of multiple frequencies," *Journal of Micromechanics and Microengineering*, vol. 19, no. 3, p. 035001, 2009/01/30 2009.
[32] M. M. R. El-Hebeary, M. H. Arafa, and S. M. Megahed, "Modeling and experimental verification of multi-modal vibration energy harvesting from plate structures," *Sensors and Actuators A: Physical*, vol. 193, pp. 35-47, 2013/04/15/ 2013.
[33] M. Han, W. Liu, B. Meng, X. Zhang, X. Sun, and H. Zhang, "Springless cubic harvester for converting three dimensional vibration energy," in *2014 IEEE 27th International Conference on Micro Electro Mechanical Systems (MEMS)*, 2014, pp. 425-428.
[34] S. Wu, P. C.-K. Luk, C. Li, X. Zhao, Z. Jiao, and Y. Shang, "An electromagnetic wearable 3-DoF resonance human body motion energy harvester using ferrofluid as a lubricant," *Applied Energy*, vol. 197, pp. 364-374, 2017.

[35] X. Tang, T. Lin, and L. Zuo, "Design and optimization of a tubular linear electromagnetic vibration energy harvester," *IEEE/ASME Transactions on Mechatronics,* vol. 19, no. 2, pp. 615-622, 2013.
[36] Y. Xu, D. Zhao, Y. Wang, and M. Ai, "Electromagnetic characteristics of permanent magnet linear generator (PMLG) applied to free-piston engine (FPE)," *IEEE Access,* vol. 7, pp. 48013-48023, 2019.
[37] Z. Li, Z. Yan, J. Luo, and Z. Yang, "Performance comparison of electromagnetic energy harvesters based on magnet arrays of alternating polarity and configuration," *Energy conversion and management,* vol. 179, pp. 132-140, 2019.
[38] A. Bibo, R. Masana, A. King, G. Li, and M. Daqaq, "Electromagnetic ferrofluid-based energy harvester," *Physics Letters A,* vol. 376, no. 32, pp. 2163-2166, 2012.
[39] Y. Wang, Q. Zhang, L. Zhao, Y. Tang, A. Shkel, and E. S. Kim, "Vibration energy harvester with low resonant frequency based on flexible coil and liquid spring," *Applied Physics Letters,* vol. 109, no. 20, p. 203901, 2016/11/14 2016.
[40] S. H. Chae, S. Ju, Y. Choi, Y.-E. Chi, and C.-H. Ji, "Electromagnetic Linear Vibration Energy Harvester Using Sliding Permanent Magnet Array and Ferrofluid as a Lubricant," (in eng), *Micromachines,* vol. 8, no. 10, p. 288, 2017.
[41] B. Marinkovic and H. Koser, "Smart Sand—a wide bandwidth vibration energy harvesting platform," *Applied Physics Letters,* vol. 94, no. 10, p. 103505, 2009/03/09 2009.
[42] D. Mallick, A. Amann, and S. Roy, "A nonlinear stretching based electromagnetic energy harvester on FR4 for wideband operation," *Smart Materials and Structures,* vol. 24, no. 1, p. 015013, 2014/11/27 2014.
[43] G. Aldawood, H. T. Nguyen, and H. Bardaweel, "High power density spring-assisted nonlinear electromagnetic vibration energy harvester for low base-accelerations," *Applied Energy,* vol. 253, p. 113546, 2019/11/01/ 2019.
[44] X. Dai, X. Miao, L. Sui, H. Zhou, X. Zhao, and G. Ding, "Tuning of nonlinear vibration via topology variation and its application in energy harvesting," *Applied Physics Letters,* vol. 100, no. 3, p. 031902, 2012/01/16 2012.
[45] A. R. M. Foisal, C. Hong, and G.-S. Chung, "Multi-frequency electromagnetic energy harvester using a magnetic spring cantilever," *Sensors and Actuators A: Physical,* vol. 182, pp. 106-113, 2012/08/01/ 2012.
[46] M. Salauddin, M. Halim, and J. Park, "A magnetic-spring-based, low-frequency-vibration energy harvester comprising a dual Halbach array," *Smart Materials and Structures,* vol. 25, no. 9, p. 095017, 2016.
[47] Q. Zhang, Y. Wang, and E. S. Kim, "Electromagnetic energy harvester with flexible coils and magnetic spring for 1–10 Hz resonance," *Journal of Microelectromechanical Systems,* vol. 24, no. 4, pp. 1193-1206, 2015.
[48] F. Cottone, L. Gammaitoni, H. Vocca, M. Ferrari, and V. Ferrari, "Piezoelectric buckled beams for random vibration energy harvesting," *Smart Materials and Structures,* vol. 21, no. 3, p. 035021, 2012/02/17 2012.
[49] F. Cottone, P. Basset, H. Vocca, L. Gammaitoni, and T. Bourouina, "Bistable electromagnetic generator based on buckled beams for vibration energy harvesting," *Journal of Intelligent Material Systems and Structures,* vol. 25, no. 12, pp. 1484-1495, 2014.
[50] W. Liu, F. Formosa, A. Badel, A. Agbossou, and G. Hu, "Investigation of a buckled beam generator with elastic clamp boundary," *Smart Materials and Structures,* vol. 25, no. 11, p. 115045, 2016/10/27 2016.
[51] B. Yan *et al.*, "Scavenging vibrational energy with a novel bistable electromagnetic energy harvester," *Smart Materials and Structures,* vol. 29, no. 2, p. 025022, 2020/01/17 2020.
[52] N. Yu, H. Ma, C. Wu, G. Yu, and B. Yan, "Modeling and experimental investigation of a novel bistable two-degree-of-freedom electromagnetic energy harvester," *Mechanical Systems and Signal Processing,* vol. 156, p. 107608, 2021/07/01/ 2021.
[53] P. Podder, A. Amann, and S. Roy, "Combined Effect of Bistability and Mechanical Impact on the Performance of a Nonlinear Electromagnetic Vibration Energy Harvester," *IEEE/ASME Transactions on Mechatronics,* vol. 21, no. 2, pp. 727-739, 2016.
[54] A. Erturk and D. J. Inman, "Broadband piezoelectric power generation on high-energy orbits of the bistable Duffing oscillator with electromechanical coupling," *Journal of Sound and Vibration,* vol. 330, no. 10, pp. 2339-2353, 2011/05/09/ 2011.
[55] K. Paul, A. Amann, S.Roy, "Tapered nonlinear vibration energy harvester for powering Internet of Things", Applied Energy, vol. 283, pp. 116267, 2021.
[56] B. P. Mann and N. D. Sims, "Energy harvesting from the nonlinear oscillations of magnetic levitation," *Journal of Sound and Vibration,* vol. 319, no. 1, pp. 515-530, 2009/01/09/ 2009.

[57] D. F. Berdy, D. J. Valentino, and D. Peroulis, "Kinetic energy harvesting from human walking and running using a magnetic levitation energy harvester," *Sensors and Actuators A: Physical*, vol. 222, pp. 262-271, 2015/02/01/ 2015.
[58] Y. Zhao, X. Ling, Z. Wang, W. Gong, G. Li, "Acceleration stretching based electromagnetic energy harvester on Train Induced Vibration of the Beijing Harbin Railway Subgrade", Shock and Vibration, 2020.
[59] C. Pronello, "Analysis of tram induced vibrations affecting roads and buidlings in standard urban sites", Int. J. Acous. Vib., vol. 8, no. 1, pp. 21, 2003
[60] J. T. Gaunt, C. D. Sutton, "Highway bridge vibration studies", 1981.
[61] G. Iannace, G. Ciaburro, A. Trematerra, "Heating, ventilation and air conditioning (HVAC) noise detection in open plan offices using recursive partitioning", Buidlings, vol. 8, no. 12, pp. 169, 2018.
[62] P. L. Green, E. Papatheou, N.D. Sims, "Energy harvesting from human motion and bridge vibrations:An evaluation of current nonlinear energy harvesting solutions", Journal of Intelligent Material Systems and Structures, vol. 24, no. 12, pp. 1494-1505, 2013.
[63] D.Zhu, S. Beeby, "A broadband electromagnetic energy harvester with a coupled bistable structure", Journal of Physics: Conference Series, vol. 476, no. 1, 2013.
[65] Y. Prawoto, "Seeing auxetic materials from the mechanics point of view: A structural review on the negative Poisson's ratio," *Computational Materials Science*, vol. 58, pp. 140-153, 2012/06/01/ 2012.
[66] P. Eghbali, D. Younesian, A. Moayedizadeh, and M. Ranjbar, "Study in circular auxetic structures for efficiency enhancement in piezoelectric vibration energy harvesting," *Scientific Reports*, vol. 10, no. 1, p. 16338, 2020/10/01 2020.
[67] F. Ebrahimian, Z. Kabirian, D. Younesian, and P. Eghbali, "Auxetic clamped-clamped resonators for high-efficiency vibration energy harvesting at low-frequency excitation," *Applied Energy*, vol. 295, p. 117010, 2021/08/01/ 2021.
[68] K. Chen, Q. Gao, S. Fang, D. Zou, Z. Yang, and W.-H. Liao, "An auxetic nonlinear piezoelectric energy harvester for enhancing efficiency and bandwidth," *Applied Energy*, vol. 298, p. 117274, 2021/09/15/ 2021.
[69] K. Chen, S. Fang, Q. Gao, D. Zou, J. Cao, and W.-H. Liao, "An enhanced nonlinear piezoelectric energy harvester with multiple rotating square unit cells," *Mechanical Systems and Signal Processing*, vol. 173, p. 109065, 2022/07/01/ 2022.
[70] S. Leadenham, "M-shaped asymmetric nonlinear oscillator for broadband vibration energy harvesting: Harmonic balance analysis and experimental validation," *Journal of Sound and Vibration*, vol. 333, pp. 6209–6223, 11/24 2014.
[71] Y. Gu, W. Liu, C. Zhao, and P. Wang, "A goblet-like non-linear electromagnetic generator for planar multi-directional vibration energy harvesting," *Applied Energy*, vol. 266, p. 114846, 2020/05/15/ 2020.
[72] M. Gao, Y. Wang, Y. Wang, and P. Wang, "Experimental investigation of non-linear multi-stable electromagnetic-induction energy harvesting mechanism by magnetic levitation oscillation," *Applied Energy*, vol. 220, pp. 856-875, 2018/06/15/ 2018.
[73] H. Deng *et al.*, "Poly-stable energy harvesting based on synergetic multistable vibration," *Communications Physics*, vol. 2, no. 1, p. 21, 2019/02/26 2019.
[74] C. Wang, S.-K. Lai, J.-M. Wang, J.-J. Feng, and Y.-Q. Ni, "An ultra-low-frequency, broadband and multi-stable tri-hybrid energy harvester for enabling the next-generation sustainable power," *Applied Energy*, vol. 291, p. 116825, 2021/06/01/ 2021.
[75] M. Salauddin, R. M. Toyabur, P. Maharjan, and J. Y. Park, "High performance human-induced vibration driven hybrid energy harvester for powering portable electronics," *Nano Energy*, vol. 45, pp. 236-246, 2018/03/01/ 2018.
[76] F. U. Khan and I. Ahmad, "Review of Energy Harvesters Utilizing Bridge Vibrations," *Shock and Vibration*, vol. 2016, p. 21, 2016, Art. no. 1340402.
[77] L. Janak, Z. Hadas, and J. Smilek, "Reliability assessment of electromechanical energy harvesting systems establishment of devices' key characteristics for application in safety-critical systems," in *2016 17th International Conference on Mechatronics-Mechatronika (ME)*, 2016, pp. 1-4: IEEE.
[78] J. C. Park, D. H. Bang, and J. Y. Park, "Micro-fabricated electromagnetic power generator to scavenge low ambient vibration," *IEEE Transactions on Magnetics*, vol. 46, no. 6, pp. 1937-1942, 2010.
[79] Y. Yang, U. Radhakrishna, D. Ward, A. P. Chandrakasan, and J. H. Lang, "A Silicon MEMS EM vibration energy harvester," *Journal of Physics: Conference Series*, vol. 1407, no. 1, p. 012022, 2019/11/01 2019.
[80] Ö. Zorlu and H. Külah, "A MEMS-based energy harvester for generating energy from non-resonant environmental vibrations," *Sensors and Actuators A: physical*, vol. 202, pp. 124-134, 2013.

[81] F. Khan, F. Sassani, and B. Stoeber, "Nonlinear behaviour of membrane type electromagnetic energy harvester under harmonic and random vibrations," *Microsystem Technologies,* vol. 20, no. 7, pp. 1323-1335, 2014.
[82] Y. Yang, U. Radhakrishna, J. F. Hunter, T. W. Eagar, and J. H. Lang, "An Electromagnetic Translational Vibration Energy Harvester Fabricated in MP35N Alloy," *Journal of Microelectromechanical Systems,* vol. 29, no. 6, pp. 1518-1522, 2020.
[83] P. Wang, H. Liu, X. Dai, Z. Yang, Z. Wang, and X. Zhao, "Design, simulation, fabrication and characterization of a micro electromagnetic vibration energy harvester with sandwiched structure and air channel," *Microelectronics Journal,* vol. 43, no. 2, pp. 154-159, 2012/02/01/ 2012.
[84] F. Khan, F. Sassani, and B. Stoeber, "Copper foil-type vibration-based electromagnetic energy harvester," *Journal of Micromechanics and Microengineering,* vol. 20, no. 12, p. 125006, 2010.
[85] P. Podder, P. Constantinou, D. Mallick, A. Amann, and S. Roy, "Magnetic Tuning of Nonlinear MEMS Electromagnetic Vibration Energy Harvester," *Journal of Microelectromechanical Systems,* vol. 26, no. 3, pp. 539-549, 2017.
[86] D. Mallick, A. Amann, and S. Roy, "High Figure of Merit Nonlinear Microelectromagnetic Energy Harvesters for Wideband Applications," *Journal of Microelectromechanical Systems,* vol. 26, no. 1, pp. 273-282, 2017.
[87] D. Mallick, A. Amann, and S. Roy, "High figure of merit nonlinear microelectromagnetic energy harvesters for wideband applications," *Journal of Microelectromechanical Systems,* vol. 26, no. 1, pp. 273-282, 2016.
[88] H. Liu, Y. Qian, N. Wang, and C. Lee, "An In-Plane Approximated Nonlinear MEMS Electromagnetic Energy Harvester," *Journal of Microelectromechanical Systems,* vol. 23, no. 3, pp. 740-749, 2014.
[89] Y. Li, J. Li, A. Yang, Y. Zhang, B. Jiang, and D. Qiao, "Electromagnetic Vibrational Energy Harvester With Microfabricated Springs and Flexible Coils," *IEEE Transactions on Industrial Electronics,* vol. 68, no. 3, pp. 2684-2693, 2021.
[90] R. Skomski, P. Manchanda, P. Kumar, B. Balamurugan, A. Kashyap, and D. J. Sellmyer, "Predicting the Future of Permanent-Magnet Materials," *IEEE Transactions on Magnetics,* vol. 49, no. 7, pp. 3215-3220, 2013.
[91] J. M. D. Coey, "Hard Magnetic Materials: A Perspective," *IEEE Transactions on Magnetics,* vol. 47, no. 12, pp. 4671-4681, 2011.
[92] Y. Jiang *et al.*, "Fabrication of a vibration-driven electromagnetic energy harvester with integrated NdFeB/Ta multilayered micro-magnets," *Journal of Micromechanics and Microengineering,* vol. 21, no. 9, p. 095014, 2011.
[94] M. Han, Z. Li, X. Sun, and H. Zhang, "Analysis of an in-plane electromagnetic energy harvester with integrated magnet array," *Sensors and Actuators A: Physical,* vol. 219, pp. 38-46, 2014/11/01/ 2014.
[95] M. Han, Q. Yuan, X. Sun, and H. Zhang, "Design and Fabrication of Integrated Magnetic MEMS Energy Harvester for Low Frequency Applications," *Journal of Microelectromechanical Systems,* vol. 23, no. 1, pp. 204-212, 2014.
[96] Q. Zhang and E. S. Kim, "Micromachined Energy-Harvester Stack With Enhanced Electromagnetic Induction Through Vertical Integration of Magnets," *Journal of Microelectromechanical Systems,* vol. 24, no. 2, pp. 384-394, 2015.
[97] K. Tao, G. Ding, P. Wang, Z. Yang, and Y. Wang, "Fully integrated micro electromagnetic vibration energy harvesters with micro-patterning of bonded magnets," in *2012 IEEE 25th International Conference on Micro Electro Mechanical Systems (MEMS)*, 2012, pp. 1237-1240.
[98] W. Zhang, Y. Dong, Y. Tan, M. Zhang, X. Qian, and X. Wang, "Electric Power Self-Supply Module for WSN Sensor Node Based on MEMS Vibration Energy Harvester," *Micromachines,* vol. 9, no. 4, 2018.
[99] R. Han, N. Wang, J. Wang, J. Gu, and X. Li, "Silicon-chip based electromagnetic vibration energy harvesters fabricated using wafer-level micro-casting technique," *Journal of Micromechanics and Microengineering,* vol. 31, no. 3, p. 035009, 2021/02/04 2021.
[100] K. Wang, X. Dai, C. Ren, and G. Ding, "Fully Integrated Microsolenoid With Closed Magnetic Circuit for High Power Density MEMS Electromagnetic Vibration Energy Harvesters," *IEEE Magnetics Letters,* vol. 12, pp. 1-5, 2021.
[101] H. Wu *et al.*, "A micro-electromagnetic vibration energy harvester with higher power density and wider bandwidth utilizing 3D MEMS coils," *Applied Physics Letters,* vol. 119, no. 21, p. 213904, 2021/11/22 2021.
[102] L. Wang, T. J. Kazmierski, B. M. Al-Hashimi, S. P. Beeby, and R. N. Torah, "An integrated approach to energy harvester modeling and performance optimization," in *2007 IEEE International Behavioral Modeling and Simulation Workshop*, 2007, pp. 121-125: IEEE.
[103] W. Liu, Z. Feng, J. He, and R. Liu, "Maximum mechanical energy harvesting strategy for a piezoelement," *Smart Materials and Structures,* vol. 16, no. 6, p. 2130, 2007.

[104] J. C. Rodriguez, V. Nico, and J. Punch, "A Vibration Energy Harvester and Power Management Solution for Battery-Free Operation of Wireless Sensor Nodes," *Sensors*, vol. 19, no. 17, 2019.
[105] M. Ghovanloo and K. Najafi, "Fully integrated wideband high-current rectifiers for inductively powered devices," *IEEE Journal of solid-state circuits*, vol. 39, no. 11, pp. 1976-1984, 2004.
[106] C. Peters, J. Handwerker, D. Maurath, and Y. Manoli, "A sub-500 mV highly efficient active rectifier for energy harvesting applications," *IEEE Transactions on Circuits and Systems I: Regular Papers*, vol. 58, no. 7, pp. 1542-1550, 2011.
[107] M. Magno, D. Kneubühler, P. Mayer, and L. Benini, "Micro kinetic energy harvesting for autonomous wearable devices," in *2018 International symposium on power electronics, electrical drives, automation and motion (SPEEDAM)*, 2018, pp. 105-110: IEEE.
[108] J. F. Dickson, "On-chip high-voltage generation in MNOS integrated circuits using an improved voltage multiplier technique," *IEEE Journal of Solid-State Circuits*, vol. 11, no. 3, pp. 374-378, 1976.
[109] L. Costanzo, A. L. Schiavo, and M. Vitelli, "Design Guidelines for the Perturb and Observe Technique for Electromagnetic Vibration Energy Harvesters Feeding Bridge Rectifiers," *IEEE Transactions on Industry Applications*, vol. 55, no. 5, pp. 5089-5098, 2019.
[110] L. Costanzo, T. Lin, W. Lin, A. L. Schiavo, M. Vitelli, and L. Zuo, "Power Electronic Interface With an Adaptive MPPT Technique for Train Suspension Energy Harvesters," *IEEE Transactions on Industrial Electronics*, vol. 68, no. 9, pp. 8219-8230, 2021.
[111] S. Chamanian, B. Çiftci, H. Uluşan, A. Muhtaroğlu, and H. Külah, "Power-efficient hybrid energy harvesting system for harnessing ambient vibrations," *IEEE Transactions on Circuits and Systems I: Regular Papers*, vol. 66, no. 7, pp. 2784-2793, 2019.
[112] H. Yu, J. Zhou, X. Yi, H. Wu, and W. Wang, "A hybrid micro vibration energy harvester with power management circuit," *Microelectronic Engineering*, vol. 131, pp. 36-42, 2015.
[113] M. Kundurthi, D. Mallick, and A. Jain, "System level modeling and optimization of hybrid vibration energy harvesters," in *2020 IEEE International Symposium on Circuits and Systems (ISCAS)*, 2020, pp. 1-5: IEEE.
[114] E. E. Aktakka and K. Najafi, "A Micro Inertial Energy Harvesting Platform With Self-Supplied Power Management Circuit for Autonomous Wireless Sensor Nodes," *IEEE Journal of Solid-State Circuits*, vol. 49, no. 9, pp. 2017-2029, 2014.
[115] M. Yao, X. Wang, Q. Wu, Y. Niu, and S. Wang, "Dynamic analysis and design of power management circuit of the nonlinear electromagnetic energy harvesting device for the automobile suspension," *Mechanical Systems and Signal Processing*, vol. 170, p. 108831, 2022/05/01/ 2022.
[116] M. Yao, J. Li, and Y. Niu, "Adaptive impedance matching for power management circuit for a piezoelectric energy harvester on the bridge," *Sensors and Actuators A: Physical*, vol. 331, p. 112986, 2021/11/01/ 2021.

Chapter 3: A Meso-scale Vibration Energy Harvester for Improved Wireless Communication- A Feasibility Study

This chapter is based on the following publication- K. Paul, D. R. Gawade, R. B.V.B. Simorangkir, B. O'Flynn, J. L. Buckley, A. Amann, S. Roy, "A Concertina-Shapes Vibration Energy Harvester-Assisted NFC Sensor With Improved Wireless Communication Range", *IEEE Internet of Things Journal,* pp. 1-13, 2022.

3.1 Introduction

This chapter presents the design and fabrication of a resonant Vibration Energy Harvester (VEH) that comprises interleaved springs, manifesting a concertina shaped structure that can enable large mechanical amplitudes of oscillation. Within a relatively small volume ($9cm^3$), this concertina-VEH yields a large power density of $455.6\mu W/cm^3g^2$ while operating at a resonant frequency of 75Hz. The small volume of this device as well as the low level of acceleration (0.2g) aids to yield this high energy density from this resonant device. Additionally, the feasibility of the implemented VEH to support NFC based wireless sensor platforms, that is yet uncharted, is also investigated in this work. A very low-power consumption Near Field Communication (NFC) wireless sensor node has been designed and developed for this purpose. The developed concertina VEH has been employed to power the electronics interface of this NFC sensor. Using mechanical energy derived from as low as 0.2g excitation, our study shows that the VEH can enhance the electromagnetic interaction between the transmitting antenna and the reader, resulting in a 120% increase in wireless communication range for the NFC sensor node. The performance of this device has been compared with reported contemporary resonant generators and it stands out owing to the capability of extracting substantial mechanical energy from low to moderate acceleration (0.2-0.6g) level that in turn delivers sufficient energy at the application node without the need of any external charge storage element (capacitor/supercapacitor). Such a high-performance energy harvester assisted NFC sensor node has the potential to be used in a wide range of Internet of Things (IoT) platforms as a reliable and sustainable power solution.

3.2 Requirement of reliable and sustainable power source from application perspective

Amongst the popular wireless communication standards such as NB-IoT (Narrowband Internet of Things), SigFox (a French global network provider), LoRaWAN (Long Range Wide

Area Network), BLE (Bluetooth Low Energy) and NFC (Near Field Communication), the NFC technology offers a unique benefit of a very low power requirement [1] while transmitting data. Recent studies have reported that typically 900µW of power is consumed by NFC-based sensor interfaces while offering a communication range up to 4.5cm [2-5]. The communication range of an NFC platform largely depends on several parameters such as the reader type, NFC antenna size, coupling between the NFC reader and tag, RFID air interface and power consumption of the front-end electronics. With an NFC type 5 enabled smartphone as a reader, a maximum communication range of 7cm could be achieved, which increases to 1 m when a 13.56MHz reader (ISO/IEC 15693) is employed [2, 6]. Nowadays, the inclusion of NFC technology in smartphones enables on-call data acquisition through reader/smartphones, which substantially reduces the installation cost of NFC sensors [2, 7]. This allows frictionless migration of the data from the edge to the cloud, which paves the way for a number of low communication-range applications such as health monitoring [8], food quality monitoring [9], gas monitoring [10], structural health monitoring [11], etc. A battery assisted NFC sensor node offers enhanced communication range [3]. As the battery powers the front-end electronics associated with the sensor node, the power harvested through the NFC aids in communicating the data-modulated signal by strengthening the electromagnetic interaction between the NFC antenna and the reader. However, the degradation of battery life owing to thermal/mechanical stress, as well as chemical reactions [12], poses a great challenge in the usage of batteries for NFC sensor nodes. Hence, assisting the NFC with an energy harvester to power the sensor hardware and to enhance the range of communication appears to be a viable approach that would open wider fields of application.

In this chapter, we present a novel resonant VEH demonstrator and provide a feasibility study on its potential for supporting wireless sensor platforms to achieve the above-discussed goal. We designed and developed a linear interleaved spring on FR4 material that comprises two linear springs arranged in series, offering a relatively low natural frequency of oscillation (<200 Hz) with a small footprint, while exhibiting large out-of-plane oscillations at resonance. Section 3.3 outlines the design guidelines and fabrication of the resonant VEH structure that extracts mechanical energy through electromagnetic transduction. Resembling the shape of the ‘concertina’ musical instrument, the fabricated spring exhibits large displacements while demonstrating linear spring-force characteristics [13, 14]. The electrodynamical characterization of this concertina-VEH is presented in Section 3.4. The resistive load optimization and the frequency response of the VEH for a fixed optimized load have been

discussed. Large deformation of the 'concertina' spring translates into enhanced voltage induction through the magnet-coil assembly that results in large power delivered across a suitable load for low excitation. As a concept demonstrator, we have designed and developed a low-power NFC sensor node that is described with functional block diagrams in Section 3.5. In Section 3.6, we demonstrate the efficacy of the developed VEH to power the front-end electronics of the NFC sensor, which strengthens the electromagnetic interaction between the transmitter antenna and the receiver, resulting in an enhanced range of communication. Finally, in Section 3.7, through an exhaustive comparison, we demonstrate the efficacy of the developed VEH in extracting energy from weak vibrations and powering a wireless sensor platform, thereby offering an improved range of communication. Such a system could be exploited in a wide range of IoT based applications, e.g. temperature and humidity monitoring of industrial cleanroom environments while extracting mechanical energy from installed Air Conditioning systems.

3.3 Design and fabrication of the Concertina VEH

Typically, an electromagnetic VEH structure comprises a mechanical resonator or a spring that vibrates in response to an externally applied mechanical excitation, and a magnet-coil assembly that is employed to facilitate the electromagnetic transduction. Figure 3.1 shows the proposed VEH comprising a spring structure that holds an assembly of magnets on the central stage. The spring is fixed to a rigid support on the base through the outer perimeter and the rest of the spring is suspended and allowed to vibrate. Close to the magnet, a rigidly fixed coil is inserted vertically. On external excitation, the spring vibrates in the vertical direction, which enables the magnets to exhibit out-of-plane displacements with respect to the fixed coil, inducing voltage across the coil. In this work, the concertina spring architecture is laser micromachined on a 300µm thick FR4 sheet.

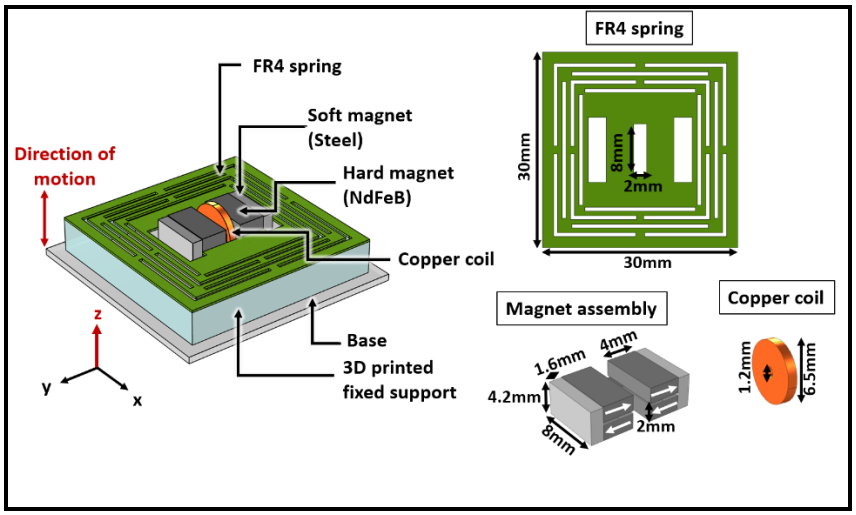


Figure 3.1: Schematic of the conceived Electromagnetic vibration energy harvester. The red arrow indicates the out-of-plane motion of the VEH.

FR4 stands for the low-cost 'Flame retardant' materials that are popularly used in printed circuit boards (PCBs) and a wide range of electrical and electronics applications owing to the electrical insulation properties. The low Young's modulus (approximately 21-24GPa) of the FR4 material aids in scaling the natural frequency of oscillation of the resonator down, enabling the VEH to efficiently harness mechanical energy from ambient vibration sources as a significant fraction of this energy is distributed in the low-frequency range (<200Hz) [15, 16]. In addition to the above, the FR4 sheet derives mechanical strength from the constituent interwoven fibreglass, which results in mechanically robust VEH structures. In the literature, FR4 based spring structures have been tested in laboratory vibration environment for more than 10 million cycles [17] without any mechanical failure. In another reliability test [18], FR4 device has been subjected to 100MPa stress and has been mechanically stable for up to 250 million cycles of operation. Table 3.1 shows the comparison of different spring constituent materials and comparison of the maximum displacement exhibited by the fabricated springs. The modulus of elasticity (Young's modulus) parameter, which directly influences the dominant frequency of oscillation of the spring structure, is compared for different materials including Silicon, Silicon-on-Insulator, Nickel, Copper, Alloy, PDMS (Polydimethylsiloxane) and FR4. The Young's modulus of PDMS (360kPa) and FR4 (21GPa) structures are significantly lower than the rest of the materials, which, in turn, aids in bringing the frequency of oscillation down to a lower frequency range. However, designing intricate springs on PDMS that would exhibit large out of-plane displacements could be challenging considering the mechanical stability and durability of the spring architecture. Hence, considering the

mechanical robustness, low cost, and low elasticity modulus we have chosen FR4 as the spring constituent material for the resonant VEH.

Table 3.1: Comparison of spring materials and associated properties of EMVEH springs

Spring material	Young's modulus	Spring type	Resonant frequency	Max. Displacement exhibited by the fabricated spring
Silicon [19]	*170-90GPa	MEMS	143 Hz 156Hz	0.409 mm 0.351 mm
Silicon-on-insulator [20]	180GPa	MEMS	367 Hz 587Hz	~ 125 µm (0.5N) ~ 80 µm(0.5 N)
Nickel [21]	165GPa	MEMS	648 Hz	100 µm (50 mN)
Copper foil [22]	128GPa	Micro-	371 Hz	142.4µm (resonance)
Electroplated copper [23]	*110-130GPa	MEMS	94.5 Hz	259.1µm (resonance)
PDMS [24]	360kPa	MEMS	93 Hz	~ 110µm (1.3µN)
FR4 this work	21GPa	Macroscale	75 Hz	2500 µm 2N

Four sintered Neodymium-Iron-Boron (NdFeB) magnets are epoxy bonded on the central stage (16mm × 10mm) of the FR4 spring such that oppositely polarized magnets are on each side of the 8mm × 2 mm slot at the centre dedicated for the coil, as shown in Fig. 3.1. To intensify the magnetic flux gradient around the coil, soft magnetic steel keepers are used to guide the magnetic flux from the oppositely polarized pair of magnets, which aids in forming a closed path of magnetic field lines through the coil. A miniaturized copper wire-wound coil (outer and inner diameter 6.5mm and 1.2mm respectively, thickness 1mm, 2500 turns and 700Ω resistance) is inserted through the dedicated slot. To keep the coil stationary with respect to the magnets, it is fixed with the base platform through a 3D printed fixture.

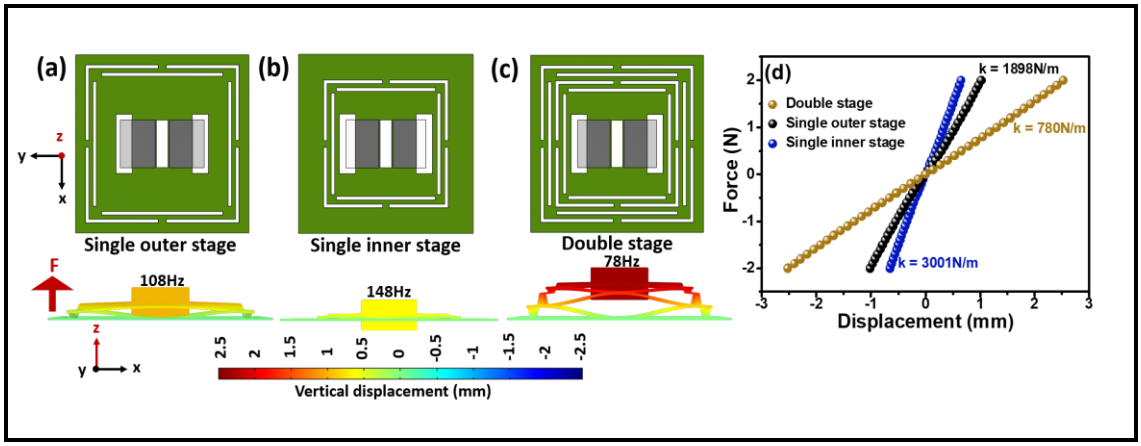


Figure 3.2: The design of Concertina springs with (a) single stage on the outer side, (b) single stage on the inner side, (c) double stage spring in series. All have been shown along with the displacement profile for an applied force F. (d) The comparison of the spring force vs displacement characteristics for the designed springs.

The spring architecture is designed with the motivation of increasing the out-of-plane compliance to enhance the electromagnetic interaction and hence the extractable electrical energy. The outer dimension of the spring is 30mm × 30mm. The width of each spring arm is 0.7mm. As shown in Fig. 3.2(a), a single stage of the spring (outer), which comprises four sets of springs, instigates vertical out-of-plane displacement of the central load owing to the interleaved spring architecture. Resembling the shape of the 'concertina' musical instrument, we call these concertina springs. The primary motivation behind selection of this spring design is to allow the spring to exhibit large out of plane displacements while keeping the spring stiffness still in the linear regime. This type of square concertina design aids in implementing linear force-displacement variation even at large displacement [13, 14], on the other hand circular designs have been reported in the literature to offer nonlinear restoring forces at large displacement arising from the stretched springs [25]. With a single-stage concertina spring (on the outer side), the VEH exhibits small out-of-plane displacements, as shown in Fig. 3.2(a), when excited at 108Hz which is the natural frequency of oscillation of the structure. Approximately 2N external force is required to displace the load 1mm normal to the plane. These characteristics manifest a rather stiff spring, yielding a spring stiffness coefficient of 1898N/m. On the other hand, a single-stage concertina spring on the inner side makes the spring even stiffer and allows the central load to displace only 0.7mm for a similar level of force at 148Hz frequency of oscillation, resulting in a large spring stiffness coefficient of 3001N/m (Fig. 3.2(b)). The small displacement exhibited by the single-stage spring restricts the coil from experiencing large magnetic flux variation resulting from the displacement of the magnet

assembly. Adding the concertina springs in series could potentially enhance the out-of-plane compliance by offering a reduced equivalent spring stiffness (k_{eq}) as compared with the individual single stage of springs [26].

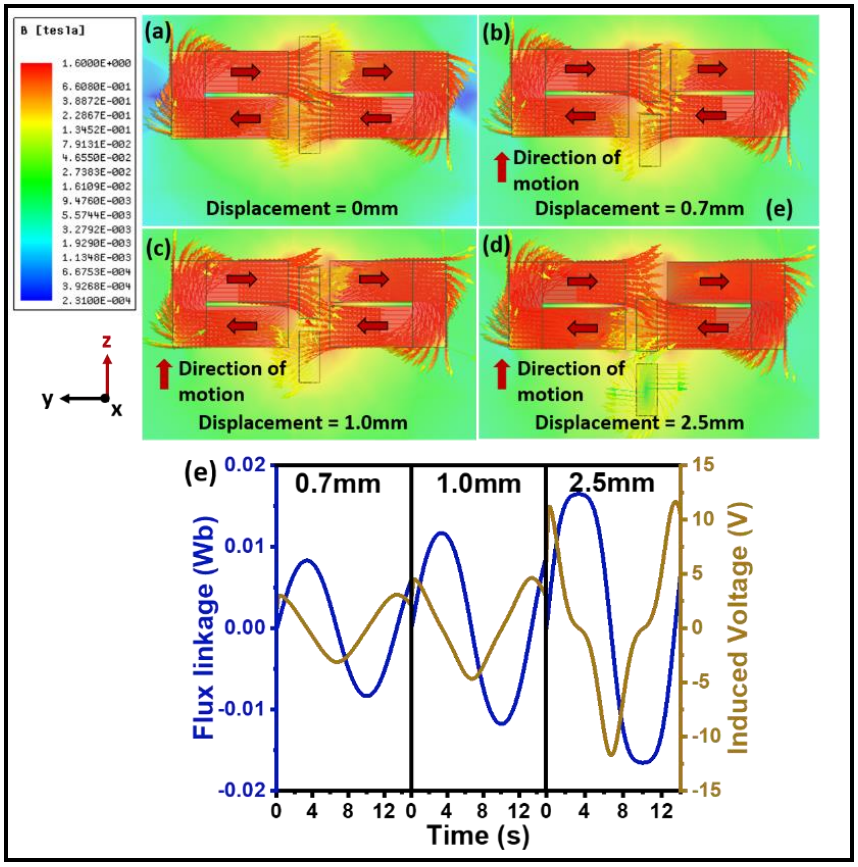


Figure 3.3: The electromagnetic interaction between the coil and the magnet assembly and the corresponding variation of magnetic field lines have been shown in (a) for no displacement, (b) for 0.7 mm displacement, (c) for 1 mm displacement and (d) for 2.5 mm displacement of the magnets from the equilibrium position. (e) The variation of magnetic flux linkage and the induced voltage for different displacement of the magnet.

As shown in Fig. 3.2(c), the second set of concertina springs that are connected in series with the first stage of springs are relatively smaller. The spring stiffness coefficient of the double stage concertina topology reduces to 780N/m, which is much lower than the stiffness that each of the individual concertina stages offers. The interleaved structure of the spring instigates larger out-of-plane displacements for similar external excitation compared with the rest of the spring topologies, as shown in Fig. 3.2(d). Arranging these concertina springs in series also helps to scale the frequency of oscillation down from 148Hz to 78Hz. In this context, it is to be noted that the patterns and especially the length of the spring (the width of each spring

is fixed to 0.7mm) plays a key role in influencing the spring stiffness and the frequency of oscillation of the structure. This can be verified by revisiting Fig. 3.2(b) that has the shortest length of springs, resulting in larger spring stiffness and higher frequency of oscillation. In contrast with this, the spring with a single stage on the outer end (Fig. 3.2(a)) demonstrates larger compliance and lower frequency owing to the longer springs, which is further enhanced when two stages of springs are used together in the double stage concertina design (Fig. 3.2(c)) that efficiently reduces the spring stiffness as well as the frequency of oscillation. Adding more of such interleaved spring stages could potentially scale down and tune the natural frequency of oscillation of the spring structure as well as further enhance the amplitude of displacement. However, that comes at the cost of increased footprint of the VEH device. Moreover, very large displacement of the spring from the position of static equilibrium could have an adverse effect on the electromagnetic interaction and hence on the deliverable power since, at very large displacements, the magnetic field lines emerging from these small magnets would be too feeble for the coil to interact with. Hence, we limit our study up to the double stage of concertina-springs.

Ansys Maxwell [27] has been employed as the finite element analysis tool to investigate the electromagnetic interaction between the coil and the magnet assembly for the different spring topologies using single stage and double stage concertina springs, considering open circuit conditions. Following Faraday's law, the relative motion between the coil and the magnet induces a voltage V into the coil, which depends on the magnetic flux ϕ and can be represented as,

$$V = -N\frac{d\varphi}{dt} = -N\frac{d\varphi}{dz}\frac{dz}{dt}, \tag{3.1}$$

Where, N is the number of turns of the coil. Therefore, a larger gradient of magnetic flux would result in higher induced voltage and power. Figure 3.3(a) shows the magnetic flux distribution when the VEH is stationary. The arrows indicate the direction of magnetization as well as the magnetic flux lines. The soft magnet blocks on both sides of the magnets aid in routing the magnetic flux lines in a way that intensifies the flux distribution across the coil that is placed at the centre. The maximum obtainable out-of-plane displacement has been considered when studying the magnetic flux linkage with the coil and the induced voltage into the coil. With a single stage of concertina springs at the inner side (as shown in Fig. 3.2(b)) of the spring topology, the maximum displacement is 0.7mm, which allows 8mWb magnetic flux linkage, resulting in a maximum of 4V-induced voltage across the coil. This improves when the concertina spring is placed at the outer side of the spring design (maximum displacement 1mm);

the magnetic flux linkage enhances to 11mWb and proportionately the induced voltage increases to 6V, as shown in Fig. 3.3(e). The magnetic flux linkage reaches a maximum of 16.5mWb with the double stage concertina springs design that offers large out-of-plane displacement (2.5mm). Fig. 3.3(d) shows that, with 2.5mm displacement, the coil segments experience a drastic change of magnetic flux lines through them, yielding a large magnetic flux gradient. This reflects onto the improved induced voltage of 11.2V. Hence, we have selected the double stage concertina springs for further analysis and experiments.

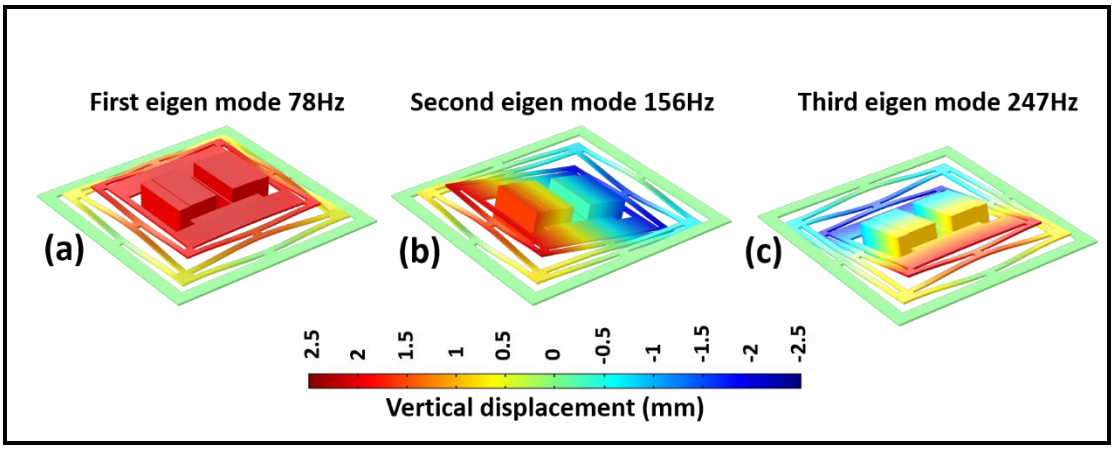


Figure 3.4: The first three modes of oscillation of the concertina spring structure: (a) at 78 Hz, (b) at 156 Hz, and (c) 247 Hz. The out-of-plane and torsional modes of vibrations have been portrayed.

The solid mechanics module of COMSOL multiphysics [28] has been used to investigate the modes of vibration of the designed double concertina VEH. We consider here only the first three eigenmodes at 78Hz, 156Hz and 247Hz (Fig.3.4). The first mode corresponds to the out-of-plane displacement of the springs, and the other two modes manifest tilts occurring at higher frequencies. From the perspective of mechanical energy harvesting, large out-of-plane vibration is desirable to extract substantial mechanical energy through the conceived design, whereas it is beneficial to supress in-planar motion or other degrees of freedom which may not contribute to efficient mechanical energy extraction from this design. In fact, such adjacent modes of vibration close to the primary desired mode may result in loss of energy scavenging owing to the distribution of energy over these modes. The interleaved spring architecture of the concertina-VEH promotes the desired out-of-plane vibrations, and as evident from Fig. 3.4, the design effectively supresses the other consecutive modes of vibrations as they are spread over higher frequency domain.

3.4 Experimental Characterization of the VEH and Discussions

The electromechanical characteristics of the conceived VEH have been investigated with a Bruel and Kjær Shaker unit that consists of an LDS V455 permanent magnet shaker, LDS vibration controller, PA1000L power amplifier and a DeltaTron 4517-002 piezoelectric accelerometer mounted on the shaker to monitor the amplitude of excitation and feedback the signal to the controller. The controller in turn generates a signal that is fed to the power amplifier, which then amplifies the signal and sends the drive current signal to the shaker for generating the desired vibrations. The VEH is mounted on the shaker and excited with harmonic vibrations of fixed amplitudes (e.g. 0.1g to 1g) while the frequency of the excitation is swept from 65Hz to 85Hz with a constant sweep rate of 1Hz/sec. The induced voltage across the coil of the VEH is recorded with a digital oscilloscope (Picoscope 3000series). The experimental setup is shown in Fig. 3.5.

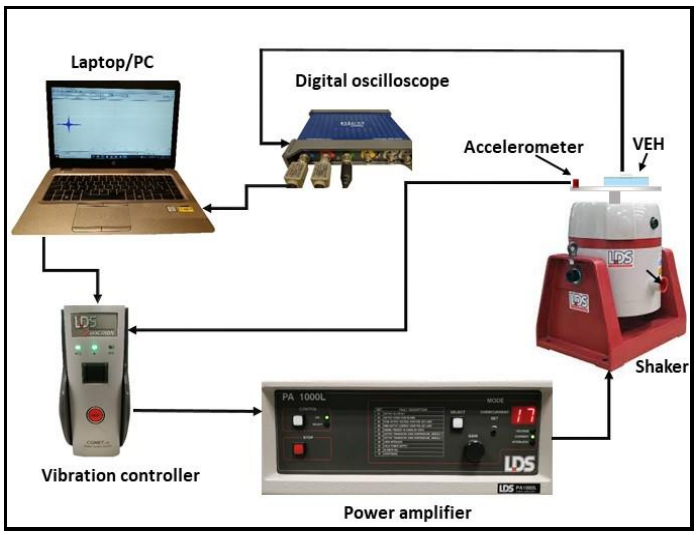


Figure 3.5: Schematic of the experimental setup for the electrodynamic characterization of the developed linear concertina-VEH.

The frequency of resonance of the VEH is found to be 75Hz from the initial frequency sweeps in the open circuit conditions, which is slightly lower than the 78Hz resonance that we obtained through the finite element analysis. To quantify the sharpness of resonance, or in other words, the linearity of the system, the Q-factor of this VEH has been experimentally obtained using the ring-down method [29]. The VEH has been excited at the resonant frequency with 0.5g amplitude of harmonic vibrations. The decay of the response is observed once the excitation is withdrawn. The open-circuit Q-factor is represented as,

$$Q_{oc} = \frac{\pi f_0 \Delta t}{\ln \frac{V_1}{V_2}} = \frac{1}{2\rho_m} \tag{3.2}$$

Where f_0 is the frequency of resonance, V_1 and V_1 are the voltages at the limits of the time interval Δt, and ρ_m is the mechanical damping ratio that is inversely proportional to the Q_{OC}. Using this relation, the Q_{OC} is measured to be 546.17, and the mechanical damping ratio is calculated to be 0.0009. These two factors are strongly dependent on the design of the spring and could be further tailored by altering the design that is by adding or reducing the number of concertina spring stages for the spring structure.

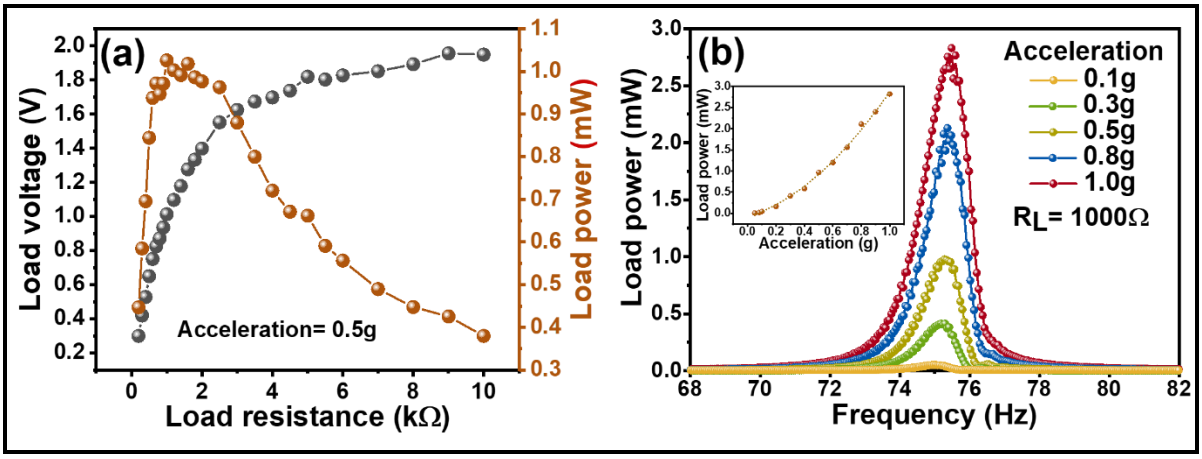


Figure 3.6: (a) The variation of load voltage and power delivered across the load with respect to the variation of the resistive load for the developed linear VEH with concertina springs that is shown at the inset. (b) The variation of the power delivered across the optimized resistive load as the frequency of excitation is varied. The Inset shows the level of powered delivered to the load as a function of the amplitude of acceleration.

A suitable resistive load is often connected across the VEH to extract the usable electrical energy for the target applications. In this case, the VEH is driven at the resonant frequency with a fixed amplitude of excitation 0.5g, and the resistive load across the VEH is varied from 200Ω to 10kΩ to find the optimal load condition that will result in maximum power extraction from the VEH. As shown in Fig. 3.6(a), the power delivered across the resistance maximizes for 1kΩ load and the delivered power peaks at 1.02mW for 0.5g excitation. On increasing the value of the load resistance further, the power gradually drops and the voltage saturates at 1.9V for a load of 10kΩ. The variation of the power delivered across the optimal load 1kΩ with respect to the frequency of excitation, for different amplitudes of the drive has been investigated. For very low amplitudes of excitation, such as 0.1g, the VEH delivers a low peak load power of 46µW at 75Hz (Fig. 3.6(b)). On increasing acceleration, the VEH generates more electrical power while resonating at 75Hz. The VEH delivers a maximum of 2.9mW power when the amplitude of excitation increases to 1g, offering a half-power bandwidth of

1.16Hz. The inset of Fig. 3.6(b) shows the variation of the obtainable power at 75Hz as a function of the amplitude of excitation. The obtainable load power increases quadratically with the amplitude of external excitation (Power = $B_0 + B_1 * (\text{Acc.}) + B_2 * (\text{Acc.})^2$ where B_0=-0.08mW, B_1=1.06mW/g, B_2=1.9mW/g^2). The high out-of-plane compliance of the double stage concertina spring structure aids in enhancing the electromagnetic interaction, which translates into large extractable power from a relatively small footprint.

3.5 Design and fabrication of the NFC based sensor node

The constraints of the target application primarily influence the selection of wireless technology. NB-IoT, SigFox, LoRaWAN, WiFi, and ZigBee are among popular commercial wireless communication solutions that offer a long range of communication at the cost of a higher transmission power requirement. However, the widespread usage of smartphones that typically comprise embedded BLE and NFC plays a key role behind the popularity of these two wireless technologies, which allow for on-call data acquisition wirelessly within a shorter communication range. In particular, NFC technology, that has been used for this work, is a short-range and contactless communication technology that outperforms BLE in terms of its power requirement. We summarize and compare the key performance metrics of the different wireless technologies in Table 3.2. NFC technology exploits inductive coupling between two loop antennas in close proximity to facilitate reliable data communication, and operates within the worldwide available unlicensed radio frequency band of 13.56MHz [30]. A block diagram of a battery-less NFC temperature and relative humidity sensor with a reader (in this case NFC type 5-enabled smartphone) is shown in Fig. 3.7. The role of the smartphone in this setup is to wirelessly power the sensor and to wirelessly read the data that the sensor generates.

In principle, upon placing the smartphone near the NFC sensor hardware, the time-varying electromagnetic fields generated from the NFC transmitter of the smartphone (shown in Fig. 3.7(a) through the signal symbol) induces current into the NFC loop antenna in the sensor hardware through inductive coupling. A fraction of the harvested RF power is employed to power the frontend electronics of the sensor and the remaining power is used to facilitate the communication of the data acquired by the sensor through the NFC radio. The detailed process is illustrated in Fig. 3.7(a).

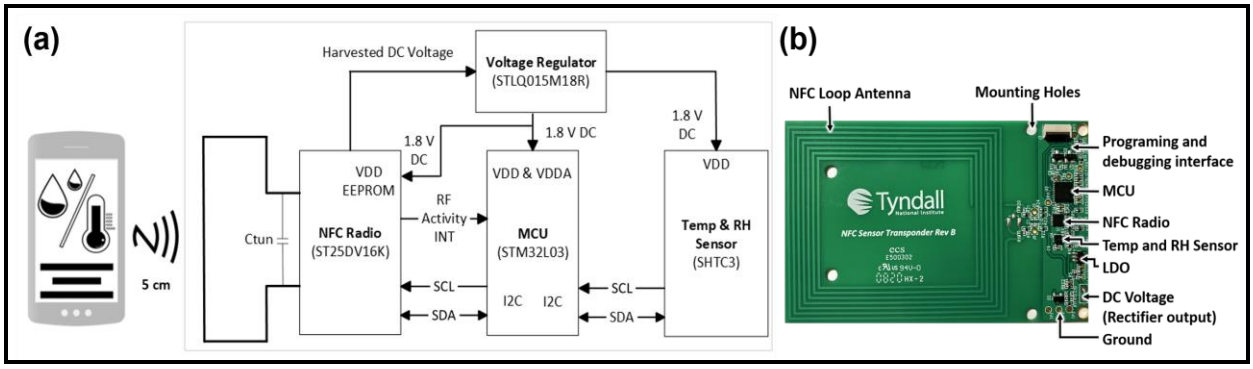


Figure 3.7: (a) The functional block diagram of the NFC sensor hardware. (b) The developed NFC sensor hardware [24].

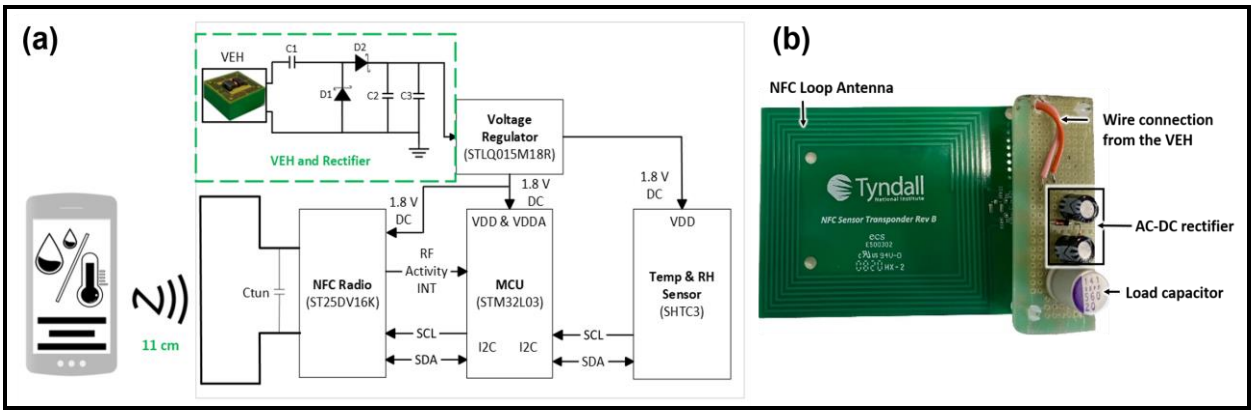


Figure 3.8: (a) The functional block diagram of the NFC sensor hardware when assisted with the developed concertina VEH. (b) The developed NFC sensor hardware along with the AC-DC rectification stage integrated to facilitate the rectification of incoming AC voltage from the VEH.

As shown, the loop antenna feeds the induced RF power to the NFC radio transceiver. The RF front-end of this NFC radio consists of energy harvesting circuitry, which converts the harvested RF power into the DC voltage. Following this RF-DC conversion, a low dropout voltage regulator (LDO) is used to regulate this incoming DC voltage into a steady DC supply (i.e., 1.8V DC) for the following sensor electronics stage e.g. the microcontroller unit (MCU), the sensor, and all other circuitry. Once the required power is received, the sensor is activated and can function to measure the target physical parameters such as temperature, relative humidity, and so on. Through the I2C protocol, the sensor communicates this acquired data with the microcontroller unit using the remaining RF power that was harvested through the smartphone. This data is then written into the user area of the NFC radio's dual access non-volatile memory (EEPROM) and it is read through the smartphone wirelessly using the dedicated read command. The time taken by the NFC sensor node from harvesting the power from the reader to communicating the data back to the reader is often referred to as "tapping time," which is dependent on the microcontroller's computational speed and the data

transmission rate. The voltage and clock settings have been optimized (i.e., Clock source = Multispeed internal oscillator clock, MCU peripheral clock (f_{CLK}) = 0.524MHz, I2C core input clock (f_{I2CIN}) = 1.028MHz, core voltage (V_{CORE}) = 1.2V, and supply voltage (V_{DD}) = 1.8V) considering the trade-off between the computational speed and DC power consumption. The DC power required by the NFC sensor hardware to be fully functional is measured to be 597µW, which is considerably reduced with respect to the previously reported value of 900µW [2]. Our developed NFC sensor (Fig. 3.7(b)) requires a minimum tapping time of 6.79s.

Table 3.2: Comparison of wireless communication technologies

Wireless Technology	Wireless comm. range(m)	DC Sleep current (µW)	Tx RF power (mW)	Reference (mW)
NB-IoT	10000	10	252-900	[31, 32]
SigFox	10000	2.1	66	[31, 33]
LoRaWAN	5000	2.2	103-264	[31, 34]
WiFi	250	13.2	775.7	[31, 35]
ZigBee	100	2.97	115-152	[31, 36]
BLE	20	2.91	21.12	[31, 38]
NFC	0.07	2.34	0.198	[6]

The NFC sensor hardware prototype is shown in Fig. 3.7(b), which comprises a loop antenna and following Commercial Off-The-Shelf (COTS) components: an NFC radio (ST25DV16KJFR6D3), MCU (STM32L031K6U6), LDO (STLQ015M18R) from STMicroelectronics, as well as temperature and humidity sensors (SHTC3) from Sensirion AG. The sensor hardware uses a standard 0.8mm thick 4-layer FR4 substrate. The detailed operation of the developed NFC sensor hardware with a smartphone, along with its performance characteristics, including the power consumption (0.9mW), wireless communication range (4.5cm), and sensor characterization, has been reported in [2].

In this work, we exploit the mechanical energy harvesting capability of the developed concertina VEH to power the frontend electronics of the NFC sensor hardware. The functional block diagram of the NFC sensor hardware assisted with the developed VEH is given in Fig. 3.8(a). The NFC sensor, along with the AC-DC rectification unit, is shown in Fig. 3.8(b). By connecting the VEH energy harvester, the RF energy harvested from the smartphone can be focused to facilitate the communication of the data acquired by the sensor back to the smartphone. The VEH would act as a sustainable power source that offers the capability of continuously providing power to the electronics interface to support the NFC sensor hardware, as a replacement for batteries that only offer a limited lifetime. To pair the NFC sensor with

the developed VEH, further optimizations have been performed on the hardware and the firmware of the previously reported NFC sensor. To allow for an extraction of sufficient electrical energy, even from a low amplitude vibration, a double-stage voltage multiplier circuit [39, 40] consisting of two capacitors (10µF each) and two diodes (Small-signal Schottky Diode, part number BAT85T/R) has been employed to rectify the incoming AC signal from the VEH. Following the rectification stage, a 560µF (20V) conductive polymer aluminium solid capacitor (SEPF series) has been added to store the energy and to supply it to the NFC sensor hardware circuitry when required. The voltage regulator is activated upon receiving a minimum voltage of 2.66V from the VEH. This regulator then provides a steady 1.8V DC supply to the rest of the associated sensor electronics. To keep the overall footprint of the system small, the voltage multiplier circuit, along with the storage capacitor, has been implemented on a PCB board mounted on top of the remaining electronics of the NFC sensor node with a vertical spacer. As mentioned previously, the tapping time, which is the time take by the sensor node from harvesting RF power to reading the acquired data through the reader, depends largely on the microcontroller's computational speed and the corresponding data transmission rate. Upon the VEH integration (Fig. 3.8), the tapping time of the NFC sensor node has decreased from 6.79 s to 1.95s. This shorter tapping time might be attributed to the VEH supplying adequate power to the electronics to perform continuous data acquisition and processing. Hence, the tapping time only accounts for the time taken for communicating the processed data to the reader.

3.6 Feasibility experiment of battery-less and VEH assisted NFC sensor node platform

In this section, we demonstrate the significance of the developed concertina VEH when implemented to assist the developed NFC sensor node platform representing an autonomous wireless platform system. The experimental set-up used in this study is depicted in Fig. 3.9(a). The VEH is mounted on the shaker unit, which emulates ambient mechanical vibrations in a laboratory environment. The shaker unit is covered with a plastic casing and, on top of it, a communication range measurements set-up for the developed NFC hardware has been placed, which comprises a base that holds the NFC sensor hardware, and a moveable stage that carries the reader (smartphone). 'NFC for iPhone' and 'Simply NFC' application interfaces have been used to read the data from the NFC sensor. This set-up is used to vary the distance between the NFC loop antennas in the sensor hardware and that of the smartphone. The AC-DC rectifier stage, as mentioned in the previous section, has been fabricated on copper stripboard and

mounted on top of the NFC hardware to minimize the length of the wired connections and to reduce the footprint. The output of the VEH is connected to the input of the rectifier stage through wired connections.

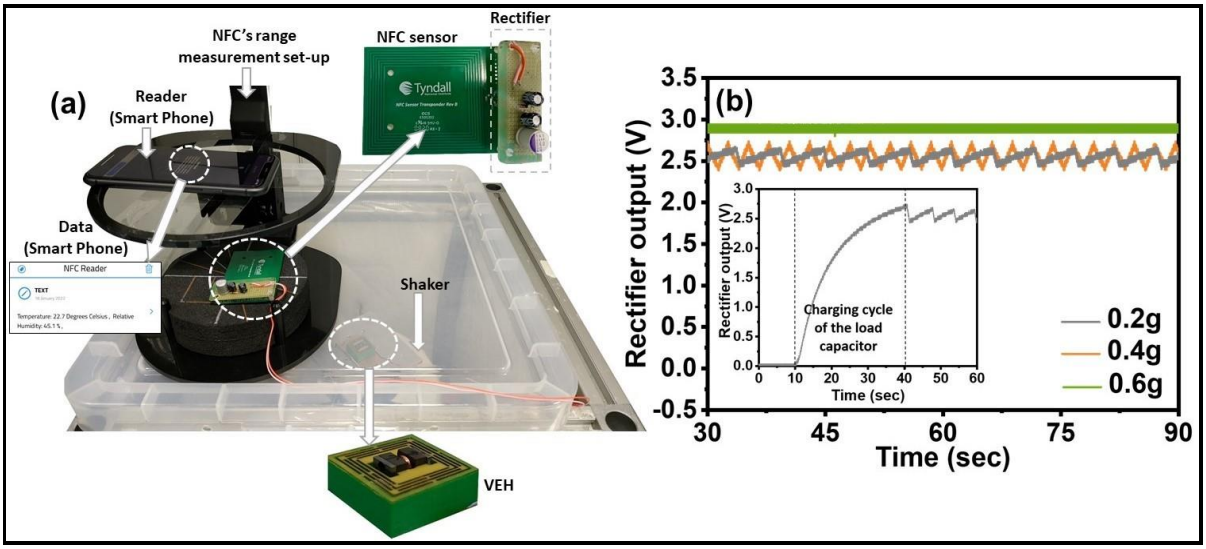


Figure 3.9: (a) The experimental set-up of employing the developed VEH to support the NFC sensor hardware. The VEH is placed on the shaker under the cover. (b) The variation of the rectified voltage across the load capacitor for different amplitudes of excitation of the VEH. The inset shows the fast charging cycle of the load capacitor used in this experiment.

Upon applying a harmonic excitation on the VEH at the resonant frequency (75Hz), the extracted electrical energy passes through the rectification stage and is stored into the load capacitor. Fig. 3.9(b) shows the variation of the rectified signal when the NFC sensor interface is connected to it as a load. We have selected this capacitor for its fast charging capability. The amplitudes of the excitation are varied from 0.2g to 0.6g that typically represents the amplitudes of vibrations that can be experienced on, for instance, clothes drying machine, blending machine, car dashboard [41, 42], etc. As shown in the inset of Fig. 3.9(b), the capacitor takes approximately 30s to charge from 0 to 2.66V, when such a low vibration amplitude of 0.2g is employed. Once the voltage input to the NFC sensor hardware exceeds 2.66V, the integrated low dropout voltage regulator (LDO) enters into the active state and provides a steady DC supply of 1.8V to the following circuitry consisting of the microcontroller and temperature-humidity sensor, along with the NFC radio transceiver. If the NFC reader (in this case a smartphone) is near the NFC sensor hardware, the data packet from the sensor is transmitted through the NFC radio to the reader. The energy drawn to facilitate this communication brings the voltage across the capacitor down from 2.66V to 2.4V, which puts the microcontroller, and the sensors back into off mode until the capacitor charges back to 2.66V. In the case of 0.2g

vibration, this occurs over a 4.7s time interval. This charging and discharging of the capacitor is reflected in the rectified voltage as ripples, as shown in Fig. 3.9(b).

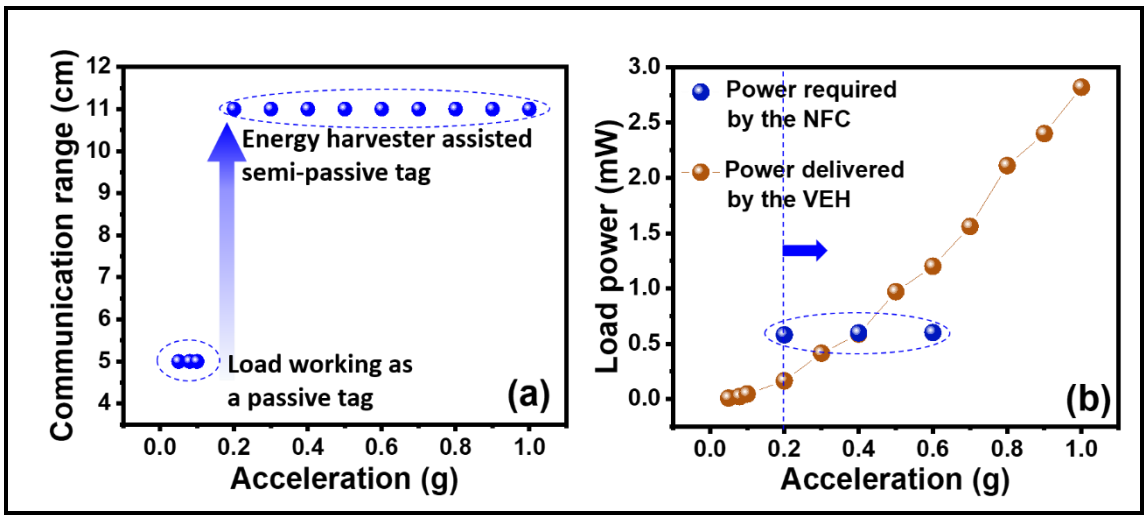


Figure 3.10: The variation of the power delivered by the VEH across the optimized load has been shown in (a) Demonstrates the communication range the NFC hardware provides as a function of the amplitude of excitation of the VEH. (b) The blue points show the power consumption of the NFC sensor hardware when the amplitude of excitation for the VEH changes from 0.2g to 0.6g.

As described in Section 3.5, for the conventional passive NFC tags, the energy received from the reader/smartphone by the tag loop antenna, which is translated into a regulated 1.8V DC, is partly employed to power the electronics in the NFC sensor hardware and partly for communicating (EPROM) the data-modulated signal back to the reader. The portion of power left for the latter then determines the strength of the load modulated signal or equivalently the communication range of the NFC tags. For the NFC sensor hardware used in this work, it provides a communication range of 5cm when not connected to any additional source of energy. In the case of the VEH assisted NFC tag, the VEH supplies the power required by the electronics. Therefore, the NFC sensor hardware can retain the RF power harvested from the reader fully for communicating back the sensing data-modulated signal to the reader and hence provides a larger communication range, i.e., 11cm or 120% improvement as shown in Fig. 3.10(a).

Figure 3.10(b) shows the variation of the deliverable power of the VEH as a function of the amplitude of excitation. The power required by the NFC sensor hardware to be fully functional is measured to be 597µW (shown by the blue dots). It is noticed that, with 0.2g drive amplitude, 164µW power can be extracted across the load resistance of 1kΩ. Such a low vibration is deemed sufficient to support the NFC sensor, leading to an increased

communication range, though with a longer capacitor charging time from 2.4V to the required 2.66V (see Fig. 3.9(b)). The obtainable energy from the VEH increases with increasing amplitude of the external excitation. Since a larger power of 598µW is delivered when the VEH is excited with 0.4g acceleration (matching the required power level of the NFC sensor hardware), the capacitor charges faster between 2.4V to 2.66V, shortening the charging time to 1.2s, as shown in Fig. 3.9(b), while extending the communication range up to 11cm. It is interesting to note that, by further increasing the amplitude of excitation, e.g. for 0.6g, the VEH provides substantial energy which drives the NFC sensor hardware interface autonomously, thereby implementing a sustainable power source to support the NFC hardware. In Fig. 3.9(b), the steady supply from the rectification stage (green line) indicates that the capacitor at this stage would no longer be required to store and supply energy to the circuitry associated with the NFC.

3.7 Comparison with the state-of-the-art VEHs and envisaged IoT application

A comparison of the performance of the developed VEH with state-of-the-art VEHs is presented in Table 3.3. The key parameters of comparison are the footprint (volume) of the VEH device used to power the wireless platform, the amplitude of excitation, the power density, which is a primary figure-of-merit (delivered power per unit volume per unit excitation) and the charge storage capacitor. The resonant electromagnetic generator presented in [43] has a large footprint of 123.75cm^3, which reduces the overall power density to only 25.8µW/cm3g^2. The electromagnetic and piezoelectric generator in [44] and [45] also have large device volume, and from the application perspective, these devices require large storage capacitors to power the target application. The piezoelectric transducer presented in [46] although generates large deliverable power, but the frequency of operation is very high (39,110Hz) and the electromagnetic transducer presented in [47] have high operation frequency (2840Hz) as well as high device volume (206cm^3) which makes it unsuitable for MEMS integration. The hybrid energy-harvesting device comprising of electromagnetic and triboelectric transducer in [48] offers a relatively smaller footprint while yielding large power density of 954.7µW/cm^{3}g^2, however, it still requires a storage capacitor to power the target electronics. On the other hand, the energy harvester presented in [49] requires a supercapacitor to store the charge deliver the required power to the target application node while the energy harvester supplies energy to the supercapacitor. The concertina-VEH presented in this chapter

on the other hand extracts mechanical energy from as low as 0.2g acceleration level, and with increased excitation, the harvested energy increases considerably such that it does not require any storage capacitor. This is a great benefit in terms of implementation and integration of the energy harvesting system with the rest of the electronics interface. The table 3.3 shows a comparison between these different transducers that have been mentioned above, in terms of the footprint, the developed VEH device outpaces all the rest of the devices. Additionally, the device starts to power the wireless sensor node at a very low level of acceleration, which makes this suitable for a wide range of IoT based application scenarios. The wireless communication system has also been developed and optimized carefully to minimize the power consumption so that the autonomous wireless platform with enhanced communication range is functional, even for weak vibrations. To the author's best knowledge, this work is a first of its nature presenting a detailed feasibility study of combining high efficiency vibration energy harvester with emerging NFC technology to implement a robust and sustainable wireless communication platform for IoT applications.

As demonstrated, the developed concertina-VEH is sensitive to low levels of vibrations, which enables this energy harvesting system to transduce mechanical energy even from the weak vibrations, opening up the scope for exploiting this benefit in some niche application areas. For example, in the context of industrial cleanroom environments, continuous monitoring of temperature and relative humidity, and maintaining their variation range between 18-21°C and 30-50% respectively is an imperative requirement for minimizing microbial growth, static charge build up, delicate equipment damage as well as for the user's comfort [50]. The Heating, Ventilation, and Air Conditioning (HVAC) units installed inside the cleanroom offers substantial mechanical energy distributed around the resonant frequency of the concertina-VEH [16, 51]. In the context of the above mentioned application scenario, the mechanical energy from HVAC system will be consistently available since the HVAC in a clean-room has to be operational all the time to keep the contaminants at a minimum, which ensures perpetual mechanical energy extraction through the concertina-VEH. This opens up the scope for installing the developed concertina-VEH on the HVAC systems, which would enable the harvester to generate substantial energy. The delivered power through the harvester could be employed to power the electronics interface of the NFC based sensor node, while enhancing the range of communication of the NFC node. Hence, the developed NFC sensor node could report on the vital physical parameters of the cleanroom environment while being

assisted through the concertina-VEH, which would harness mechanical energy from the ceiling HVAC units.

Table 3.3: Comparison of state-of-the-art harvesters and their performance with the developed VEH and wireless powering system

Ref.	Excitation (g)	Resonant frequency(Hz)	Volume (cm^3)	Delivered power (µW)	Power density ($\mu W/cm^3g^2$)	Communication protocol	Load capacitance (µF)
EM (resonant) [43]	~ 0.5	33	123.75	~ 800	25.8	Radio Transceiver Short-burst 2.4GHz proprietary	23.5
EM (resonant) [44]	3	6	420	119000	31.5	No demonstration with wireless sensor platform	680
PE (resonant) [45]	0.25	100	200	~ 4000	320	Radio Transceiver	500
PE (resonant) [46]	0.2	39,110	NA	~ 3800	NA	Radio Transceiver	100
EM (resonant) [47]	~ 0.5	28,40	~ 206	6500	126.2	No demonstration with wireless sensor platform	NA
EM+TE (resonant) [48]	0.6	4.5	~ 29.3	10070	954.7	Directly powered portable electronics	22
EM (resonant) [49]	0.73	13	~ 93	980	19.77	LoRaWAN and BLE	Supercapac -itor
This work	0.2	75	9	164	455.6	NFC	560
This work	0.6	75	9	1200	370.36	NFC	Not required

The presented concertina spring topology offers the unique scope of tuning the natural frequency of oscillation of the device by adding more stages of concertina springs. Such flexibility could be well exploited for niche application area such as harnessing mechanical energy from human body by scaling down the frequency, typically less than 10Hz, through additional stages of concertina springs. NFC sensor system could be implemented on flexible material [52, 53] for the ease of integration on human body. The concertina VEHs together with flexible NFC sensor system could implement a sustainable and robust wireless platform for human health monitoring. The successful demonstration of the developed concertina VEH supporting the constructed NFC sensor node also implies a possible avenue to implement the VEH for other types of wireless communication platform. This includes those based on the far-field communication (e.g., [54] and [55]) to allow for the development of sustainable and robust wireless sensing systems with an even higher communication range.

3.8 Conclusion

A battery-less Vibration Energy Harvester (VEH) assisted NFC (Near Field Communication) sensor node has been presented in this chapter. The resonant FR4 based VEH comprises interleaved springs that are connected in series, building a concertina shape that exhibits a large amplitude of displacement (2.5mm) within a small footprint of $9cm^3$ when subjected to external excitation. Owing to this enhanced out-of-plane compliance, the VEH offers a large power density of $455.6\mu W/cm^3g^2$ when operating at the resonance. This makes the concertina VEH a potential candidate for assisting the developed low power consuming NFC sensor node. With the VEH powering the electronic interface of the sensor node, the electromagnetic interaction between the transmitting antenna and the reader embedded in smartphone enhances which in turn brings a 120% improvement in the range of communication of this wireless sensor node. The excellent dynamic response of the concertina-VEH enables it to effectively harness mechanical energy even from weaker vibrations (e.g. 0.2g harmonic excitation). For lower amplitudes of excitation, a storage capacitor of 560µF has been used to provide a steady DC supply to the sensor interface. However, for moderate acceleration levels (0.6g), the concertina-VEH generates considerably large power (1.2mW), making the capacitor redundant for steadily powering the sensor electronics.

3.9 References

[1] D. R. Gawade *et al.*, "A Museum Artefact Monitoring Testbed using LoRaWAN," in *2021 IEEE Symposium on Computers and Communications (ISCC)*, 5-8 Sept. 2021 2021, pp. 1-3, doi: 10.1109/ISCC53001.2021.9631253.

[2] D. R. Gawade *et al.*, "A Smart Archive Box for Museum Artifact Monitoring Using Battery-Less Temperature and Humidity Sensing," *Sensors*, vol. 21, no. 14, 2021, doi: 10.3390/s21144903.

[3] C. Peres, M. Emam, H. Jafarzadeh, M. Belcastro, and B. O'Flynn, "Development of a low-power underwater nfc-enabled sensor device for seaweed monitoring," *Sensors*, vol. 21, no. 14, p. 4649, 2021.

[4] P. Escobedo, M. Bhattacharjee, F. Nikbakhtnasrabadi, and R. Dahiya, "Smart bandage with wireless strain and temperature sensors and batteryless NFC tag," *IEEE Internet of Things Journal*, vol. 8, no. 6, pp. 5093-5100, 2020.

[5] X. Qian, Z. Li, Z. Meng, N. Gao, and Z. Zhang, "Flexible RFID Tag for Sensing the Total Minerals in Drinking Water via Smartphone Tapping," *IEEE Sensors Journal*, vol. 21, no. 21, pp. 24749-24758, 2021.

[6] STMicroelectronics. "NFC / RFID, ST25 product overview." https://www.st.com/content/ccc/resource/sales_and_marketing/presentation/product_presentation/group1/a9/5d/77/96/be/9a/48/7e/ST25_NFC_RFID_product_overview/files/ST25_product_overview.pdf/jcr:content/translations/en.ST25_product_overview.pdf.

[7] D.R.Gawade, "A battery-less NFC sensor transponder for museum artefact monitoring-a review of NFC sensor technology and a proposed solution," in *IARIA*, 2019.

[8] P. Escobedo *et al.*, "Smart facemask for wireless CO2 monitoring," *Nature Communications*, vol. 13, no. 1, p. 72, 2022/01/10 2022, doi: 10.1038/s41467-021-27733-3.

[9] R. Raju, G. E. Bridges, and S. Bhadra, "Wireless Passive Sensors for Food Quality Monitoring: Improving the Safety of Food Products," *IEEE Antennas and Propagation Magazine*, vol. 62, no. 5, pp. 76-89, 2020, doi: 10.1109/MAP.2020.3003216.

[10] P. Escobedo *et al.*, "Flexible Passive near Field Communication Tag for Multigas Sensing," *Analytical Chemistry*, vol. 89, no. 3, pp. 1697-1703, 2017/02/07 2017, doi: 10.1021/acs.analchem.6b03901.

[11] C. Strangfeld, S. Johann, and M. Bartholmai, "Smart RFID Sensors Embedded in Building Structures for Early Damage Detection and Long-Term Monitoring," *Sensors*, vol. 19, no. 24, 2019, doi: 10.3390/s19245514.

[12] X. Hu, L. Xu, X. Lin, and M. Pecht, "Battery lifetime prognostics," *Joule*, vol. 4, no. 2, pp. 310-346, 2020.

[13] D. Grech, K. S. Kiang, J. Zekonyte, M. Stolz, R. J. K. Wood, and H. M. H. Chong, "Highly linear and large spring deflection characteristics of a Quasi-Concertina MEMS device," *Microelectronic Engineering*, vol. 119, pp. 75-78, 2014/05/01/ 2014, doi: https://doi.org/10.1016/j.mee.2014.02.016.

[14] D. Grech *et al.*, "A Quasi-Concertina force-displacement MEMS probe for measuring biomechanical properties," *Sensors and Actuators A: Physical*, vol. 275, pp. 67-74, 2018/06/01/ 2018, doi: https://doi.org/10.1016/j.sna.2018.03.031.

[15] Y. Zhao, X. Ling, Z. Wang, W. Gong, and G. Li, "Acceleration Frequency Characteristics of the Freight-Train-Induced Vibration of the Beijing-Harbin Railway Subgrade," *Shock and Vibration*, vol. 2020, 2020.

[16] G. Iannace, G. Ciaburro, and A. Trematerra, "Heating, ventilation, and air conditioning (HVAC) noise detection in open-plan offices using recursive partitioning," *Buildings*, vol. 8, no. 12, p. 169, 2018.

[17] P. Podder, A. Amann, and S. Roy, "A bistable electromagnetic micro-power generator using FR4-based folded arm cantilever," *Sensors and Actuators A: Physical*, vol. 227, pp. 39-47, 2015/05/15/ 2015, doi: https://doi.org/10.1016/j.sna.2015.03.043.

[18] G. Hatipoglu and H. Ürey, "FR4-based electromagnetic energy harvester for wireless sensor nodes," *Smart Materials and Structures*, vol. 19, no. 1, p. 015022, 2009/12/14 2009, doi: 10.1088/0964-1726/19/1/015022.

[19] Y. Li, J. Li, A. Yang, Y. Zhang, B. Jiang, and D. Qiao, "Electromagnetic vibrational energy harvester with microfabricated springs and flexible coils," *IEEE Transactions on Industrial Electronics*, vol. 68, no. 3, pp. 2684-2693, 2020.

[20] D. Mallick, A. Amann, and S. Roy, "High figure of merit nonlinear microelectromagnetic energy harvesters for wideband applications," *Journal of Microelectromechanical Systems*, vol. 26, no. 1, pp. 273-282, 2016.

[21] S. Sun, X. Dai, Y. Sun, X. Xiang, G. Ding, and X. Zhao, "MEMS-based wide-bandwidth electromagnetic energy harvester with electroplated nickel structure," *Journal of Micromechanics and Microengineering*, vol. 27, no. 11, p. 115007, 2017.

[22] F. Khan, F. Sassani, and B. Stoeber, "Copper foil-type vibration-based electromagnetic energy harvester," *Journal of Micromechanics and Microengineering*, vol. 20, no. 12, p. 125006, 2010.
[23] P. Wang, K. Tanaka, S. Sugiyama, X. Dai, X. Zhao, and J. Liu, "A micro electromagnetic low level vibration energy harvester based on MEMS technology," *Microsystem technologies*, vol. 15, no. 6, pp. 941-951, 2009.
[24] Z. Yang, N. Ismail, C. Son, P. M. Ferreira, and S. Kim, "Broadband, tunable, miniaturized vibration energy harvester using nonlinear elastomer beams and stretchable interconnects," *Advanced Materials Technologies*, vol. 4, no. 12, p. 1900783, 2019.
[25] G. Aldawood, H. T. Nguyen, and H. Bardaweel, "High power density spring-assisted nonlinear electromagnetic vibration energy harvester for low base-accelerations," *Applied Energy*, vol. 253, p. 113546, 2019/11/01/ 2019.
[26] G. Aldawood, H. T. Nguyen, and H. Bardaweel, "High power density spring-assisted nonlinear electromagnetic vibration energy harvester for low base-accelerations," *Applied Energy*, vol. 253, p. 113546, 2019/11/01/ 2019, doi: https://doi.org/10.1016/j.apenergy.2019.113546.
[27] "Ansys Maxwell Low Frequency EM Field Simulation." https://www.ansys.com/products/electronics/ansys-maxwell.
[28] "Structural Mechanics Module." https://www.comsol.com/structural-mechanics-module.
[29] S. P. Beeby *et al.*, "A micro electromagnetic generator for vibration energy harvesting," *Journal of Micromechanics and Microengineering*, vol. 17, no. 7, pp. 1257-1265, 2007/06/05 2007, doi: 10.1088/0960-1317/17/7/007.
[30] P. White and M. Roland, "Near Field Communication (NFC) Technology and Measurements White Paper."
[31] S. Popli, R. K. Jha, and S. Jain, "A survey on energy efficient narrowband internet of things (NBIoT): architecture, application and challenges," *IEEE Access*, vol. 7, pp. 16739-16776, 2018.
[32] "Datasheet: Quectel BC95-G Multi-band NB-IoT Module with Ultra-low Power Consumption " https://www.quectel.com/wp-content/uploads/pdfupload/Quectel_BC95-G_NB-IoT_Specification_V1.9.pdf.
[33] "STMicroelectronics, "S2-LP Ultra-low power, high performance, sub1 GHz transceiver." " https://www.st.com/en/wireless-connectivity/s2-lp.html.
[34] "Datasheet: Sub-G Module Data Sheet CMWX1ZZABZ-078 " https://content.arduino.cc/assets/mkrwan1310-murata_lora_module-type_abz.pdf.
[35] T. Instruments. "CC3200 SimpleLink Wi-Fi and Internet-of-Things Solution, a Single-Chip Wireless MCU." https://www.ti.com/lit/ds/symlink/cc3200.pdf?ts=1645017142783&ref_url=https%253A%252F%252Fwww.ti.com%252Fproduct%252FCC3200.
[36] L. C. Antonio. "Zolertia RE-Mote." https://github-wiki-see.page/m/Zolertia/Resources/wiki/RE-Mote.
[37] Z. Jianyong, L. Haiyong, C. Zili, and L. Zhaohui, "RSSI based Bluetooth low energy indoor positioning," in *2014 International Conference on Indoor Positioning and Indoor Navigation (IPIN)*, 2014: IEEE, pp. 526-533.
[38] "Nordic Semiconductor, "nRF52840, Product Specification."." https:// infocenter.nordicsemi.com/pdf/nRF52840 PS v1.2.pdf.
[39] S. Filiz and U. Yunus, "A Comparative Study: Voltage Multipliers for Rf Energy Harvesting System," *Communications Faculty of Sciences University of Ankara Series A2-A3 Physical Sciences and Engineering*, vol. 61, no. 1, pp. 12-23, 2019.
[40] S. S. Chouhan, M. Nurmi, and K. Halonen, "Efficiency enhanced voltage multiplier circuit for RF energy harvesting," *Microelectronics Journal*, vol. 48, pp. 95-102, 2016/02/01/ 2016, doi: https://doi.org/10.1016/j.mejo.2015.11.012.
[41] S. Roundy, P. Wright, and J. M. Rabaey, "A Study of Low Level Vibrations as a Power Source for Wireless Sensor Nodes," *Computer Communications*, vol. 26, pp. 1131-1144, 07/01 2003, doi: 10.1016/S0140-3664(02)00248-7.
[42] D. Bhatia *et al.*, "Continuous scavenging of broadband vibrations via omnipotent tandem triboelectric nanogenerators with cascade impact structure," *Scientific Reports*, vol. 9, no. 1, p. 8223, 2019/06/03 2019, doi: 10.1038/s41598-019-44683-5.
[43] O. Rubes, J. Chalupa, F. Ksica, and Z. Hadas, "Development and experimental validation of self-powered wireless vibration sensor node using vibration energy harvester," *Mechanical Systems and Signal Processing*, vol. 160, p. 107890, 2021/11/01/ 2021, doi: https://doi.org/10.1016/j.ymssp.2021.107890.
[44] M. Gao, P. Wang, Y. Cao, R. Chen, and D. Cai, "Design and Verification of a Rail-Borne Energy Harvester for Powering Wireless Sensor Networks in the Railway Industry," *IEEE Transactions on Intelligent Transportation Systems*, vol. 18, no. 6, pp. 1596-1609, 2017, doi: 10.1109/TITS.2016.2611647.

[45] E. K. Reilly, F. Burghardt, R. Fain, and P. Wright, "Powering a wireless sensor node with a vibration-driven piezoelectric energy harvester," *Smart Materials and Structures*, vol. 20, no. 12, p. 125006, 2011/11/14 2011, doi: 10.1088/0964-1726/20/12/125006.

[46] S. Lee, B. D. Youn, and B. C. Jung, "Robust segment-type energy harvester and its application to a wireless sensor," *Smart Materials and Structures*, vol. 18, no. 9, p. 095021, 2009.

[47] M. Perez, S. Chesné, C. Jean-Mistral, K. Billon, R. Augez, and C. Clerc, "A two degree-of-freedom linear vibration energy harvester for tram applications," *Mechanical Systems and Signal Processing*, vol. 140, p. 106657, 2020/06/01/ 2020, doi: https://doi.org/10.1016/j.ymssp.2020.106657.

[48] M. Salauddin, R. M. Toyabur, P. Maharjan, and J. Y. Park, "High performance human-induced vibration driven hybrid energy harvester for powering portable electronics," *Nano Energy*, vol. 45, pp. 236-246, 2018/03/01/ 2018, doi: https://doi.org/10.1016/j.nanoen.2017.12.046.

[49] J. C. Rodriguez, V. Nico, and J. Punch, "A Vibration Energy Harvester and Power Management Solution for Battery-Free Operation of Wireless Sensor Nodes," *Sensors*, vol. 19, no. 17, 2019, doi: 10.3390/s19173776.

[50] T. Sandle. "A Humidex For The Cleanroom: Why Temperature And Humidity Control Matters." https://www.ivtnetwork.com/article/humidex-cleanroom-why-temperature-and-humidity-control-matters#:~:text=The%20appropriate%20range%20for%20cleanroom,influence%20the%20main%20risk%20factors.

[51] Y. Hu and Y. Xu, "A wideband vibration energy harvester based on a folded asymmetric gapped cantilever," *Applied Physics Letters*, vol. 104, no. 5, p. 053902, 2014, doi: 10.1063/1.4863923.

[52] A. Noda, "Wearable NFC Reader and Sensor Tag for Health Monitoring," in *2019 IEEE Biomedical Circuits and Systems Conference (BioCAS)*, 17-19 Oct. 2019 2019, pp. 1-4, doi: 10.1109/BIOCAS.2019.8919200.

[53] M. Zulqarnain *et al.*, "A flexible ECG patch compatible with NFC RF communication," *npj Flexible Electronics*, vol. 4, no. 1, p. 13, 2020/07/15 2020, doi: 10.1038/s41528-020-0077-x.

[54] S. N. R. Kantareddy, I. Mathews, R. Bhattacharyya, I. M. Peters, T. Buonassisi, and S. E. Sarma, "Long range battery-less PV-powered RFID tag sensors," *IEEE Internet of Things Journal*, vol. 6, no. 4, pp. 6989-6996, 2019.

[55] A. Sharif *et al.*, "Low-cost inkjet-printed UHF RFID tag-based system for internet of things applications using characteristic modes," *IEEE Internet of Things Journal*, vol. 6, no. 2, pp. 3962-3975, 2019.

Chapter 4: Tapered Nonlinear Vibration Energy Harvester for Powering Internet of Things

This chapter is based on the following publication- K. Paul, A. Amann, S. Roy, "Tapered nonlinear vibration energy harvester for powering Internet of Things", Applied Energy, vol. 283, 2021, pp. 116267, 2019.

4.1 Introduction

In this chapter, we design, develop and demonstrate high power density nonlinear wideband energy harvesters using novel tapered spring architectures in an autonomous wireless sensor node system. These spring structures exhibit a nonlinear restoring force arising from the atypical stress distribution that can be additionally tuned by changing the taper-ratio in the structure. We investigate different tapering designs in order to achieve optimal spring hardening nonlinearities. This nonlinearity aids in widening the operable bandwidth, making the harvesters suitable for scavenging energy from real-world broadband vibrations. We obtain power densities of the order of $2660\mu W/cm^3g^2$ in the nonlinear energy harvester, outpacing most contemporary energy scavengers. We present a modified Perturb and Observe algorithm that allows tracing of the maximum power point in the context of non-stationary vibration conditions. We use the fabricated nonlinear device to power a wireless sensor node that reports on vital physical parameters (humidity, temperature), thereby enabling a resilient remote data acquisition system. This demonstrates the potential of our design to provide a sustainable energy source for platforms within the Internet of Things.

4.2 Technology gap and a potential solution

The majority of the reported VEHs involve a linear spring-mass resonator architecture, which offers a narrow bandwidth of operational frequencies. This is suitable for narrowband and stationary excitations [1, 2]. However, real-world vibration may possess a broadband spectrum with one or more peaks, which may change in amplitude or frequency over time. Hence, there has been substantial research to develop strategies to broaden the operable frequency range of VEHs. Kim *et al.* reported a two degree-of-freedom VEH that is designed to extract and convert the mechanical energy both from translational and rotational motion [3]. Owing to the multiple resonant peaks arising from the different degrees-of-freedom, it exhibits a substantially increased frequency bandwidth compared to traditional single degree-of-freedom systems. Song *et al.* designed an array of magnetically coupled piezoelectric beams possessing gradually varying resonant frequencies, which helped in transducing the mechanical energy into

electrical energy over a broader frequency range [4]. Arrangements of external magnets have also been used to facilitate bidirectional frequency tuning by exploiting the attractive and repulsive forces between the magnets [5]. Zhao *et al.* presented an aeroelastic VEH [6] which extracts and converts energy both from mechanical vibrations and wind flow. The mechanical stopper integrated with this harvester aids in broadening the operable bandwidth by coupling the excitation frequencies coming from wind flow and external vibrations. Despite all the above-mentioned strategies, the additional beams, stoppers and external magnets increase the overall footprint of the device, which restricts its practical applicability. Therefore, a simple but efficient method to increase the bandwidth of VEHs by using nonlinear spring structures has been investigated recently [7]. This allows for the design of a suitable potential profile [8, 9] that is capable of harvesting energy over a desired frequency range, while maintaining a small footprint. Monostable [10-13] and bi-stable [14-17] oscillators are commonly used for energy harvesting, exhibiting single and double potential wells respectively. Here we focus on the monostable variant, which offers dynamic flexibility that helps in tuning the overall harvester performance along with simplicity in implementation [18, 19].

The monostable nonlinearity has been incorporated into the energy harvesters by means of magnetic interaction [20, 21]. However, in these structures, the prerequisite of external magnets adds complexity to its implementation. The impetus towards maximizing the scavenged energy output from a small footprint (similar to that of a sensor node) has driven the research towards enhancing the performance of the VEH by modifying the associated geometries. Clamped-Clamped and Clamped-guided spring architectures have been widely used in the field of nonlinear vibration energy harvesting. Electromagnetic [11] and piezoelectric [10] transduction mechanisms have both been used, in which the nonlinearity arises from the cubic restoring force associated with the stretching of the thin spring arms as a consequence of large deformation. However, the degree of nonlinearity mostly relying on the thickness of the thin suspension structure leaves very little scope for alteration of the same with small geometrical manipulation without compromising the structural stability. Over the past decade, linearly and exponentially tapered cantilever structures have been widely employed [22, 23] for the implementation of piezoelectric vibration energy harvesters. This type of geometry offers the unique liberty of tailoring and optimizing the length to base width ratio and the degree of tapering [24] to control the stress distribution, which in turn improves the performance of the harvester. Combining the advantages of both geometrical manoeuvring approaches, in this work we employ tapered fixed-guided spring structures that demonstrate a strong nonlinear restoring force arising from stretching in addition to bending at a high

amplitude of oscillation. The tapering in the spring architecture additionally allows for tuning the degree of nonlinearity by utilizing the atypical stress distribution of such geometrical structures. This enhances the power density of the VEH substantially when compared to the traditional system. The objective of this work is to explore the potential of tapered nonlinear vibration energy harvesters as a sustainable source of energy for powering the WSNs, which are an indispensable component of the IoT platform.

In this chapter, we investigate the performance of two such Electromagnetic Vibration Energy Harvesters (EM-VEH) employing FR4 (Flame Retardant 4) based tapered spring structures. Although the spring stretching based nonlinearity have been explored in the domain of mechanical energy harvesting, however exploring tapered geometries to implement this effect is relatively unexplored. A novel geometry is used to incorporate a stretching-strain based spring hardening nonlinearity into the vibration energy harvesting system. The selection of this geometry allows tailoring the nonlinearity without majorly relying on altering the thickness of the spring. Section 4.3 outlines the design considerations and fabrication of the harvester prototypes P1 (two tapered spring arms) and P2 (four tapered spring arms). The open circuit and the load performance of the harvesters are evaluated and discussed in Section 4.4, along with a comparison of their performance with devices previously reported in the literature. Section 4.5 deals with the development of a complete vibration energy harvesting system. In that section, we investigate the Maximum Power Point Tracking (MPPT) of such nonlinear energy harvesters. Lastly, we demonstrate the powering of a Wireless Sensor Node (Cypress IoT kit) through one of the fabricated harvester prototype, which could potentially open the path for the implementation of a battery-less WSN for perpetual condition monitoring in a wide range of applications. For example, the food and pharmaceutical industry demands a continuous monitoring of the product quality during transport, which could be enabled through such a device.

4.3 Modelling, parameter selection and fabrication of the EMVEH

4.3.1 Design and fabrication of the EMVEH

The alteration of the degree of nonlinearity in the conventional fixed-guided spring architecture is difficult because it depends critically on the thickness of the spring arms [11]. Moreover, the frail link to the load end in these structures allows additional degrees of freedom associated with torsion and rotation, as well as the desired out-of-plane movement. When subjected to a large amplitude of vibration, the thin springs are prone to get damaged owing to these motions.

In this context, the trapezoidal spring structure opens up the scope for easy alteration of the strain and stress distribution by modifying the proportion of tapering. These architectures not only offer easier alteration of the degree of nonlinearity as compared with traditional springs, but also the broad fixed ends of the trapezoidal section help in restricting the additional degrees of freedom of motion.

At the outset of this section, we will demonstrate how the degree of tapering influences the stress distribution in a fixed-guided spring architecture and later we will evaluate the performance of two nonlinear VEH prototypes, which employ a set of tapered spring arms. Fig.4.1 shows four different spring architectures where the tapering of spring arms has been gradually increased. The width of the spring arm reduces linearly towards the load end with a rate $\delta = (w_1 - w_2)/L_1$ where, w_1 and w_2 are the widths of the trapezoidal section at the fixed end and the load end respectively. In the structure, L_1 and L_3 are the lengths of the tapered section and L_2 is the width of the central stage holding the mass. The width of the spring at a point can be then expressed as-

$$\boldsymbol{w(x)} = \begin{cases} \boldsymbol{w_1 - \delta x, 0 \le x \le L_1} \\ \boldsymbol{w_1 - \delta(L_1 + L_2 + L_3 - x), (L_1 + L_2) \le x \le L_1 + L_2 + L_3} \\ \boldsymbol{w_2, L_1 \le x \le L_1 + L_2} \end{cases} \tag{4.1}$$

The degree of tapering plays an important role in influencing the aerodynamical behaviour of aircraft wings. Generally, the proportion of taper in such a structure is quantified as the taper ratio [34], which is the ratio of the length of the tip to the base of the wing. We have employed the taper ratio as the parameter to quantify the degree of tapering and to study its effect on the stress distribution of the spring under consideration.

$$\boldsymbol{Taper\ ratio = \beta = \frac{w_2}{w_1}} \tag{4.2}$$

In this study, we have considered four different spring architectures, where the taper ratio is gradually decreased from 1 to 0.17, keeping the length of the broad end and the total length of the springs fixed. The spring has a thickness of 0.25mm. We employed the Solid Mechanics physics interface with the Structural Mechanics module of COMSOL multiphysics to simulate the stress distribution along the length of the springs and to study the variation of the displacement with the applied force for each of the tapered structures. The springs are fixed at the broader end and the rest of the structure is allowed to vibrate on external excitation. A boundary load is applied to the mass attached to the central part of the spring. We have used a

'user-controlled mesh' with maximum and minimum element sizes of 3.5mm and 0.63mm respectively, and the maximum element growth rate was 1.5. First, we employed a stationary study and included the 'geometric nonlinearity' to find the stress distribution along the line of symmetry of the spring structure, as shown in Fig. 4.1. Subjected to similar load conditions, the stress rises steeply with increased tapering of the spring at the load end for out-of-plane motion. Fig.4.1(f) reveals the variation of the stress distribution along the line of symmetry of each architecture. The narrow beam width at the load end enhances the stress (force per unit area) as compared to the rectangular spring. To show the effect of tapering on the degree of nonlinearity, we used the parametric sweep tool in COMSOL to apply a varying load to the structure and recorded the corresponding displacement of the tapered end. Fig. 4.1(e) reveals the relation between the displacement and the applied force which appears due to the combined effect of bending and stretching of the spring. Up to 0.2mm of deflection, the spring stiffness is approximately linear; beyond this, the nonlinear nature of the spring stiffness comes into play. The degree of nonlinearity enhances as the taper-ratio is gradually reduced. The atypical stress distribution, along with the low thickness of the springs, aids in inducing such a nonlinear restoring force into the system.

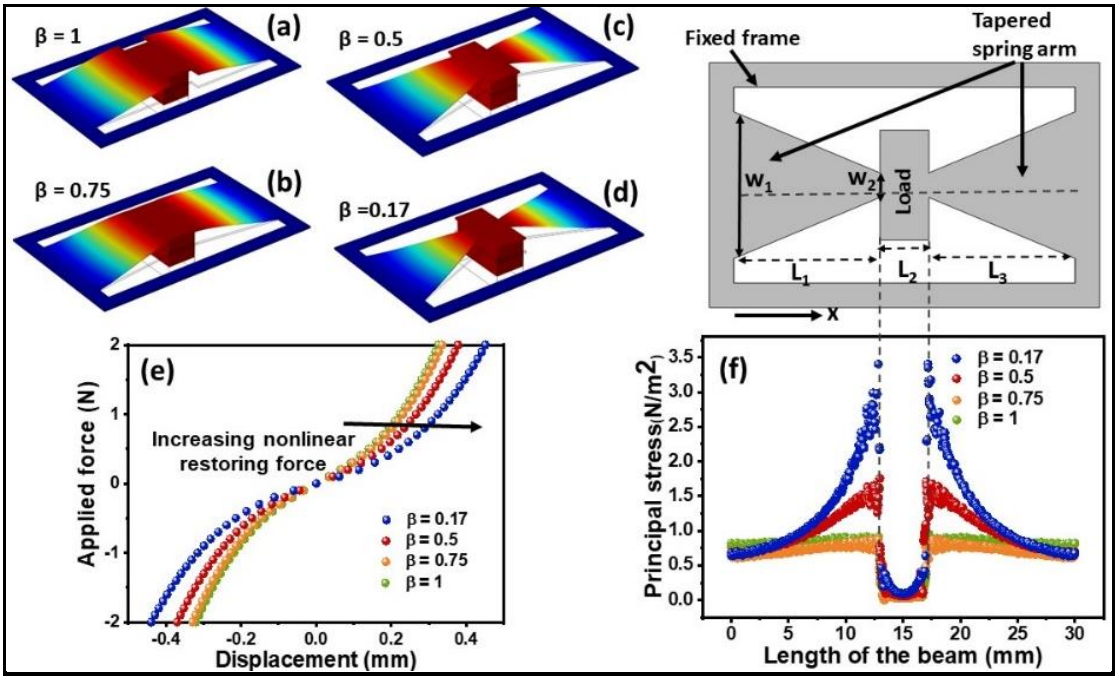


Figure 4.1: Tapered FR4 spring architecture with spring arms having (a) 1 (b) 0.75 (c) 0.5 (d) 0.17 taper ratio and the variation of their (e) nonlinear restoring force, (f) principal stress distribution along the length of the beam is shown.

Two VEH prototypes have been designed to exploit this atypical stress distribution, which could potentially induce the stretching based strain when the spring vibrates and undergoes large deflection in the out-of-plane motion. The detailed schematic of both the prototypes is shown in Fig.4.2. Structure P1 has dimensions 35mm × 19mm × 0.25mm and the structure P2 is 38mm × 26.3mm × 0.25mm. Each structure is fixed at the outer frame and the rest of it is free to move on vibration (Fig. 4.4). A central stage (8.3mm × 10.4mm) which is dedicated for the assembly of the magnets is held by a couple of slotted tapered spring structure in P1 (each has a broad end of width 8.6 mm and the narrow end is 4.3mm) and four such springs are used in P2. In the spring structure P2, the four tapered spring arm fixes the entire spring geometry more rigidly to the stationary outer frame, which further reinforces the spring to exhibit cubic nonlinearity for larger deflection arising from the stretching of these four spring arms. Hence, subjected to external excitation, such spring geometry aids to escape bending that involves linear spring force-displacement variation, rather strengthens stretching which induces strong nonlinearity into the system. On the other end, the spring geometry P2 also helps to promote the desired large out-of-plane displacement while supresses other degrees of freedom, which has been discussed later in this section. The taper-ratio of 0.5 has been selected here by optimizing the structural stability and the desired out-of-plane modes of vibrations within the low frequency range. The grids in both of the spring design have been included with the motivation of increasing the stress (= force/area) by reducing the effective area that the force acts on, also the grids aids to reduce the effect of air drag on the damping of the spring motion. An 8mm × 2mm slot is left at the centre for the vertical arrangement of the coil. The two spring structures have been laser micro-machined on 250µm thick FR4 sheets. FR4 is a grade of 'Flame retardant' low-cost anisotropic material, which is popularly used in printed circuit boards. It has been used as the material for the fabrication of the nonlinear spring structures owing to its low Young's modulus (typically 22GPa) that aids in reducing the frequency of oscillation of the device, making it more efficient in scavenging a significant fraction of the mechanical energy, which is distributed mostly in the low frequency range [25].

The magnet assembly comprises four high energy density sintered NdFeB N50 (8mm × 4mm × 2mm) magnets along with a couple of soft magnetic (steel keeper) blocks (8mm × 4.2mm × 1.6mm) arranged to create a closed magnetic flux path, thereby intensifying the flux density in a precise location [1] (Fig. 4.3). They are epoxy bonded to the central platform of P1 and P2, which is specifically designed for them. The enamelled wire-wound copper coils of 1mm inner diameter, 6mm outer diameter and 2500 turns have been fixed vertically to the base

platform through a rigid 3D printed structure. The resistances of the coils used with P1 and P2 are 1022Ω and 1046Ω, respectively. The electromagnetic interaction due to the out-of-the-plane displacement of the moving magnets with respect to the static coil has been studied with the Ansys Maxwell finite element analysis tool [8]. The resulting values of the electromagnetic coupling coefficient (γ) are 14.1Wb/m and 14.3Wb/m for P1 and P2, respectively.

The Solid Mechanics interface of the COMSOL Multiphysics platform has been used to perform finite element analysis of the conceived energy harvester units. The first few eigen-modes of P1 are at 81Hz, 108Hz and 351Hz, where the first one is responsible for the out-of-plane motion and the latter two correspond to the sideways tilt and flip respectively (Fig. 4.4(a)). The first few eigen-modes for P2 at 90Hz, 167Hz and 385Hz (Fig.4.4(b)) demonstrate similar dynamics to P1. It should be noted here that the four-arm geometry of spring structure P2 as explained before aids in promoting the desired large out-of-plane deflection, and at the same time restricts the other degrees of motion arising from twist, tilt and rotational motion. As can be observed from this analysis, the separate between the first two modes for P1 is only 27Hz, but that for the spring P2 is 77Hz. Hence, clearly the spring geometry in P2 helps in separating the higher order modes, which would benefit the overall performance of the energy-harvesting unit. Under small displacement, the restoring force of these springs mostly reflects the bending of the structures, until the displacement exceeds the thickness of beams. Beyond this displacement, it shows stretching induced nonlinear behaviour and the spring stiffness involves both bending and stretching components. The resulting nonlinearity is portrayed in Fig.4.4 for the first two modes. Figs. 4.4(a) and (b) also present the experimentally obtained force-displacement relationship of the FR4 spring structures; the details of the experiment and further analysis are presented in following sections. The linear (k) and nonlinear (k_n) spring stiffness coefficients obtained from the stationary analysis of the 0.25mm thick structures P1 and P2 are 1298 N/m and 10×10^9 N/m^3, 2130 N/m and 21×10^9 N/m^3 respectively. The degree of nonlinearity could be further enhanced by reducing the thickness of the structure, allowing a higher amplitude of displacement, but the stationary analysis reveals structural instabilities owing to the gravitational pull for lower thickness of FR4 spring structures. Hence, the optimized thickness of 0.25mm has been chosen in this case to bring nonlinear effects into the system without compromising the structural integrity.

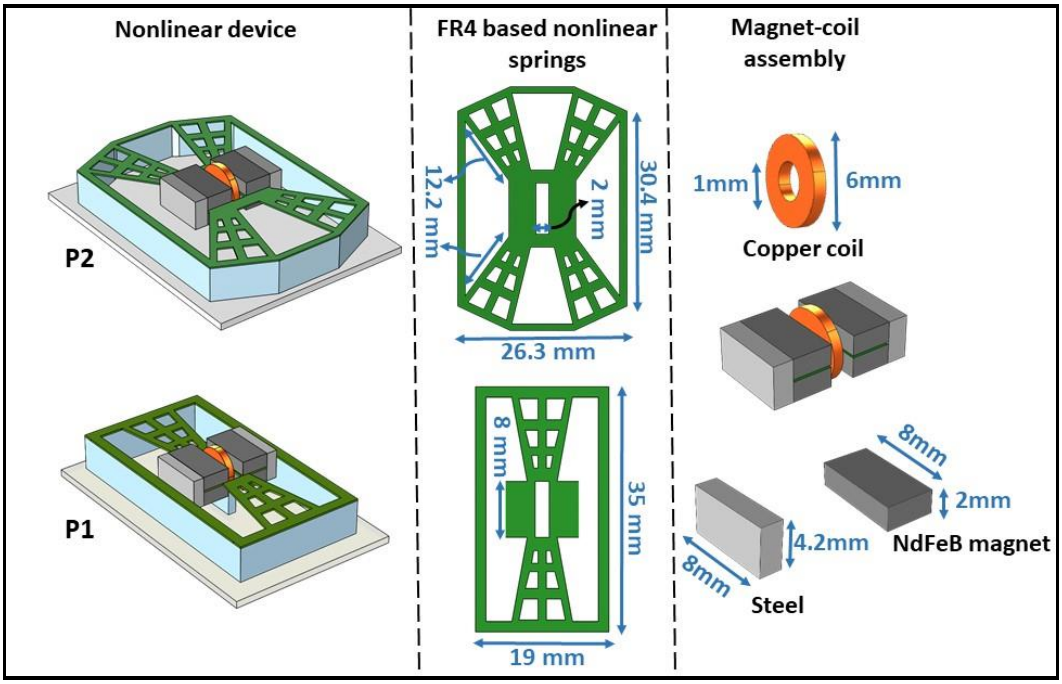


Figure 4.2: Detailed schematic of the prototypes P1 and P2.

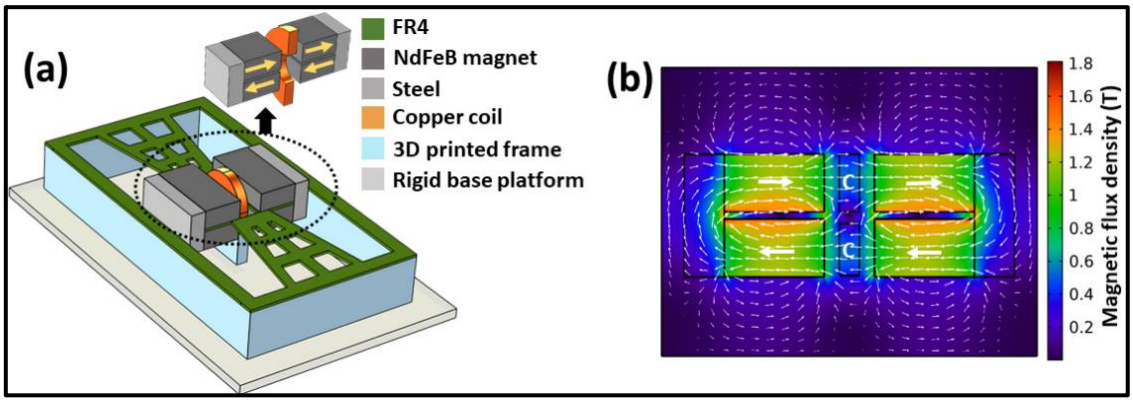


Figure 4.3: (a) Schematic of the prototype P1, (b) Schematic and direction of magnetization in the coil-magnet assembly of P1.

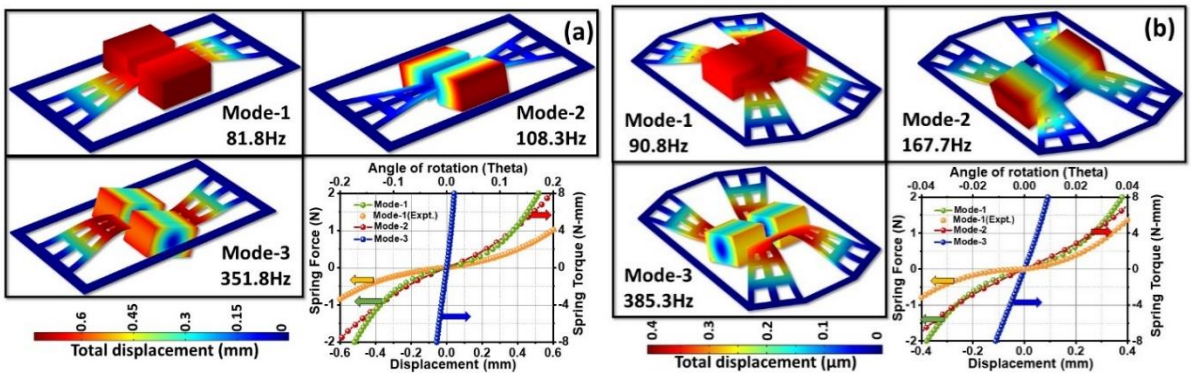


Figure 4.4: Finite element analysis of the spring structures depicting different modes of P1 (a) and P2 (b). The variation of the spring force with the amplitude of displacement corresponding

to mode-1 and the variation of spring torque with angle of rotation corresponding to mode-2, 3 have been shown. Experimentally obtained force-displacement corresponding to Mode-1 is shown (in orange).

4.3.2 Dynamical analysis

The governing equation of the electromechanical oscillator that exhibits electromagnetic transduction can be approximated by [17, 26],

$$\boldsymbol{m\ddot{x} + c_m\,\dot{x} + \frac{\partial U(x)}{\partial x} + \gamma I = -m\ddot{z}} \tag{4.3}$$

Where m is the mass of the system, c_m is the mechanical damping factor, $\frac{\partial U(x)}{\partial x}$ is the total spring force associated with the system, I is the induced current in the coil and γ is the electromagnetic coupling factor. The system is subjected to an external excitation $\ddot{z}$ causing displacement of the form $z = Z_0\,sin(\omega t)$.

In this work, we are considering a monostable oscillator with Duffing potential $U(x)$ that involves the energy stored in the spring due to bending $U_b(x) = \frac{1}{2}kx^2$ and stretching $U_s(x) = \frac{1}{4}k_n x^4$, where, k and k_n are the linear and non-linear spring stiffness coefficients. For the sake of simplicity, we limit our analysis to cubic nonlinearity only, hence the higher order terms have not been considered here. The electrical energy is extracted across a suitable load (resistive) R_L, and then the external conversion circuit involving the coil resistance R_c, inductance L can be modelled using Kirchhoff's voltage law as,

$$\boldsymbol{L\dot{I} + (R_c + R_L)I = \gamma\dot{x}} \tag{4.4}$$

Neglecting the effect of L at low frequencies and using the equations (4.3) and (4.4) above, the electrodynamical representation of the oscillator takes the form,

$$\boldsymbol{m\ddot{x} + \left(2m\rho\omega + \frac{\gamma^2}{R_c+R_L}\right)\dot{x} + kx + k_n x^3 = m\omega^2 Z_0\,sin(\omega t)} \tag{4.5}$$

Where ρ is the mechanical damping coefficient. This equation has been numerically solved with the fourth-order Runge-Kutta method using mathematical tools of MATLAB to find the voltage and power in the open-circuit (Fig. 4.6(c) and (d)) and closed circuit (Fig. 4.7(c) and (d)) configurations. The results are compared with the experimental findings and are explained in the Experimental Methods, Results and Discussion section.

4.4 Experimental methods, results and discussion

4.4.1 Spring stiffness measurements

To experimentally verify the force-displacement relationship of the fabricated FR4 springs, we have used the mechanical test system 'Instron 5565' (Fig.4.5) and subjected the devices to compressive load. The test set-up consists of a load frame that holds the crosshead, which moves up or down when tensile or compressive load is applied on the specimen. For this test we used a load cell that is capable of delivering up to 500N compressive force on the device under test through the attached fixtures. The load cell converts the measured load into electrical signal and the Bluehill software linked with Instron displays this load along with the corresponding displacement. To ensure better accuracy, the load frame is displaced at a slow speed of 1mm/min. Since we have only used this set-up for compressive loads, to emulate the effect of the tensile force on the device, we have subjected the opposite side of the device to similar compressive load condition. The obtained force-displacement considering the out-of-plane movement of the FR4 springs has been shown in Fig. 4.4(a) and (b). The linear and nonlinear spring stiffness coefficient are 705.5N/m, 2.5×10^9N/m^{3}and 775.8N/m, 13.1×10^9N/m^{3}for P1 and P2 respectively. The discrepancy between the experimental data and those obtained from the model can be attributed to the following factors. First, in the model we have considered nominal thickness of 0.25mm of the FR4 springs, whereas in practice there is a possibility of thickness variation in the FR4 sheet. Second, the anisotropic nature of the FR4 material is not taken into account in the model, which would have reasonable effect on the spring stiffness. Third, the experimentally obtained value of the linear spring stiffness coefficient is lower than those of the model. This is due to the fact that, the structures with which the FR4 springs are fixed to the base platform are considered to have infinite stiffness in the model but in practical application the 3D printed fixtures are not infinitely rigid. The stiffness coefficients are employed in the dynamical model to predict the frequency response of the system in both the closed and open circuit condition.

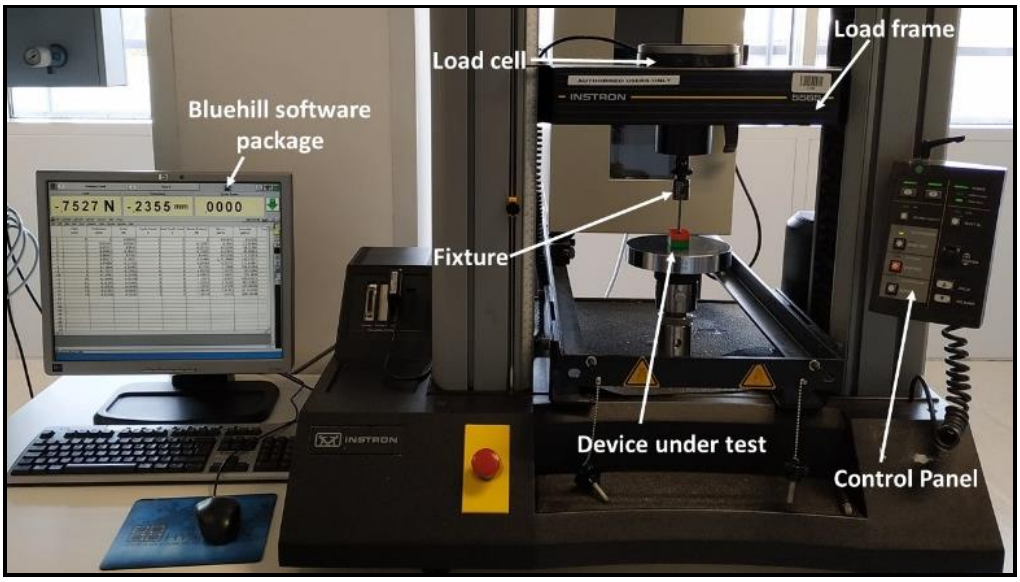
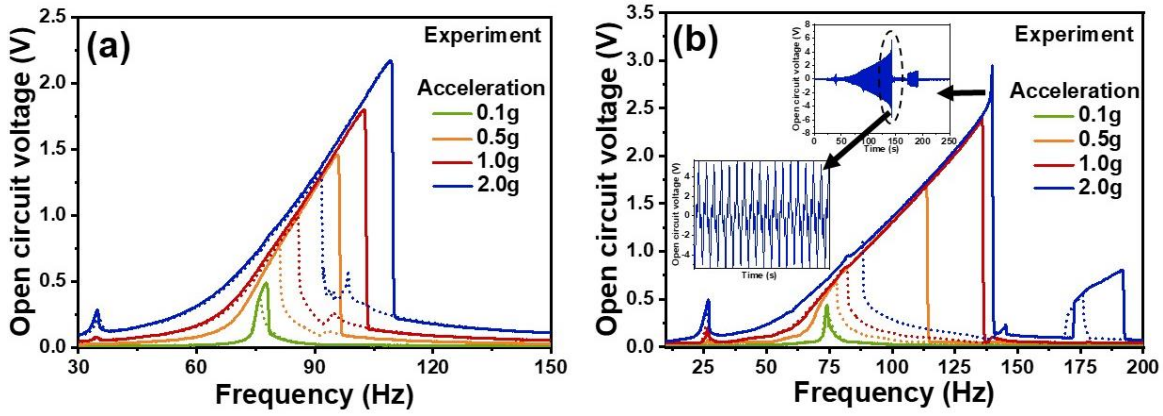


Figure 4.5: The Instron test set-up for the measurement of force-displacement relationship of the FR4 spring structure.

4.4.2 Open circuit condition

For a relatively lower level of acceleration such as 0.1g, the response from both of the system P1 and P2 is nearly resonant in nature as the response is almost identical irrespective of whether the frequency is swept in the forward or in the reverse direction (resonant frequency 70Hz and 74Hz for P1 and P2 respectively). From the COMSOL modelling, the first few eigen modes of P1 are at 81Hz, 108Hz and 351Hz and that of P2 are at 90Hz, 167Hz and 385Hz. In both cases, the experimental values of the natural frequencies of oscillation are lower than that obtained from COMSOL. The 3D printed structures, which fix these spring structures to the shaker plate in the experiments does not possess infinite stiffness as it does in case of the finite element analysis. This lowers the value of the spring stiffness and pulls down the frequency of vibration in contrast to those obtained from the finite element analysis.



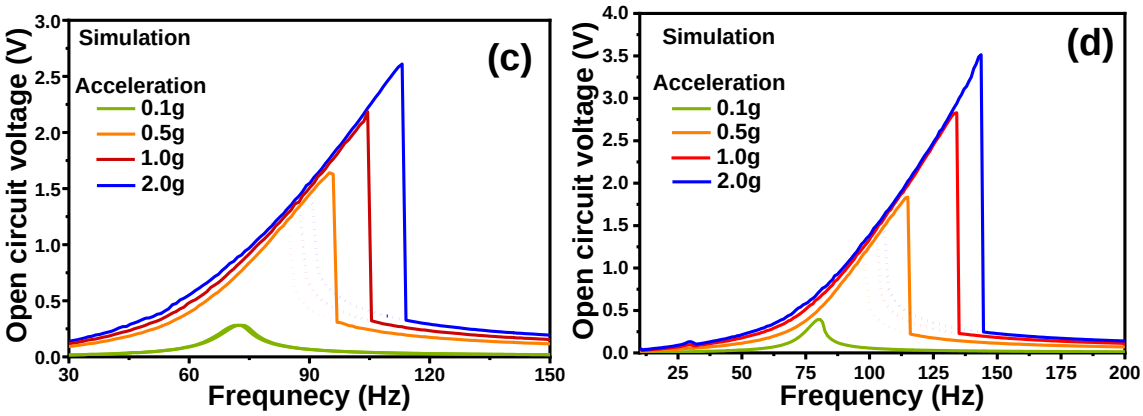


Figure 4.6: (a) The open circuit voltage measurement of the prototype P1. (b) The open circuit voltage measurement of the prototype P2. Time domain signal at the inset portrays the peculiar sharp peak of the open circuit voltage at 2g. The simulated results are shown in (c) and (d) for the prototype P1 and P2 respectively.

With the increasing amplitude of external excitation, the response of both system becomes gradually non-resonant (Fig. 4.6(a) and (b)). As the axial strain on the spring structure builds up forcing it to stretch, the oscillators start exhibiting complex nonlinear dynamic behaviour, for example the jump phenomena. When the system is subjected to a harmonic excitation with slowly varying frequency, the response from the system jumps either up (broken line) or down (solid line) at a certain frequency also termed as the saddle node point. This non-resonant nature and the multistability aids in enhancing the bandwidth of operation significantly as compared with its linear counterpart.

The voltage output from P1 increases as the frequency is from lower to higher values for 0.5g excitation, the at 96Hz which is the jump down frequency, the response falls off the high energy state steeply. On the reverse sweep of frequency with 0.5g excitation, the response follows a low energy state until at 81Hz, which is the jump up frequency as the response at this frequency yields larger voltage and meets the previous energy state that was followed during the forward sweep of driving frequency. With increasing amplitude of acceleration, the jump frequencies tends to increases as the nonlinearity in the system strengthens. In addition to this, an additional relatively smaller peak is observed at 34Hz at higher amplitudes of the external driving force which can be attributed to the activation of super-harmonics [37, 38] at almost half of the fundamental frequency of vibration of P1 (Fig.4. 6(a)). The appearance of such super-harmonic resonances are characteristic feature of nonlinear dynamical systems such as Duffing oscillators that allows the extraction of significant amount of vibrational energy even from comparatively lower frequency. In the reverse sweep of the open circuit voltage for P1, an additional peak is noticed at 98Hz, which could be due to the adjacent eigen modes, mostly

responsible for titling motion as found in the finite element analysis. In the forward sweep there is no such trace found which indicates that this is a highly damped oscillation mode. Initially the shaker plate excites only excites the modes responsible for the out-of-plane motion, at a higher level of acceleration the sufficient mechanical energy fed into the system also excites the other associated modes.

The open circuit voltage is found to ramp up from 0.4V at 0.1g acceleration to 2.9V at 1g acceleration for the P2 prototype. The response of the system demonstrates strong nonlinear characteristics with increasing amplitude of excitation, the jump down frequency increases from 113Hz for 0.5g to 136Hz for 1g excitation. At the higher external excitation level (1g), a voltage peak arising from a super-harmonic component is observed at 27Hz, almost at $1/3^{rd}$ of the fundamental frequency of oscillation (74Hz). A peculiar trend is noticed in the higher excitation amplitude regime where, with increasing the acceleration from 1g to 2g, the peak voltages increased from 2.4V to 2.9V without any significant bandwidth enhancement (inset of Fig. 4.6(b)). The emergence of an additional nonlinear mode at higher frequency around 175Hz is observed which accounts for the wobbles and instabilities in the structure at the higher forcing amplitude. This additional mode strengthens with higher acceleration by drawing significant amount of power from the primary nonlinear mode. This is why, despite feeding substantial energy through forcing, the peak voltage or the bandwidth of the primary mode does not enhance as expected. It indicates the possibility of coupling between these two adjacent modes that are exchanging energy between each other. Fig. 4.6(c) and (d) depicts that there is good qualitative agreement between the experimental results and the results obtained through numerical modelling as explained in the previous section. However, the 'jump' frequencies slightly differ as the two results are compared quantitatively. For example, with 2g acceleration amplitude, the response jumps from the high-energy branch to the low energy branch at 109Hz for P1, whereas numerically that point shifts to 113Hz. Similarly, for P2 the jump frequency obtained from the model is 144Hz, whereas experimentally the jump occurs at 139Hz at 2g acceleration. This can be due to the energy dissipation that takes place due to the effect of stretching, which is not taken into account in the numerical modelling. Also, the additional modes that are experimentally observed at 98Hz and 175Hz for P1 and P2 respectively are not reproduced in the numerical results. This disparity can be attributed to the fact that we consider only one degree of freedom for modelling, whereas in reality the complex 3D system possesses additional degrees of freedom. In addition to this, the open circuit voltage as obtained through the model is also higher than what has been experimentally observed. This can be explained by considering the damping. In the model, we only consider the damping,

which is proportional to the velocity of movement of the spring, whereas the damping experienced by the device in real world can have more complex dependency on the velocity.

4.4.3 Load performance

In the next part of the experiment, the output voltage is measured for both of the fabricated prototypes P1 and P2 at a fixed level of acceleration of 0.5g across variable load resistors ranging from 200Ω to 8kΩ. The devices are excited with a predefined sinusoidal vibration close to their peak power frequencies. The peak load power was found to be 550μW across 1.6kΩ load resistance for P1 and 520μW across 1.8kΩ load for P2 with peak load voltages 943mV and 966mV respectively (inset of Fig. 4.8). Next, the effect of the amplitude of external excitation on the load power of the system has been studied experimentally with the optimum load resistance. For P1, the half power bandwidth at 0.1g acceleration is found to be 2.6Hz with a peak load power of only 9.7μW. Upon on escalating the input acceleration, the peak load power increases to 0.63mW for 1g acceleration level resulting in widening of the bandwidth to 10Hz (Fig. 4.7(a)). Similarly, for P2 the peak load power and the bandwidth at 0.1g acceleration level are 20μW and 1.5Hz, which surges to 1.3mW and 23Hz at 1g (Fig. 4.7(b)). It is interesting to study the bursts of power in the low frequency range in P2 due to the super-harmonics. At around 28Hz for 1g acceleration, this mode extracts 9.6μW of electrical power into the load resistance, which is significantly higher than the rest of the low frequency range. In addition to this, in the high frequency zone at 178Hz a sudden burst of power of 1.8μW comes from the additional nonlinear mode, which has been identified and explained in the open circuit voltage plots as well. The experimentally obtained load characteristics of the device are compared with the numerical results (Fig. 4.7(c) and (d)). The overall trend of how the system response varies with the change to the excitation amplitude agrees well with the experimental results.

If the optimum load resistance, i.e. the value of load across which maximum output power is obtained is considerably greater than the resistance of the coil employed then it indicates strong electromagnetic coupling between the coil and the magnet resulting in larger electromagnetic flux linkage [27]. The electrical damping [28] associated with the system is dependent on the resistances of the coil (R_c), load (R_L) and on the electromagnetic coupling (γ) between the coil and the magnet. Taking into consideration the significant predominance of the vibrational energy distribution over the low frequency domain (f <200Hz), the effect of coil inductance (ωL) on the electrical damping (C_e) can be neglected as compared with the sum of the coil and load resistance. The damping can be expressed as,

$$C_e = \frac{n^2\left(\frac{d\Phi}{dz}\right)^2}{(R_c+R_L)} = \frac{\gamma^2}{(R_c+R_L)} \quad (4.6)$$

where,Φ is the magnetic flux linkage, n is the number of coil turns and $n\left(\frac{d\Phi}{dz}\right)$ represents the electromagnetic coupling γ .By increasing the load resistance for a fixed level of external forcing, the electrical damping associated with the system reduces, and this opens up the scope for modulation of the load power response of such nonlinear oscillators just by tailoring the load resistance (Fig. 4.8). This is possible when the electromagnetic coupling is strong enough so that the electrical damping in the system dominates over the parasitic damping. For 200Ω resistance, the electrical damping gets larger and the peak load power is only 180μW for P1 and 140μW for P2. However, increasing the load resistance to 1600Ω, 3200Ω and eventually to 8000Ω the bandwidth clearly increases but the power does not increase continuously. The peak load power reaches a maximum for the optimum load resistance of 1.6kΩ and 1.8kΩ for P1 and P2 respectively. Further increasing the load reduces the electrical damping significantly, which enhances the operable bandwidth at the cost of reduced peak load power. Therefore, this study brings out a clear trade-off between the magnitude of extracted power and the bandwidth of operable frequencies. Hence, the requirements of the target application can be met by altering load resistance, in particular when the electrical/electromagnetic damping associated with the system is dominating over mechanical damping.

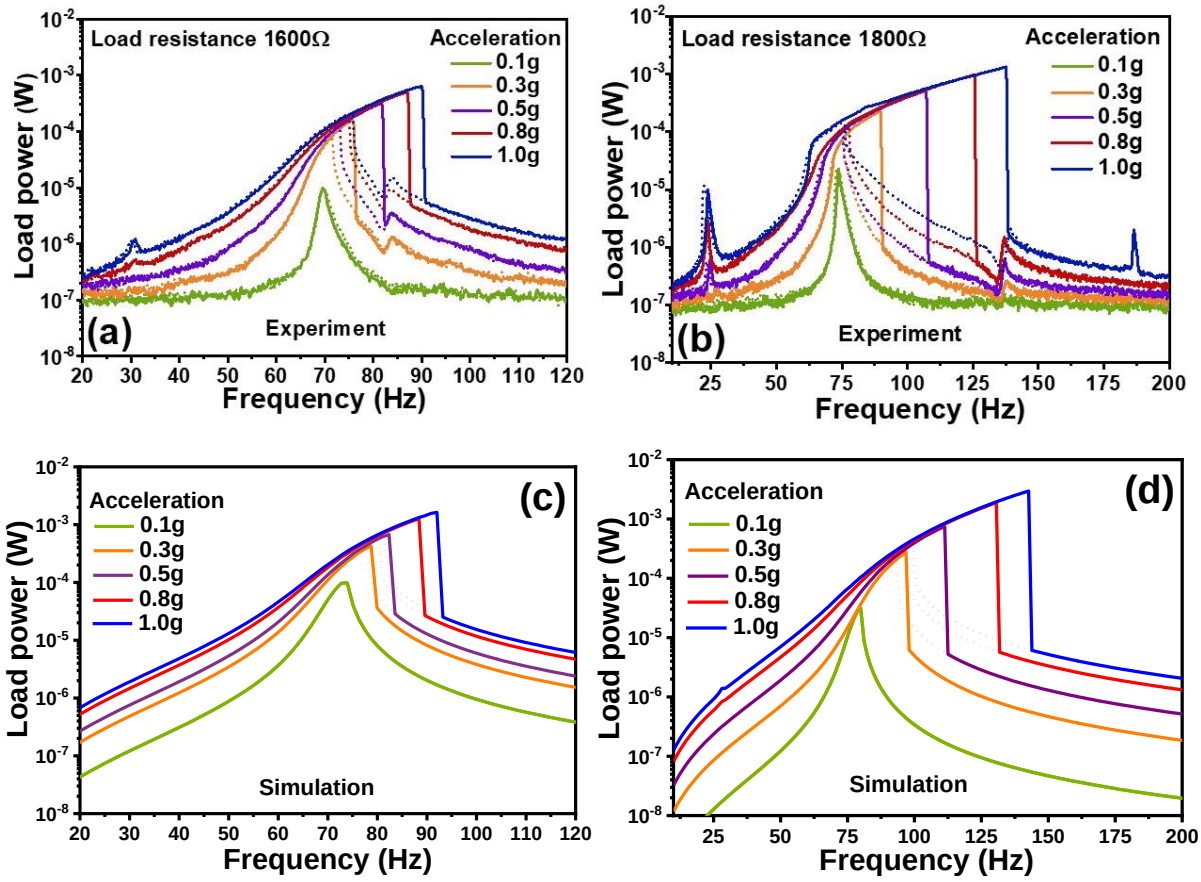


Figure 4.7: Variation of the load power at optimum load resistance with frequency for the prototype (a) P1 and (b) P2. The simulated results are shown in (c) and (d) for P1 and P2 respectively.

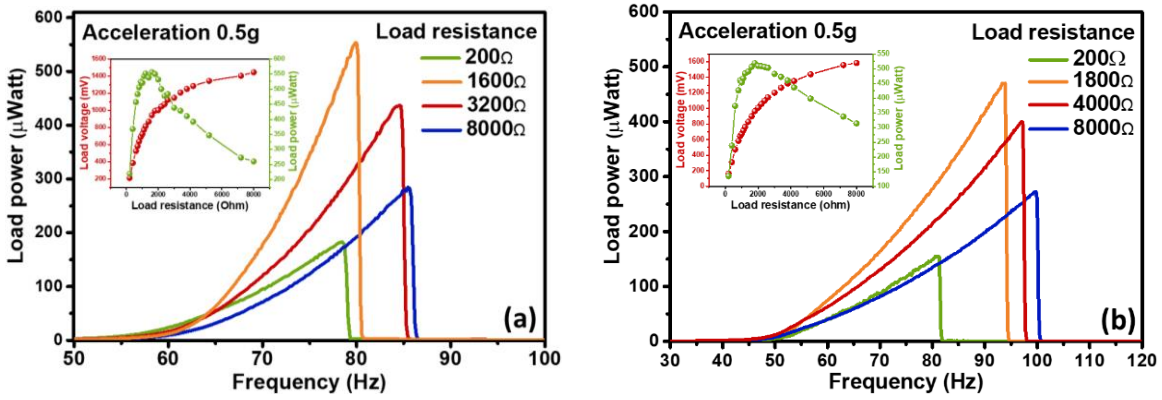


Figure 4.8: Variation of the load power with load resistance at 0.5g acceleration for P1 (left) and P2 (right).

The inherent wideband characteristics of the nonlinear oscillators make it easier to compare the different oscillators by considering their bandwidths at half of the peak power points. However, the concept of such bandwidth comparison could be misleading for the nonlinear oscillators as truncating the peak power could eventually lead to bringing the half power point further down

and deceptively indicating the enhancement of the bandwidth at that point. However, such an enhancement would be at the cost of compromising the obtainable power from the harvester. Rather, the enhancement of the width of the bi-stable or hysteresis region in this context could be a more reliable parameter to assess the effectiveness of the incorporated nonlinearity in the system. Fig. 4.9 shows the variation of the hysteresis width of the nonlinear energy harvester units with the amplitude of external excitation at the respective optimum load resistance. The solid line corresponds to the jump-down frequencies and the dotted line represents the jump-up frequencies and the hysteresis width, which in this case is considered to be the bandwidth of the response that is calculated as the difference between the jump frequencies ($f_{jump\text{-}down}$ - $f_{jump\text{-}up}$) at each level of excitation.

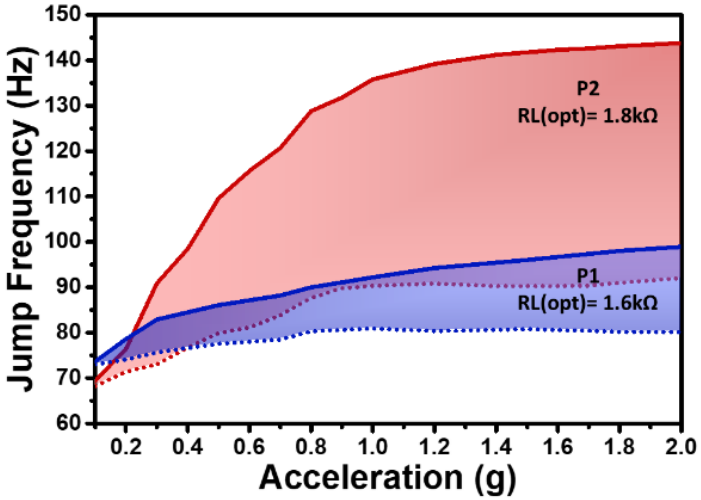


Figure 4.9: Comparison plot of the variation of hysteresis width of P1 and P2 with external excitation amplitude.

At lower acceleration, the hysteresis width ($f_{jump\text{-}down}$ - $f_{jump\text{-}up}$) is quite low for both of the harvesters up to 0.2g, which is expected as in this regime the system demonstrates nearly resonant behaviour. On further increasing the magnitude of external forcing, the structures experience strain arising from stretching instead of only bending, which makes the restoring force a nonlinear function of the displacement. This in turn widens the hysteresis region dramatically. The jump down frequency shifts toward higher frequency more drastically due to the hardening nonlinearity as opposed to the jump-up frequency, which does not vary much with respect to the fundamental frequency of oscillation despite of the presence of strong nonlinearity [41]. At 0.2g, the 4.5Hz and 4.7Hz hysteresis width increases to 11Hz and 45Hz at 1g for P1 and P2 respectively. The prototype P2, which has a higher degree of nonlinearity,

clearly shows a wider hysteresis region that enables the system to scavenge the vibrational energy from a broader range of frequencies.

The performance metrics often fail to express the efficiency of the overall system taking into account all the parameters such as- the device volume, amplitude of external acceleration, frequency of excitation etc. In addition to this, the target requirement also changes. For example, if the application requires resonant VEH, the peak load power is an important scale of performance evaluation for them as opposed to the bandwidth. On the contrary, if the target application needs an energy scavenger with broader bandwidth, then along with the high power, a wider range of operable frequency becomes an important parameter for harvester performance. Here, we aim to highlight the efficacy of the conceived tapered geometry employed in a nonlinear wideband energy harvester as compared to the conventional device topologies. Table 4.1 shows the comparison of the device performance based on the operable bandwidth that it offers, and the power density (=peak power/volume. acceleration^2). The generator reported in [4] offers a 30Hz bandwidth at 1g while yielding 243μW/cm^{3}g^2 power density. On the other hand, the power density reduces significantly for the nonlinear generator reported in [11], which potentially could be a result of the reduced device volume of 0.78cm^3. The energy harvesting system reported in [5] has a large device volume, which in turn reflects onto the large power density of 875μW/cm^{3}g^2. However, both of the energy harvesters reported in [16] and [13] delivers lower power density owing to their low device volume. In this context, the tapered energy harvesters P1 and P2 not only offers low device footprint such as 0.83cm^3 and 1.23cm^3 respectively, but also offers considerably large power density (2660μW/cm^{3}g^2 and 1692μW/cm^{3}g^2 from P1 and P2 respectively) and wider bandwidth of operable frequency (maximum of 45Hz with 1g excitation). In calculating the power density for our device, we have considered the overall footprint that the device occupies instead of the volume of the material only.

Table 4.1: Comparison of contemporary VEH devices with P1 and P2

Reference	Size scale/ Volume (cm^3)	Bandwidth/ operable frequency (Hz)	Power density (μW/cm^{3}g^2)
[4]	1.78*	~ 30Hz at 1g	243μW/cm^{3}g^2 at 78Hz
[11]	0.78	10Hz at 1g	0.45μW/cm^{3}g^2 at 244Hz
[5]	50	22-32 Hz at 0.08g	875μW/cm^{3}g^2 (= $\frac{280\mu W}{50cm^3\ 0.08^2 g^2}$) around 22-32Hz**

[16]	2.97	Bandwidth increased by 5Hz at 0.5g	~30μW/cm^{3}g^2 (= $\frac{7.4\mu W/cm^3}{0.5^2\ g^2}$) at 35Hz**
[13]	6	4.5Hz at 1g	483.3μW/cm^3 g^2 (= $\frac{2.9mW}{6cm^3\ 1g^2}$)at 150Hz**
This work, P1	0.83	9Hz at 0.5g 11Hz at 1g	2660μW/cm^{3}g^2 (= $\frac{665\mu W/cm^3}{0.5^2\ g^2}$) at 79Hz
This work, P2	1.23	29Hz at 0.5g 45Hz at 1g	1692μW/cm^{3}g^2 (= $\frac{423\mu W/cm^3}{0.5^2\ g^2}$)at 106Hz

4.5 Demonstration of complete Energy Harvesting solution

4.5.1 Variation of Maximum Power Point for Nonlinear EM-VEH

The growing interest of establishing a robust network of deployed wireless sensor nodes (WSNs) to create a responsive environment around us, while connecting the physical world to the digital world at the user end demands for a sustainable power source to replace the batteries in such nodes. The high efficiency vibration energy harvesters are one of the potential substitute to batteries. However, their performance depends critically on the ambient vibration conditions [29, 30]. The embedded electronics in the majority of commercially available WSNs typically require 3-3.3V DC voltage to power them up. Hence, to meet the power requirement of the subsequent load circuitry, the AC output of the energy harvester must be rectified. However, this rectified voltage cannot be fed directly to the load as it depends on the excitation amplitude and frequency. Hence, after this AC-DC conversion a suitable DC voltage regulation (DC-DC conversion) is required as a part of an efficient power management approach (Fig. 4.10).

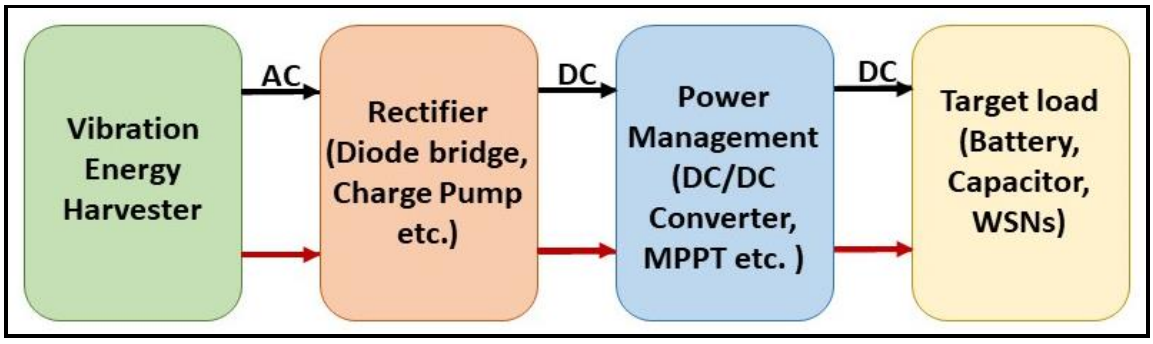


Figure 4.10: System architecture for powering a target load through ambient Vibrational Energy Harvesting.

To enhance the extracted energy from such harvesters, it is necessary to dynamically track the point of maximum obtainable power that varies with the vibration frequency and acceleration.

The Maximum Power Point Tracking (MPPT) controller is a prevalent component of the power management circuit that alters the duty cycle of the DC-DC converters, allowing the system to look for the voltage corresponding to the maximum electrical power. Various MPPT strategies, mainly for the Photovoltaic (PV) power system have been reported [31-33], for example, Perturb and Observe, Fractional Open Circuit Voltage and Fractional Short Circuit Current etc. Among these, one of the simple approaches is the Perturb and Observe mechanism, which involves perturbation of the operation point of the VEH at definite sampling interval while measuring the DC voltage. Furthermore, it checks if the measured voltage is greater or less than that of the previous sample, and accordingly it drives the system either in the same or in the reverse direction to find the MPP. This strategy has been recently used with the resonant electromagnetic vibration energy harvester [34], in which the sampling frequency along with the amplitude of the perturbation duty cycle is tailored to drive the system voltage towards MPP. However, an intelligent MPPT algorithm for the nonlinear energy scavengers, which possess non-identical electromechanical characteristics compared to the conventional resonant harvesters, has not been explored in detail yet.

The following experiment has been performed in order to provide an insight in to the trend of Maximum Power Point variation for Nonlinear VEHs, when subjected to different vibration conditions. The power extracted from the VEH optimizes when the output impedance of the energy harvester matches with that of the interfacing circuitry. The AC output of the harvester prototypes has been rectified employing the Dickson charge pump configuration, which is used for rectifying and boosting up the low AC voltage output [35, 36]. Owing to the simple electrical circuit and high efficiencies, this particular configuration is often used with the vibration energy harvesters, enabling it to power the target loads. Hence, a charge-pump interface has been implemented in this case consisting of capacitors C_1 to C_4 each of 1μF and four Zener diodes D_1 to D_4 (Fig. 4.13). The load resistance connected across the rectifier output has been varied from 200Ω to 10kΩ while the corresponding load voltage is measured and the load power is calculated. For the sake of simplicity, the load in this case has been considered resistive unlike the practically available reactive load. For both P1 and P2, this experiment has been performed in two sets, firstly by varying the amplitude of external excitation while keeping the frequency of excitation fixed and well within the hysteresis region (Fig.4.11(a) and (c)). Secondly, by keeping the amplitude of excitation fixed and varying the frequency of excitation over the hysteresis region while maintaining the oscillator response in the high-energy branch (Fig. 4.11(b) and (d)).

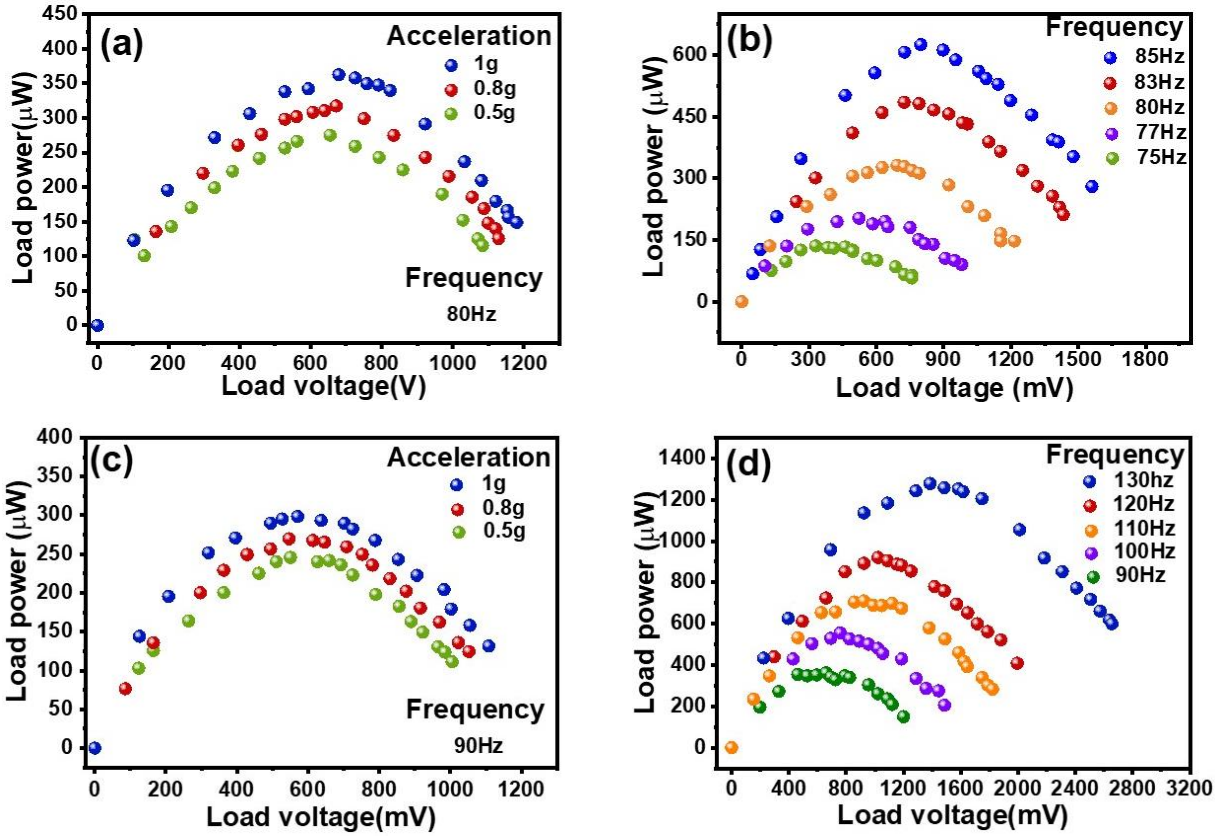


Figure 4.11: Variation of Load power with respect to load voltage at different level of external acceleration for P1 (a) and P2 (c). Variation of Load power with respect to load voltage at different values of excitation frequency for P1 (b) and P2 (d).

From the load power-voltage characteristics, we can observe that the load power initially increases with increasing load voltage; it attains a maximum value and eventually drops beyond that point with increasing load voltage. The amplitude of the applied force is varied keeping the frequency fixed at 80Hz for P1 and 90Hz for P2. The variation of the load power with the load voltage is shown in Fig. 4.11(a) and (c). Although the acceleration has been varied from 0.5g to 1g, no significant change either in the optimum power point or the overall variation has been observed as is prominent in a conventional resonant system [34, 37]. This can be explained by the load performance of both the prototypes in Fig.4.7(a) and (b). As the acceleration is increased, the excess energy pumped into the system at the specified frequencies aid in widening the hysteresis width rather than contributing towards enhancing the peak load power. Hence, in the next set of experiments the amplitude of vibration was fixed at 1g for both the prototypes and the frequency of excitation has been varied over the hysteresis region- 75Hz to 85Hz and 90Hz to 130Hz for P1 and P2 respectively. In Fig.4.11(b) and (d) the variation of the load power-voltage has been portrayed, while the shift in the variation for different frequencies can be very clearly observed. The maximum power for P1 changes from

327μW to 796μW when the frequency is changed from 75Hz to 85Hz. These results also agree with the load performances (Fig.4.7) of the devices, where a significant change of load power can be observed over the specified range of frequencies.

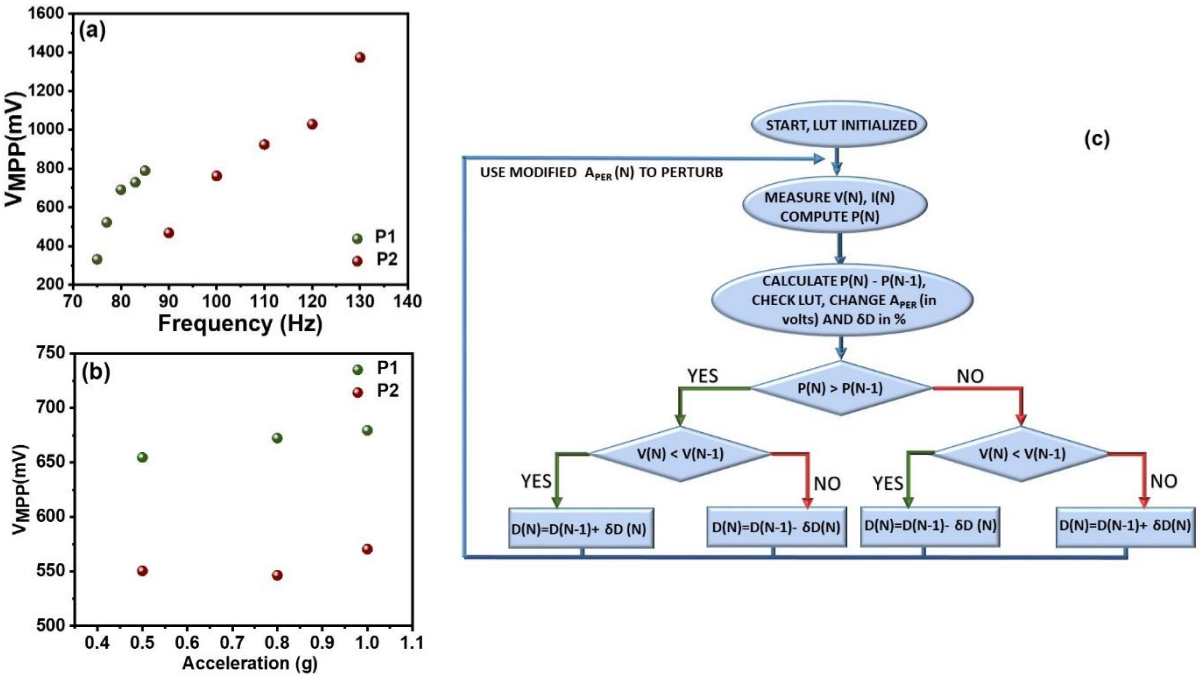


Figure 4.12: Variation of the DC voltage corresponding to the maximum power point with (a) frequency variation (b) amplitude of external force variation for P1 and P2 as obtained from Fig. 9. The adjacent flow chart (c) depicts a suitable Perturb and Observe strategy.

The unimodal distribution of the power in Fig. 4.11 is well suited for employing Perturb and Observe strategy for the tracking of the maximum power point. However, as opposed to the conventional algorithm for the linear VEH, this algorithm would need modification to adapt to a real-world vibration environment and drive the operating point towards MPP. The trend of variation of the DC voltage (V_{MPP}) corresponding to the maximum power point is different when the frequency of operation, or the amplitude of excitation is changed (Fig. 4.12). At a fixed amplitude of acceleration, the V_{MPP} changes from 331mV to 789mV over a frequency band of 10Hz for P1. However, no significant variation could be noticed in V_{MPP} when the acceleration amplitude is doubled from 0.5g to 1g. Hence, the size of the perturbation (A_{PER}) along with the duty cycle (δD) of the DC-DC converter needs to be dynamically adjusted to facilitate the efficient tracking of V_{MPP}. In order to save the system from losing the direction of tracking when it is subjected to fast changing environment, the knowledge of such variation of V_{MPP} as obtained from initial experiments can be conveniently programmed into the MPPT controller in the form of a lookup table (LUT). Once the tracking starts (Fig. 4.12(c)), following

a predefined perturbation, the MPPT controller measures the DC output from the system and computes the power P(N). Furthermore, it computes the change in the obtained power as compared to the last sample and the corresponding DC voltage. Accordingly, the controller modifies the duty cycle D(N) associated with the DC-DC converter until it finds the MPP. Unlike the traditional tracking, at this point the system could check the LUT to find if the change in V_{MPP} corresponds to that of frequency variation or acceleration change. Accordingly, the controller can then assign a suitable A_{PER} and δD to use in the $N+1^{th}$ trial. The overall performance of such an energy harvesting system relies critically on the individual efficiency of the converter blocks. This requires an accurate MPPT algorithm to optimize the power extraction. This study opens up the scope for development of a suitable MPPT strategy dedicated for such a complex nonlinear system. This will aid in extracting the maximum possible mechanical energy from the harvesters when subjected to real life time-varying vibrations. It is to note that real world application scenario especially considering stochastic excitation with this type of nonlinear device is a challenge owing to the intrinsic multistable characteristics of the device does not always ensure achieving and sustaining high-energy state. However, a potential alternative is to use controlled electrical actuation [19], which is a viable route to switch the state of this system to higher energy state, while enabling the VEH to capture substantial mechanical energy from real-world vibrations.

4.5.2 Powering of a wireless sensor node

A robust communication network is nowadays indispensable in the transportation chain of food and medicinal products. The cold chain of perishable food requires careful monitoring of the temperature and the humidity (arising from the agri-food transpiration) when they are transported to significantly reduce food spoilage [38]. Similarly, continuous supervision is imperative during the transportation of pharmaceuticals as the majority of drugs and vaccines lose their potency if the temperature departs from the recommended level [39]. The critical challenge is continuous in-situ monitoring of the environment when they are transported from the warehouse or manufacturer to a different distributor. This can be facilitated through a resilient self-powered wireless sensor network. The high power density VEH prototype developed in this work could be employed to power such a WSN network by harvesting energy from the vibrations of the truck that carries the product. Magnuson et al. [40] reported the vibrations recorded from a loaded truck driven on highways and the vibration in the vertical direction was found to be spread over a broadband of 40Hz to 180Hz with peak amplitudes less than 1g. This is suitable for driving the intrinsically broadband VEH fabricated in this work.

In order to power the wireless sensor nodes perpetually through vibration energy harvesting, the essential requirement is effective mechanical energy tapping along with efficient energy conversion and distribution. The power demand varies for different sensors and their associated electronics, accordingly the power conditioning circuitry connecting the source to the target node changes. In this work, we have selected the Cypress IoT kit (S6SAE101A00SA1002) which comes with Bluetooth-Low-Energy (BLE) wireless connectivity. It consists of an energy harvesting motherboard containing mainly the Power Management IC S6AE101A, Temperature and Humidity Sensor (Si7020-A10) and CYBLE-022001-00 EZ BLE. The other part of the kit is a PC compatible BLE-USB Bridge accommodating the CYBL 10162-56LQXI PRoC BLE device and a wiggle antenna along with antenna matching network. While this kit is specifically designed to scavenge photovoltaic energy or to run on a coin-cell primary battery (3V DC), but the ultra-low-power start-up of the PMIC (250nA current consumption and 1.2µW power for start-up) makes it an attractive choice to be used with vibrational energy harvesters. Typically, the motherboard requires 3.3V DC to operate and communicate the acquired data through Bluetooth connectivity. The wireless sensor node transmits the gathered data at 6-second intervals.

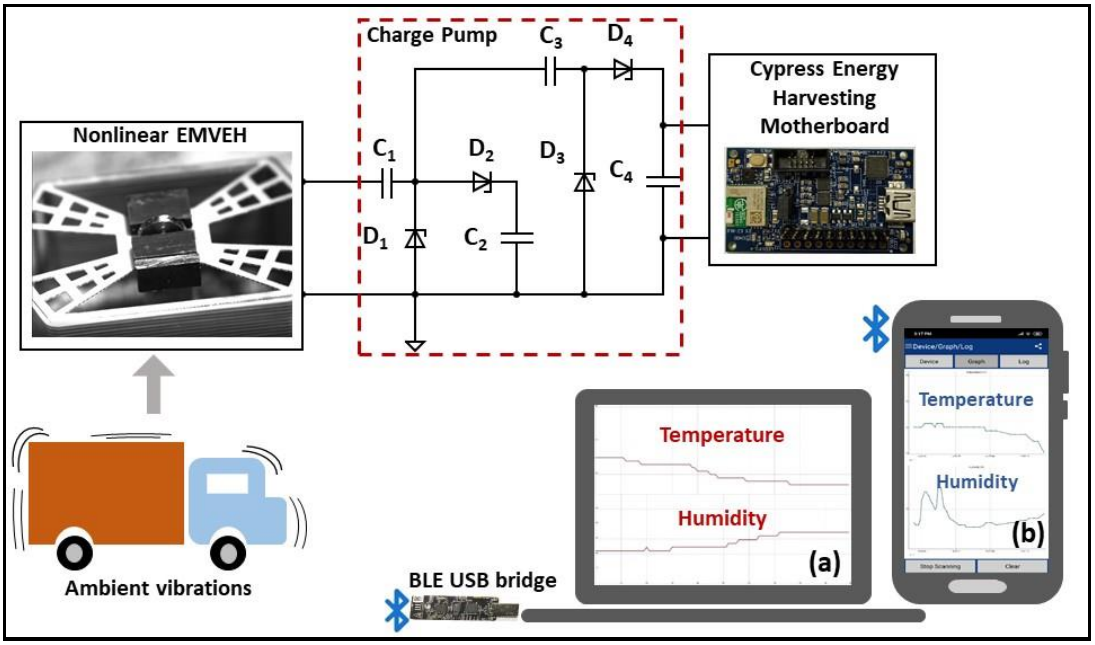


Figure 4.13: Overview of the energy harvesting system powering the Cypress IoT kit, (a) Logged data in the PC through wireless communication established by the BLE USB bridge (b) Logged data in the smart phone through CYPRESS BLE Beacon app when the motherboard is configured as a stand-alone wireless sensor node and it communicates through wireless Bluetooth connectivity.

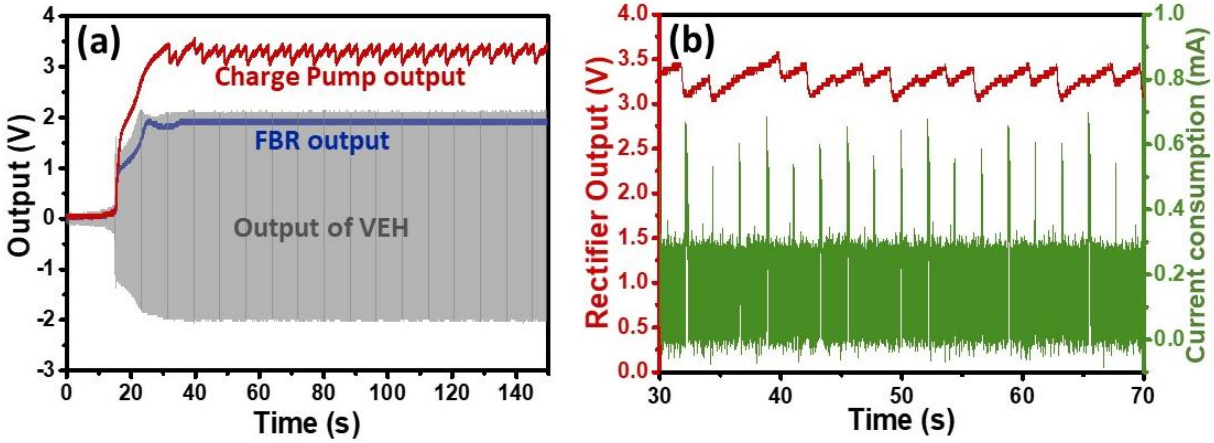


Figure 4.14: (a) Output voltage of the vibration energy harvester, full bridge rectifier and the charge pump circuit connected across the harvester in grey, blue and red respectively. (b) Output voltage of the charge pump circuit attached across the harvester and the current consumption of the motherboard associated with the IoT kit.

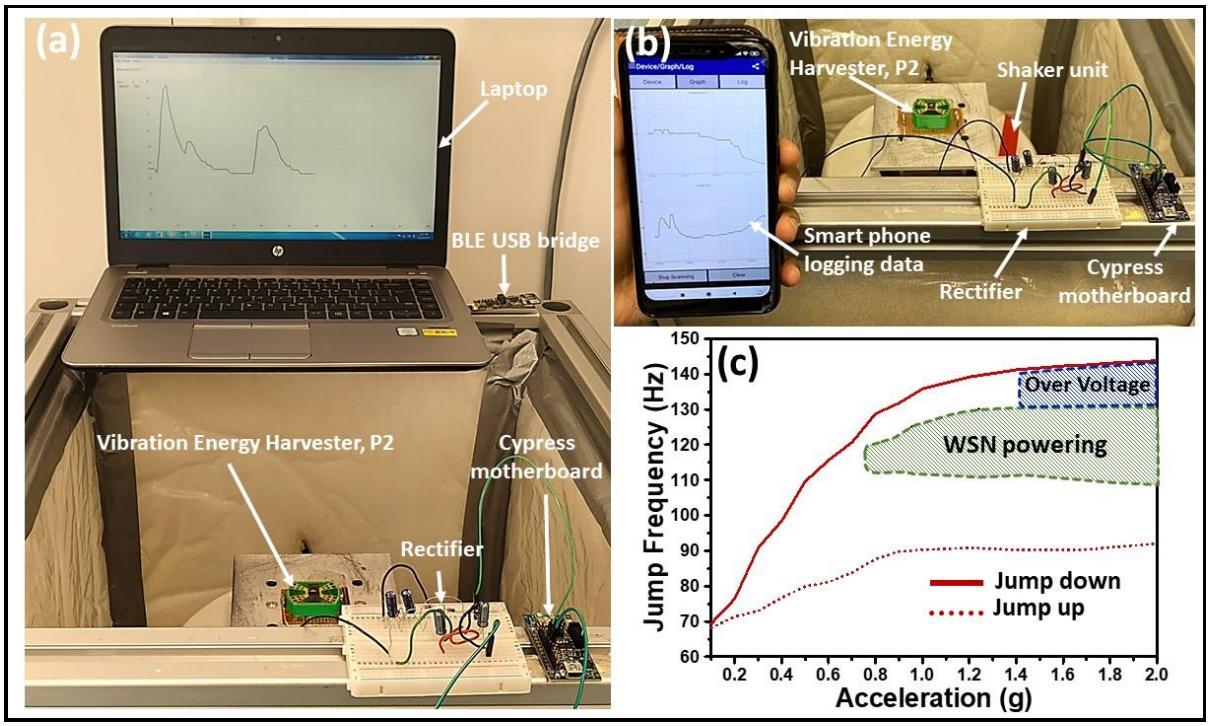


Figure 4.15: Depiction of the energy harvesting system with the target sensor node, (a) logging sensor data in laptop through the BLE USB bridge, (b)logging data directly in smart phone through Bluetooth connectivity. (c) Illustration of the operable range of frequency and acceleration where the wireless sensor node could be powered by P2.

Throughout our study, we can clearly observe that P2 is superior in performance to P1, which is why we have chosen P2 prototype to power the target sensor node (Fig. 4.13). The interfacing circuitry between the harvester and the motherboard should provide a steady DC voltage of 3.3V to the motherboard. Hence, a charge-pump type rectification interface has been

implemented in this case consisting of capacitors C_1 to C_4 each of 1μF and four Zener diodes D_1 to D_4 to enhance the output of the harvester unit from 2V to 3.8V DC voltage (when the harvester is driven with harmonic excitation at 0.7g, and the frequency is ramped up from 70Hz to 108Hz at a 1Hz/sec sweep rate). The charge pump circuit delivers the power to the load by the charging and discharging of the associated capacitors, functioning as a switching regulator. This particular rectification strategy is appropriate for the low current demanding target applications. Fig. 4.14(a) shows a comparison of rectified voltage produced by the charge-pump rectifier (in red) with a full bridge rectifier (in blue). The voltage drop across the diodes of the full bridge rectifier restricts the output whereas the charge pump circuit enhances the output from 2V to 3.8V, which is sufficient to power the subsequent load. The stable DC output from this interface is provided to the IoT kit motherboard through the dedicated pins. On receiving sufficient power from the source, the PMIC starts charging an integrated output capacitor, further depending on the internal switching and the level of voltage in the capacitor, the stored power gets delivered to the load.

The BLE beacon of the IoT kit broadcasts 30 bytes of information periodically once it gets sufficient energy to initiate the operation. The associated communication protocol allows the kit to read data from the humidity and temperature sensor, which is then transmitted as a part of the advertisement packet. The ripples in the output of the rectifier as shown in the Fig.4.14 correspond to the point where the transmitter on the motherboard establishes communication with the receiver and transmits the gathered data. The current intake of the motherboard shows peaks of 0.7mA for the transmission of information that correspond to the dip in these ripples. The motherboard establishes BLE connection with a PC through the BLE USB bridge, which is programmed with initial firmware that aids it to log the data from the sensors and display on the PC screen (Fig. 4.15(a)). This enables the user to monitor the real-time data from dedicated sensors through smart phones. The embedded Bluetooth in this phone establishes communication with the motherboard and through a compatible mobile app (e.g. CYPRESS BLE Beacon used in this case). The raw received data is processed and displayed on the phone screen (Fig.4.15(b)).

Fig. 4.15(c) shows the operable range of frequencies of P2 when it is subjected to the varying amplitude of excitation. As shown previously in Fig. 4.7, on increasing the acceleration of excitation, the hysteresis width of the harvester unit enhances, and that is shown by the area shaded with red. From 115Hz at 0.7g acceleration P2 supplies adequate power to the Cypress IoT kit so that it transmits the sensor data. The area shaded in green in Fig. 4.15(c) shows the range of acceleration and frequency that is suitable for operating this wireless sensor node with

P2. The energy lost in the rectification stage has caused the harvester's response to fall off the high-energy branch earlier in the low to moderate level of acceleration (up to 1.2g). Beyond this, the voltage delivered by the source to the IoT kit goes beyond the safe limit of operation (2-5.5V). This region is shaded in blue as the overvoltage zone.

In the experiments so far, we only studied harmonic excitations, however in reality non-harmonic or in other words random excitations are often found. In order to test the practical applicability of the vibration energy harvester unit, it has been subjected to the random excitation imparted by a car in motion. The harvester unit has been mounted on the rear part of a Honda Civic car and it is connected to the wireless sensor platform through a rectifier circuit. A slamstick [41], which is a vibration data logger, has been used here to record the vibrations of the car (Fig. 4.16(b)). When the car was in motion, the harvester started powering the sensor node (Cypress IoT kit), and through the CYPRESS BLE Beacon mobile app the raw data was received in a smart phone. The data packets were received at an irregular interval, unlike the case when the harvester was subjected to harmonic excitation, reporting a temperature of 24.5˚C and 74% humidity (inside the car). Fig. 4.16(a) shows a snippet of the time trace of the vibrations experienced in the car. The inset shows the frequency range over which substantial mechanical energy was found to be distributed, having peaks over 12Hz, 50Hz, 71Hz and 93Hz. We received data packets over the shown time range, in Fig. 4.16(c) we further show the number of data packets received per second over that period. It is noticeable that few of the data packets were received when the vibrations had spikes, as marked with red arrows in Fig. 4.16(c), which may correspond to the bumps in the road. Similar spikes can be seen at the time instants marked with black arrow, however, no successful reception of data packets could be observed here. This may be attributed to the fact that although the amplitude of acceleration at this peak is as high as 0.9g to 1.2g, but the corresponding frequency component may not fall into the bandwidth over which it is possible to excite the device and extract substantial mechanical energy through it. The performance of the harvester unit could be further enhanced by optimizing the spring geometry. This would yield higher power at an even lower level of external excitation which along with wider operable bandwidth. These improvements could open up the possibility of using such harvester to power the network of WSNs for a wide range of applications.

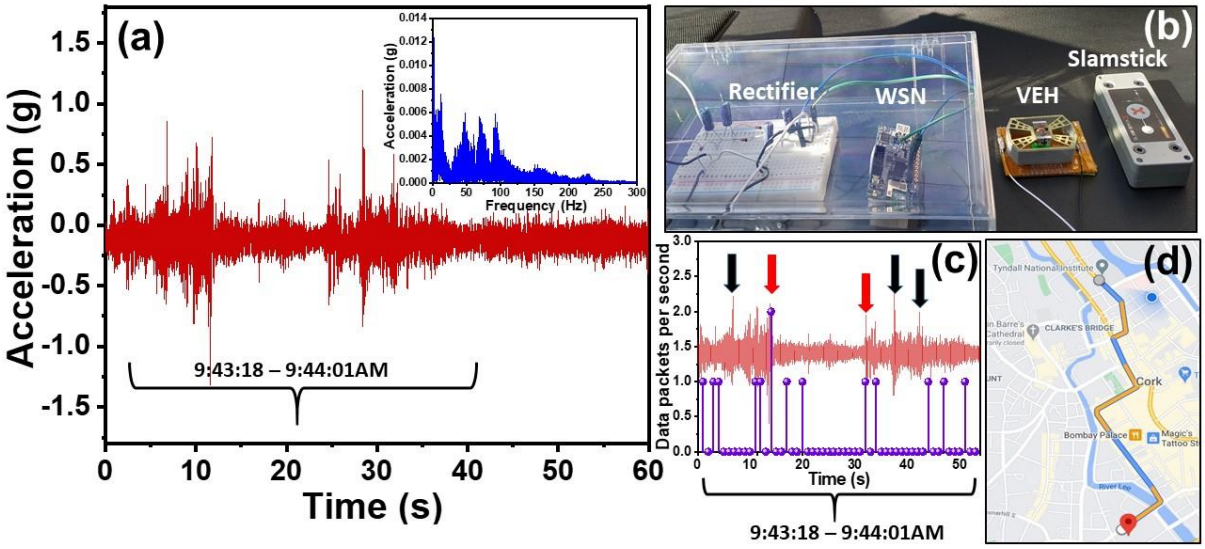


Figure 4.16: (a) Time trace of the vibration experienced in the rear part of a car recorded with data logger (Slamstick), the inset shows the frequency range over which substantial mechanical energy was found to be distributed in the car. (b) Shows the experimental set-up consisting of the rectifier, sensor node, the energy harvester unit and a slamstick (vibration data logger) to record the vibrations from the car. (c) Illustrates the number of data packets received over a small snippet of time and (d) shows the path that the car traversed around Tyndall National Institute.

4.6 Conclusion

This work described in chapter-4 demonstrates the implementation of tapered FR4 (Flame Retardant 4) based spring architecture in an electromagnetic Vibration Energy Harvester (VEH). This harvester exhibits spring hardening nonlinearity based on large deformations, with a relatively small footprint. The atypical stress distribution of the tapered thin spring structure has been exploited to obtain a suitable nonlinearity. Through detailed experimental investigation, we have showed the efficacy of using these energy harvester prototypes to yield a power density as high as 2660μW/cm^{3}g^2, outpacing many of the contemporary reported devices. The inclusion of strong nonlinearity in this system resulted in an enhanced bandwidth of 45Hz at 1g acceleration, which makes it suitable for extracting mechanical energy from real-world wideband vibration spectrum. Furthermore, we provided a thorough analysis of the variation of the maximum power point and proposed a modified Perturb and Observe strategy for tracking the maximum power point in order to optimize the extractable electrical power. The fabricated energy harvester unit is also used to address the issue of providing continuous power to wireless sensor networks. This is challenging for a non-resonant VEH because of the requirement of a steady 3-3.3V DC supply to power the integrated electronics associated with a wireless sensor node. Despite this challenge, our prototype has powered such a wireless sensor node (using a Cypress IoT kit) consisting of a temperature and humidity sensor. The

transmitted data is logged in a PC and smartphone through well-established Bluetooth connectivity. This makes the energy harvester a potential candidate for establishing a battery-less wireless sensor network in a wide range of application, including the food and pharmaceutical transportation chain ensuring enhanced quality and safety of the valuable products in this chain.

4.7 Reference:

[1] S. P. Beeby *et al.*, "A micro electromagnetic generator for vibration energy harvesting," *Journal of Micromechanics and Microengineering*, vol. 17, no. 7, pp. 1257-1265, 2007/06/05 2007.

[2] S. H. Chae, S. Ju, Y. Choi, Y.-E. Chi, and C.-H. Ji, "Electromagnetic Linear Vibration Energy Harvester Using Sliding Permanent Magnet Array and Ferrofluid as a Lubricant," (in eng), *Micromachines*, vol. 8, no. 10, p. 288, 2017.

[3] I.-H. Kim, H.-J. Jung, B. M. Lee, and S.-J. Jang, "Broadband energy-harvesting using a two degree-of-freedom vibrating body," *Applied Physics Letters*, vol. 98, no. 21, p. 214102, 2011.

[4] H.-C. Song *et al.*, "Broadband dual phase energy harvester: Vibration and magnetic field," *Applied Energy*, vol. 225, pp. 1132-1142, 2018/09/01/ 2018.

[5] V. R. Challa, M. G. Prasad, Y. Shi, and F. T. Fisher, "A vibration energy harvesting device with bidirectional resonance frequency tunability," *Smart Materials and Structures*, vol. 17, no. 1, p. 015035, 2008/01/08 2008.

[6] L. Zhao and Y. Yang, "An impact-based broadband aeroelastic energy harvester for concurrent wind and base vibration energy harvesting," *Applied Energy*, vol. 212, pp. 233-243, 2018/02/15/ 2018.

[7] X. Wang *et al.*, "A frequency and bandwidth tunable piezoelectric vibration energy harvester using multiple nonlinear techniques," *Applied energy*, vol. 190, pp. 368-375, 2017.

[8] P. Podder, D. Mallick, A. Amann, and S. Roy, "Influence of combined fundamental potentials in a nonlinear vibration energy harvester," *Scientific Reports*, Article vol. 6, p. 37292, 11/22/online 2016.

[9] S. Roy, P. Podder, and D. Mallick, "Nonlinear Energy Harvesting Using Electromagnetic Transduction for Wide Bandwidth," *IEEE Magnetics Letters*, vol. 7, pp. 1-4, 2016.

[10] B. Marinkovic and H. Koser, "Smart Sand—A Wide Bandwidth Vibration Energy Harvesting Platform," *Applied Physics Letters - APPL PHYS LETT*, vol. 94, 03/09 2009.

[11] D. Mallick, A. Amann, and S. Roy, "A nonlinear stretching based electromagnetic energy harvester on FR4 for wideband operation," *Smart Materials and Structures*, vol. 24, 01/01 2015.

[12] B. P. Mann and N. D. Sims, "Energy harvesting from the nonlinear oscillations of magnetic levitation," *Journal of Sound and Vibration*, vol. 319, no. 1, pp. 515-530, 2009/01/09/ 2009.

[13] P. Constantinou and S. Roy, "A 3D printed electromagnetic nonlinear vibration energy harvester," *Smart Materials and Structures*, vol. 25, no. 9, p. 095053, 2016/08/24 2016.

[14] F. Cottone, H. Vocca, and L. Gammaitoni, "Nonlinear Energy Harvesting," *Physical Review Letters*, vol. 102, no. 8, p. 080601, 02/23/ 2009.

[15] A. Erturk and D. J. Inman, "Broadband piezoelectric power generation on high-energy orbits of the bistable Duffing oscillator with electromechanical coupling," *Journal of Sound and Vibration*, vol. 330, no. 10, pp. 2339-2353, 2011/05/09/ 2011.

[16] P. Podder, A. Amann, and S. Roy, "A bistable electromagnetic micro-power generator using FR4-based folded arm cantilever," *Sensors and Actuators A: Physical*, vol. 227, pp. 39-47, 2015/05/15/ 2015.

[17] P. Podder, A. Amann, and S. Roy, "Combined Effect of Bistability and Mechanical Impact on the Performance of a Nonlinear Electromagnetic Vibration Energy Harvester," *IEEE/ASME Transactions on Mechatronics*, vol. 21, no. 2, pp. 727-739, 2016.

[18] S. Zhao and A. Erturk, "On the stochastic excitation of monostable and bistable electroelastic power generators: Relative advantages and tradeoffs in a physical system," *Applied Physics Letters*, vol. 102, no. 10, p. 103902, 2013/03/11 2013.

[19] D. Mallick, A. Amann, and S. Roy, "Surfing the High Energy Output Branch of Nonlinear Energy Harvesters," *Physical Review Letters*, vol. 117, no. 19, p. 197701, 11/04/ 2016.

[20] G. Aldawood, H. T. Nguyen, and H. Bardaweel, "High power density spring-assisted nonlinear electromagnetic vibration energy harvester for low base-accelerations," *Applied Energy*, vol. 253, p. 113546, 2019/11/01/ 2019.

[21] K. Fan, Q. Tan, Y. Zhang, S. Liu, M. Cai, and Y. Zhu, "A monostable piezoelectric energy harvester for broadband low-level excitations," *Applied Physics Letters*, vol. 112, no. 12, p. 123901, 2018.

[22] A. Vyas *et al.*, "A Micromachined Coupled-Cantilever for Piezoelectric Energy Harvesters," (in eng), *Micromachines,* vol. 9, no. 5, p. 252, 2018.
[23] H. Salmani, G. H. Rahimi, and S. A. Hosseini Kordkheili, "An Exact Analytical Solution to Exponentially Tapered Piezoelectric Energy Harvester," *Shock and Vibration,* vol. 2015, p. 13, 2015, Art. no. 426876.
[24] S. Paquin and Y. St-Amant, "Improving the performance of a piezoelectric energy harvester using a variable thickness beam," *Smart Materials and Structures,* vol. 19, no. 10, p. 105020, 2010/08/18 2010.
[25] S. Roundy, P. Wright, and J. M. Rabaey, "A Study of Low Level Vibrations as a Power Source for Wireless Sensor Nodes," *Computer Communications,* vol. 26, pp. 1131-1144, 07/01 2003.
[26] R. L. Harne and K. W. Wang, "A review of the recent research on vibration energy harvesting via bistable systems," *Smart Materials and Structures,* vol. 22, no. 2, p. 023001, 2013/01/28 2013.
[27] D. Mallick and S. Roy, "Bidirectional electrical tuning of FR4 based electromagnetic energy harvesters," *Sensors and Actuators A: Physical,* vol. 226, pp. 154-162, 2015/05/01/ 2015.
[28] C. R. Saha, T. O'Donnell, H. Loder, S. Beeby, and J. Tudor, "Optimization of an electromagnetic energy harvesting device," *IEEE Transactions on Magnetics,* vol. 42, no. 10, pp. 3509-3511, 2006.
[29] D. Maurath, P. F. Becker, D. Spreemann, and Y. Manoli, "Efficient Energy Harvesting With Electromagnetic Energy Transducers Using Active Low-Voltage Rectification and Maximum Power Point Tracking," *IEEE Journal of Solid-State Circuits,* vol. 47, no. 6, pp. 1369-1380, 2012.
[30] C. Lu, C. Tsui, and W. Ki, "Vibration Energy Scavenging System With Maximum Power Tracking for Micropower Applications," *IEEE Transactions on Very Large Scale Integration (VLSI) Systems,* vol. 19, no. 11, pp. 2109-2119, 2011.
[31] A. Reza Reisi, M. Hassan Moradi, and S. Jamasb, "Classification and comparison of maximum power point tracking techniques for photovoltaic system: A review," *Renewable and Sustainable Energy Reviews,* vol. 19, pp. 433-443, 2013/03/01/ 2013.
[32] R. Bradai *et al.*, "Experimental assessment of new fast MPPT algorithm for PV systems under non-uniform irradiance conditions," *applied energy,* vol. 199, pp. 416-429, 08/01 2017.
[33] A. Belkaid, I. Colak, and O. Isik, "Photovoltaic maximum power point tracking under fast varying of solar radiation," *Applied Energy,* vol. 179, pp. 523-530, 2016/10/01/ 2016.
[34] L. Costanzo and M. Vitelli, "Resonant electromagnetic vibration harvesters applications: Optimization of P&O MPPT technique parameters," in *2018 Thirteenth International Conference on Ecological Vehicles and Renewable Energies (EVER)*, 2018, pp. 1-8.
[35] A. Dudka, P. Basset, F. Cottone, E. Blokhina, and D. Galayko, "Wideband Electrostatic Vibration Energy Harvester (e-VEH) Having a Low Start-Up Voltage Employing a High-Voltage Integrated Interface," *Journal of Physics: Conference Series,* vol. 476, p. 012127, 2013/12/04 2013.
[36] J. F. Dickson, "On-chip high-voltage generation in MNOS integrated circuits using an improved voltage multiplier technique," *IEEE Journal of Solid-State Circuits,* vol. 11, no. 3, pp. 374-378, 1976.
[37] L. Costanzo, A. L. Schiavo, and M. Vitelli, "Design Guidelines for the Perturb and Observe Technique for Electromagnetic Vibration Energy Harvesters Feeding Bridge Rectifiers," *IEEE Transactions on Industry Applications,* vol. 55, no. 5, pp. 5089-5098, 2019.
[38] S. T. Hammond *et al.*, "Food Spoilage, Storage, and Transport: Implications for a Sustainable Future," *BioScience,* vol. 65, no. 8, pp. 758-768, 2015.
[39] G. H. Haan, J. Van Hillegersberg, E. De Jong, and K. Sikkel, "Adoption of wireless sensors in supply chains: a process view analysis of a pharmaceutical cold chain," *Journal of theoretical and applied electronic commerce research,* vol. 8, no. 2, pp. 138-154, 2013.
[40] C. F. Magnuson and L. T. Wilson, "Shock and vibration environments for large shipping containers on rail cars and trucks," Sandia Labs., Albuquerque, NM (USA)1977.
[41] *Midé Slamtick, Shock and Vibration data loggers*. Available: https://www.mouser.ie/pdfdocs/slam-stick-vibration-data-loggers-datasheet.pdf

Chapter 5: Time resolved Eye Diagrams to exploit Hidden High Energy Branches in a Nonlinear Wideband Vibration Energy Harvester

This chapter is based on the following publication- K. Paul, A. Amann, S. Roy, "Exploration of high energy branches in a novel electromagnetic vibration energy harvester combining multiple nonlinearity"- Submitted to Physical Review Applied, Under review.

5.1 Introduction

A wideband vibration energy harvester with multiple nonlinear forces is investigated in this chapter. The nonlinearities are due to repulsive magnets and hardening springs, which gives rise to multistabilities between a number of energy branches. Not all branches are accessible by a simple up or down sweep of the driving frequency and in particular, the highest energy branch is often hidden, requiring a suitable frequency schedule to be accessed. Detailed theoretical understanding of the energy branch structure along with robust experimental methods are essential for characterizing each of the energy branches to enhance the energy output from such vibration energy harvesting system. We introduce a graphical representation in the form of eye diagrams based on time-resolved measurements of acceleration and output voltage to study the dynamical features of the different branches. This generic approach allows us to optimize the design, which results in 1.3mW of power generated at 1g over 44Hz frequency bandwidth while maintaining a small footprint of 1.23cm^3. The energy conversion ratio of this energy harvesting system at 120Hz drive frequency is 0.52 for the high-energy branch.

5.2 The knowledge gap and a potential solution

In this epoch of Internet of Things (IoT), the lack of a sustainable power source significantly impedes the pervasive deployment of autonomous sensors nodes. To address this cardinal issue, Vibration Energy Harvesters (VEHs) have emerged as a promising renewable energy source [1, 2] due to the abundance of vibrations in the domestic and industrial environment. However, the characteristically narrow frequency bandwidth, and hence the poor off-resonance performance of traditional linear VEHs [3] makes them unsuitable for harnessing substantial mechanical energy from ambient vibrations, which is spread over a broad spectrum of

frequency. The challenge is therefore to design a VEH with large energy output over a wide frequency range.

A wider operable bandwidth is obtainable by using a VEH with a nonlinear restoring force [4, 5] and in the past VEHs possessing monostable [6-8], bistable [9-11], tristable [12], quadstable [13], and polystable [14] potential energy functions have been studied experimentally. From a theoretical point of view, VEHs can be modelled as driven nonlinear oscillators [15], which also appear in many other fields, including optics, photonics [16-18], biomechanics [19], and electronics [20]. It is well known that, even in simple periodically driven systems the presence of nonlinearity can give rise to complex dynamical features, including multistability, dynamic symmetry breaking and frequency locking [21-24].

In the context of VEHs, the phenomenon of multistability translates into the presence of multiple energy branches, which coexist for a given set of driving parameters. For example, in the classical case of a hardening nonlinearity [25] as in the Duffing oscillator [23, 26], high-energy and low-energy branches coexist. The selection of the dynamical state depends on the initial conditions and the frequency schedule of the drive. Additionally, fully isolated resonances with large amplitudes are also possible [27]. From an application point of view, it is desirable to maintain the system in the branch with the highest energy output, and various mechanisms for achieving and sustaining these high energy branches have been devised in the past [28-30]. Thus, a route to further increase the energy output and frequency bandwidth using more sophisticated nonlinearities appears possible. However, the increased complexity of the resulting energy branch structure requires detailed theoretical understanding and powerful experimental methods to characterize different branches.

The graphical representation of the dynamics of linear and nonlinear oscillators is a powerful tool for the estimation of energy generation [31], energy transfer as well as the comparison of the performance with an ideal oscillator [32]. Particularly, the area enclosed in the force-displacement plane is useful for the investigation of the involved damping mechanism and the energy dissipated through the oscillator [33, 34]. However, the potential of this graphical tool for characterizing complex nonlinear systems and the associated energy branches, which could lead to a more efficient energy harvesting system, is still unexplored.

In this work, we present a wideband vibration energy harvester that combines nonlinear forces arising from the spring hardening and from repulsive magnetic interactions in a single device. We investigated the complex energy branch structure in this case. It was found that the highest-energy branch might be hidden in the sense that a particular frequency schedule is required to reach it. Using our knowledge of the branch structure, we achieved this high-energy

branch even at a low level of excitation. To characterize the various energy branches experimentally, we took time-resolved measurements of acceleration and voltage outputs. This allows us to plot eye diagrams in a force-displacement plane, where the enclosed areas (eyes) represent the energy transacted within one period of the external drive. The different eye shapes bear useful information about the nonlinearities involved and allow us to efficiently characterise the various energy branches experimentally. The visual representation using eye-diagrams is similar to the well-known thermodynamic cycles in the context of combustion engines [35], where the enclosed area also represents the transacted energy per cycle. By demonstrating the usefulness of eye-diagrams in improving the design of our device, we seek to establish this as a generic tool for wider application in the VEH community and beyond.

5.3 Frequency response: Hidden energy branch

The employed tapered FR4 (Flame Retardant 4) spring architecture (laser micromachined), as shown in Fig. 5.1, exploits the unique stress distribution [36] arising from the tapered geometry to introduce a strong cubic nonlinear restoring force, while maintaining a small footprint of 1.23cm^3. Two pairs of repulsive permanent magnets, one pair fixed to the FR4 spring and the other mounted on movable rails are used (bottom Fig. 5.1) to destabilize the central position of the load. Different parameters of the VEH are listed in Table 5.1. The experimental set-up is shown in Fig. 5.2. The electrodynamical characterization of the developed prototype has been performed with a Bruel and Kjær LDS V455 permanent magnet shaker that emulates real-world vibrations in a laboratory environment. The vibration of the shaker is controlled by an LDS Comet controller, and the output signal from the controller is fed to an LDS PA 1000L power amplifier. With a sweep rate of 1Hz/sec, the frequency of the excitation has been ramped up from 50Hz to 200Hz, and similarly swept back to 50Hz for different amplitudes of excitation (0.1g to 2.0g). A small piezoelectric CCLD accelerometer (DeltaTron 4517-002) placed near the harvester monitors the acceleration over frequency sweeps and feeds it back to the vibration controller (A1). Simultaneously, another accelerometer (A2) placed near the harvester monitors the amplitude of excitation and feeds to the g-meter (Environmental Equipments Ltd. Model 2025). The response from the harvester across an optimized load resistance 2kΩ is recorded with a digital oscilloscope (Picoscope 3000 series). Concurrently, the output from the g-meter is recorded with the same oscilloscope. The 3D printed rails, as shown in Fig. 5.1 have been used to vary the distance d between the repulsive sets of magnets.

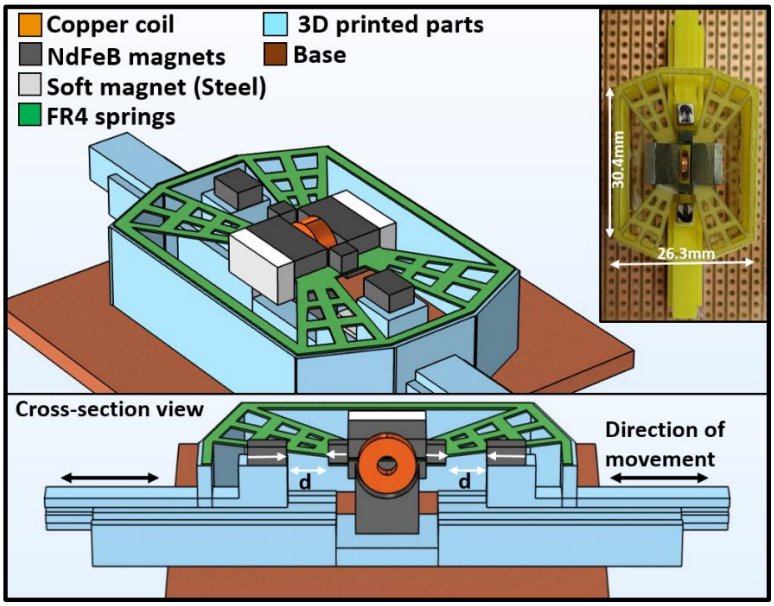


Figure 5.1: Schematic view (top) and cross-section view (bottom) of the VEH. White arrows indicate the polarity of the magnets. The fabricated VEH prototype is shown at the inset.

Fig. 5.3(a) shows the variation of load power during driving frequency sweeps while the distance between the repulsive pairs of magnets and the amplitude of excitation are fixed at 2.5mm and 0.8g, respectively. As the driving frequency is swept up from 50Hz to 200Hz, the extracted power increases slowly (magenta) up to 0.1mW at point A. Beyond this point, the power gradually decreases for higher driving frequencies. On sweeping the frequency of the drive down from 200Hz to 50Hz, the response jumps up at B, and the VEH delivers more power across the load, maximizing up to 0.28mW (grey). The load power then reduces for lower driving frequencies and jumps down at the point C to a low energy state. The top and bottom inset of Fig. 5.3(a) shows the time trace of small amplitude oscillations exhibited by the VEH in the vicinity of A and B.

Interestingly, as shown in Fig. 5.3(b), higher energy output can be achieved by designing a specific drive frequency schedule. While sweeping the frequency of the external drive down from 200Hz, instead of going all the way up to 50Hz, we turn the drive frequency up from 92Hz which is between the two jumping points B and C, as depicted by the arrow in Fig. 5.3(b). During this up sweep, the VEH now delivers large power output (brown) of up to 0.85mW at the point D before falling down to a low energy state. The inset in Fig. 5.3(b) shows the large amplitude of oscillation as the VEH achieves the high-energy state.

Table 5.1: Different parameters of the VEH

Title of the parameters	Values
Dimension of FR4 spring	$38\times23.3\times0.25$ mm^3
Dimension of the coil slot	8×2 mm^2
Outer diameter of the coil	6mm
Inner diameter of the coil	1mm
Number of turns in coil	2500Ω
Coil resistance (Measured)	1032Ω
Dimension of NdFeB N50 magnets	$8\times4\times2$ mm^3
Dimension of soft magnetic blocks	$8\times4.2\times1.6$ mm^3
Dimension of repulsive magnets fixed to FR4	$2\times2\times2$ mm^3
Dimension of repulsive magnets on moving rail	$4\times2\times2$ mm^3
Electromagnetic coupling (Calculated)	15Wb/m
Inertial mass (Measured)	3×10^{-3}kg
Optimized load resistance (Measured)	2kΩ

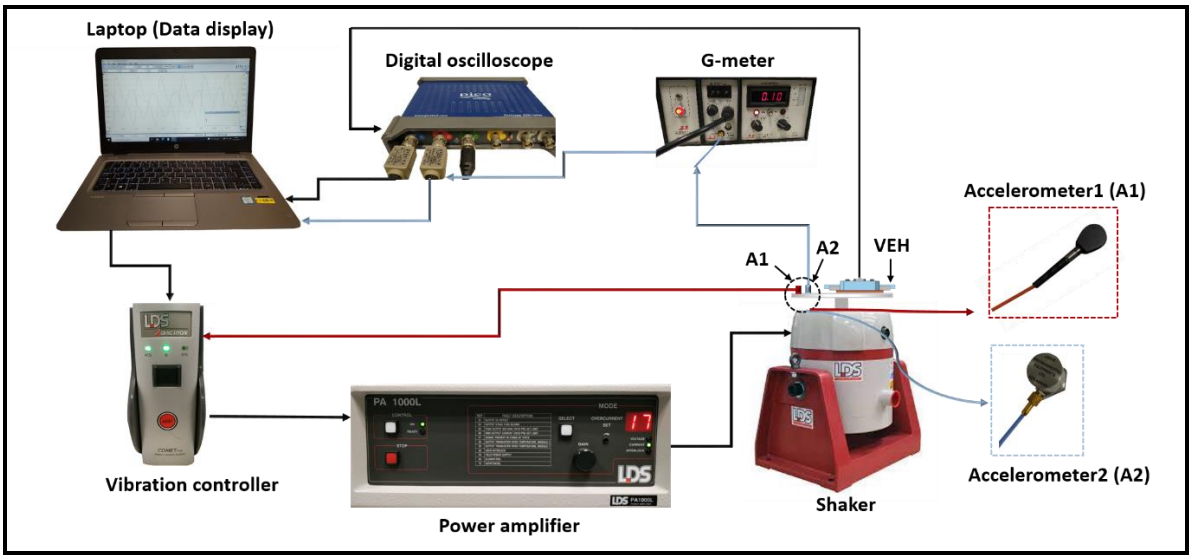


Figure 5.2: Schematic view of the experimental set-up for concurrent experimental measurement of the load voltage and the amplitude of excitation fed to the VEH to construct the eyes.

This high output is not achieved in the simple up and down sweep as shown in Fig. 5.3(a) and it is a consequence of the existence of multiple stable energy branches that are shown

in Fig. 5.4(a). More explicitly, there is a low energy branch EB1 (dark blue) which is the only stable branch at low frequencies and it terminates at the point A. Then there is an intermediate energy branch EB2 (light blue), the only stable branch at the high frequencies which terminates at B. Finally, there is a high-energy output branch EB3 (yellow) which extends from C to D, and can only be selected through particular frequency schedule of the drive. It is interesting to note that, between the points B and A, all the three energy branches co-exist, and the frequency schedule of the drive determines which of the three branches is selected.

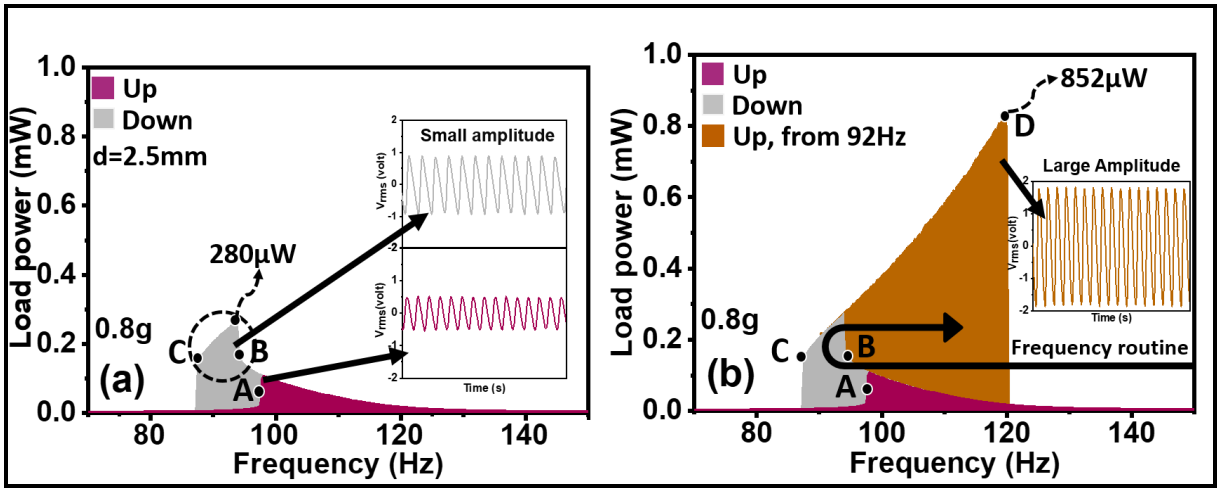


Figure 5.3: Variation of load power with (a) conventional up and down sweep and (b) designed frequency sweep of the drive for 0.8g excitation. The top and bottom inset of (a) are the time traces of the VEH's response on up and down sweep respectively. The inset of (b) shows the time trace of the VEH's response corresponding to large power output.

The energy branches depend also on the acceleration of the drive. In Fig. 5.4(b), we show the extent of the energy branches in the acceleration-frequency plane (with d =2.5mm). The dot symbols mark the experimentally obtained boundaries of the respective energy branches. The linear frequency of the oscillator is at 115Hz for very low acceleration (0.1g) of the external drive. With increasing acceleration, the two energy branches EB1 and EB2 overlap and form a hysteresis region of up to 14Hz at 0.4g. Then at a drive of 0.5g the high-energy branch EB3 starts to emerge (yellow region in Fig. 5.4(b)). As a consequence of its position in the overlap region between EB1 and EB2, the branch EB3 can only be achieved by following the frequency schedule as explained before. This energy branch (EB3) extends up to 76Hz as the external drive increases to 2g and provides the largest energy output of all branches. It should be notes that the high energy branch EB3 aids that system to generate more energy over a considerably wider bandwidth of operable frequencies which makes it a potential candidate for harnessing mechanical energy from broadband vibrations. However, the multistable

characteristics of this VEH makes it difficult to achieve and sustain the high-energy state consistently. Using controlled electrical actuation [28] is a viable route to switch the state of this system to higher energy state, while enabling the VEH to capture substantial mechanical energy from real-world vibrations.

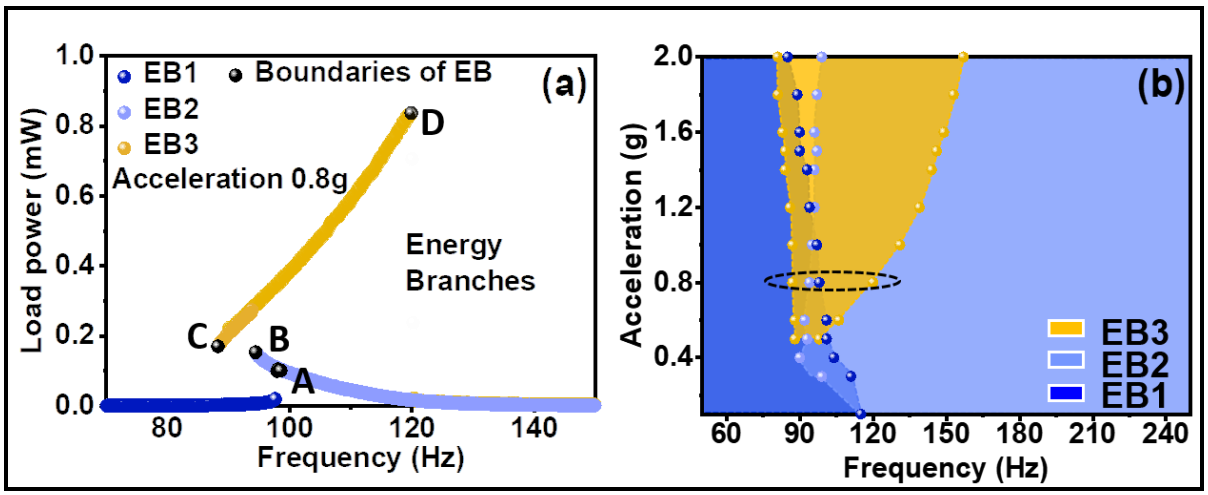


Figure 5.4: (a) Shows the extent of the energy branches EB1, EB2 and EB3 for 0.8g drive amplitude. The branch EB3 is achieved through the designed frequency routine. (b) Shows the mapping of energy branches EB1, EB2 and EB3 on the acceleration-frequency plane.

5.4 Eye diagrams

In order to investigate the dynamical features of the energy branches, and in particular, to compare the energy transaction through these energy branches, we now introduce the concept of eye diagrams, which provide intuitive insight into the various dynamical states based on experimentally observable quantities. Let us consider the following general equation of motion for our driven system,

$$\boldsymbol{m\ddot{z} + c\dot{z} + \gamma I + \frac{\partial U(z)}{\partial z} = F\, sin\omega_0 t} \tag{5.1}$$

Here, z is the displacement, m is the mass of the system, c is the mechanical damping parameter, γ is the electromagnetic coupling factor, I is the current through the load resistor R_L which is expressed as $I = \frac{\gamma \dot{z}}{R_C + R_L}$, $U(z)$ is the potential energy, and $F\, sin\omega_0 t$ is the external drive. Let us now assume that the period of the solution $z(t)$ equals the period of the external drive $T = \frac{2\pi}{\omega_0}$ and let us further assume that at a time T_0 the displacement $z(T_0)$ is at a maximum.

Multiplying both sides of equation (5.1) by $\dot{z}$ and integrating over one period T leads to the condition,

$$\boldsymbol{E_m + E_e = E_f} \tag{5.2}$$

With,

$$\boldsymbol{E_m = \int_{T_0}^{T_0+T} c\,\dot{z}^2\,dt,\;\; E_e = \int_{T_0}^{T_0+T} \gamma\, I(t)\,\dot{z}\,dt,\;\; E_f = \int_{T_0}^{T_0+T} F\,sin\omega_0 t\,dt} \tag{5.3}$$

Here, E_m, E_e and E_f represents the mechanical contribution to the dissipated energy over one period, the electromagnetically transduced energy over one period of the drive, and the energy injected through the external excitation respectively.

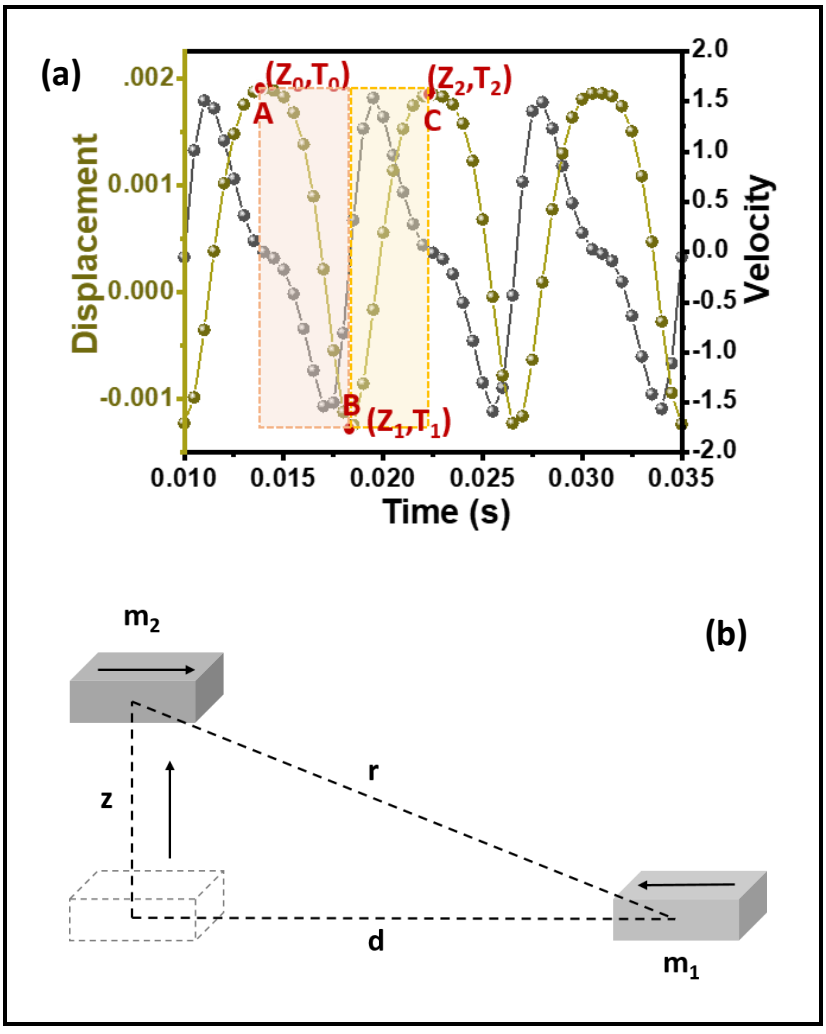


Figure 5.5: (a) Plot of a nonlinear displacement and velocity as a function of time. The point *A* and *B* represents the local maxima, and *C* represents the local minima of the displacement function. (b) The electromagnetic interaction between the fixed and the moving repulsive set of magnets.

Equation (5.2) represents the energy balance of these energies associated with the energy harvesting system. Motivated by similar representations of the energy balance in combustion engines, let us now represent the two sides of equation (5.2) as an enclosed area in a suitable force-displacement plane. We do this by substituting the integration in time t by an integration in the displacement z. Since $z(t)$ is a non-monotonous function, the substitution is split up into time intervals $[T_{k-1}, T_k]$ where, T_k is a maximum (minimum) of $z(T_k)$ for even (odd) k for $k = 0, \ldots\ldots, 2n$, where, n is the number of minima per period T. This also implies $T_{2n} = T_0 + T$. This is illustrated for the case $n = 1$ in Fig. 5.5(a). Defining $\hat{t}_k(z)$ as the inverse function of $z(t)$ on the interval $[T_{k-1}, T_k]$ then yields,

$$\boldsymbol{E_x = \sum_{k=1}^{2n} \int_{z_{k-1}}^{z_k} F_{xk}(z)\, dz} \tag{5.4}$$

Where the subscript x refers to either m, e or f and $F_{mk}(z) = c\dot{z}(\hat{t}_k(z))$, $F_{ek}(z) = \gamma I(\hat{t}_k(z))$, $F_{fk}(z) = F\ sin(\omega_0\ \hat{t}_k(z))$ are the corresponding forces. Equation (5.4) shows that the energies E_m, E_e and E_f appearing in (5.2) can be interpreted intuitively as the areas enclosed by the functions $F_{mk}(z)$, $F_{ek}(z)$ and $F_{fk}(z)$ in a displacement versus force diagram.

5.5 Reduced order model

To describe the dynamics of the system, a Reducer Order Model (ROM) will be derived in this section. We consider the effect of the repulsive pair of magnets as shown in Fig. 5.5(b). We express the potential energy arising from the interaction of the magnetic dipoles m_2 and m_1 which are at a distance d apart. We further consider that $\boldsymbol{m_1} = m_1 r_x$ and $\boldsymbol{m_2} = -m_2 r_x$ and let $r^2 = d^2 + z^2$ where z is the vertical displacement of the magnet m_2 which is fixed on the FR4 spring. The potential energy can be then expressed [37],

$$\boldsymbol{U_{mag}(z) = \frac{\mu_0}{4\pi(d^2+z^2)^{\frac{3}{2}}}\left[\frac{3m_1m_2d^2}{d^2+z^2} - m_1m_2\right]} \tag{5.5}$$

The total potential energy associated with this system considering the contribution from the linear and nonlinear spring force arising from the FR4 spring bending and stretching respectively is expressed as,

$$\boldsymbol{\frac{\partial U_{overall}}{\partial z} = kz + k_n z^3 + \frac{\partial U_{mag}(z)}{\partial z} = kz + k_n z^3 + F_{mag}(z)} \tag{5.6}$$

Then, the equation of motion in (5.1) would take the following form,

$$\ddot{z} + \frac{c}{m}\dot{z} + \frac{\gamma^2}{m(R_C+R_L)}\dot{z} + \frac{k}{m}z + \frac{k_n}{m}z^3 + \frac{F_{mag}(z)}{m} = \frac{F}{m}\,sin\omega_0 t \tag{5.7}$$

With the motivation of re-scaling this equation (5.7), we choose the dimensionless time parameter $\tau = \omega t$,

$$\frac{d}{dt} = \frac{d\tau}{dt}\frac{d}{d\tau} = \omega\frac{d}{d\tau}$$

$$\frac{d^2}{dt^2} = \omega^2\frac{d}{d\tau}$$

$$\omega_0 t = \omega_0\frac{t}{\tau}\,\tau = \frac{\omega_0}{\omega}\tau = \hat{\omega}\tau \tag{5.8}$$

Substituting this back into equation (5.7) and choosing $\omega = \sqrt{\frac{k}{m}}$ we get,

$$\frac{d^2z}{d\tau^2} + \frac{c}{m}\sqrt{\frac{m}{k}}\frac{dz}{d\tau} + \frac{\gamma^2}{m(R_C+R_L)}\sqrt{\frac{m}{k}}\frac{dz}{d\tau} + z + \frac{k_n}{k}z^3 + \frac{F_{mag}(z)}{k} = \frac{F}{k}\,sin\hat{\omega}\tau \tag{5.9}$$

Rescaling z such that $\hat{z} = za$, choosing $\frac{k_n}{k} = a^2$, and simplifying the damping term as $\frac{c}{\sqrt{mk}} + \frac{\gamma^2}{\sqrt{mk}\ (R_C+R_L)} = D_{total}$, the simplified equation of motion takes the following form,

$$\frac{d^2\hat{z}}{d\tau^2} + D_{total}\frac{d\hat{z}}{d\tau} + \hat{z} + \hat{z}^3 + \frac{\mu_0 m_1 m_2 a}{4\pi m d^3 k}\left[\frac{-2\frac{\hat{z}}{a}}{d^2\left(\frac{\hat{z}^2}{a^2d^2}+1\right)^{\frac{5}{2}}} - \frac{5\frac{\hat{z}}{a}\left(2-\frac{\hat{z}^2}{a^2d^2}\right)}{d^2\left(\frac{\hat{z}^2}{a^2d^2}+1\right)^{\frac{7}{2}}}\right] = \frac{Fa}{k}\,sin\hat{\omega}\tau \tag{5.10}$$

We further introduce the non-dimensional parameters $\hat{d} = ad$, $\hat{F} = \frac{Fa}{k}$ and $\left(\frac{3}{4\pi}\right)\left(\frac{\mu_0 m_1 m_2}{k}\right) = \frac{\hat{p}}{a^5}$. We then get the following Reduced Order Model,

$$\frac{d^2\hat{z}}{d\tau^2} + D_{total}\frac{d\hat{z}}{d\tau} + \hat{z} + \hat{z}^3 + \hat{p}\frac{\hat{z}}{\hat{d}^5}\left[\frac{\left(\frac{\hat{z}^2}{\hat{d}^2}-4\right)}{\left(\frac{\hat{z}^2}{\hat{d}^2}+1\right)^{\frac{7}{2}}}\right] = \hat{F}\,sin\hat{\omega}\tau \tag{5.11}$$

The linear and nonlinear parameters that have been used in this model are shown in Table 5.2.

Table-5.2: Parameters and their values used in the ROM

Parameter	Expression	Unit	Value
k	Linear spring stiffness	N/m	2085.6
k_n	Nonlinear spring stiffness	N/m^3	21×10^9
a	$\sqrt{\frac{k_n}{k}}$	m^{-1}	3.2×10^3
c	$2m\omega_0\rho_m$	Ns/m	0.01
D_{total}	$\frac{c}{\sqrt{mk}}+\frac{\gamma^2}{\sqrt{mk}\ (R_C+R_L)}$	Dimensionless	0.0042+0.0297=0.034
$\hat{d}$	$d \times a$ (let $d = 2.0765mm$)	Dimensionless	6.6671
μ_0	Free scape permeability	H/m	12.57×10^{-7}
m_1	Magnetic moment	Am^2	12×10^{-3}
m_2	Magnetic moment	Am^2	7.5×10^{-3}
$\hat{p}$	$\left(\frac{3}{4\pi}\right)\left(\frac{\mu_0 m_1 m_2}{k}\right)a^5$	Dimensionless	4.16×10^{-3}
$\hat{F}$	$\frac{Fa}{k}$ (let $F = 8.6m/s^2$)	Dimensionless	0.0397

This Reduced Order Model (ROM) has now been used to investigate the dynamic response of the system and to check the consistency of the experimental results. The magnitude of the applied force and the distance between the magnets are fixed at 0.86g and 2.0765mm respectively. As shown in Fig. 5.6(a), with traditional up and down sweep of frequency, a sudden jump is observed at $\hat{\omega} = 0.6$ which is marked by the point B. On designing a frequency routine as explained before to achieve the higher energy state, we observed a similar high-energy response from the system, bounded by the points C and D as the drive frequency is swept from 0.56 to 2.2 that is shown in Fig. 5.6(b). Qualitatively this model represents the dynamics involved with the presented nonlinear energy harvesting system that are experimentally shown in Fig. 5.3(b).

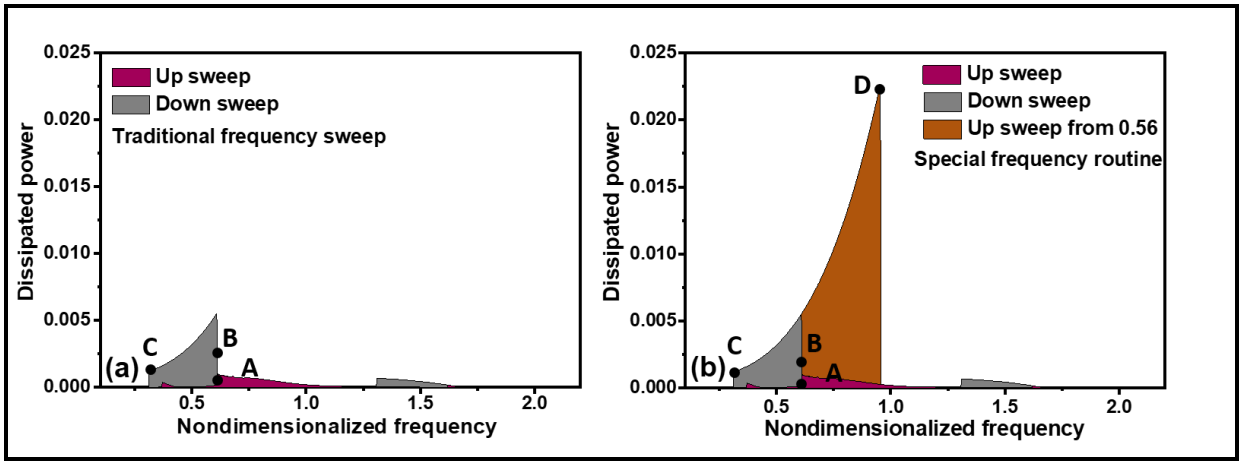


Figure 5.6: (a) Shows the dynamic response of the system using the ROM with traditional frequency sweeps, (b) shows the response with the special frequency routine to achieve the hidden high-energy state.

5.6 Experimental methods, results and discussions

To experimentally determine the function $F_{ek}(z)$, the electromagnetic force, we measure the VEH's output voltage V_L. This allows us to obtain $\dot{z} = \frac{V_L\,(R_C+R_L)}{\gamma R_L}$. We then calculate the displacement z by integrating the velocity $\dot{z}$. Fig. 5.7 depicts the resulting force displacement diagram for fixed acceleration and various values of the interspacing between the repulsive magnets d. The enclosed area corresponds to the energy E_e transduced in one period. As this shape resembles the shape of an eye, we call this an *eye diagram*. The eye for the VEH topology with $d = 2.5mm$ encloses the largest area among all eyes and therefore represents the largest energy transaction into the electrical domain per forcing period.

Further, to experimentally determine the function $F_{fk}(z)$, we measure the external acceleration fed to the oscillator using a piezoelectric accelerometer attached to the base of the excitation source and we multiply this with the mass of the system (3×10^{-3} kg) to obtain $F_{fk}(z)$. The displacement is obtained from the electromotive force measurement as explained before. An example is shown in Fig. 5.8(f) for the two branches EB1 and EB3. The area enclosed in the $F_{fk} - z$ plane stands for the amount of mechanical energy fed to the VEH from the drive. Due to the energy balance in equation (5.2), this corresponds to the area in the $F_{ek} - z$ plane as shown in Fig. 5.8(a). In Fig. 5.8(a)-(j) we compare the eye diagrams in the $F_{ek} - z$ plane with the corresponding diagrams in the $F_{fk} - z$ plane for various frequencies. We observe that the shape of the eye evolves differently for the three different branches that are shown Fig.

5.4(a). In particular, the branch EB3 corresponds to large areas enclosed in Fig. 5.8(d) and (i), while the co-existing branch EB2 only encloses a small area.

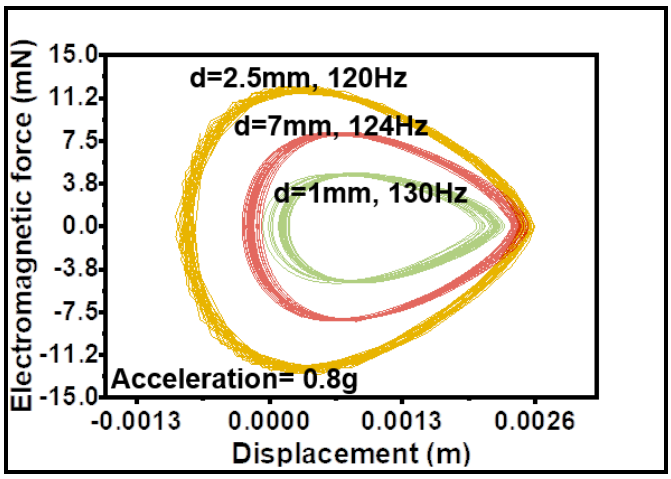


Figure 5.7: The eyes corresponding to the electromagnetically transduced energy for discrete values of *d* (=1mm, 2.5mm, and 7mm) are shown.

The area enclosed by the eye corresponding to this high-energy branch EB3 in Fig.5.8(i) represents 98µJ mechanical energy that is fed into the nonlinear VEH through the external excitation (E_f). On the other hand, the area enclosed by the eye for EB3 in Fig.5.8 (d) depicts the fraction of this mechanical energy, 51µJ, that is transacted into electrical domain by the VEH. The energy conversion efficiency of the VEH (E_e) per cycle. Now we define the energy conversion ratio from mechanical to electrical domain as,

$$\boldsymbol{Energy\ Conversion\ ratio} = \frac{E_e}{E_f} \tag{5.12}$$

It is important to note that this energy E_e is dissipated in both the coil and the load resistance; only the fraction that is dissipated across the load resistor represents the usable energy which could be utilized in a target application. The energy values as mentioned above obtained from the area of the reflects an energy conversion efficiency of 0.52. On the other hand, the eye corresponding to EB2 in Fig.5.8(i) represents only 2.5µJ mechanical energy acquired from the external force; only 0.3µJ of this energy is transacted as usable electrical energy, yielding a conversion efficiency of 0.12. Similarly, the EB1 only converts 0.9µJ energy into the electrical domain, a fraction of 8µJ energy that the drive provides to the VEH, resulting a conversion efficiency of only 0.11. Interestingly, this efficiency increases to 0.91 when the energy contribution from the energy branch EB3 is taken into account. The conversion efficiency

corresponding to each energy branches for the 90Hz, 100Hz, 110Hz and 120Hz drive frequency has been summarized in Table 5.3.

Furthermore, the shape of the eye diagrams for EB3 deviate strongly from the simple ellipse, which is characteristic for a harmonic oscillator. We therefore conclude that EB3, which is only obtained through a special frequency schedule, is inherently connected to the nonlinear force in our system. The eye diagrams are therefore a useful tool to experimentally explore the nonlinear character of the various co-existing branches. To connect to the well-studied linear case, let us consider the shape of the eyes corresponding to the energy branch EB1 in Fig.5.8(a) and (f). They are close to the shape of an ellipse, which suggests that the VEH performs harmonic oscillations, similar to a simple linear harmonic oscillator. In this case, the phase difference between displacement and the input excitation determines the enclosed area and thereby the energy transacted during one cycle. This corresponds to the well-known role of the phase in the linear oscillator, where a phase difference of $\frac{\pi}{2}$ corresponds to the peak of the resonance. It is to be noted that the phase is a useful tool for linear oscillators where the periodic signals only consist of a single harmonic component, i.e. $F(t) = F_0 \sin(\omega t)$; in contrast for a nonlinear system in general multiple frequency components are present, for example $F(t) = F_0 \sin(\omega\, t) + F_1 \sin(2\omega t + \varphi)$, and the relationship between two signals cannot be expressed in terms of a single phase. We have included a mathematical example here for explaining the role of phase in linear and nonlinear oscillators. Let us consider that the response of the system is expressed through the displacement $d(t) = d_0 \sin(\omega t - \varphi)$ where ω is the frequency and φ is the phase difference between the applied force and the response of the system. We can find the energy that is injected into the system through the external drive,

$$\boldsymbol{E_{linear} = \int_0^T F(t)d(t)dt}$$

$$\boldsymbol{E_{linear} = \frac{F_0 d_0 \omega}{2} \int_0^T [sin(2\omega t - \varphi) + sin\varphi]\, dt = \frac{F_0 d_0 \omega T}{2} sin\varphi} \qquad (5.13)$$

This shows the contribution of phase φ in controlling the energy transaction and hence in influencing the performance of such a linear system. Let us now visit a nonlinear system considering the displacement of the form $d(t) = d_0 \sin(\omega t - \varphi_1) + d_0 \sin(2\omega t - \varphi_2)$ which comprises higher harmonic components along with different phases φ_1 and φ_2. Now considering the same external forcing as that of the linear system, the energy fed into this nonlinear system can be expressed as,

$$E_{Nonlinear} = \int_0^T F_0 sin(\omega t)[\omega d_0 \cos(\omega t - \varphi_1) + 2\omega d_0 \cos(2\omega t - \varphi_2)]dt$$
$$= \frac{F_0 d_0 \omega}{2} \int_0^T [\sin(2\omega t - \varphi_1) + sin\varphi_1]\, dt + \frac{2F_0 d_0 \omega}{2} \int_0^T [\sin(3\omega t - \varphi_2) + sin\varphi_2]\, dt$$
$$= \frac{F_0 d_0 \omega T}{2} sin\varphi_1 + F_0 d_0 \omega T\, sin\varphi_2 \quad (5.14)$$

This point towards the fact that it is not straightforward to define the relation of the energy transaction through a nonlinear system with the phase associated with the signal/signals. In fact, owing to the presence of higher harmonic components, the energy fed to the system depends on multiple phases, which in this example is φ_1 and φ_2. Hence, the phase is not a well-defined quantity in the context of nonlinear systems. For linear systems, the signals are often expressed in terms of the amplitude and frequency, along with the phase. The resonance for such a linear transducer takes place when the voltage and current signal are in-phase [38]. In this context, the well-known Lissajous's figure is a useful tool that are used to graphically depict the relation of the phase difference between the driving signal and the response to the resonance of the system [39].

All of the eyes from the high-energy state EB3 have asymmetrical shape, which indicates that the strong nonlinear restoring force arising from the stretching of the spring as well as from the repulsive magnetic interactions predominates here. Similarly, the energy state EB2 possess very little asymmetry in the eyes corresponding again to weak nonlinearities. It is to be noted that the phase is not a well-defined quantity in case of the nonlinear oscillators owing to the non-harmonic nature of the associated signals. Hence, it is not a straightforward route to correlate the performance of the system with the phase.

Table-5.3: Efficiency of energy transaction from mechanical to electrical domain through different energy branches

Frequency	EB1	EB2	EB3
90Hz	11%		91%
100Hz	-	53%	63%
110Hz	-	32%	62%
120Hz	-	11%	52%

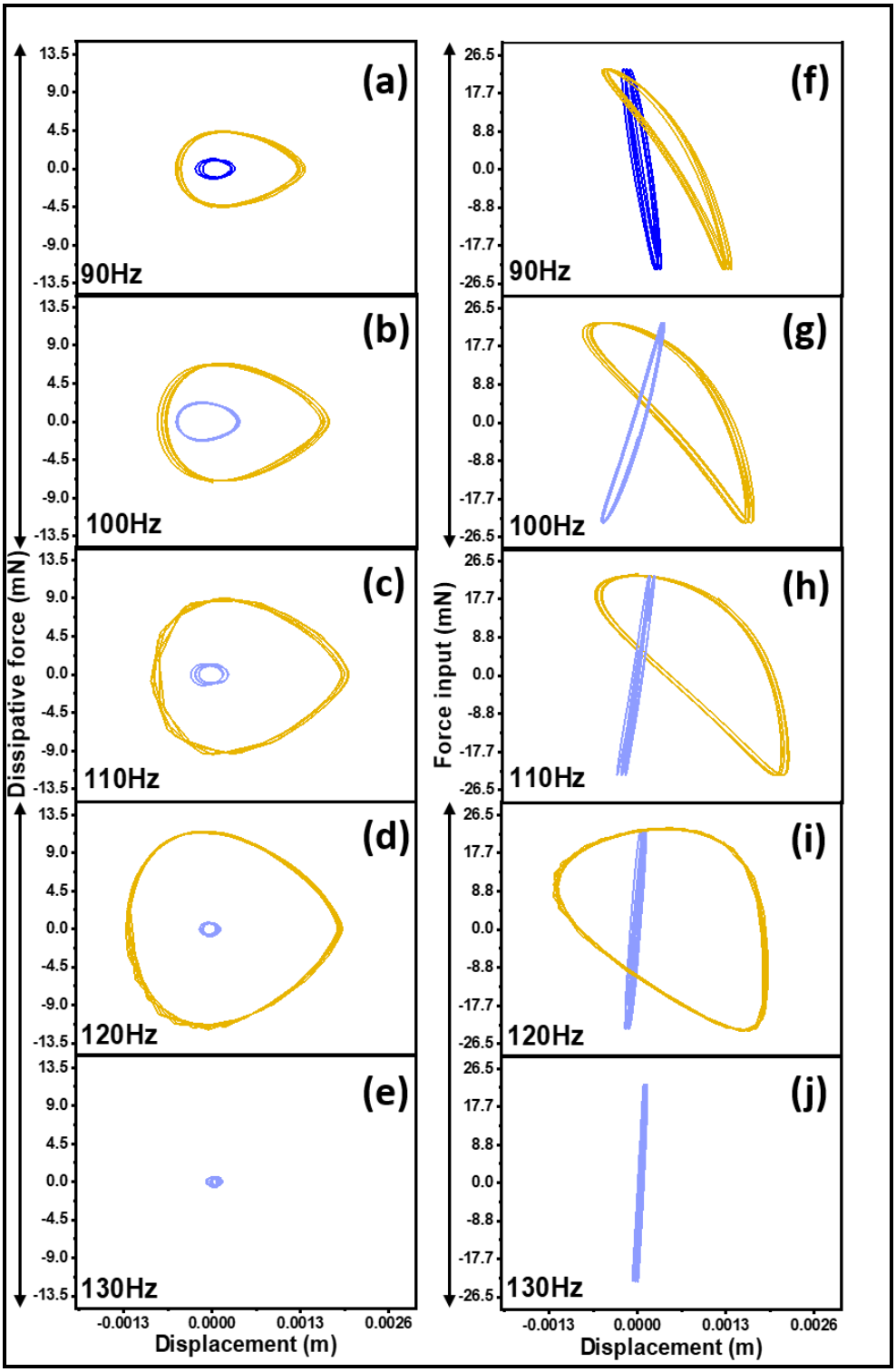


Figure 5.8: With d=2.5mm, the eyes corresponding to electrical energy dissipating through involved damping are shown in (a)-(e). The eyes representing mechanical energy injection into the VEH are shown in (f)-(j). The colours of these eyes correspond to the different energy branches depicted in Fig.2(a) and Fig.3.

As discussed above, the shape of the eyes are different for each energy branch. This fact can be exploited for the discovery of previously unknown branches. Let us for example

revisit the frequency down-sweep in Fig.5.3(a). In this case, the small jump in the load power at point *B* reveals the presence of another branch. Such a jump is however not guaranteed to be visible in all cases where a transition between branches occurs. In contrast, if we consider the transition between the light blue eye in Fig.5.8(g) for 100Hz and the yellow eye in Fig. 5.8(f) for 90Hz, we see that the shape and orientation of the eye markedly changes in addition to the enclosed area. This provides therefore a much stronger signal for a branch change and in this case prompts us to further explore the hidden branch EB3, which turns out to feature the largest energy output available in this device.

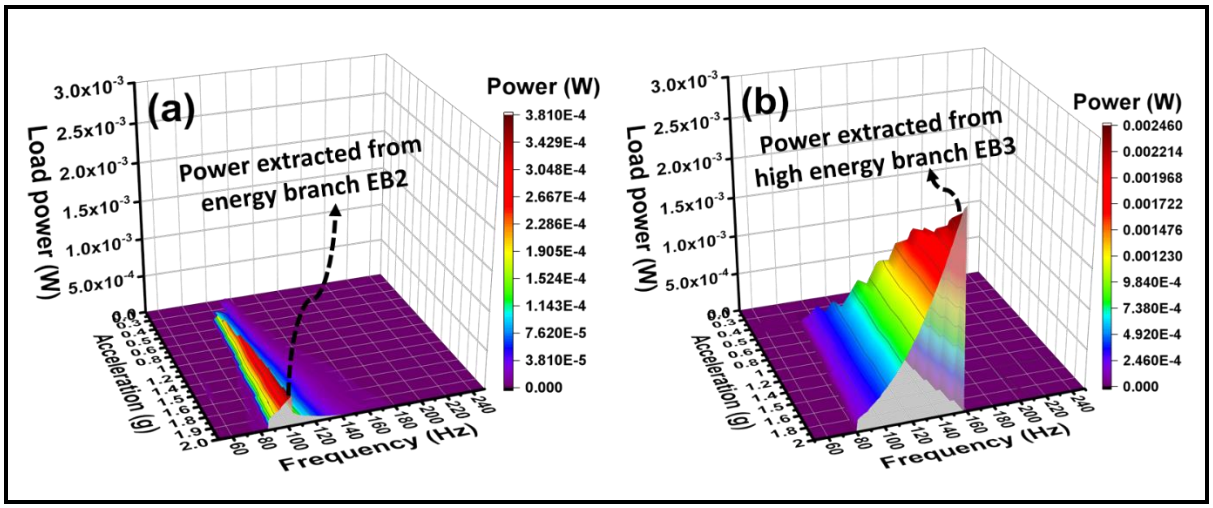


Figure 5.9: Variation of the deliverable power of the VEH as a function of the frequency and amplitude of the drive for d =2.5mm, (a) with conventional up and down frequency sweep and (b) with specifically designed frequency routine.

In order to illustrate the difference in power output obtainable for given input frequency and acceleration, let us consider Fig.5.9(a) and (b). In Fig. 5.9(a) we show the load power as the drive frequency is simply swept down from 250Hz to 50Hz, while the acceleration is fixed for each sweep. On the other hand, in Fig.5.9(b) the power obtained by following the specific frequency schedule (to achieve higher energy state) as explained before is shown. We observe that in the regime, where the branches EB2 and EB3 overlap, the branch EB3 has a much higher energy output which is shown in Fig. 5.9(b). For example, at 0.5g drive amplitude, the peak load power approximately doubles from 0.18mW to 0.33mW, when the system follows EB3 instead of EB2. The delivered power increases to 1.3mW for 1g, with a 44Hz bandwidth. As shown in Fig. 5.9(b), the load power further increases with increasing acceleration up to 2.8mW while offering a large bandwidth of up to 76Hz at 2g. Such wide operable frequency bandwidth of this device corresponding to the branch EB3 offers the unique benefit of using this device for harnessing real-world vibrations where apriori knowledge of the comprising frequency

components are not available. In the weakly excited regime, this VEH essentially behaves as a linear resonator. The obtainable frequency bandwidth is as low as 3.19Hz for 0.1g excitation, which restrains the efficiency of this VEH for harvesting energy from broadband vibrations. Hence, bandwidth is a key performance metric, which outlines the advantage of employing such nonlinear devices compared with its linear counterpart which despite of meeting the resonance condition offers low bandwidth of frequency.

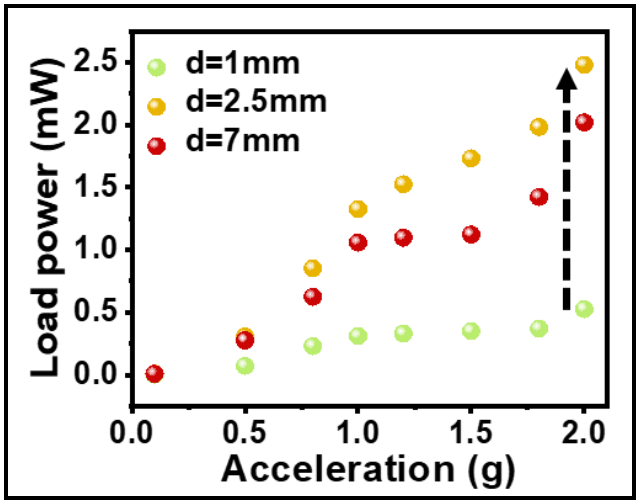


Figure 5.10: The performance comparison of the VEH topologies in terms of the extracted power across a resistive load 2kΩ for different values of interspacing between the repulsive magnets d (=1mm, 2.5mm, and 7mm).

Fig. 5.10 shows a comparison of peak load power obtained from this VEH for different values of the interspacing between the repulsive magnets d. When the magnets are very close ($d = 1mm$), the strong repulsive force between the magnets results in very low electrical power generation. For example, for a 1g drive, the extracted peak load power is only 0.32mW. In contrast, if the magnets are at a large distance ($d = 7mm$), the VEH exhibits larger oscillations about the equilibrium state. This improves the deliverable power to 1mW. As the magnets are placed at an intermediate value of $d = 2.5mm$, the associated nonlinear effects both from the spring stretching and the magnetic interaction result in a large peak load power of 1.3mW that is extracted from the energy branch EB3. This corresponds to approximately 30% and 300% improvement in the power outcome as compared with the VEH topology with $d = 7mm$ and $d = 1mm$, respectively. Therefore, this demonstrates the effectiveness of using a repulsive pair of magnets at an optimized distance to enhance the overall performance of the VEH.

5.7 Conclusion

To summarize, a wideband vibration energy harvester is presented in this chapter with multiple nonlinear force acting on the system that gives rise to a number of energy branches. Some of these branches are “hidden” in the sense that they are not fully reached by simple frequency up or down sweeps. We designed a particular frequency schedule to reach those branches, which substantially improved the energy output. The different branches have been experimentally characterised through eye diagrams, which directly illustrate the magnitude of the transacted energy per cycle. The energy-harvesting device yields 1.3mW power (at 1g) across a suitable load resistor providing an enhanced operable frequency bandwidth of 44Hz. This energy harvesting system transduces mechanical energy into usable electrical energy at a conversion efficiency of 52%.

5.8 References

[1] M. Gao, P. Wang, Y. Cao, R. Chen, and D. Cai, "Design and verification of a rail-borne energy harvester for powering wireless sensor networks in the railway industry," *IEEE Transactions on Intelligent Transportation Systems,* vol. 18, no. 6, pp. 1596-1609, 2016.

[2] B. Yang, Z. Yi, G. Tang, and J. Liu, "A gullwing-structured piezoelectric rotational energy harvester for low frequency energy scavenging," *Applied Physics Letters,* vol. 115, no. 6, p. 063901, 2019.

[3] A. Cammarano, S. A. Neild, S. G. Burrow, and D. J. Inman, "The bandwidth of optimized nonlinear vibration-based energy harvesters," *Smart Materials and Structures,* vol. 23, no. 5, p. 055019, 2014/03/25 2014.

[4] F. Cottone, H. Vocca, and L. Gammaitoni, "Nonlinear Energy Harvesting," *Physical Review Letters,* vol. 102, no. 8, p. 080601, 02/23/ 2009.

[5] S. Roy, P. Podder, and D. Mallick, "Nonlinear energy harvesting using electromagnetic transduction for wide bandwidth," *IEEE Magnetics Letters,* vol. 7, pp. 1-4, 2015.

[6] B. Marinkovic and H. Koser, "Smart Sand—A Wide Bandwidth Vibration Energy Harvesting Platform," *Applied Physics Letters - APPL PHYS LETT,* vol. 94, 03/09 2009.

[7] K. Fan, Q. Tan, Y. Zhang, S. Liu, M. Cai, and Y. Zhu, "A monostable piezoelectric energy harvester for broadband low-level excitations," *Applied Physics Letters,* vol. 112, no. 12, p. 123901, 2018/03/19 2018.

[8] D. Mallick, A. Amann, and S. Roy, "A nonlinear stretching based electromagnetic energy harvester on FR4 for wideband operation," *Smart Materials and Structures,* vol. 24, no. 1, p. 015013, 2014/11/27 2014.

[9] B. Yan *et al.*, "Scavenging vibrational energy with a novel bistable electromagnetic energy harvester," *Smart Materials and Structures,* vol. 29, no. 2, p. 025022, 2020.

[10] P. Podder, A. Amann, and S. Roy, "A bistable electromagnetic micro-power generator using FR4-based folded arm cantilever," *Sensors and Actuators A: Physical,* vol. 227, pp. 39-47, 2015/05/15/ 2015.

[11] S. Roy, P. Podder, D. Mallick, and A. Amann, "Broadband vibrational energy harvesting device combining multiple nonlinearity," ed: Google Patents, 2021.

[12] S. Zhou, J. Cao, D. J. Inman, J. Lin, S. Liu, and Z. Wang, "Broadband tristable energy harvester: Modeling and experiment verification," *Applied Energy,* vol. 133, pp. 33-39, 2014/11/15/ 2014.

[13] Z. Zhou, W. Qin, and P. Zhu, "Harvesting performance of quad-stable piezoelectric energy harvester: Modeling and experiment," *Mechanical Systems and Signal Processing,* vol. 110, pp. 260-272, 2018/09/15/ 2018.

[14] H. Deng *et al.*, "Poly-stable energy harvesting based on synergetic multistable vibration," *Communications Physics,* vol. 2, no. 1, p. 21, 2019/02/26 2019.

[15] C. Jeevarathinam, S. Rajasekar, and M. Sanjuan, "Theory and numerics of vibrational resonance in Duffing oscillators with time-delayed feedback," *Physical Review E,* vol. 83, no. 6, p. 066205, 2011.

[16] L. Pickup *et al.*, "Optical Bistability under Nonresonant Excitation in Spinor Polariton Condensates," *Physical Review Letters,* vol. 120, no. 22, p. 225301, 05/30/ 2018.

[17] F. Mueller, S. Heugel, and L. J. Wang, "Optomechanical stochastic resonance in a macroscopic torsion oscillator," *Physical Review A*, vol. 79, no. 3, p. 031804, 03/23/ 2009.
[18] T.-X. Lu, Y.-F. Jiao, H.-L. Zhang, F. Saif, and H. Jing, "Selective and switchable optical amplification with mechanical driven oscillators," *Physical Review A*, vol. 100, no. 1, p. 013813, 2019.
[19] R. L. Harne and K. W. Wang, "Dipteran wing motor-inspired flapping flight versatility and effectiveness enhancement," *Journal of The Royal Society Interface*, vol. 12, no. 104, p. 20141367, 2015/03/06 2015.
[20] L. Chua, "Nonlinear circuits," *IEEE Transactions on Circuits and Systems*, vol. 31, no. 1, pp. 69-87, 1984.
[21] S. Houri, D. Hatanaka, M. Asano, and H. Yamaguchi, "Demonstration of multiple internal resonances in a microelectromechanical self-sustained oscillator," *Physical Review Applied*, vol. 13, no. 1, p. 014049, 2020.
[22] S. Wieczorek, B. Krauskopf, T. B. Simpson, and D. Lenstra, "The dynamical complexity of optically injected semiconductor lasers," *Physics Reports*, vol. 416, no. 1-2, pp. 1-128, 2005.
[23] U. Parlitz and W. Lauterborn, "Superstructure in the bifurcation set of the Duffing equation ẍ + dẋ + x + x3 = f cos(ωt)," *Physics Letters A*, vol. 107, no. 8, pp. 351-355, 1985/02/25/ 1985.
[24] K. Wiesenfeld, P. Colet, and S. H. Strogatz, "Frequency locking in Josephson arrays: Connection with the Kuramoto model," *Physical Review E*, vol. 57, no. 2, p. 1563, 1998.
[25] R. Potekin, K. Asadi, S. Kim, L. A. Bergman, A. F. Vakakis, and H. Cho, "Ultrabroadband microresonators with geometrically nonlinear stiffness and dissipation," *Physical Review Applied*, vol. 13, no. 1, p. 014011, 2020.
[26] T. Yang and Y. Bellouard, "Laser-induced transition between nonlinear and linear resonant behaviors of a micromechanical oscillator," *Physical Review Applied*, vol. 7, no. 6, p. 064002, 2017.
[27] A. Marchionne, P. Ditlevsen, and S. Wieczorek, "Synchronisation vs. resonance: Isolated resonances in damped nonlinear oscillators," *Physica D: Nonlinear Phenomena*, vol. 380, pp. 8-16, 2018.
[28] D. Mallick, A. Amann, and S. Roy, "Surfing the High Energy Output Branch of Nonlinear Energy Harvesters," *Physical Review Letters*, vol. 117, no. 19, p. 197701, 11/04/ 2016.
[29] J. Wang and W.-H. Liao, "Attaining the high-energy orbit of nonlinear energy harvesters by load perturbation," *Energy Conversion and Management*, vol. 192, pp. 30-36, 2019/07/15/ 2019.
[30] J. P. Udani and A. F. Arrieta, "Sustaining high-energy orbits of bi-stable energy harvesters by attractor selection," *Applied Physics Letters*, vol. 111, no. 21, p. 213901, 2017/11/20 2017.
[31] W. Kwak and Y. Lee, "Optimal design and experimental verification of piezoelectric energy harvester with fractal structure," *Applied Energy*, vol. 282, p. 116121, 2021.
[32] A. H. Hosseinloo and K. Turitsyn, "Fundamental limits to nonlinear energy harvesting," *Physical Review Applied*, vol. 4, no. 6, p. 064009, 2015.
[33] Z. Li, L. Zuo, G. Luhrs, L. Lin, and Y.-x. Qin, "Electromagnetic energy-harvesting shock absorbers: design, modeling, and road tests," *IEEE Transactions on vehicular technology*, vol. 62, no. 3, pp. 1065-1074, 2012.
[34] X. Lv, L. Liu, Y. Liu, and J. Leng, "Dielectric elastomer energy harvesting: maximal converted energy, viscoelastic dissipation and a wave power generator," *Smart Materials and Structures*, vol. 24, no. 11, p. 115036, 2015.
[35] B. Andresen, R. S. Berry, A. Nitzan, and P. Salamon, "Thermodynamics in finite time. I. The step-Carnot cycle," *Physical Review A*, vol. 15, no. 5, p. 2086, 1977.
[36] K. Paul, A. Amann, and S. Roy, "Tapered nonlinear vibration energy harvester for powering Internet of Things," *Applied Energy*, vol. 283, p. 116267, 2021/02/01/ 2021.
[37] D. J. Griffith and G. Ruppeiner, "Introduction to electrodynamics," ed: American Association of Physics Teachers, 1981.
[38] G. A. Hallock and M. A. Meier, "Resonant transducers for solid-state plasma density modulation," *Review of Scientific Instruments*, vol. 87, no. 4, p. 044902, 2016.
[39] H. Liu *et al.*, "A Fe–Ga alloy cantilever film vibration harvester with a double-stage signal processing circuit and its main performance testing," *Mechatronics*, vol. 63, p. 102264, 2019.

Chapter 6: Design optimization of MEMS EM-VEH using Patterned Magnet Array

This chapter is based on the following publications- K. Paul, D. Mallick and S. Roy, "Performance improvement of MEMS Electromagnetic Vibration Energy Harvester using optimized patterns of micromagnet array," *IEEE Magnetics Letters*, vol. 12, pp. 1-5, 2021.
D. Mallick, K. Paul, T. Maity, and S. Roy, "Magnetic performances and switching behavior of Co-rich CoPtP micro-magnets for applications in magnetic MEMS," *Journal of Applied Physics*, vol. 125, no. 2, p. 023902, 2019.
S. Roy, D. Mallick, and K. Paul, "MEMS-Based Vibrational Energy Harvesting and Conversion Employing Micro-/Nano-Magnetics," *IEEE Transactions on Magnetics,* vol. 55, no. 7, pp. 1-15, 2019.

6.1 Introduction

In the conventional Meso/MEMS scale electromagnetic vibration energy harvesters, sintered permanent magnet (for example NdFeB block) is often used which hinders the path of further miniaturization as well as poses great challenge in batch fabrication. Although thin film of permanent magnets allows ease in batch fabrication, but the detrimental effect of demagnetizing field, which arises due to the geometry of the films, drastically reduces the obtainable stray magnetic fields from the thin film. This reduces the electromagnetic coupling with the coil and further degrades the overall performance of the vibration energy harvester. Optimization of patterns and integration of patterned arrays of micromagnets potentially could circumvent this issue. However, there is a distinct knowledge gap in providing a suitable design optimization study to enhance the performance of the device. Hence, in this chapter, we bridge this gap through detailed analytical framework and thorough finite element analysis. We provide an insight into the manipulation of the stray magnetic fields emerging from the patterned array of magnets that will systematically maximize the magnetic flux density at a precise location in the MEMS electromagnetic vibration energy harvesters (EM-VEH). This enhances the electromagnetic interaction with the coil dramatically resulting in substantially improved output power while making the harvesters a potential candidate for powering wireless sensor platform for Internet of Things.

6.2 Challenge with integrating conventional bulky Permanent Magnets

In previous chapters, the macro/meso-scale implementation of EM VEH devices has been discussed. The micro-scale implementation of such devices remains a challenge. One of the

major reasons behind is the lack of high-performance micro-magnets required for such devices. As the ambient vibrations have their energy spread over a wide range of frequency, with a clear predominance over the low frequency domains, so to harness these vibrations effectively, bulky rare earth based magnets are used conventionally in the electromagnetic transducers. Apart from the high temperature requirement in the traditional fabrication, these magnets also do not allow easy scaling down as the electromagnetic forces scales down dramatically with volume, which hinders the implementation of a fully integrated MEMS energy harvesting system. Furthermore, it is a well-known fact in MEMS that the surface related phenomenon have a favourable scaling effect as compared to volume related effects. This is due to the fact that surface (S) scales as the square of length (L) whereas volume (V) scales as the cube of length. Therefore, as L decreases, its S/V ratio increases. Unfortunately, the strength of magnetic flux of a magnet depends on its volume, even though the magnetic flux density available from a permanent magnet is independent of its size. There are several reported works that have already demonstrated the effect of scaling laws on the performance of EM generators [1, 2]. Arnold [2] derived the power scaling law for oscillatory resonant EM generators. According to [3], the mechanical damping effect is dominating when the device is scaled down to micro/MEMS scale, on the other hand for a large scale device the electrical damping dominates among other dampers. Hence, the power output from a MEMS scale generator is restricted by large mechanical damping as the mass and velocity decreases. This indirectly owes to the inability to produce large electromagnetic coupling at the MEMS scale. Revisiting the expression for electrical damping from chapter-2,

$$c_e = \frac{n^2 \left(\frac{d\emptyset}{dz}\right)^2}{R_c + R_L + j\omega L} \tag{6.1}$$

We can conclude that the damping largely depends on the coil parameters such as the number of coil turns n and the coil resistance R_c, along with the electromagnetic coupling, which is governed by the spatial magnetic flux gradient $\frac{d\emptyset}{dz}$. Hence, optimizing the electromagnetic interaction between the coil and magnets is of utmost importance to enhance the performance of these energy harvesters in MEMS scale.

Another great challenge in implementing a high-efficiency MEMS scale electromagnetic VEH is the shape dependent detrimental effect on microscale magnets. A magnetic element of finite length gives rise to an opposing internal magnetic field due to the creation of poles near its edges which is called the 'Demagnetizing field' (**H_d**) [4] as shown in Fig. 6.1.

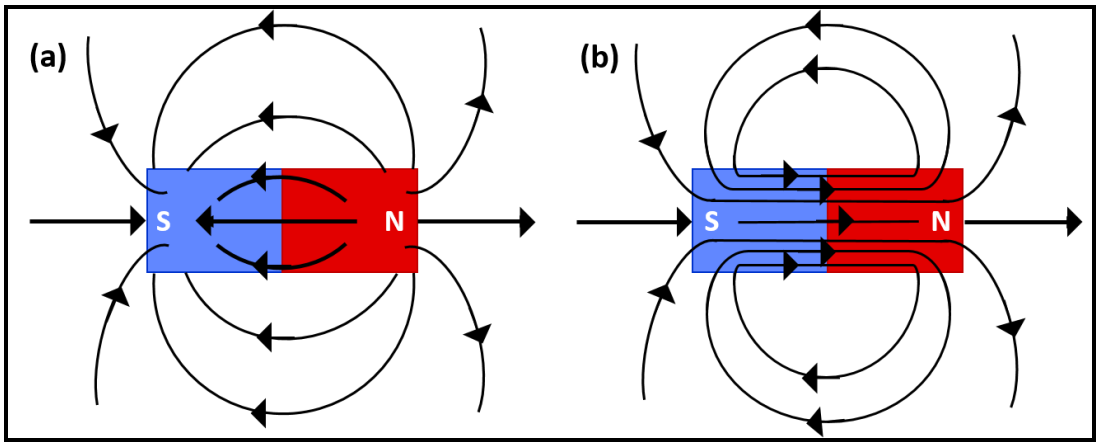


Figure 6.1: The lines in figure (a) shows the magnetic field H inside and outside the material and that of figure (b) shows the magnetic induction B in and around the magnetic material. Inside material the B and H lines point in opposite direction.

The flux closing path of minimum energy between two poles passing through the specimen causes this field which depends on the magnetization strength (**M**) in the material and on the shape of the magnetic element, and it effectively reduces the overall magnetic field (**H**) expected from the magnet. The following relations-can verify this,

$$\boldsymbol{H_d = -D.M} \tag{6.2}$$

$$\boldsymbol{H = H_{app} - D.M} \tag{6.3}$$

$$\boldsymbol{(BH) = \mu_0 D\,(1-D)M^2} \tag{6.4}$$

Where, $\mathbf{H_{app}}$ is the applied magnetic field, which gets affected due to this demagnetizing field, **D** is the demagnetization factor, which depends on the geometry of the sample and has a value between 0 and 1 depending on the shape of the magnet. Equation (6.4) shows the effect of the demagnetizing field on the energy product of the magnetic material. Dipole-dipole interaction and directional dependency of the geometrically induced demagnetizing field in ferromagnetic materials engenders shape anisotropy in the magnetic specimen, which is not an intrinsic property of the material unlike the magnetocrystalline anisotropy. Influence of this opposing field is even more prominent in the case of thin film magnetic materials. Thin films with perpendicular and parallel magnetization have $D \sim 1$ and $D \sim 0$ respectively, which leads to vanishing energy product for both the case. Hence, uniformly magnetized thin film of magnets produces stray magnetic fields mostly from the edges, resulting in wastage of a large part of the magnetic material leading to a poor performance of the integrated energy harvester.

Therefore, the key challenge lies in the development of a CMOS compatible batch fabricated hard magnetic material with high-energy product as a promising alternative to the rare earth based magnets in the MEMS vibration energy harvesters.

6.3 Patterned array of Micromagnets

In order to maximize the interaction between the coil and magnets and to reduce the effect of demagnetizing field on the performance of the harvester unit, an appealing solution is to replace the block or thin film of magnets by array of magnets, thereby reducing the wastage of magnetic material and intensifying the stray magnetic field within a small volume. We propose to replace a block of permanent magnet by micro-patterned array of magnets, diminishing the demagnetization effect and enhancing the magnetic stray field. In that case, the magnetic flux density can be intensified over a small space due to increase of the edges of magnetic elements, which is shown quantitatively in Fig. 6.2 using FEM simulation in COMSOL Multi Physics solver. In the simulation, the total volume of the whole block (on the left panel) and square magnetic array (on the right panel) are kept the same, including the interspacing between the magnetic elements in the array. For the block, a 1×1 mm^2 structure is considered, while the thickness is kept fixed at 10μm for all the simulations. In case of the patterned structure, 50×50 μm^2 square shaped structures are considered while the inter-space between successive patterned elements is assumed to be 50 μm as well. The magnetization direction is taken to be along the perpendicular to the plane of the magnet. The coercivity (H_C) and remanent magnetic induction (B_R) values used in the simulation are taken to be 268 kA/m and 0.4T [5]. It is observed, that the stray field that appears is only from the edge of the magnets (as shown in the bottom-left panel of Fig.6.2), which validates the aforementioned theory. The scale bar is kept same for both whole block and patterned magnets for even comparison. While the largest magnetic flux density appears at the edge region, which is about 0.4 mT, it is reduced almost to zero in other regions, as can be also observed through the cross-sectional view. The plots at the bottom of Fig. 6.2 shows the magnetic flux density along a line through the middle of the magnetic structures on the surface of the magnets. For the block magnet, the sharp peaks of the maximum field are observed exactly above the edge of the block magnets whereas the field reduces to zero elsewhere. In case of the patterned magnet, these peaks are observed at each edge of the patterned structure periodically.

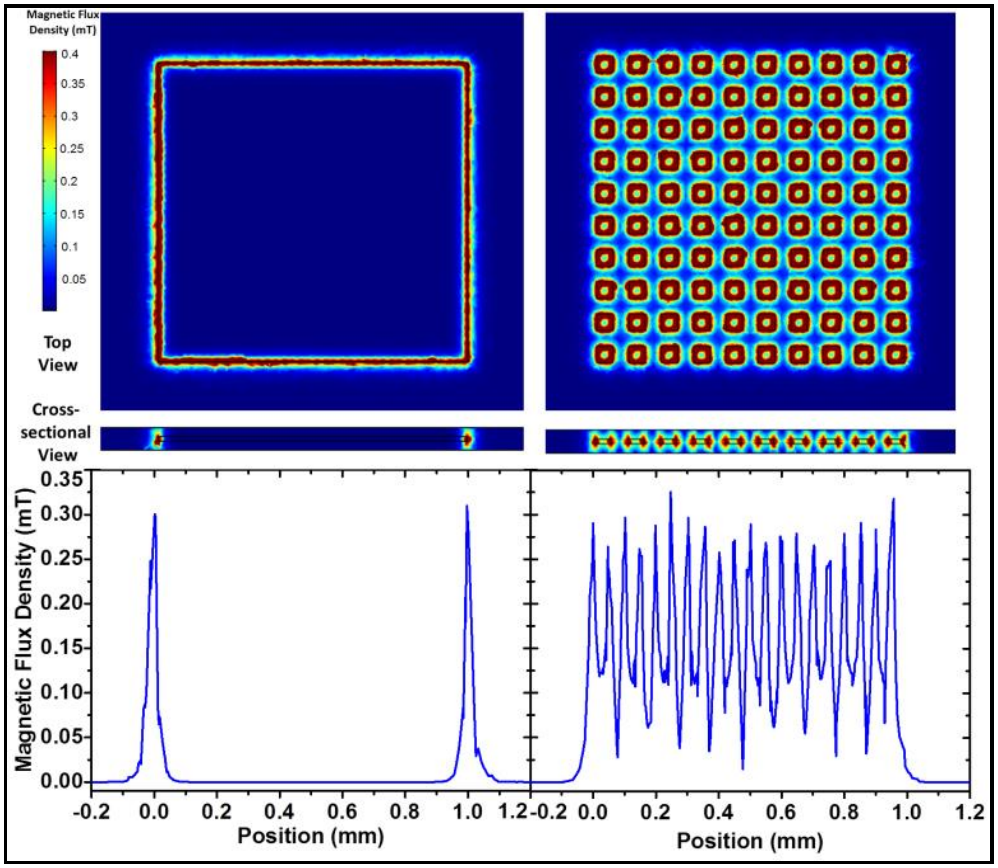


Figure 6.2: FEM simulation using COMSOL to show the advantage of using micro-patterns (right) compared to a block (left) of integrated permanent magnet, minimizing the demagnetization field. Both top view (on surface of the magnets) and cross-sectional view are shown. Plots below show the variation of magnetic flux density along a line through the middle of the magnetic structures.

The distribution of the magnets and the shape/geometry of each of the micromagnets influence the obtainable magnetic flux density from the magnet array. Hence, we studied the effect of the height of elements in the array and the interspacing between the elements, which is shown in Fig. 6.3. The magnetic flux density has been mapped at an observation height of 10μm from the top surface of the magnetic elements. The observation plane is fixed at this height to gain a deep insight on the available magnetic flux so that the coil could be suitably placed at this height for facilitating the electromagnetic transduction. From Fig. 6.3(a), we can clearly observe that- (i) if the patterns are closely spaced (such as 10μm element distance) then the magnetostatic interaction between the adjacent/neighbouring elements degrades the stray field arising from each of the magnets, and magnetic response of the patterned array resembles that of a block of magnet with effective stray magnetic field arising mostly from the outmost edges which are relatively free from any prominent magnetostatic interaction. In this case, if we increase the height of the magnets from 10μm to 100μm, the stray field from the edges

strengthens as compared with the earlier case due to the added magnetic volume. The effect of the magnetostatic interaction becomes even more clear when the interspacing between the adjacent magnets are varied from 10µm to 100µm, as shown in Fig. 6.3(b). For smaller interspacing between the elements in the array, the interaction between the magnets casts a detrimental effect on the overall stray magnetic field obtained from the magnet, but this type of interaction reduces with increasing interspacing and the edges of each of the micro-magnets in the array contributes to the generation of sufficient magnetic stray field and behaves as individual magnets but at the cost of reduced magnetic volume.

To understand the effect of different parameters of the patterned structures, such as length/width/diameter, height, inter-spacing distance and shape, detailed FEM simulations have been performed. We have considered square and circular patterned structures. The side lengths of the squares and the diameter of the circles are assumed to be 50 µm while the height of the patterns (or effectively the aspect ratio) are varied. The average magnetic flux density (B_a) is calculated at 10 µm (Fig. 6.4 (a), (b)), 30 µm (Fig. 6.4 (c), (d)) and 50 µm (Fig. 6.4 (e), (f)) distances above the magnet surfaces. It is to be noted that, magnetic properties are dependent on thickness and varies with it. However, we have considered same magnetic parameters for all our simulation for simplicity of the analysis. In addition, the feature sizes of each pattern elements and separation between them are large enough to avoid any nano-scale interactions such exchange coupling and dipolar interaction. In order to calculate the magnetic flux density in COMSOL, a plane is defined at the desired heights and surface average is calculated which determines the average magnetic field over the entire plane at that height. For all the simulations, the total area (including the gaps between successive patterned structures) is kept fixed to $1mm^2$. The simulation results are shown in Fig. 6.4. The corresponding inset figures show the variation of B_a for variation inter-pattern spacing distances for different aspect ratios (AR = width/height). In all cases, B_a increases as the pattern height is increased due to increase of total magnetic volume.

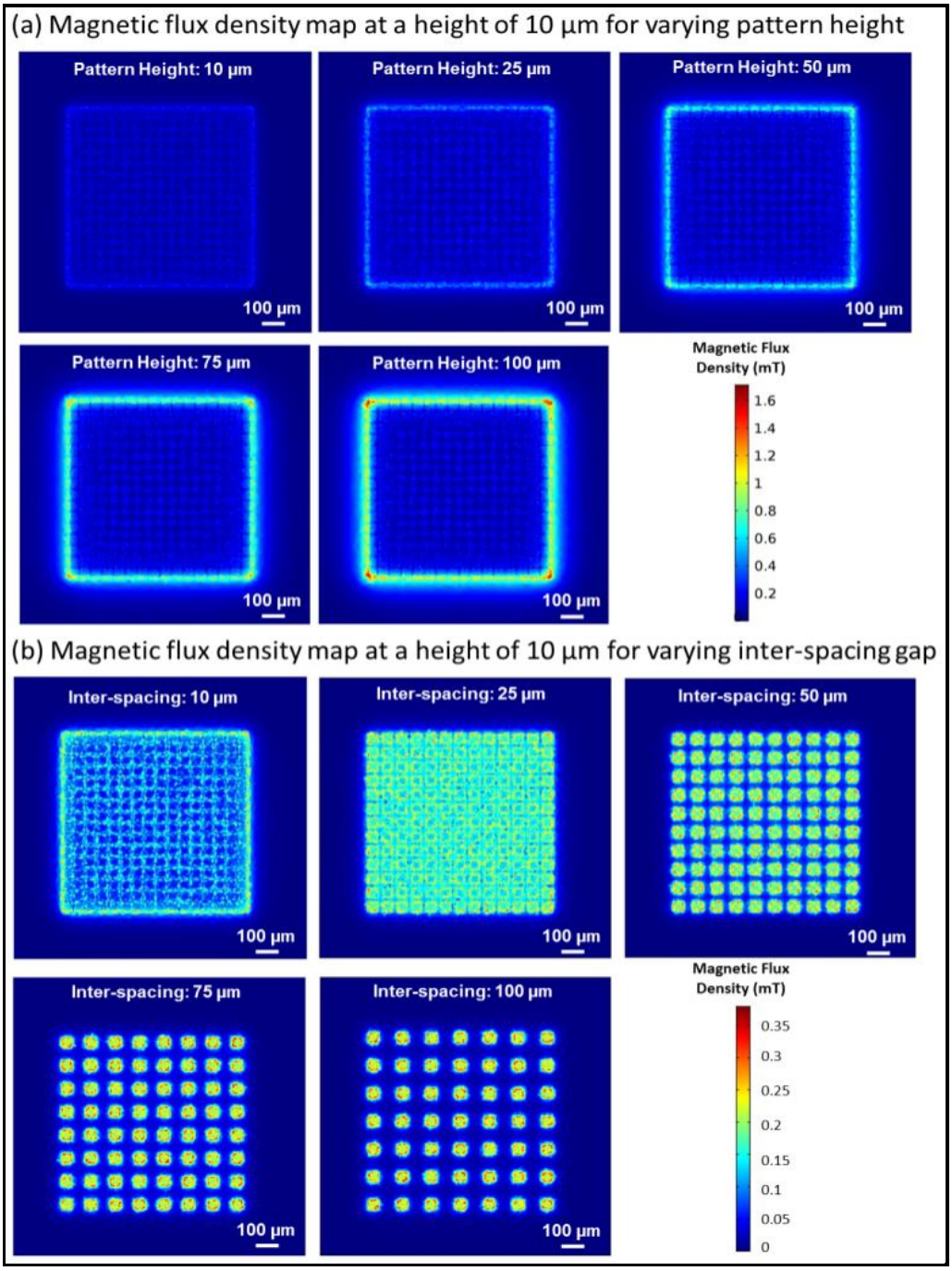


Figure 6.3: Variation of the average magnetic field with (a) pattern heights and (b) interspacing of the pattern elements observed at a distance of 10um above the surface of the patterned magnet structures.

In coherence with the previous Figure, the separation gap between the patterns plays more prominent role on the design. At lower observation height (10 µm), the stray field is much stronger and is the main area of interest. Here, the maximum B_a is generated for the 50 µm inter-spacing gap, which is equal to the feature size of the patterns, for most of the pattern

heights (or alternatively for most ARs). The B_a value drops on either increase or decrease of the inter-spacing gaps.

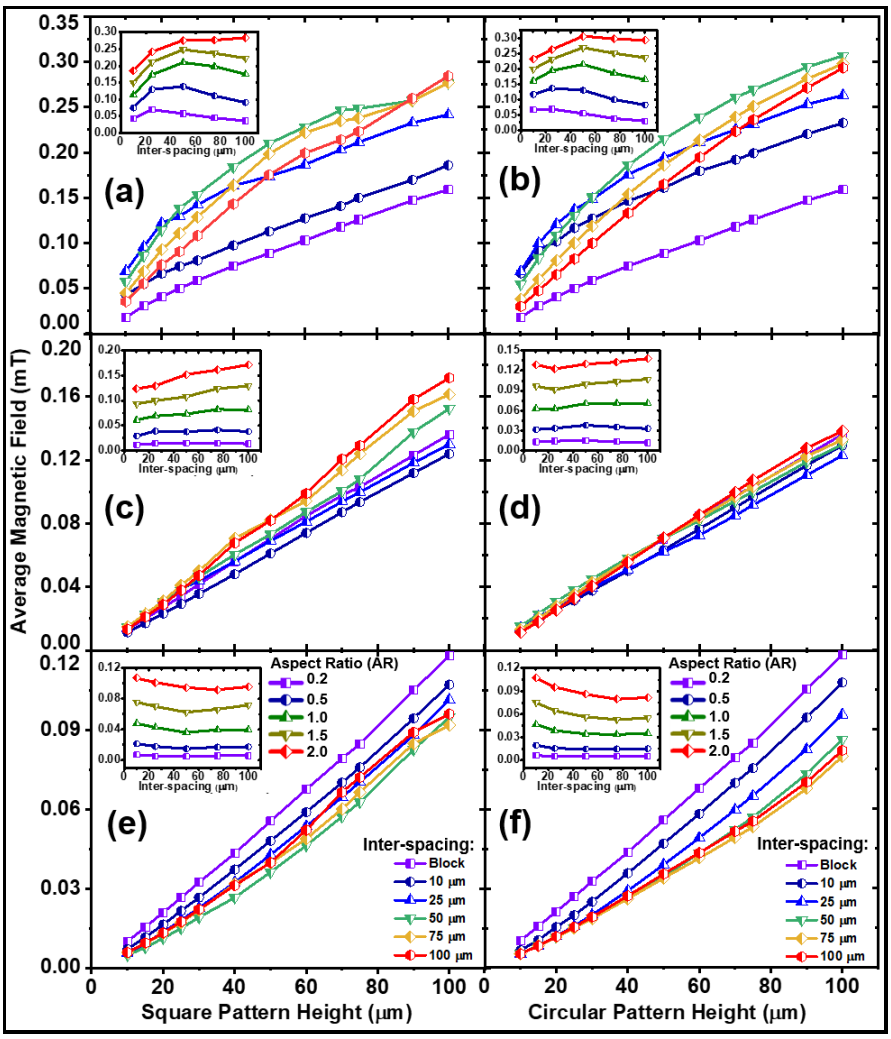


Figure 6.4: Variation of average magnetic field with pattern heights observed at a distance of (a) & (b) 10 μm (c) & (d) 30 μm and (e) & (f) 50 μm above the surface of the magnetic structures for different inter-pattern gap values. The same for the continuous block of magnet is also shown in each plot as a reference. Inset show the variation of average magnetic field as a function of inter-spacing distances of the patterns with different aspect ratios (ARs).

This can be explained using the magnetic flux mapping of Fig. 6.4 (b). As the gap is increased, there are regions of no flux density between successive patterns, which reduces the B_a. For smaller gaps, the only significant flux arises from the outer edges only with almost no flux from the inner regions reducing the B_a value. At 30-μm observation height, the overlapping field distributions are too weak to reach. The more intense fields from the edges of the patterns with larger inter-spacing plays crucial role there and maximum B_a is observed for higher inter-spacing values. With further increase of observation height (50 μm), the patterns with the

lowest inter-spacing shows the highest B_a. In that case, most stray fields are too feeble to reach such observation height. Possibly only contributing factor there is the uninterrupted fields from the extreme outer edges of the magnetic structures. At higher observation heights, the inter-spacing gap plays less significant role as B_a does not change noticeably for any of the ARs, which is indicated in the insets of Fig. 6.4. Thus it can be concluded that the for any magnetic field based MEMS devices, micro-patterning provides significant advantages over a simple film/block of magnet and the most of this advantage can be availed by keeping the target object (micro-coil for magnetic actuators/transducers or cells/biological entities for microfluidic components) close to the patterned permanent magnets. At lower observation height, the maximum flux density is obtained for patterns where the inter-spacing gap is comparable to the corresponding pattern feature sizes. The flux density changes in a complicated manner with increase of observation height.

6.4 Design optimization using patterned array of magnets

With the motivation of enhancing the electromagnetic coupling between the coil and the magnets, the finite element method simulations are carried out to further play with the shape anisotropy of thin film of ferromagnetic material. We studied the variation of output power of the system with the size of the magnets in the array, the interspacing between the magnetic elements in the array and with the aspect ratio (ratio of axial length to lateral length) of the magnets. A novel device topology is conceived in which the magnet array is placed only above one side of the rectangular spiral coil, as shown in Fig. 6.5, which is supported by the silicon spring structure designed to induce in-plane vibration. Under external excitation the coil moves from a region offering high magnetic flux density to a region of zero magnetic flux, hence experiences a colossal rate of change of magnetic flux through it, which in turn induces proportional voltage into the coil resulting in higher output power. The rectangular spiral coil has been used for this simulation and array of patterned magnets are placed only above one part of the coil (region B) but the other part (region A) is kept empty. When the coil moves, region B experiences a strong interaction with the magnetic fields whereas that of region A feels almost no change of magnetic flux through it which leads to generation of large output power. The induced voltage obtained from this topology can be written as,

$$\boldsymbol{V = Nlv\,(B_{region\,B} - B_{region\,A})} \tag{6.5}$$

where, N is the number of turns in the coil, l is the mean length of the coil, v is the velocity of movement, $(B_{region\ B} - B_{region\ A})$ gives the difference of average value of magnetic field experienced in the coil, larger this difference, more will be the induced voltage.

To demonstrate the advantages of replacing block of permanent magnet by micropatterned arrays, a novel device topology is adopted, as shown in Fig. 6.6(a). The device consists of a micro-fabricated silicon spring structure (natural frequency of oscillation 500Hz) with an integrated double-layer electroplated copper coil (144 turns and 190Ω internal resistance) and a separate substrate containing different micropatterned magnets. Bonded NdFeB magnets are considered for this analysis which ensures the goal of batch fabrication using the standard photolithographic patterning technique and offers superior magnetic properties [6] which aids in enhancing the overall performance of the microscale vibration energy harvesters. These two substrates are bonded with required alignments to develop a complete micro-scale VEH device, as shown in Fig. 6.6(a). The magnetic array is placed only above one side of the coil so that the latter can be move from a region of high magnetic flux density to minimum flux density, generating large flux gradient and large induced voltage. In the previous FEM simulation, the volume of the magnets changed as the block of magnets was replaced with patterns, rather the total area covered by the two were kept fixed. Since the interspacing between the elements in the patterned array is increased, the total magnetic volume reduces which is not ideal for a one to one comparison. So in the following FEM simulation we considered a thin film of height 50 µm (which is achievable using conventional thin film deposition processes) and 250 µm (which can be obtained using powder based bonded magnets). Then we considered patterned structures- cube, cylinders and stripes with equal volume as that of the thin film, the magnetic volume lost in the spacing between the magnetic elements have been compensated by the height of the magnetic elements in each of the patterns. The details of the design parameters are listed in Table 6.1.

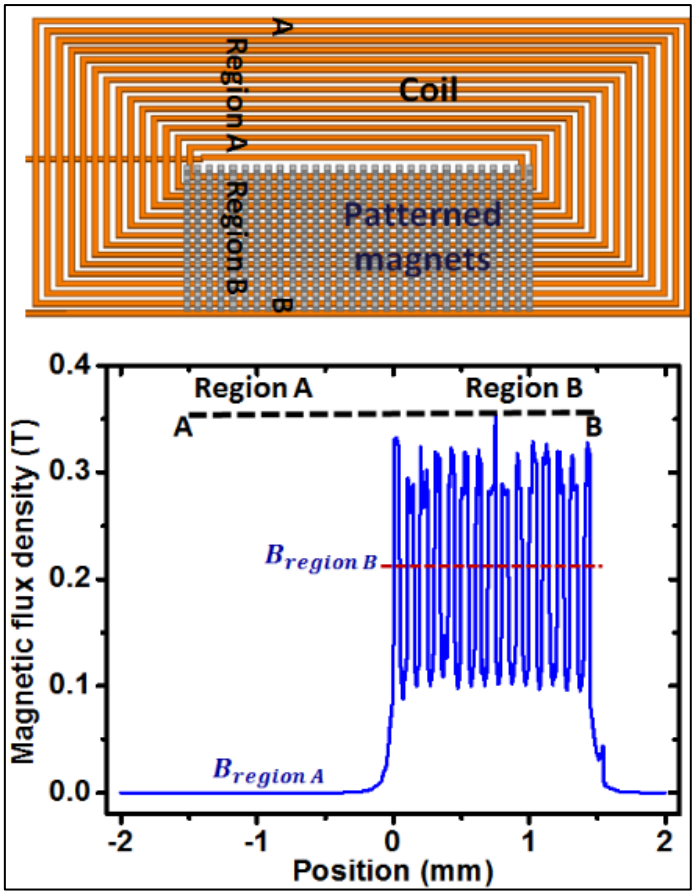


Figure 6.5: Figure showing the design strategy to improve the electromagnetic interaction.

We calculated the load power for different pattern so that the optimized pattern could be identified from it, considering double layer electroplated copper coils having 144 turns and 190Ω resistance ($\mathbf{R_c}$). The power delivered across a resistive load of 190Ω ($\mathbf{R_L}$) has been calculated using,

$$\boldsymbol{P_L} = \frac{\boldsymbol{V_L^2}}{\boldsymbol{R_c + R_L}} \tag{6.6}$$

From Fig. 6.6 (b) we can observe that the stripe patterned structures for lower thickness of the magnets offers higher load power as the number of edges parallel to the coil direction is maximized as compared to the square or circular shapes, which have edges in perpendicular to the coil directions. However, when considering the magnetic film with higher thickness the maximum power is obtained for the magnetic block structure as for thick magnets the demagnetization effect is reduced whereas the interaction between the stray fields of adjacent patterns plays destructive role in the overall flux density for the patterned structures. To summarize, the magnetic field distribution of each magnet in the array and the interaction between the adjacent magnets has some prominent effect on the overall performance of the

structure, hence, the performance of the miniaturized energy harvester relies on intelligent design strategy that boosts the electromagnetic interaction between the coil and the magnets.

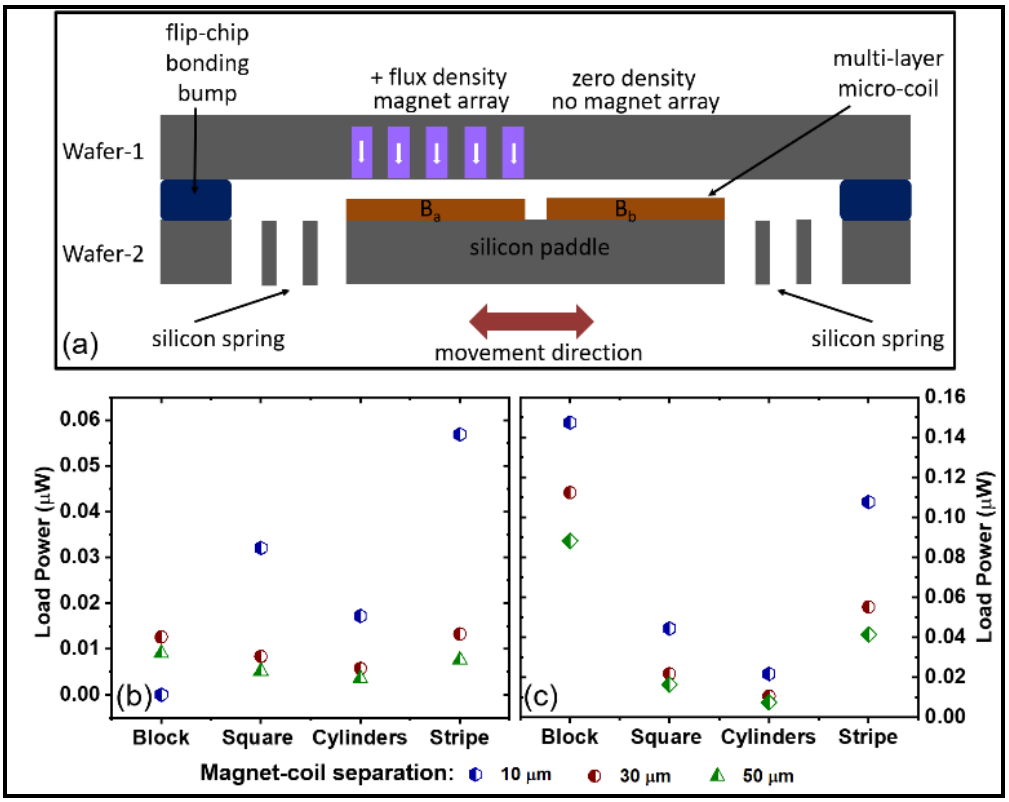


Figure 6.6: (a) Schematic of a simple integrated EM VEH device. Comparison of output power for various micro-pattern shapes with block height of (b) 50 μm, (c) 250 μm.

We identified and analysed few of the critical limiting factors to the performance of MEMS scale electromagnetic VEHs. Not only the device volume, but also the extent of integration influences the performances of these microgenerators. In the following section of this chapter, we present sophisticated and careful choice of technologies that potentially leads to improved level of power generation from MEMS scale VEHs. The magnetic flux distribution of magnets have been calculated analytically, which has been corroborated with the finite element analysis results. Since the following analysis investigates the performance of a device, the magnet patterns, coils have been re-optimized to enhance the electromagnetic interaction, which significantly influences the power outcome from the device.

Table 6.1- Different parameters for the proposed topology

Components	Parameters	Values	
Mechanical Spring	Resonance Frequency	500Hz	
	Inertial Mass	6.14×10^{-5} kg	
	Footprint	$6\times6mm^2$	
Microcoil	Number of coil turns	144	
	Coil resistance	190Ω	
Micromagnets	Magnetic Remanence	0.6T	
	Magnetization direction	Perpendicular to the plane of magnets	
	Shape of magnet	Lower thickness (50µm)	Higher thickness (250µm)
	Block Magnet	$1600\times700\times50\mu m^3$	$1600\times700\times250\mu m^3$
	Square patterns (each)	$50\times50\times200\mu m^3$	$50\times50\times1000\mu m^3$
	Circular patterns (each)	$Ø50\times255\mu m^3$	$Ø50\times1273\mu m^3$
	Stripe patterns (each)	$1600\times50\times100\mu m^3$	$1600\times50\times500\mu m^3$

6.5 MEMS linear and nonlinear VEH with optimized patterned micromagnets

In the following section, we propose the design and performance analysis of fully integrated MEMS electromagnetic vibration energy harvesters that consist of optimized patterns of micro-magnets. The distribution and shape parameters of these micro-magnets have been optimized through detailed finite element analysis, along with in-plane moving linear and non-linear spring architecture incorporating the conducting micro-coils. Through analytical formulation and detailed thorough finite element analysis, we present a systematic design strategy study to optimize the magnet-coil interaction in a precise location within a small footprint. The compact device topology yielded an electromagnetic coupling as high as 62.9mWb/m with the optimized stripe shaped micro-magnets and rectangular micro-coils. The nonlinear spring topology demonstrated 6 times improvement in the half power bandwidth compared with its linear counterpart, at the cost of the reduced power density. The proposed designs can be developed using standard MEMS fabrication methods leveraging the CMOS compatible integration at the system level for potential applications in Internet of Things.

6.5.1 Introduction to the problem and a potential route to overcome the challenge

The recent advancements in low power electronics have scaled down the power requirements of microelectronic devices to microwatts level [7]. However, the widespread utilization of low power wireless sensor networks (WSNs) in remote healthcare [8], surveillance [9] and military application [10] demands for a sustainable power source instead of the energy-limited and environment polluting batteries. Particularly a resilient WSN is imperative in the aviation industry to implement a reliable condition monitoring system inside the aircraft comprising of multiple temperature, pressure and humidity sensors [11]. Considering the overall weight and volume restrictions inside the aircraft, a miniaturized sustainable powering source is indispensable to implement a self-powered efficient wireless sensor network. Scavenging mechanical energy from ubiquitous ambient vibration has drawn significant research focus [12, 13] as a potential solution to such powering issue. Substantial vibrational energy is available over the frequency range 100-1000Hz with acceleration in different direction varying from 0.28g to 1.02g from the fuselage [14], armrest, tray-table and other parts of a commercial aircraft. In terms of reliability and longevity, the electromagnetic vibration energy harvester (EM-VEH) is undoubtedly advantageous over other transducers. Over time the performance of the coil or the magnet doesn't degrade due to aging as happens owing to the depolarization [15] or discharge issue [16] in case of piezoelectric and electrostatic transducers respectively. The macroscale electromagnetic vibration energy harvester (EM-VEH) outpaces the contemporary transducers in efficiently transducing the mechanical energy into usable electrical power. However, the major roadblock in the implementation of a high efficiency MEMS scale EM-VEH is the lack of high energy density miniaturized permanent hard magnets compatible with the established Integrated Circuit (IC) fabrication technology [17].

Over the last decade, substantial development in the field of permanent hard magnetic material has enabled it to be exploited in wide range of magnetic MEMS application including sensors and actuators [18], microfluidics [19] and high density data storage media [20] in the form of a continuous thin film or patterned micromagnets. Different popular fabrication technologies such as electrodeposition [5], sputtering [21], dry packing of magnetic powders [22], screen printing [23] have been used by several research groups to fabricate high energy product CMOS compatible permanent hard magnets. The detrimental effect of the shape dependent demagnetizing field [4] reduces the stray magnetic field lines emerging from a continuous thin film of magnets [24], which degrades the overall magnetic performance. The

high magnetic field gradient of the order of 10^6 T/m [25] produced by the patterned micromagnets offers the scope of spatial manipulation of the magnetic field lines. This can be of particular interest in the field of MEMS EM-VEH where the output performance of the device relies largely on the strength of the interaction between the coil-magnet assembly. Majority of the reported MEMS vibration energy harvesters employing different shapes of microcoils such as serpentine [26], rectangular [24], square [27] produces output power as low as hundreds of picowatts to few nanowatts primarily due to the lack of efficient interaction between the coil turns and micromagnets. Although substantial attention has been dedicated towards the development of the micromagnets of various shapes and compositions for different purposes, but the effect of the optimized distribution and consequent electromagnetic interactions of those magnets on the performance of the EM-VEH devices has not been deeply explored yet.

On the other hand, the output power and its distribution over the frequency spectrum is also dependent on the device dynamics other than relying on the electromagnetic coupling factor. Most of the developed MEMS EM-VEH are resonant type [28-30], which provides excellent output power when subjected to vibration having discrete peaks. However, substantial mechanical energy in the form of ambient vibrations is distributed over a wide range of frequency, which demands for a broadband energy scavenger for efficient energy conversion. Lately the deliberate inclusion of nonlinearity through geometric manipulation of the associated spring structures [31, 32] has become a popular choice of the scientific community to implement wideband energy harvesters. Subjected to large out-of-plane displacements, such springs demonstrate nonlinear restoring force that aids in widening the bandwidth of operation of the device. MEMS scale buckled beam based energy harvester have been reported [33] with piezoelectric transducer which exploits large snapping motion at relatively low frequency, exhibiting as large as 200μm buckling while offering 50% bandwidth under 70Hz operation frequency with 0.5g excitation. The nonlinearity arising from stretching strain have also been exploited with an out-of-plane motion in MEMS scale [34], which offers a considerably large power density of $2W/cm^3$. Whereas, in-plane moving structures facilitates stronger electromagnetic interaction between the coil and the magnet edges as compared with its out-of-plane counterpart [24, 35], but the development of in-plane moving stretching based nonlinear device is still relatively unexplored.

The following section provides an insight into the tunability of the magnetic field lines emerging from micropatterned magnets and shows a systematic approach through analytical

formulation and detailed finite element analysis for the optimization of the corresponding magnetic flux density. This results into increased EM coupling vis-à-vis output power density from narrowband (linear) as well as wideband (nonlinear) MEMS scale EM-VEHs. Experimentally, optimizing the electromagnetic interaction between the magnet and the coil can be a difficult task considering the cost and time involved in the fabrication process. The evaluation of the electromagnetic coupling associated with the system through theoretical analysis or through finite element analysis has become lately a well-accepted approach to circumvent this issue [36, 37] and to provide a firm experimental roadmap. Therefore, an elegant design strategy to exploit the enhanced stray magnetic fields arising from optimized patterns of array of micro-magnets has been discussed here in the first place. Four novel topologies have been proposed to integrate the coil and magnet in a compact MEMS transducer that can be implemented using batch-fabrication methodologies. Through finite element analysis, we provide a firm road map to enhance the electromagnetic coupling of the coil magnet assembly by employing square and rectangular coil geometry. Further, the design of in-plane moving linear and nonlinear MEMS spring architectures are presented, and the overall performance of the devices are compared in terms of bandwidth and obtained power density, highlighting the trade-off between the two.

6.5.2 Finite element analysis (FEA) and optimization of magnetic flux density

The EM-VEH works based on the Faraday's principle of induction in which the relative motion between the magnet and the coil induces voltage (V) into the later-

$$\boldsymbol{V = N.B_{effective}.l.v.} \tag{6.7}$$

where, N is the number of turns in the coil, $B_{effective}$ is the effective change in magnetic flux density that interacts with the coil, l is the length of the coil and v is the velocity with which the coil and the magnet move with respect to each other. This is more generalized approximation of the electromagnetic interaction taking place where the electromagnetic damping coupling is assumed to be linear [38]. However, the nature of the magnetic flux density variation in such a system induces nonlinear interaction between the magnet and the coil. This nonlinear interaction has taken into account by considering the dependence of the magnetic flux gradient on the relative position of the coil and the magnet [36, 39], and through parametrical study it has been shown that such nonlinear coupling can enhance the performance of an electromagnetic transducer with optimized parameters as compared with the linear

counterpart. Recently the electromagnetic coupling of an EM-VEH has been modelled exploiting this nonlinear interaction where expressing both the electromagnetic force and the electromotive force associated with the system are expressed in the form of polynomial shape functions that are linearly dependent on the relative velocity and nonlinearly related to the distance between the coil and the magnet. Regardless of the approach followed the induced voltage and hence the output power from such a system can be clearly enhanced by intensifying the variation and the strength of the magnetic flux density, which in turn would boost the electromagnetic coupling in the magnet-coil assembly.

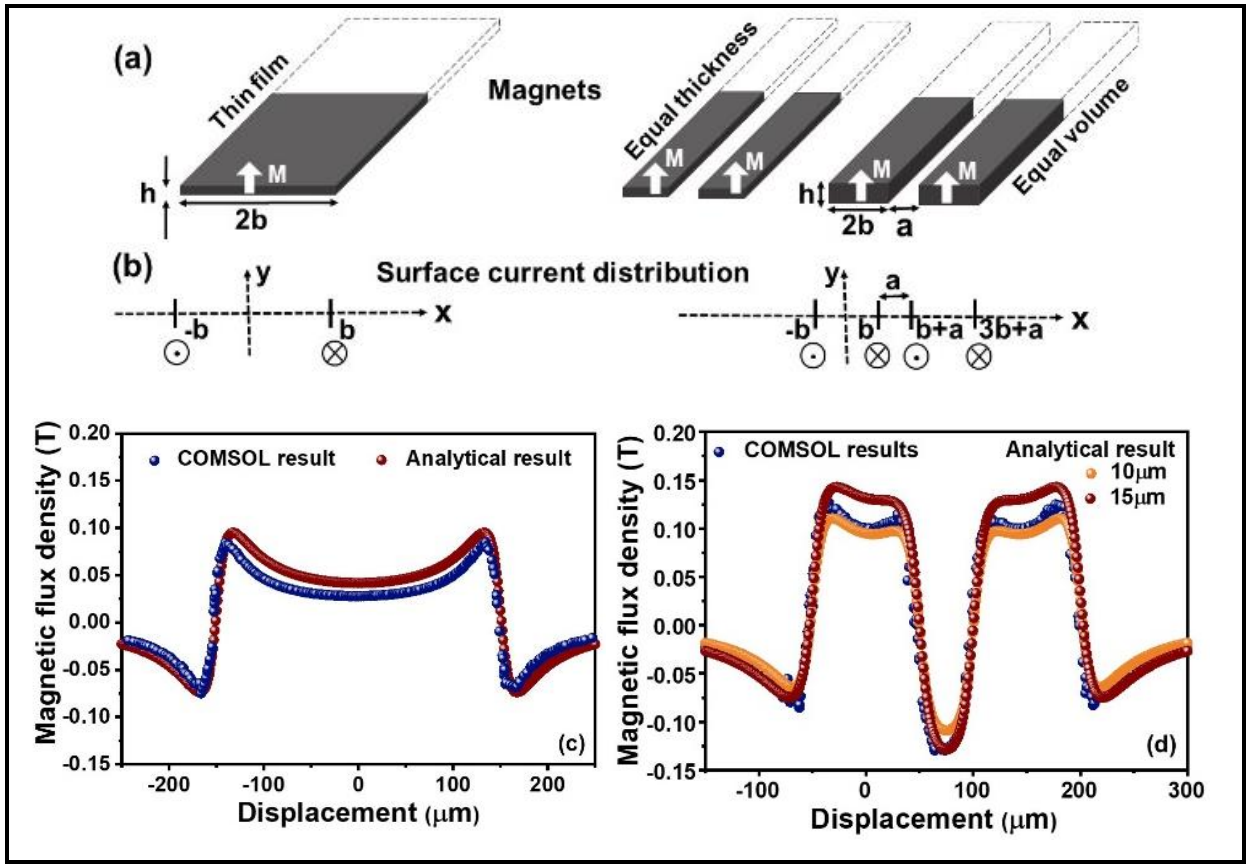


Figure 6.7 (a) shows a block of magnet (on left) and a replacement of the magnet with stripe patterns separated by a distance 'a' (on right) having out-of-plane magnetization. (b) Depicts the surface current representation of the magnets in (a). (c) And (d) shows the distribution of the vertical component of magnetic flux density on a plane that is 10μm away from the top surface of the magnet and stripe patterns respectively.

However, the critical bottleneck in the implementation of a fully integrated high-performance EM-VEH is the lack of high-energy product hard magnets, which are compatible with the matured CMOS fabrication technology. Conventionally thin film of permanent magnet is employed for the microscale transducers, but the shape dependent 'Demagnetizing field' (H_d)

affects the magnetic performance of these miniaturized energy harvesters as explained in the previous section. This detrimental effect causes the stray magnetic fields to emanate mostly from the edge of the magnet as it weakens the stray fields emanating from elsewhere, leaving the rest of the magnet ineffective.

To perceive this effect on the magnetic flux density of an infinitely long block of magnet, we represent the magnet by its equivalent surface current distribution as shown in Fig. 6.7. The vertical component of magnetic flux density for such a magnet can be expressed as [40],

$$\boldsymbol{B_1(x,y)} = \frac{\mu_0 M_s}{2\pi}\left\{\boldsymbol{tan^{-1}}\frac{2h(x+b)}{(x+b)^2+y^2-h^2} - \boldsymbol{tan^{-1}}\frac{2h(x-b)}{(x-b)^2+y^2-h^2}\right\} \tag{6.8}$$

Where, μ_0 is the permeability of free space, M_s is the saturation magnetization of the material, h is the height of the magnetic element and b is the width of the magnet. Now if we replace this block of magnet by couple of smaller magnetic elements having an interspacing a, then the vertical component of magnetic flux density takes the form,

$$\boldsymbol{B_2(x,y)} = \frac{\mu_0 M_s}{2\pi}\left\{\begin{array}{l}\boldsymbol{tan^{-1}}\frac{2h(x+b)}{(x+b)^2+y^2-h^2} - \boldsymbol{tan^{-1}}\frac{2h(x-b)}{(x-b)^2+y^2-h^2} + \\ \boldsymbol{tan^{-1}}\frac{2h(x-b-a)}{(x-b-a)^2+y^2-h^2} - \boldsymbol{tan^{-1}}\frac{2h(x-3b-a)}{(x-3b-a)^2+y^2-h^2}\end{array}\right\} \tag{6.9}$$

Here, Fig. 6.7(a) shows an infinitely long thin film of magnet having width 300µm and height 10µm on left and a couple of stripe shaped magnets each having width 100µm and interspacing 50µm on right. All magnets are assigned out of plane magnetization as indicated in the figure. The equivalent surface current distribution of the magnets is depicted in Fig. 6.7(b). The vertical component of magnetic flux density of the thin film at a distance of 10µm from the top of the magnet peaks to 0.09T (Fig. 6.7(c)) which corresponds to the edge of the magnet. However, owing to the detrimental effect of the demagnetizing field, the magnitude of magnetic flux density decreases to 0.04T at the middle of the thin film. In order to enhance the obtainable strength and variation of the magnetic flux density, the thin film of magnet is replaced by a pair of stripe shaped magnets having height equal to that of thin film of magnet (Fig.6.7(d)). The increased number of magnet element edges in these array aids in intensifying the magnetic flux density peaks as compared with the thin films [41, 42]. The flux density peaks to 0.15T for each of the patterns, the magnetic fields interact destructively in the space between the magnets, and rises again to the peak value for the next pattern. However, while replacing the thin film with patterned array of magnets keeping the occupied area same, substantial magnetic volume is compromised which accounts for the interspacing between the

elements in the array. Hence, to further intensity of magnetic flux distribution, the magnetic volume lost in the interspacing is compensated by altering the height of the magnets in the array. Fig. 6.7(d) portrays this advantage where the curve in orange represents the magnet array having equal height (10µm) and that in red (15µm) represents the array with equal magnetic volume as that of the thin film of magnet. In this case, the improvement in magnetic flux density might seem relatively small, but this strategy could bring significant enhancement when a larger array of such magnetic element is considered which has been shown in the later section. In order to corroborate the analytical model employed to evaluate the magnetic performance, the 'Magnetic Fields (mf)' module of COMSOL multiphysics has been used to depict the variation of magnetic flux density for the same magnetic structures through finite element analysis. This has been shown in blue in Fig. 6.7(c) and (d) which agrees well with the obtained analytical results. Therefore, this analysis clearly demonstrates the benefits of utilizing the patterned array of micromagnets instead of a continuous thin film of magnet in intensifying the strength and variation of magnetic flux density, which could potentially boost the induced voltage in the coil.

We study the effect of geometrical shape, interspacing of the magnetic elements in the array on the average magnetic flux density. In order to generate more stray magnetic field, the shape of the magnets can be further manipulated to obtain complex shapes, such as an octagonal prism, which has more edges. However, keeping in mind the fabrication complexity, in this study we only explore the viability of the relatively simple shapes- cuboids, cylinders and stripes. The diameter of the cylinders and the width of the cubes, stripes are considered to be 50µm. The length of each of the stripe and arrays of patterned cuboids and cylinders is 1650µm. Fig. 6.8(a) shows the mapping of z-component of magnetic flux density on a line of observation, which is 10µm away from the top surface of the magnet. The peak value of the periodic magnetic flux density variations for different shapes of magnets in this case increases dramatically to 0.09T, 0.17T and 0.18T for the stripe, cuboid and cylindrical shaped patterns respectively as compared with that of the thin film, which suffers from the degrading effect of demagnetizing field. This can be attributed to more magnet edges that result in substantially larger stray magnetic fields close to the line of observation in case of the cube or cylinder compared with the stripes. Although the magnitude of the stray field is greater for the cuboid and the cylinder, but when the coil interacts with the overall array, the adjacent elements of the magnet array destructively interact and deteriorate the overall magnetic flux density. Hence, to find the overall average magnetic flux lines that will interact with the coil and enhance the

electromagnetic interaction, considering a surface averaged magnetic flux density is a more reliable parameter of comparison.

Hence in the following study for each of the shape in the magnet array, the inter-element gap has been varied from 10µm to 100µm, keeping the overall area fixed to 1650µm ×550µm. The number of micromagnets along the shorter side of the array varies from 9 to 4, and the number of elements on the longer side of the 2-dimensional array changes from 28 to 12 (apart from the long stripe patterns) when the interspacing between the magnetic elements in the array is changed from 10µm to 100µm. The thickness of the thin magnetic film is varied from 10µm to 250µm. To replace the magnetic volume of this thin film with array of micromagnets, the height of each of the magnetic element in the array is altered for each thickness of the thin film and the variation of the average magnetic flux density of the whole array of micromagnets as a function of the total magnetic volume is plotted (the magnetic flux density is averaged at the observation plane, which is a distance of 10 µm). Fig.6.8 (b-d) depicts this variation for micromagnet arrays for different inter-element spacing (10-100µm). The magnetic flux density variation for the thin film of magnets is shown in each plot (in black) as a reference. For a fixed inter-element spacing, the volume of the magnet array is altered by adjusting the height of each of the elements for each set of the inter-element gap. When considering low volume (equivalent thickness of thin film lying between 10µm to 100µm), the increased edges in the micromagnets aids in the emergence of a stronger stray magnetic field from all of the patterned magnet array having moderate interspacing (30µm - 50µm). However, with smaller interspacing (~10µm), the magnetic flux density reduces due to the destructive magnetostatic interaction between the adjacent elements in the array. Among the patterns, the stripe shape shows superior magnetic performance which can be attributed to its long undivided sides, aiding in intensifying the magnetic flux density.

As the thin film's thickness is increased, the average magnetic flux density of the thin film outpaces that of the micromagnets- firstly due to the absence of negative magnetostatic interaction between the neighbouring elements that takes place in the micromagnets array, and secondly, owing to the reduced effect of shape-dependent demagnetizing field in relatively thicker film, the stray fields emanating from the film is stronger. Considering the MEMS-scale batch fabrication of devices and the associated packaging, we have focused on thinner magnetic films (10µm to 100µm thick) which could be implemented through electrodeposition [5], sputtering [43] or pulsed laser deposition (PLD) [44]. The benefits of using the patterned array of magnets can be fully exploited for this case where thin magnetic source (up to 100µm thick)

is desired. In such case the stripe-patterned magnets with moderate interspacing (~50μm) is superior to the thin films in producing substantial stray magnetic field as is evident from the analysis above. Such a high-performance micromagnet array can be implemented by sputtering or electrodeposition process from the fabrication point of view.

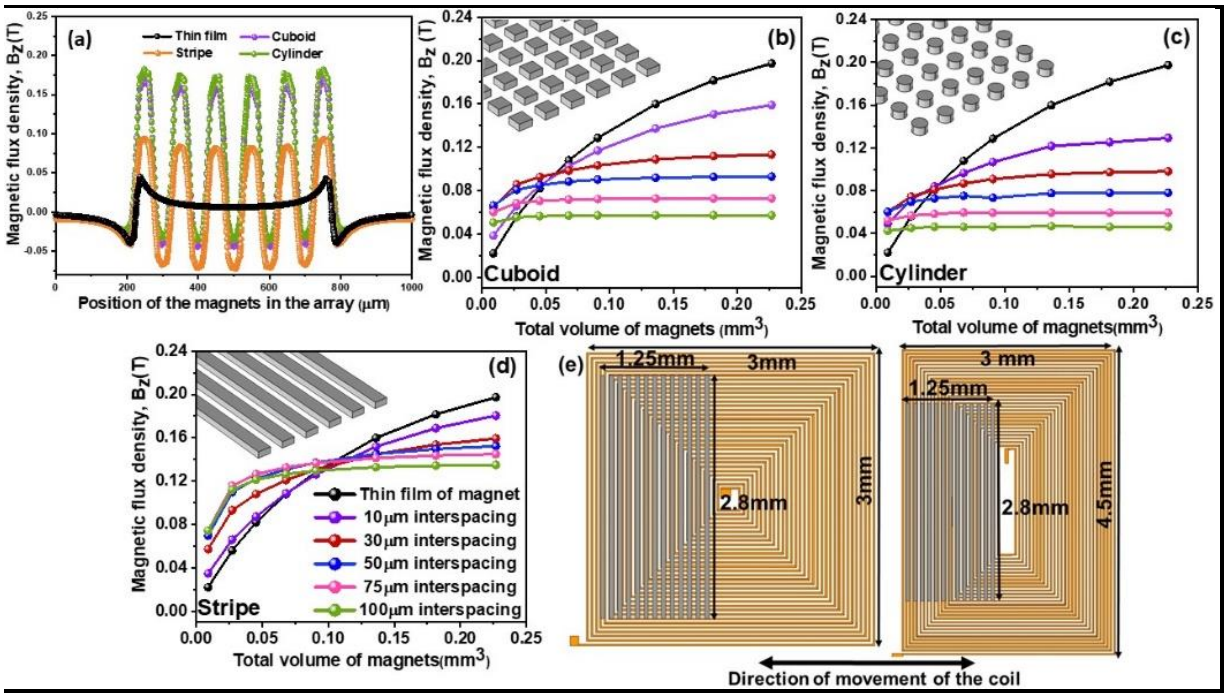


Figure 6.8: (a) Comparison of the z-component of magnetic flux density for different shapes of magnets having equal volume to that of a thin film of 10μm thickness. Plots of average magnetic flux density as a function of the total magnetic volume on a plane of observation 10μm away from the top of the array of magnets having (b)cuboid, (c)cylinder, (d)stripe-shaped elements are shown. (e) Shows schematic of the square (left) and rectangular copper coil (right) used with the stripe patterned magnets.

6.5.3 Design strategy

With the motivation of enhancing the overall performance of the MEMS EM-VEH, we have proposed four device topologies (Fig.6.9). Two different coil topology has been considered here- a rectangular and a square shaped microfabricated coil having the coil resistance (R_c) [45],

$$\boldsymbol{R_c = \frac{2\rho_{copper}(D+d)}{(D-d)^2}\,(4n^3 - 4n^2 + n)} \qquad (6.10)$$

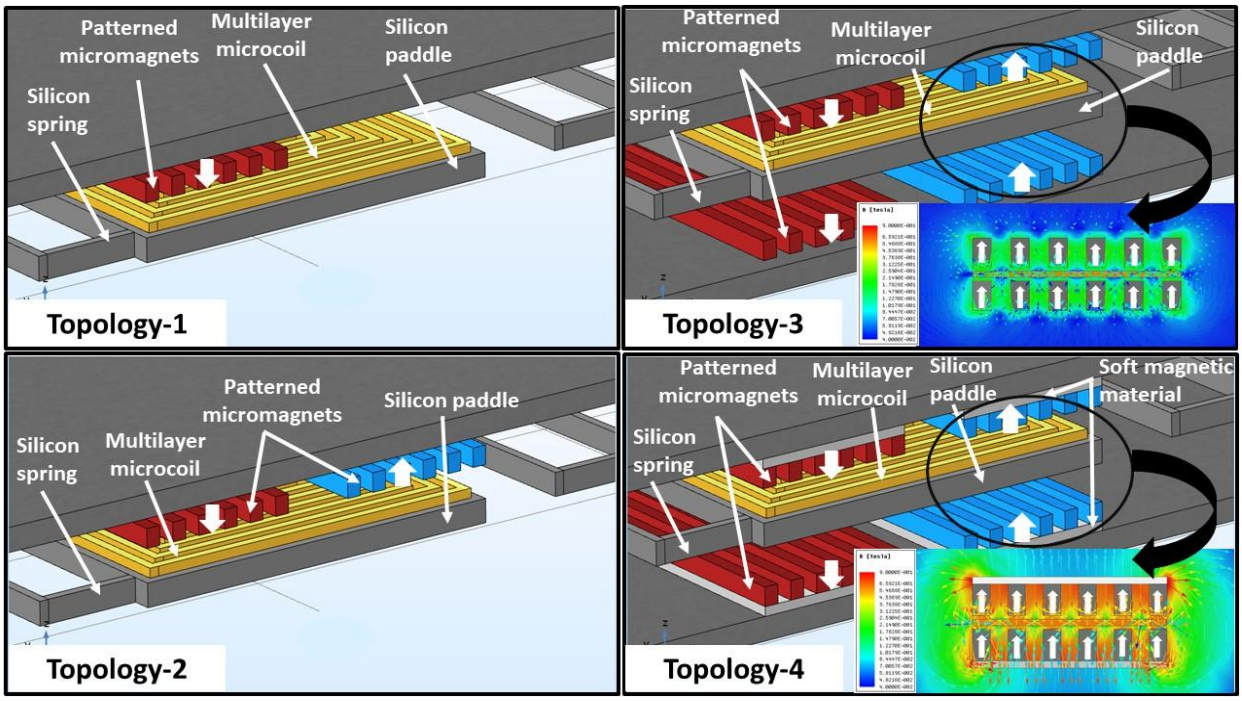


Figure 6.9: Proposed topologies for the MEMS EM-VEH.

Where, D is the outer dimension of the coil, d is the inner dimension of the coil, ρ_{copper} is the resistivity of copper and n is the number of turns in the microfabricated coil. Both the coils are considered to have 144 turns yielding 266Ω and 165Ω resistance for the rectangular and the square microcoil respectively. The in-plane moving silicon MEMS spring holds the microcoils on the central paddle and additional substrate layer is assembled that carries the patterned micromagnets. In order to electrically isolate the microfabricated coil, thin layer of alumina will be sputtered on the silicon substrate and following this, a thin layer of titanium and copper will be sputtered as seed layers for the electrodeposition of copper coil structure. Contact bond pads will be formed on the stationary section of the spring structure, the coil lines will follow through the spring arms until the bond pads to allow the outward flow of current through the coil. For the present analysis, we have considered array of stripe shaped micromagnets having 50µm inter-element spacing and each having 2.8mm length, 0.05mm breadth and 0.96mm height as a replacement of a 50µm (height) thin film having lateral dimensions of 2.8mm×1.25mm. In Topology-1, the magnets are only on one side of the microcoil. Subjected to in-plane excitation, the coil experiences high magnetic flux gradient as it moves from a region of dense magnetic flux to a region of negligible flux due to this coil-magnet arrangement. This aids in inducing large voltage across the coil. For the second topology, oppositely polarized patterned magnets have been used to further enhance the change of magnetic flux.

In topology-3, another substrate layer containing the oppositely polarize stripe magnets are bonded at the bottom of the MEMS spring. Since all of the stripe shapes magnets are assigned out-of-plane magnetization, the vertically emerging field lines form a close loop across the microcoil. Although, the polarization of the magnets on the top and bottom of the coil also aids in closing the flux lines, around the coil, however, a significant share of the emerging magnetic field lines from the patterned magnets fringes out and fails to interact with the coil efficiently. Hence, in topology-4, to minimize the divergence of stray fields emerging from the magnet array, additional layers of soft magnetic material are incorporated on the side of the magnet array away from the coil. The top and bottom patterned magnet assembly in topology-4 aids to direct the magnetic field lines more towards the coil to substantially enhance the electromagnetic interaction.

Two types of MEMS spring have been designed to implement the conceived topologies. Both type of the springs is dedicated for in-plane motion to enable more efficient electromagnetic interaction between the optimized coil-magnet assemblies as compared with the equivalent out-of-plane springs [24]. One of the spring is resonant type comprising of a 4.5mm×3mm central paddle connected to the outer fixed support through a pair of 1.9mm long and 50µm meandered arms (Fig. 6.10(a)). Such resonant spring topologies aid in scavenging vibrational energy possessing discrete frequency peaks. However, they are inefficient in harnessing majority of the vibrational energy, which is spread over wide range of frequencies. Recently the incorporation of nonlinearity into energy harvesting system by introducing spring hardening has become an attractive way of realizing a wideband mechanical energy harvester. However, traditionally these structures have been designed to facilitate out-of-plane vibration, which in this case will be less efficient in terms of demonstrating strong electromagnetic interaction. Hence the other spring structure designed for the present analysis consists of thin short beams (each having 1800µm length and 30µm width) between the fixed support and the in-plane moving central paddle which demonstrates nonlinear restoring force (nonlinear spring stiffness coefficient 1.76×10^{11} N/m^3) owing to the stretching under large amplitude deflection (Fig. 6.10(b)). The 'structural mechanics module' component of COMSOL Multiphysics along with the 'solid mechanics' interface has been used to find out the natural frequency of oscillation and the mode of vibration. The fundamental modes of vibration of the linear and the nonlinear spring architectures are at 614Hz and 605Hz respectively. This frequency range has been chosen to harness substantial vibrational energy from the sources like fuselage, arm-rest or tray table of a commercial aircraft [14] so that such system can become a potential powering source

of the wireless sensor networks associated with the aviation industry. The total volume of the MEMS device is 0.05cm^3 and 0.06cm^3 for the linear and the nonlinear architecture, respectively.

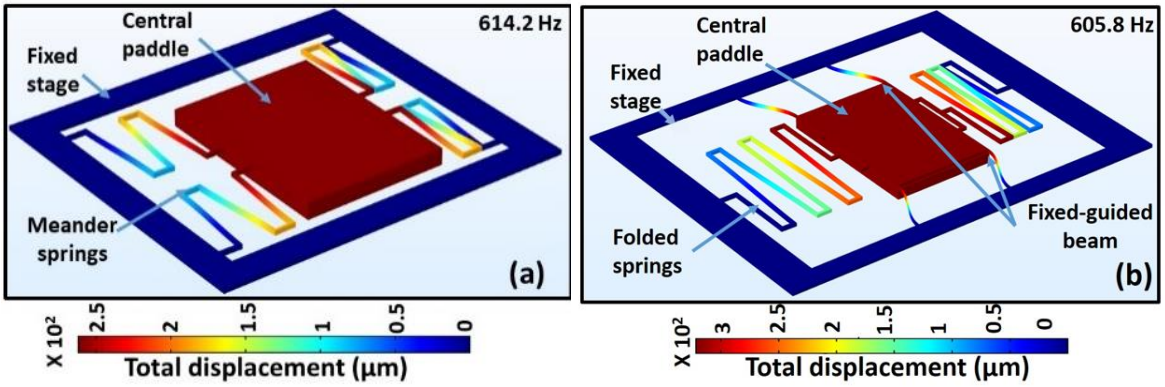


Figure 6.10: Fundamental modes of oscillation of the designed (a) Linear (b) Nonlinear MEMS spring structures.

To study the effect of nonlinearity on the overall performance of the VEHs, along with the nonlinear spring architecture demonstrated in Fig. 6.10(b) (which is referred to as (d) in Fig. 6.11), we designed three other MEMS springs that possess nonlinear stiffness coefficients which differs by orders of magnitude. The stretchable springs are arranged so that they stretch in the same direction during the in-plane vibration, to facilitate this the springs are not arranged in a mirror image symmetry. Fig. 6.11(a) shows a nonlinear spring in which the nonlinear thin springs attached with the fixed stage has been modified into a folded beam form. This lower the nonlinear spring stiffness coefficient to 5.01×10^7 N/m^3. Additionally, these folded beams restricts spring to exhibit in-planar motion when subject to external excitation. The thickness of each of the nonlinear thin spring is 100µm, whereas the width is only 30µm. Hence, this high aspect ratio of these thin nonlinear springs also aids in limiting the dominant motion of these spring to in-planar direction. In the consecutive architectures as well, the nonlinear stiffness coefficient has been changed from 2.95×10^8 N/m^3 in (b) to 4.38×10^{10} N/m^3 in (c) as the stretchable springs are changed from typical meandered shape to stepped thin beams. Further structural details of these springs have been summarized in Table 6.2.

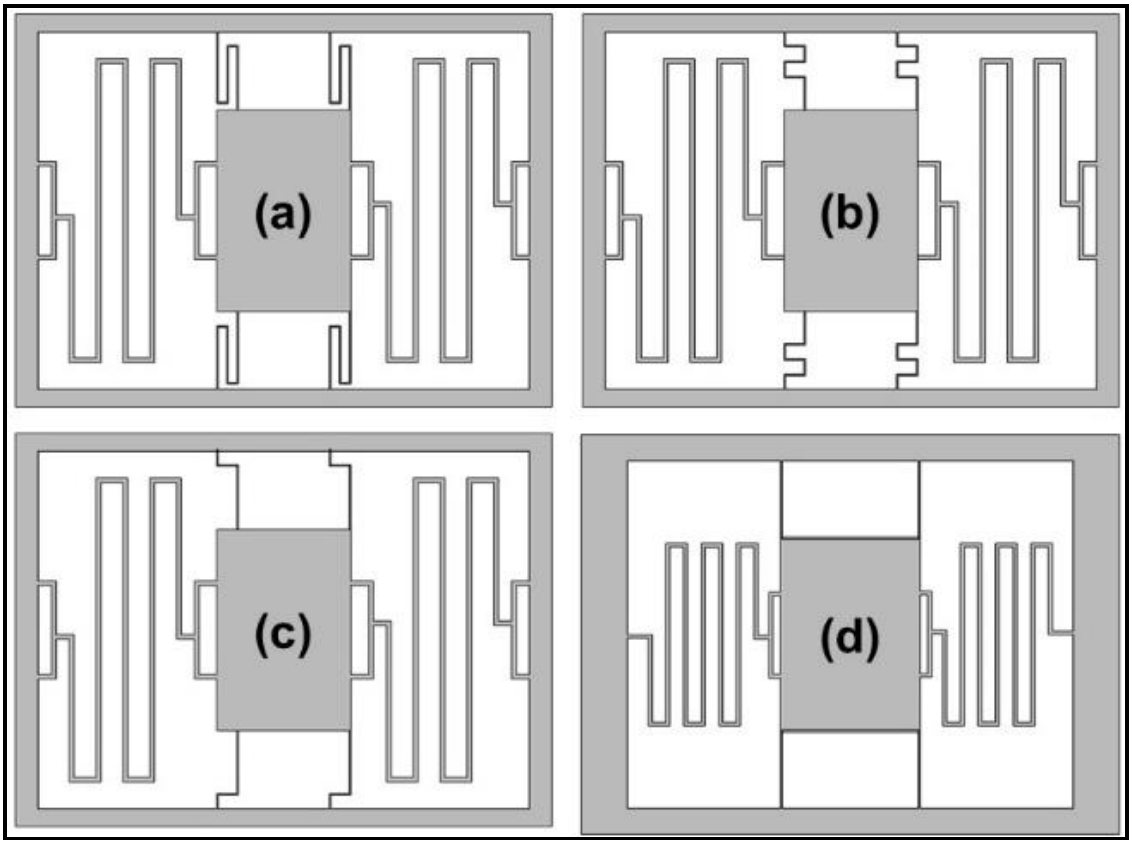


Figure 6.11: Four nonlinear spring architecture with varying nonlinear spring stiffness coefficient is presented where the stretchable springs are arranged in a way that facilitates stretching in the same direction as the central paddle moves in-plane.

6.5.4 Results and Discussion

The electromechanical equation of motion of a nonlinear electromagnetic vibration energy harvester can be represented in the form of second order spring-mass damper system-

$$\boldsymbol{m\ddot{x} + \left(2m\omega_0\xi + \frac{\gamma^2}{R_c+R_L}\right)\dot{x} + kx + k_n x^3 = F\,sin(\omega_0 t)} \quad (6.11)$$

Where, $c_m = 2m\omega_0\xi$ is the mechanical or parasitic damping, $c_e = \frac{\gamma^2}{R_c+R_L}$ is the electrical damping associated with the system, k, k_n are the liner and the nonlinear spring stiffness coefficient, m is the mass and $F\cos(\omega_0 t)$ is the external excitation applied on the system. Here the mechanical damping is mostly responsible for the energy that is dissipated due to the damping force introduced by the mechanical structure itself or the viscous drag which ideally should be minimized to increase the overall power output. On the other hand, the electrical energy that is produced from scavenging the mechanical energy is extracted across the electrical damper [46]. This electrical damping relies mostly on the overall impedance associated with the system and the electromagnetic interaction between the coil and the magnet,

which is expressed in terms of electromagnetic coupling (γ). Hence, the electrical energy that can be electromagnetically transduced through such a mechanical energy harvester depends largely on the electromagnetic coupling between the magnet and coil (R_C being the coil resistance) arrangement. The power extracted across a suitable load resistance R_L over a period of oscillation can be expressed as –

$$\boldsymbol{P_L = \frac{1}{T}\int_0^T \frac{\gamma^2 R_L}{(R_C+R_L)^2}\left(\frac{dz}{dt}\right)^2 dt} \tag{6.12}$$

where, $\left(\frac{dz}{dt}\right)$ is the velocity of the harvester movement, γ is the electromagnetic coupling factor $\left(= N.\frac{d\emptyset}{dz}\right)$ between the coil with N turns that experiences a gradient of magnetic flux linkage $\frac{d\emptyset}{dz}$ and T is the time period of oscillation Hence, substantial electromagnetic interaction is imperative in enhancing overall power performance of the MEMS EM-VEH. To investigate the effect of different coil geometries on the electromagnetic coupling, a rectangular (4.5mm×3mm×0.01mm) and a square (3mm×3mm×0.01mm) shaped micro coil each having 144 coil turns with resistance 266Ω and 165Ω respectively has been employed. Ansoft Maxwell simulation tool has been used to investigate the electromagnetic interaction between these coils and the micromagnets through transient analysis. For this study, we have considered sputtered NdFeB material with a coercivity of 924kA/m and retentivity of 1.23T [47].

The volume of a 50μm thin film of permanent magnet has been replaced by an array of stripe magnets (2.8mm×0.05mm×0.96mm) to manipulate the emanating stray magnetic field. The height of each stripe (13 such stripes have been used) micromagnet has been adjusted to compensate the loss of magnetic volume in the interspacing between the magnets in the array. Table 6.3 summarizes the electromagnetic coupling obtained using both of the coils. It can be noticed that irrespective of the type of magnet arrangements chosen, the coefficient of the electromagnetic interaction is almost the same when the square shaped micro coil is used. Owing to the geometry of this coil, a large part of the fields coming from the stripe magnet interacts with the coil turns transversely which does not aid in substantial flux linkage with the coil. Only in the case of Topology-4, the stripe magnets yielded an improved EM coupling of 38.37mWb/m over that of the thin film being 31.66mWb/m, which suffers from the effect of the demagnetizing field.

Table 6.2. Structural details of the MEMS spring structures

Spring Structure	Overall dimension	Length of spring arm (Each meandered arm)	Length of stretched (fixed-guided) spring	Width of stretched spring
Nonlinear-a	12 X 8.8 X 0.1 mm^3	35mm	4.74mm	30μm
Nonlinear-b	12.13 X 8.93 X 0.1 mm^3	35.13mm	3.23mm	30μm
Nonlinear-c	12 X 8.8 X 0.1 mm^3	35mm	2.2mm	30μm
Nonlinear-d	11.6 X 9.2 X 0.1 mm^3	30.03mm	1.8mm	30μm
Linear	10 X 8.8 X 0.1 mm^3	9.2mm	**X**	**X**

Table 6.3. Value of the EM coupling obtained from FEM analysis with different topologies of EM-VEH

Topology	EM coupling with Square coil (mWb/m)		EM coupling with Rectangular coil (mWb/m)	
	Thin Film	Stripe pattern	Thin Film	Stripe pattern
1	4.47	4.08	7.36	8.42
2	9.08	8.79	13.61	19.45
3	15.71	14.89	26.07	24.11
4	31.66	38.37	48.05	62.9

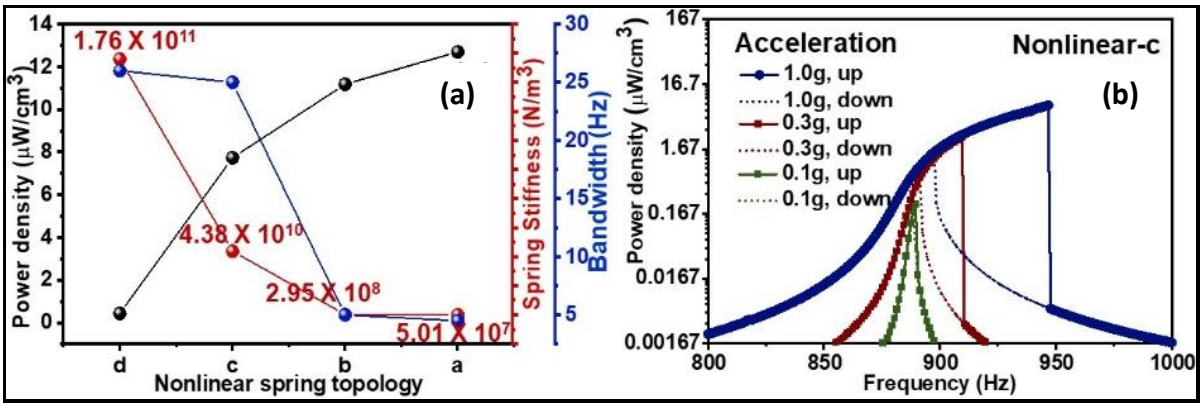


Figure 6.12: (a) Variation of power density and obtainable half-power bandwidth with respect to the nonlinear spring stiffness of the different nonlinear spring architecture with mechanical damping fixed at 0.001 using topology 4 with rectangular coil. (b) Shows the variation of load power density of spring-c with frequency.

Using the rectangle shaped microcoil with Topology-1 results in an enhanced EM coupling of 7.36mWb/m for a 50μm thin film as compared with that of the square coil, which turns into 8.42mWb/m when the thin film is replaced with an array of stripe micromagnets.

The EM coupling improves with the rectangular coil as the stray magnetic fields emerging from each side of the long edges of the patterned/unpatterned magnets interacts with the parallel tracks of the coil longitudinally when the central paddle of the MEMS spring exhibits in-plane vibrations. However, due to the geometrical shape of the square coil, significant fraction of the coil tracks is in the transverse direction with respect to the micromagnets, which does not promote substantial electromagnetic interaction between the coil turns and magnetic field lines. This explains the lower EM coupling obtained with the square coil as compared with the rectangular coil.

Unlike the square coil, on external excitation when the rectangular shaped coil on the central paddle of the MEMS spring exhibits in-plane motion, the stray magnetic fields emerging from each side of the long edges of stripe patterned magnets interacts with the parallel tracks of the coil. This promotes substantial electromagnetic interaction between each turn of the coil and the magnetic field lines. In Topology-2, where oppositely polarized adjacent magnet layer is used, the stripe patterns show superior interaction with the coil than the thin film, contributing an EM coupling of 19.45mWb/m. However, in the third topology that consists of four arrays of magnets, having the adjacent array oppositely polarized, the fields lines from the stripes fringes out while forming a close flux line between the magnets, giving almost similar EM coupling as with thin film. In order to substantially reduce the divergence of the magnetic field lines and to further increase the electromagnetic coupling, in Topology-4 an additional layer of soft magnetic material is added on the base of each magnet array. We have used $Ni_{45}Fe_{55}$ electrodeposited alloy as the soft magnetic material with the saturation magnetization of 1.2×10^{6} A/m [48]. The addition of this layer (thickness of the soft magnet layer= 20μm) aids to concentrate the magnetic field lines emanating from the oppositely polarized patterned magnets towards the coil. The inset of Fig.6.9 shows the variation of magnetic field lines for topology-3 and 4. It is evident from the simulation that this additional layer aids in concentrating the magnetic field lines towards the coil in topology-4, which in turn results in enhanced electromagnetic interaction within a small footprint. The electromagnetic coupling factor almost doubles in topology-4 using the thin films from 15.71mWb/m to 31.66mWb/m for square shaped coils and from 26.07mWb/m to 48.05mWb/m for the rectangular coil. A substantial improvement in the electromagnetic interaction could be observed using the soft magnetic base in topology-4 with the stripe magnet array and rectangular coil, which enhances the electromagnetic coupling factor from 24.11mWb/m in topology-3 to 62.9mWb/m in topology-4. This proves the efficacy of integrating qualitatively

optimized patterned magnets instead of continuous thin films to overcome the detrimental effect of the demagnetizing field.

Now to evaluate the electrodynamical performance of different nonlinear device topologies, we have considered here all the four nonlinear spring structures that are shown in Fig. 6.11 (a,b,c,d) to be assembled in Topology-4, each of them offering degree of nonlinearity differing by order of magnitude. From Fig.6.12(a) we can observe that, as the coefficient increases, the spring becomes harder to move due to the induced spring hardening nonlinearity. Although this enhances the half-power bandwidth from 5Hz (which is close to that of the linear system offering the bandwidth of 4Hz) in spring-a to 26Hz in spring-d, but it also restricts the motion of the spring which in turn affects the interaction between coil and magnet, hence the induced voltage. The power density, in this case, falls from 12.7μW/cm^3 for spring-a to 0.45μW/cm^3 for spring-d. Hence, to compare the performance of the conceived linear and the nonlinear topologies, we have selected the nonlinear spring-c (having a moderately high power density of 7.73μW/cm^3 along with high half-power bandwidth of 25Hz) along with the linear spring architecture. Fig. 6.12(b) shows the dynamic characteristics of the nonlinear MEMS EM-VEH in the form of extracted electrical power across a suitable load (266Ω). At low amplitude of external excitation (0.1g), the response of the system resembles that of a linear system and on increasing this excitation from 0.1g to 0.3g, the nonlinearity due to the effect of spring stretching comes into play, making the response of the system gradually non-resonant in nature. The response splits into two stable energy branches (on sweeping the frequency up and down, the response follows the high and low energy branch respectively) and the system can stay in either of the branches depending on the initial condition and the frequency schedule. This multistable nature of the system enhances the operable bandwidth of the vibration energy harvester.

We have considered Si-MEMS springs to hold the microcoil layer, which exhibits in-plane vibrations when subjected to external excitation. The mechanical damping of such MEMS spring structure varies with different constituent materials, as well as with different structural designs. [50] Reported the mechanical damping of 2.53×10^{-4} N-m/s for a MEMS spring architecture. So, we have considered here two different values of mechanical damping coefficient, 0.01and 0.001, as typical values, keeping the external excitation amplitude fixed at 1g, to study the effect of this damping on the overall performance of the linear (as shown in Fig. 6.10(a)) and the nonlinear (spring-c) device. The half-power bandwidth of the nonlinear structure (25Hz) is approximately six times larger than that of the linear ones (4Hz) with 1g excitation. When the mechanical damping is high (0.01), both the linear and the nonlinear

devices assembled in the topology-4 offers a power density of 0.61μW/cm^3 and 0.24μW/cm^3 with the linear and the nonlinear spring structures, respectively. However, the reduced mechanical damping factor of 0.001 aids in producing a power density of up to 52μW/cm^3 with the linear device (with 1g excitation amplitude) when it is assembled as topoplogy-4. The low damping also aids in enhancing the power output from the nonlinear device, the spring-c maximizes the power density to 7.73μW/cm^3 with the compact topology-4. Table 6.4 summarizes the performance comparison of the proposed MEMS vibration energy harvesters with the reported contemporary energy harvesters. The energy harvesting unit reported in [24] generates 0.11μW/cm^{3}g^2 power density while extracting the mechanical energy from 1.2g excitation at 48Hz. On the other hand, the MEMS deice reported in [30] yields a very large power density of 234157μW/cm^{3}g^2, however, it should be noted that the frequency of resonance is very high in this specific case (7400Hz) where not a lot of ambient mechanical energy could be found. The MEMS devices proposed in this work generates a maximum of 52μW/cm^{3}g^2 while extraction mechanical energy from vibrations of 1g at 614Hz frequency outpacing the work reported in [24] and [30].

Table 6.4- Performance comparison of EM-VEHs

Reference	Volume (mm^3)	Acceleration (g)	Resonant/ Bandwidth	Power density
[24]	67.5	1.2	Resonant peak 48Hz	0.11μW/cm^{3}g^2
[30]	30	0.11	Resonant peak 7400Hz	234157μW/cm^3 g^2
[49]	32	3	Resonant peak 82Hz, extended up to 146.5Hz	0.062 μW/cm^3 g^2
This work, linear EM-VEH	50	1	Resonant peak 614Hz, bandwidth 4Hz	52μW/cm^3 g^2
This work, Nonlinear EM-VEH (spring-c)	60	1	Non-resonant, bandwidth 25Hz (921-946Hz)	7.73μW/cm^3 g^2

Therefore, it can be concluded that when the mechanical damping is relatively small, the electromagnetic coupling associated with the electrical damping dominates and influences

the performance of the devices. The maximum power can be extracted from the harvester unit by reducing the mechanical damping to a point, comparable to the electromagnetic damping associated with the system [51]. A significant part of the mechanical damping consists of the frictional loss and the damping due to air drag. Vacuum packaging of the MEMS structures is a popular approach to circumvent the air damping [52]. The mechanical damping could be also reduced by altering the spring architecture, e.g. by making comb like structures that reduces the air damping [53]. Hence, to conclude, the most compact topology (topology-4) including the optimized patterns of micromagnets and coils can be used with the linear spring where the vibrations comprise of a single resonant peak, and those can be used with the optimized nonlinear spring (spring-c) for broadband vibrations.

6.6 Conclusion

This chapter presents the design of fully integrated MEMS EM-VEH with relatively high power density, which consists of an optimized patterned array of stripe shape magnets, and linear, nonlinear MEMS spring that carries the coil. Through analytical formulation and systematic finite element analysis, we have presented an approach to maximize the magnetic flux density in a precise location. Rectangular and square shaped micro-coils have been employed, the former demonstrating stronger electromagnetic interaction with the stripe micromagnets resulting in a dramatically improved electromagnetic coupling coefficient of 62.9mWb/m. A compact topology with designed linear spring produces a power density as high as 52μW/cm^3 at 1g acceleration with a low half power bandwidth. The nonlinear counterpart enhances the bandwidth almost six times to 25Hz at the cost of reduced power density. This detailed study opens up the scope for improving the performance of the overall device with further design optimization that will aid in powering the wireless sensor network.

6.7 References

[1] S. D. Moss, O. R. Payne, G. A. Hart, and C. Ung, "Scaling and power density metrics of electromagnetic vibration energy harvesting devices," *Smart Materials and Structures,* vol. 24, no. 2, p. 023001, 2015.

[2] D. P. Arnold, "Review of Microscale Magnetic Power Generation," *IEEE Transactions on Magnetics,* vol. 43, no. 11, pp. 3940-3951, 2007.

[3] C. R. Saha, "Modelling theory and applications of the electromagnetic vibrational generator," *Sustainable Energy Harvesting Technologies–Past, Present and Future,* pp. 55-108, 2011.

[4] J. M. D. Coey, "Hard Magnetic Materials: A Perspective," *IEEE Transactions on Magnetics,* vol. 47, no. 12, pp. 4671-4681, 2011.

[5] D. Mallick, K. Paul, T. Maity, and S. Roy, "Magnetic performances and switching behavior of Co-rich CoPtP micro-magnets for applications in magnetic MEMS," *Journal of applied Physics,* vol. 125, no. 2, p. 023902, 2019.

[6] B. Ma, J. Herchenroeder, B. Smith, M. Suda, D. Brown, and Z. Chen, "Recent development in bonded NdFeB magnets," *Journal of magnetism and magnetic materials,* vol. 239, no. 1-3, pp. 418-423, 2002.
[7] S. Roundy, P. Wright, and J. M. Rabaey, "A Study of Low Level Vibrations as a Power Source for Wireless Sensor Nodes," *Computer Communications,* vol. 26, pp. 1131-1144, 07/01 2003.
[8] P. Gope and T. Hwang, "BSN-Care: A secure IoT-based modern healthcare system using body sensor network," *IEEE sensors journal,* vol. 16, no. 5, pp. 1368-1376, 2015.
[9] N. H. Motlagh, M. Bagaa, and T. Taleb, "UAV-Based IoT Platform: A Crowd Surveillance Use Case," *IEEE Communications Magazine,* vol. 55, no. 2, pp. 128-134, 2017.
[10] F. T. Johnsen *et al.*, "Application of IoT in military operations in a smart city," in *2018 International Conference on Military Communications and Information Systems (ICMCIS)*, 2018, pp. 1-8: IEEE.
[11] S. Gao, X. Dai, Y. Hang, Y. Guo, and Q. Ji, "Airborne wireless sensor networks for airplane monitoring system," *Wireless Communications and Mobile Computing,* vol. 2018, 2018.
[12] S. Chamanian, H. Uluşan, Ö. Zorlu, S. Baghaee, E. Uysal-Biyikoglu, and H. Külah, "Wearable battery-less wireless sensor network with electromagnetic energy harvesting system," *Sensors and Actuators A: Physical,* vol. 249, pp. 77-84, 2016/10/01/ 2016.
[13] Y. Kuang, T. Ruan, Z. J. Chew, and M. Zhu, "Energy harvesting during human walking to power a wireless sensor node," *Sensors and Actuators A: Physical,* vol. 254, pp. 69-77, 2017.
[14] "Real Vibrations, NIPS lab, Aircraft power spectrum data."
[15] Q. Liao, P. Huang, Z. An, D. Li, H. Huang, and C. Zhang, "Origin of thermal depolarization in piezoelectric ceramics," *Scripta Materialia,* vol. 115, pp. 14-18, 04/01 2016.
[16] N. Miwatani, T. Fujita, Y. Kitagawa, K. Kanda, and K. Maenaka, "Design Improvement For Preventing Discharge During Fabrication Of Electrostatic Energy Harvester," *Journal of Physics: Conference Series,* vol. 773, p. 012117, 2016/11 2016.
[17] S. Roy, D. Mallick, and K. Paul, "MEMS-Based Vibrational Energy Harvesting and Conversion Employing Micro-/Nano-Magnetics," *IEEE Transactions on Magnetics,* vol. 55, no. 7, pp. 1-15, 2019.
[18] D. Niarchos, "Magnetic MEMS: key issues and some applications," *Sensors and Actuators A: Physical,* vol. 109, no. 1, pp. 166-173, 2003/12/01/ 2003.
[19] H. Li, T. J. Flynn, J. C. Nation, J. Kershaw, L. Scott Stephens, and C. A. Trinkle, "Photopatternable NdFeB polymer micromagnets for microfluidics and microrobotics applications," *Journal of Micromechanics and Microengineering,* vol. 23, no. 6, p. 065002, 2013/04/22 2013.
[20] T. Dutta, S. N. Piramanayagam, T. H. Ru, M. S. M. Saifullah, C. S. Bhatia, and H. Yang, "Exchange coupled CoPt/FePtC media for heat assisted magnetic recording," *Applied Physics Letters,* vol. 112, no. 14, p. 142411, 2018/04/02 2018.
[21] R. Fujiwara, T. Devillers, D. Givord, and N. M. Dempsey, "Characterization of the magnetic properties of NdFeB thick films exposed to elevated temperatures," *AIP Advances,* vol. 8, no. 5, p. 056225, 2018.
[22] O. D. Oniku, B. J. Bowers, S. B. Shetye, N. Wang, and D. P. Arnold, "Permanent magnet microstructures using dry-pressed magnetic powders," *Journal of Micromechanics and Microengineering,* vol. 23, no. 7, p. 075027, 2013.
[23] T. Speliotis, D. Niarchos, P. Falaras, D. Tsoukleris, and J. Pepin, "Nd-Fe-B thick films prepared by screen printing," *IEEE transactions on magnetics,* vol. 41, no. 10, pp. 3901-3903, 2005.
[24] M. Han, Z. Li, X. Sun, and H. Zhang, "Analysis of an in-plane electromagnetic energy harvester with integrated magnet array," *Sensors and Actuators A: Physical,* vol. 219, pp. 38-46, 2014/11/01/ 2014.
[25] D. L. Roy *et al.*, "Fabrication and characterization of polymer membranes with integrated arrays of high performance micro-magnets," *Materials Today Communications,* vol. 6, pp. 50-55, 2016/03/01/ 2016.
[26] Y. Tanaka *et al.*, "Electromagnetic Energy Harvester by Using NdFeB Sputtered on High Aspect Ratio Si Structure," *Journal of Physics: Conference Series,* vol. 476, p. 012095, 2013/12/04 2013.
[27] S. Kulkarni *et al.*, "Design, fabrication and test of integrated micro-scale vibration-based electromagnetic generator," *Sensors and Actuators A: Physical,* vol. 145, pp. 336-342, 2008.
[28] K. Tao *et al.*, "A novel two-degree-of-freedom MEMS electromagnetic vibration energy harvester," *Journal of Micromechanics and Microengineering,* vol. 26, no. 3, p. 035020, 2016/02/11 2016.
[29] Y. Li, J. Li, A. Yang, Y. Zhang, B. Jiang, and D. Qiao, "Electromagnetic Vibrational Energy Harvester With Microfabricated Springs and Flexible Coils," *IEEE Transactions on Industrial Electronics,* vol. 68, no. 3, pp. 2684-2693, 2021.
[30] S. Kulkarni, S. Roy, T. O'Donnell, S. Beeby, and J. Tudor, "Vibration based electromagnetic micropower generator on silicon," *Journal of Applied Physics,* vol. 99, no. 8, p. 08P511, 2006.
[31] D. Mallick, A. Amann, and S. Roy, "A nonlinear stretching based electromagnetic energy harvester on FR4 for wideband operation," *Smart Materials and Structures,* vol. 24, no. 1, p. 015013, 2014/11/27 2014.
[32] B. Marinkovic and H. Koser, "Smart Sand—A Wide Bandwidth Vibration Energy Harvesting Platform," *Applied Physics Letters - APPL PHYS LETT,* vol. 94, 03/09 2009.

[33] R. Xu, H. Akay, S.G. Kim, "Buckled MEMS Beams for Energy Harvesting from Low Frequency Vibrations", Research- Science Partner Journal, vol. 2019, 2019
[34] A. Hajati, S.G. Kim, "Ultra-wide bandwidth piezoelectric energy harvesting", Applied Physics Letters, vol. 99, pp. 083105, 2011.
[35] P. Constantinou and S. Roy, "A 3D printed electromagnetic nonlinear vibration energy harvester," *Smart Materials and Structures*, vol. 25, no. 9, p. 095053, 2016/08/24 2016.
[36] A. Sokolov, D. Mallick, S. Roy, M. P. Kennedy, and E. Blokhina, "Modelling and verification of nonlinear electromechanical coupling in micro-scale kinetic electromagnetic energy harvesters," *IEEE Transactions on Circuits and Systems I: Regular Papers*, vol. 67, no. 2, pp. 565-577, 2019.
[37] D. Zhu, S. Roberts, T. Mouille, M. J. Tudor, and S. P. Beeby, "General model with experimental validation of electrical resonant frequency tuning of electromagnetic vibration energy harvesters," *Smart Materials and Structures*, vol. 21, no. 10, p. 105039, 2012.
[38] C. Cepnik, O. Radler, S. Rosenbaum, T. Ströhla, and U. Wallrabe, "Effective optimization of electromagnetic energy harvesters through direct computation of the electromagnetic coupling," *Sensors and Actuators A: Physical*, vol. 167, no. 2, pp. 416-421, 2011.
[39] B. A. Owens and B. P. Mann, "Linear and nonlinear electromagnetic coupling models in vibration-based energy harvesting," *Journal of Sound and Vibration*, vol. 331, no. 4, pp. 922-937, 2012.
[40] E.P.Furlani, "Permanent Magnet and Electromechanical Devices," San Diego:Academic Press, 2001, pp. 207-333.
[41] V. Zablotskii, J. M. Pastor, S. Larumbe, J. I. Pérez-Landazábal, V. Recarte, and C. Gómez-Polo, "High-Field Gradient Permanent Micromagnets for Targeted Drug Delivery with Magnetic Nanoparticles," in *AIP Conference Proceedings*, 2010, vol. 1311, no. 1, pp. 152-157: American Institute of Physics.
[42] M. Han, Q. Yuan, X. Sun, and H. Zhang, "Design and Fabrication of Integrated Magnetic MEMS Energy Harvester for Low Frequency Applications," *Journal of Microelectromechanical Systems*, vol. 23, no. 1, pp. 204-212, 2014.
[43] N. Dempsey *et al.*, "High-coercivity Nd–Fe–B thick films without heavy rare earth additions," *Acta materialia*, vol. 61, no. 13, pp. 4920-4927, 2013.
[44] M. Nakano *et al.*, "Nd–Fe–B Film Magnets With Thickness Above 100${\mu}\text {m} $ Deposited on Si Substrates," *IEEE Transactions on Magnetics*, vol. 51, no. 11, pp. 1-4, 2015.
[45] S. P. Beeby and T. O'Donnell, "Electromagnetic energy harvesting," *Energy Harvesting Technologies*, pp. 129-161, 2009.
[46] Y. Lei and Z. Wen, "Study on effects of the damping ratio on output performance of micro electromagnetic vibration energy harvesters," *Microsystem Technologies*, vol. 21, no. 1, pp. 221-226, 2015.
[47] F.O.Keller and N.M.Dempsey, 2022.
[48] B. Jamieson, J. F. Godsell, N. Wang, and S. Roy, "Device Geometry Effects in an Integrated Power Microinductor With a Ni $ _ {45} $ Fe $ _ {55} $ Enhancement Layer," *IEEE transactions on magnetics*, vol. 49, no. 2, pp. 869-873, 2012.
[49] H. Liu, Y. Qian, N. Wang, and C. Lee, "An In-Plane Approximated Nonlinear MEMS Electromagnetic Energy Harvester," *Journal of Microelectromechanical Systems*, vol. 23, no. 3, pp. 740-749, 2014.
[50] D. Nguyen, E. Halvorsen, G. Jensen, and A. Vogl, "Fabrication and characterization of a wideband MEMS energy harvester utilizing nonlinear springs," *Journal of Micromechanics and Microengineering*, vol. 20, no. 12, p. 125009, 2010.
[51] T. O'Donnell, C. Saha, S. Beeby, and J. Tudor, "Scaling effects for electromagnetic vibrational power generators," *Microsystem Technologies*, vol. 13, no. 11, pp. 1637-1645, 2007/07/01 2007.
[52] R. Elfrink *et al.*, "Vacuum-packaged piezoelectric vibration energy harvesters: damping contributions and autonomy for a wireless sensor system," *Journal of Micromechanics and Microengineering*, vol. 20, no. 10, p. 104001, 2010.
[53] Y. Lu, F. Marty, D. Galayko, J.-M. Laheurte, and P. Basset, "A power supply module for autonomous portable electronics: ultralow-frequency MEMS electrostatic kinetic energy harvester with a comb structure reducing air damping," *Microsystems & Nanoengineering*, vol. 4, no. 1, p. 28, 2018/09/24 2018.

Chapter 7: Conclusions and Future Work

7.1 Introduction

The rapid advancements in Low Power Embedded Electronics along with Information and Communication technologies have enabled the paradigm of a wirelessly connected smart and responsive environment through the Internet of Things (IoT). However, one of the major impediment in the pervasive deployment of wireless sensor nodes for building a resilient self-powered network is in finding a reliable and sustainable power source as a replacement of the energy-limited batteries for these sensor nodes. These simple pre-requisites imply strict requirements for the energy supply, storage and corresponding power management to ensure 'perpetual' operation of the IoT devices, while demanding 'cable-free', 'zero maintenance' and 'long-term' solutions. The omnipresence of mechanical energy in the form of vibrations in the rural/urban domestic and industrial environment offers the unique opportunity of harnessing these vibrations and converting it into usable electrical energy to power these deployable sensor nodes through dedicated Electromagnetic Vibration Energy Harvesters (EM-VEHs). Majority of the VEHs are composed of linear oscillators with limited bandwidth of operable frequencies. On the other hand, nonlinear oscillator based VEHs offers wider bandwidth, which allows the device to harness mechanical energy more efficiently. This thesis presents the development of sustainable vibration energy harvesting solutions in both meso-scale, and micro-scale that is more challenging. The energy harvester prototypes have been designed, optimized, fabricated and exhaustively characterized. Robust mathematical models have been developed to further investigate the complex dynamical properties, especially for the nonlinear counterpart. The vibration energy harvesting capability have been demonstrated both in laboratory and real-world vibration environment and these devices have been employed to power wireless sensor platforms. In this chapter, we aim to revisit the previously presented work and highlight the key contributions of each. We also propose novel energy harvesting solution and provide a firm roadmap that would lead to enhanced energy harvesting capabilities with highly integrated miniaturized and batch fabricated VEHs.

7.2 Contributions and results of this work

Chapter 1

- The economic boomof the IoT market has been highlighted which is a key impetus behind the development of sustainable green energy source to replace batteries. The prediction of 27 billion IoT connected devices by the year 2025 [1], which potentially would result in an economic return of $3.9-$11.1 trillion per year [2] has been cited in this context.
- It has been identified that despite of great potential, the growth of the IoT market is largely restrained by the batteries that offers finite lifetime and depletes the energy faster owing to the large computational complexities, which greatly impedes the vision of fit-and-forget IoT devices, rather incurs additional maintenance cost for battery replacement.
- To address the sustainable powering issue of IOT devices, this chapter highlights the benefits of exploiting renewable energy sources, such as solar energy, thermal energy, radio frequency energy, mechanical energy etc. for replacing the batteries with sustainable power source, also known as energy harvesters. The working principle of state-of-the-art energy harvesters as well as the wide range of application area have been discussed for each energy sources.
- Different mechanical/vibration energy transduction mechanisms namely, electrostatic transduction, piezoelectric transduction, triboelectric transduction and electromagnetic transduction have been explained with suitable examples through detailed literature survey. The work presented in this dissertation aims to improve the performance of electromagnetic transducers, or in other words electromagnetic vibration energy harvesters (EM-VEHs) to enhance their practical applicability for powering the wireless sensor nodes of the IoT network.

Chapter 2

- This chapter presents a thorough literature survey on EM-VEHs while highlighting the key merits, demerits and challenges in implementing high-efficiency VEHs within a small footprint. Detailed theoretical background has been prepared for the resonant VEH, which relies on the operation of a narrowband linear oscillator.
- State-of-the-art resonant VEHs have been cited and their key performance metrics have been discussed. Various bandwidth widening strategies including frequency tuning [3, 4], exploiting array of oscillators [5], implementing multimodal oscillators [6, 7] etc. have been discussed in this context.

- Nonlinear vibration energy harvesters has been identified as a potential candidate for harnessing mechanical energy efficiently over wider range of frequencies. The detailed theoretical background presented in this chapter highlights the different obtainable nonlinear potential energy profiles such as monostable, bistable etc. which can be further extended for polystable nonlinear system.
- Advantages of inducing monostable nonlinearity into the energy harvesting system by the means of magnetic levitation [8-10] or spring stretching [11-13] have been discussed.
- Resonant and non-resonant micro-scale energy harvesters [14-16] have also been considered in this literature survey. The primary challenges and the potential routes to address those limitations have been discussed along with suitable examples from the literature.

The final section of this chapter has been dedicated towards the power conversion and power management unit [17-19]of the energy harvesting system, which interfaces the VEH with the target load.

Chapter 3

- A feasibility study has been presented in this chapter with a resonant VEH that is exploited to improve wireless communication of a wireless sensor node. The VEH is designed with concertina like springs that are optimized to exhibit large out-of-plane oscillations (2.5mm), which in turn translates into enhanced electromagnetic interaction and large power outcome.
- The fabricated device within a small footprint of only $9cm^3$, delivered large power (1200µW) at the resonance with moderate external excitation (0.6g). A low power consuming near field communication (NFC) based wireless sensor node has been chosen as the target load.
- With the VEH powering the electronics interface of the sensor node, the RF energy harvested from the reader is directed only towards facilitating the wireless communication. This brings a 120% improvement in the range of communication with the VEH extracting mechanical energy from low amplitude (0.2g) harmonic excitations.
- Autonomous monitoring of temperature and humidity in industrial cleanroom environment has been highlighted as one of the potential application area for the developed energy harvesting system.

Chapter 4

- A nonlinear wideband VEH has been designed and developed as presented in this chapter. Tapered spring architecture have been introduced here which aids in reinforcing cubic

nonlinear restoring force into the system arising from the stretching of the spring. Two VEH prototype have been fabricated on 0.25mm FR4 sheet from the optimized designs, comprising two and four tapered spring arms.

- The VEHs have been electrodynamically characterized and the frequency response has been corroborated with developed numerical model. The nonlinear VEH yields a large power density of 2660μW/cm^{3}g^2 along with large bandwidth of 45Hz at 1g acceleration.
- The developed energy harvester has been employed to power a Bluetooth communication based wireless sensor platform, which reports on ambient temperature and humidity. The VEH successfully powered this wireless sensor platform while harnessing mechanical energy from laboratory based harmonic excitation as well as from real world random vibrations (the rear part of a car).

Chapter 5

- This chapter explores the complex dynamical features of a nonlinear wideband VEH. A nonlinear wideband VEH is presented which combines nonlinear forces arising from magnetic interaction as well as from spring stretching. Tapered spring geometry has been used to instigate spring stretching.
- Through investigation of the complex energy branch structure, it was found that the highest energy branch is not achieved through a typical sweep of driving frequencies; rather a special frequency schedule is required to achieve and sustain this hidden high-energy state.
- Experimentally this high-energy branch was achieved with a low excitation amplitude. Reduced Order Model (ROM) has been developed to validate the existence of multiple energy branches coexisting for certain driving conditions.
- Force-displacement plots, that are referred in this work as eye diagrams have been presented, which are useful tool used to study the energy transaction that takes place through each of the energy branches, from time-resolved measurements. The different eye shapes bears useful information regarding the involved nonlinearities, on the other hand the area of these eye enclosed in the force-displacement plane represents the energy transacted through the respective energy branches over period of the external drive. Such a tool could be useful for wider application area beyond energy harvesting.

Chapter 6

- This chapter firstly presents the pertinent challenges in realizing high-performance permanent hard magnets for MEMS (Micro-Electro-Mechanical-Systems) scale and

addresses these bottlenecks through proposed alternatives. It has been identified that shape dependent demagnetization effect affects the performance of magnetic thin films.

- Patterned array of micromagnets are proposed as a replacement of thin films as it generates stronger stray magnetic fields emanating from each of the edges of the micromagnetic elements in the array. With exhaustive finite element analysis and analytical mathematical tool, the shape, size and distribution of the magnets in the array have been optimized to enhance the electromagnetic interaction with microfabricated coils.
- To facilitate such electromagnetic interactions, novel device topologies have been conceived that comprise of in-planar moving linear/nonlinear MEMS springs, which holds microfabricated rectangular coil. On separate substrate, patterned micromagnets are arranged in a way that forms a closed loop of magnetic field lines across the coil that maximizes the electromagnetic coupling between the magnet and coil assembly. Owing to the long parallel edges, the stripe-patterned magnets are found to be offering highest magnetic flux linkage that translates into maximum electromagnetic coupling of 62.9mWb/m.
- Novel spring designs have been proposed to implement fully integrated MEMS VEH. A compact linear MEMS spring produces a power density as high as 52μW/cm^3 at 1g acceleration; however, this VEH offers a limited bandwidth. On the other hand, the nonlinear counterpart enhances the operable bandwidth of frequencies six times compared to the linear VEH, at the cost of reduced power density of only 7.73μW/cm^3.

7.3 Existing pertinent challenges and potential solutions

Over the past couple of decades, there has been a tremendous development in the field of low power electronics, which reinforces the advancement in the field of energy harvesting. Furthermore, new technologies have been developed that aids in batch production of high-efficiency devices, which in turn promotes system level integration. In this section, few of the key challenges existing in the field of EM vibration energy harvesting have been discussed, with an emphasis on miniaturization and integration.

- Low frequency MEMS VEH- Silicon and Silicon-on-insulator material are majorly used for the fabrication of miniaturized MEMS scale VEH devices owing to the compatibility with CMOS fabrication technology as well as for the mechanical strength that the VEH structures derives from these material. This comes at the cost of high operation frequency (>500Hz) due to the large elastic modulus (~170GPa) of these materials. The scaled up operational frequency of these MEMS VEH devices casts

detrimental effect on the device performance since in the real-world application scenario a large fraction of the vibrational energy is distributed over the low frequency components (<200Hz). Hence exploiting polymeric materials for developing the VEH spring structure in order to reduce the operable frequency within the same footprint [20, 21] is a viable choice to address the frequency scaling issue. The low elasticity modulus of these polymers also enhances the displacement amplitude, which potentially could translate into enhanced performance of the VEHs. Furthermore, using polymer material for the VEHs also opens up the scope for the integration of these VEH into human body, a rich source of low frequency mechanical energy.

- CMOS compatible magnets- One of the best performing magnets for electromagnetic VEHs are the rare-earth material based magnets (NdFeB/SmCo) that are manufactured commercially using sintering technique. Despite of the high-energy product that these magnets offer, there are three major drawbacks, which limits the wide applicability of these magnets, particularly in the field of vibration energy harvesting. The manufacturing process of these rare-earth magnets require high temperature treatment [22] which makes them incompatible with the CMOS fabrication technology, furthermore, the performance of these magnets deteriorates dramatically with scaling. Above all, the limited resource of the rare-earth materials demands for potential alternative hard magnetic materials. To this end, rare-earth free metal alloys like CoPt and FePt offers superior magnetic performance [23, 24] with equiatomic ratio and $L1_0$ phase, however, this phase transition too requires high temperature treatments such as annealing. Over the past decade, significant research attention has been devoted towards investigating the performance of polymer bonded magnets such as- hard magnetic SmFeN powders bonded with PDMS with up to 300µm thickness [25], wax bonded 320µm thick micromagnets with NdFeB magnetic powder having average particle diameter 50µm [26]. Furthermore, dry-packed magnetic powders (SmFeN, NdFeB) into high-aspect ratio trenches [27, 28], which, together with the polymer/wax bonded magnets, are compatible with CMOS fabrication technology, and offers ease in batch fabrication of these magnets. However, the performance of these magnets depends largely on the packing fraction of the magnetic powders into the dedicated molds, hence careful choice of the particle size and shape is of significant importance to increase the performance of these magnets. Additive manufacturing/injection molding of highly dense bonded magnets (such as nylon bonded NdFeB magnetic powders) [29, 30] have gained popularity owing to the control over the dimension and

shape of the magnet as well as for the ease of implementation. However, the rare-earth based magnets majorly dominate these technologies. Interesting magnetic exchange interaction takes place in magnetic multilayer structures [31], especially at the boundaries between hard magnetic and soft magnetic phases, which results in increased energy product. The increase in coercivity arises from the hard magnetic material and the remanance increases owing to the soft magnetic material, which leads towards a rectangular hysteresis behaviour of the multilayer structure. The recent advancements in fabricating highly controlled magnetic thin films of (e.g. FeGa/CoFeB multi-layered films, FeAu/FePt multilayer films) through electrodeposition [32], sputtering [33] technologies makes such magnetic multilayer structures a promising alternative of rare-earth based high energy product magnets. The exchange interaction offers the degree of freedom to be tailored depending on the thickness of the soft magnetic material. Such high-performance rare-earth free magnetic structures could be well exploited for manufacturing high-performance micromagnets for energy harvesting.

- Miniaturized coil development- Along with the challenges of implementing microscale high energy density magnets, as explained in the previous chapters, implementation of high-efficiency microcoils is also a key limitation for MEMS scale VEHs. The coil parameters such as number of turns, resistance, inductance largely depends on the coil design. The number of coil turns within a given area can be maximized by optimizing the track width and spacing between each track, which are restricted by the limitations of the standard optical lithography process. The effect of the inductance at low vibrational frequency is negligible. On the other hand, reduction in the coil track width results in increased coil resistance, which casts adverse effect on the device performance. Hence, for the target VEH applications, the aim is to build highly efficient microcoils by increasing the number of turns within a fixed footprint while maintaining the coil resistance to a low value. Instead of standard lithography steps, deep reactive ion etching (DRIE) could be employed to prepare high aspect ratio silicon mold for electrodepositing copper into prepared trenches [34] that leads to high aspect-ratio microfabricated coils with lower resistance. Increasing the packing density of the conductors within a fixed volume is another alternative route to enhance the efficiency of the microcoils. Vertical layers of microcoils [35] as well as plating of coil tracks between the coil turns [36] are viable strategies for implementing reliable high-efficiency microcoils.

- Low power energy conversion- The electromagnetic MEMS VEHs offers lower output voltage; hence, it is of utmost importance for the following rectification stage to consume less power and if possible to boost the voltage/power. The traditional diode based rectifiers cause significant power loss across the rectification stage. The cold-start voltage of majority of the commercially available electronics interface are high which restricts it's applicability with MEMS scale VEHs that generates low power from ambient vibrations. Additionally, suitable maximum power point tracking (MPPT) strategy is also required to increase the overall performance of the system. Recent developments in the adaptive MPPT schemes as well as active low power consuming rectification [37] opens up the opportunity for boosting the voltage level and efficiently delivering substantial power through small scale VEHs. Furthermore, low cold-starting electronic interfaces [38] have been developed which promotes the exploitation of MEMS scale VEHs for practical applications.
- Monolithic integration- With increasing computational complexities, there is a perpetual drive towards the development of high efficiency, functionally integrated power conversion and management unit within a small footprint to aid the VEHs in powering target loads, typically wireless sensor platforms of IoT. Discrete passive components such as inductors and capacitors associated with the DC-DC conversion stage does not allow ease in scaling down the footprint of the electronics interface. At higher switching speeds (say 10-100MHz); the size of these passive components can be reduced down to the extent that these passive components allow monolithic integration. The recent developments in the field of on-silicon technology (e.g. integrated inductors) have opened up the opportunity for integrating the passive components within the same package as the power management IC, implementing Power supply on chip (PwrSoC) [39], which is revolutionizing the world of low power electronics. This level of integration along with high-performance VEH would enhance the deliverable power across the target load.

7.4 Future work, a continuation of the work in this dissertation

As pointed out in this dissertation, one of the obvious challenges in the field of vibration energy harvesting is to develop novel low frequency MEMS-scale EM-VEHs for wide-bandwidth of operational capability and efficient transduction of the mechanical energy, which in turn would improve the power density and the reliability simultaneously. The aim

is to enhance the level of integration while sustaining the normalized power density, which is the obtained power per unit volume per square of the external excitation amplitude. High power density can be obtained from macro or meso-scale devices. In this context, along with the MEMS design presented in chapter-6, the out-of-plane motion exhibiting springs geometries developed in chapter-3 and 4 will be also implemented in MEMS scale. However, as can be observed from the exhaustive literature review presented in this dissertation, on scaling these devices down to MEMS scale, the power density rapidly decreases several orders of magnitude. Hence, the future direction of this work would be devoted towards exploiting novel device topologies as well as compatible magnet integration strategy to enhance the deliverable power from MEMS scale device, which is schematically portrayed in Fig. 7.1.

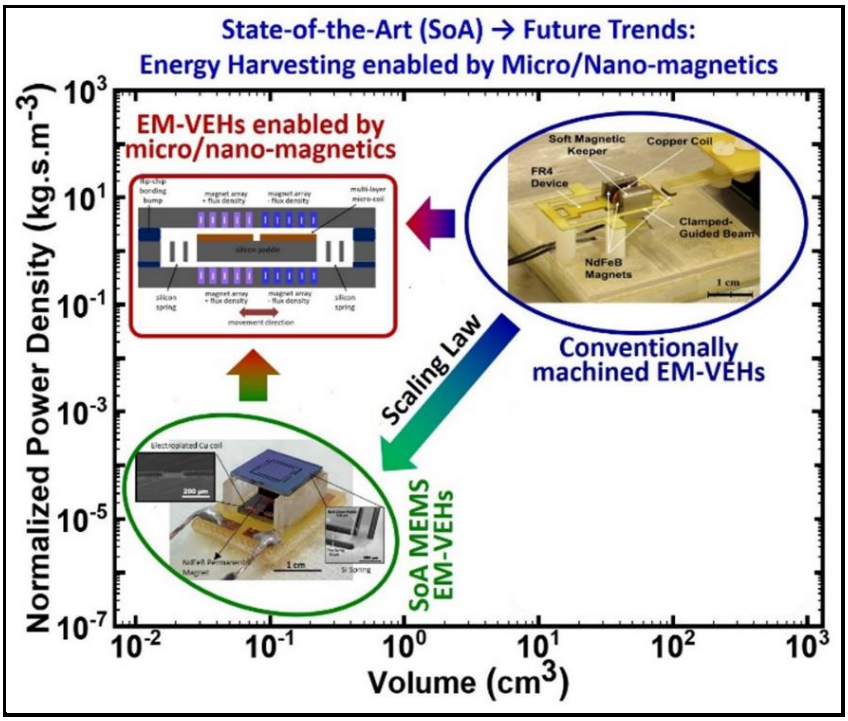


Figure 7.1: Vision of fully integrated MEMS VEH device with high normalized power density.

In chapter-4, the advantages of inducing nonlinear forces into VEHs to widen the bandwidth of operation have been demonstrated, and in chapter-6, the benefits of employing patterned array of magnets have been shown which enhances the performance of the MEMS scale VEHs. As a continuation of the presented work, it would be a logical

choice to exploit a low-cost novel technique for the fabrication of oppositely polarized, patterned micro-magnets on an in-planar flexible MEMS-spring structure, as shown in Fig. 7.2. This will boost the EM-coupling between the magnets and the micro-fabricated coils dramatically in the MEMS scale resulting in larger output power and bandwidth. Moreover, such flexible high performance magnets will find its place in attractive hitherto unexplored applications in the field of microactuator, microsensor, biomedicine, microfluidics etc. beyond energy harvesting. The nonlinear spring will be fabricated on PDMS (Polydimethylsiloxane) which would effectively scale down the frequency of oscillation (expected <100Hz) owing to the low young's modulus (0.57MPa-3.7MPa), which is desired to allow substantial energy harvesting, compared to the Silicon/SOI wafers that only offers higher frequency of oscillation (>200Hz) due to the high young's modulus (~190GPa) of the spring material.

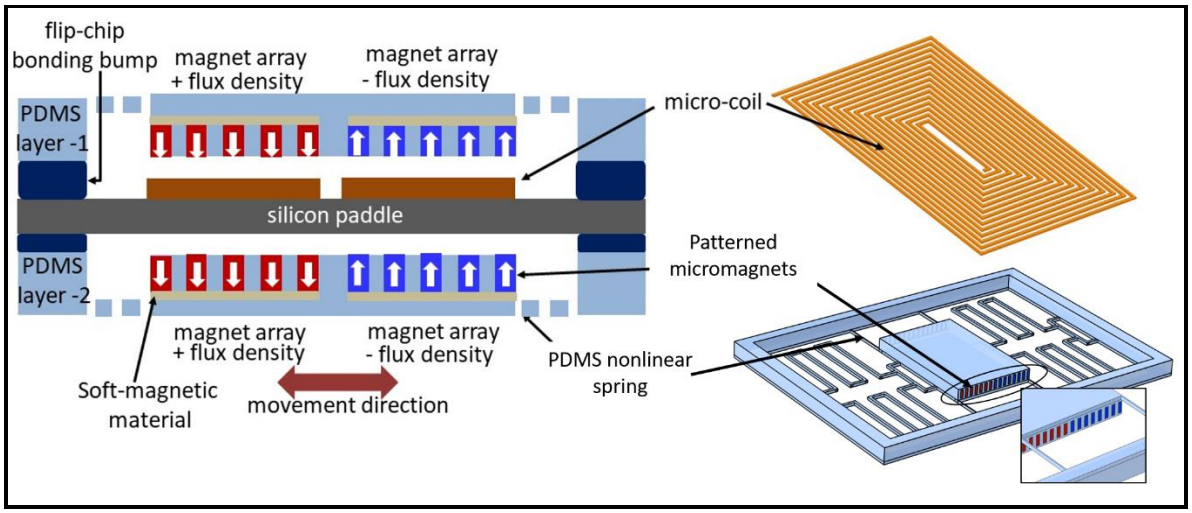


Figure 7.2: Nonlinear wideband flexible MEMS scale VEH comprising of flexible MEMS spring, embedded bonded magnets and high-density microcoil.

The optimized spring structures would be fabricated on 500µm thick double side polished Silicon-On-Insulator (SOI) wafer with the device layer of 50µm, the process flow is shown in Fig. 7.3. Two mask would be used, one to define the shape of the thin spring structure and the other mask dedicated for etching the oxide layer for back silicon etching. The device layer in the front would be etched with Deep-Reactive-Ion-Etching (DRIE). Thin layer (~5µm) of metal will be sputtered on the front side of this wafer to provide mechanical support, which would be later wet, etched to release the nonlinear mechanical spring structure. Following these steps, the obtained mechanical structures would be considered as the master mold, on which PDMS would be cast, and post curing the PDMS springs from this structure would be released.

Very thick, embedded micromagnets would be developed in PDMS trenches (separately prepared with Silicon master mold) by binding NdFeB powder with polymer such as parylene, the process flow is shown in Fig. 7.4. To facilitate the opposite polarity of the micromagnet array, magnetization mask will be used. First, the micromagnets will be pre-magnetized using a magnetizer to induce magnetic polarization everywhere. The magnetizing mask with the desired pattern will be then brought in contact with the developed magnetic structure, and a pulsed magnetic field would be applied in the opposite direction. Because of the differences in relative permeability created by the mask features, the external reversal magnetic flux is concentrated in the areas of the magnetic mask. Consequently, the magnetization of selected regions is reversed, and the desired pattern is transferred onto the micropatterns. This magnet layer would be then bonded with the central stage of the PDMS-spring with the aid of oxygen plasma. Finally, the layer of spring and flexible magnets will be flip-chip bonded together with the Silicon paddle, containing the copper microcoil, to obtain the final device that is shown in Fig. 7.2.

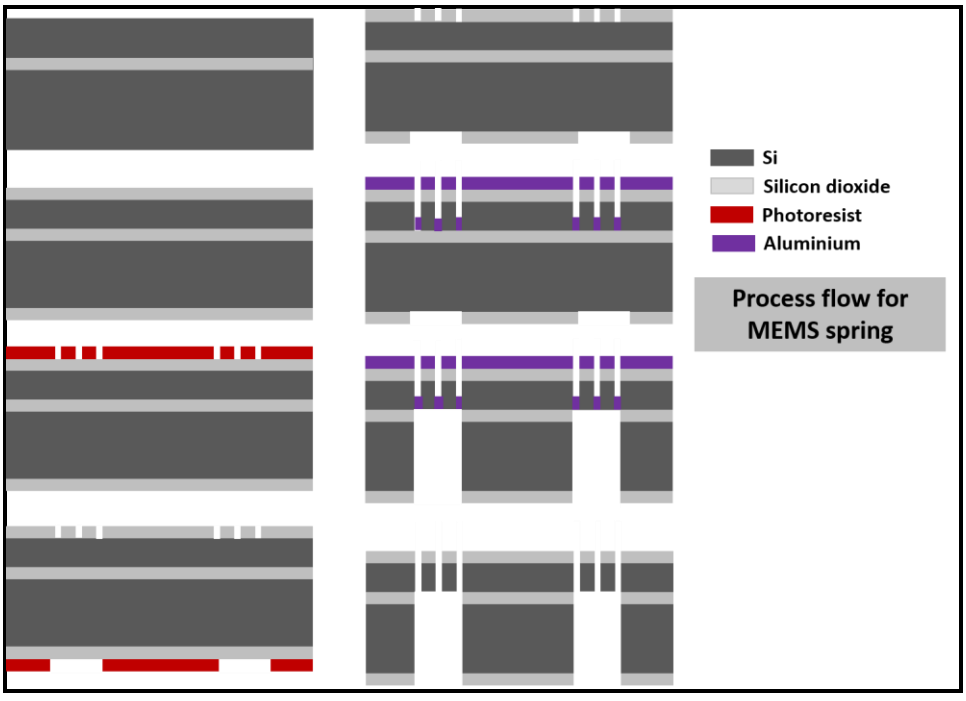


Figure 7.3: Process flow for the fabrication of MEMS spring master mold that would be used to fabricate PDMS springs.

One of the unique facet of this conceived MEMS device is the combination of micro-fabrication process to bind high-energy product NdFeB magnetic powder in PDMS

trenches using parylene binder, along with the use of soft-magnetic mask to create oppositely polarized micro-magnet assembly, which have not yet been explored in the area of EM-VEHs. The in-planar MEMS-structure and the optimized micromagnet array would reinforce the EM-interaction that results in significantly improved Normalized Power Density ($NPD=P/VA^2$;P,V and A are output power, device-volume, excitation acceleration respectively). To date there is no evidence of efforts to create such nonlinear, integrated devices delivering maximized power over a low frequency and wider bandwidth.

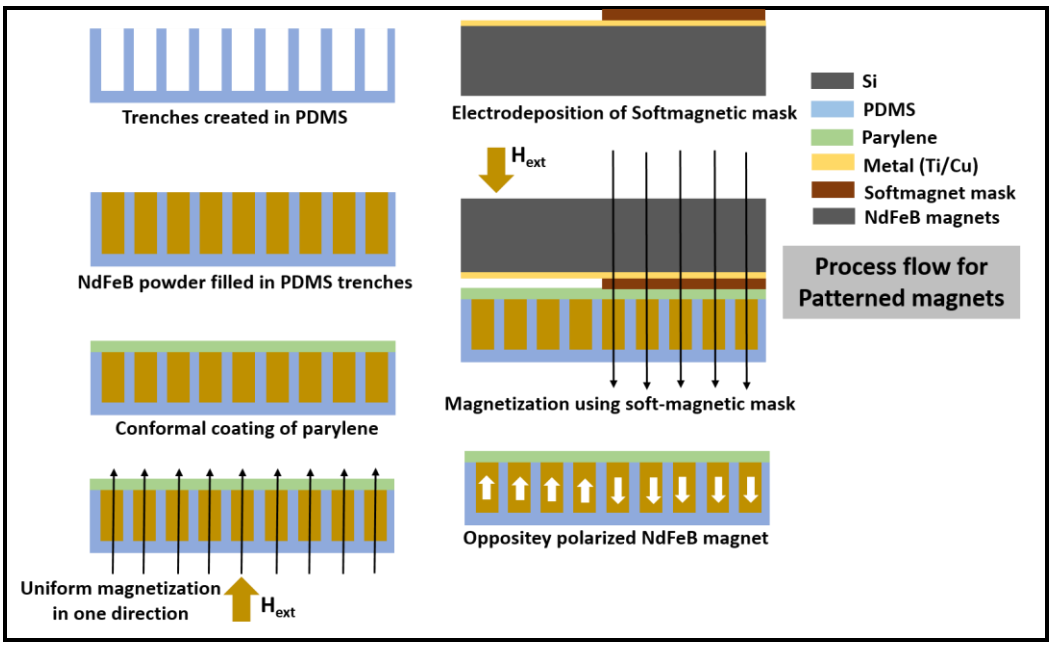


Figure 7.4: Process flow for the fabrication and specific magnetization of bonded micromagnets.

Furthermore, suitable power conversion and efficient power management system could be developed to integrate the EM-VEH in a system level, for different niche IoT based applications. This work will be uniquely placed at the intersection of Magnetic-MEMS, micro-fabrication, and nonlinear dynamics, that is benefiting from a niche interdisciplinary deep-tech eco-system.

7.5 Final remarks

The ambitious vision of connecting the physical world to the digital world through seamless migration of data from edge to cloud and to the end user has already pivoted revolutionary developments in advanced electronics in this era of Internet of Things (IoT). Wireless sensor platform, which is the key component of IoT, are employed in wide range of application area in urban and rural, domestic as well as industrial environment. There is a growing interest in

exploiting the capabilities of vibration energy harvesters as a sustainable replacement of batteries to implement autonomous wireless sensor network. The practical applicability of these energy harvesting devices are to some extent limited owing to – narrow bandwidth of devices, low power density, incompatible harvester-load interface electronics, dramatic reduction of efficiency on scaling down these devices into MEMS scale.

In this thesis, these major challenges have been identified and addressed; however, there is a large scope for development, especially in implementing highly integrated MEMS scale energy harvester for powering wireless sensor network. This could be further reinforced with compatible interface electronics that offers the capability of conditioning the extracted power from the energy harvester and route this power to run wireless sensor networks perpetually.

7.6 References

[1] S. Sinha. *State of IoT 2021: Number of connected IoT devices growing 9% to 12.3 billion globally, cellular IoT now surpassing 2 billion*. Available: https://iot-analytics.com/number-connected-iot-devices/

[2] J. Manyika *et al.*, *The Internet of Things: Mapping the value beyond the hype*. McKinsey Global Institute New York, NY, USA, 2015.

[3] D. Zhu, S. Roberts, T. Mouille, M. J. Tudor, and S. P. Beeby, "General model with experimental validation of electrical resonant frequency tuning of electromagnetic vibration energy harvesters," *Smart Materials and Structures*, vol. 21, no. 10, p. 105039, 2012.

[4] D. Mallick and S. Roy, "Bidirectional electrical tuning of FR4 based electromagnetic energy harvesters," *Sensors and Actuators A: Physical*, vol. 226, pp. 154-162, 2015/05/01/ 2015.

[5] I. Sari, T. Balkan, and H. Kulah, "An electromagnetic micro power generator for wideband environmental vibrations," *Sensors and Actuators A: Physical*, vol. 145-146, pp. 405-413, 2008/07/01/ 2008.

[6] B. Yang *et al.*, "Electromagnetic energy harvesting from vibrations of multiple frequencies," *Journal of Micromechanics and Microengineering*, vol. 19, no. 3, p. 035001, 2009/01/30 2009.

[7] M. M. R. El-Hebeary, M. H. Arafa, and S. M. Megahed, "Modeling and experimental verification of multi-modal vibration energy harvesting from plate structures," *Sensors and Actuators A: Physical*, vol. 193, pp. 35-47, 2013/04/15/ 2013.

[8] A. R. M. Foisal, C. Hong, and G.-S. Chung, "Multi-frequency electromagnetic energy harvester using a magnetic spring cantilever," *Sensors and Actuators A: Physical*, vol. 182, pp. 106-113, 2012/08/01/ 2012.

[9] Q. Zhang, Y. Wang, and E. S. Kim, "Electromagnetic energy harvester with flexible coils and magnetic spring for 1–10 Hz resonance," *Journal of Microelectromechanical Systems*, vol. 24, no. 4, pp. 1193-1206, 2015.

[10] B. P. Mann and N. D. Sims, "Energy harvesting from the nonlinear oscillations of magnetic levitation," *Journal of Sound and Vibration*, vol. 319, no. 1, pp. 515-530, 2009/01/09/ 2009.

[11] D. Mallick, A. Amann, and S. Roy, "A nonlinear stretching based electromagnetic energy harvester on FR4 for wideband operation," *Smart Materials and Structures*, vol. 24, no. 1, p. 015013, 2014/11/27 2014.

[12] B. Marinkovic and H. Koser, "Smart Sand—A Wide Bandwidth Vibration Energy Harvesting Platform," *Applied Physics Letters - APPL PHYS LETT*, vol. 94, 03/09 2009.

[13] X. Dai, X. Miao, L. Sui, H. Zhou, X. Zhao, and G. Ding, "Tuning of nonlinear vibration via topology variation and its application in energy harvesting," *Applied Physics Letters*, vol. 100, no. 3, p. 031902, 2012/01/16 2012.

[14] K. Wang, X. Dai, C. Ren, and G. Ding, "Fully Integrated Microsolenoid With Closed Magnetic Circuit for High Power Density MEMS Electromagnetic Vibration Energy Harvesters," *IEEE Magnetics Letters*, vol. 12, pp. 1-5, 2021.
[15] R. Han, N. Wang, J. Wang, J. Gu, and X. Li, "Silicon-chip based electromagnetic vibration energy harvesters fabricated using wafer-level micro-casting technique," *Journal of Micromechanics and Microengineering*, vol. 31, no. 3, p. 035009, 2021/02/04 2021.
[16] H. Wu *et al.*, "A micro-electromagnetic vibration energy harvester with higher power density and wider bandwidth utilizing 3D MEMS coils," *Applied Physics Letters*, vol. 119, no. 21, p. 213904, 2021/11/22 2021.
[17] M. Yao, X. Wang, Q. Wu, Y. Niu, and S. Wang, "Dynamic analysis and design of power management circuit of the nonlinear electromagnetic energy harvesting device for the automobile suspension," *Mechanical Systems and Signal Processing*, vol. 170, p. 108831, 2022/05/01/ 2022.
[18] Z. Wang *et al.*, "On-rotor electromagnetic energy harvester for powering a wireless condition monitoring system on bogie frames," *Energy Conversion and Management*, vol. 243, p. 114413, 2021.
[19] M. Yao, J. Li, and Y. Niu, "Adaptive impedance matching for power management circuit for a piezoelectric energy harvester on the bridge," *Sensors and Actuators A: Physical*, vol. 331, p. 112986, 2021/11/01/ 2021.
[20] Y. Li, X. Wang, S. Zhang, C. Zhou, D. Qiao, and K. Tao, "A Pendulum-like Low Frequency Electromagnetic Vibration Energy Harvester Based on Polymer Spring and Coils," *Polymers*, vol. 13, no. 19, p. 3380, 2021.
[21] Y. S. Suzuki and Y. C. Tai, "Micromachined High-Aspect-Ratio Parylene Spring and Its Application to Low-Frequency Accelerometers," *Journal of Microelectromechanical Systems*, vol. 15, no. 5, pp. 1364-1370, 2006.
[22] B. Davies, R. Mottram, and I. Harris, "Recent developments in the sintering of NdFeB," *Materials chemistry and physics*, vol. 67, no. 1-3, pp. 272-281, 2001.
[23] T. Shima, K. Takanashi, Y. K. Takahashi, and K. Hono, "Coercivity exceeding 100kOe in epitaxially grown FePt sputtered films," *Applied Physics Letters*, vol. 85, no. 13, pp. 2571-2573, 2004/09/27 2004.
[24] H. An *et al.*, "Highly (001) oriented L10-CoPt/TiN multilayer films on glass substrates with perpendicular magnetic anisotropy," *Journal of Vacuum Science & Technology A*, vol. 33, no. 2, p. 021512, 2015/03/01 2015.
[25] E. Fontana *et al.*, "Fabrication and Characterization of Polymer-Bonded Flexible Anisotropic Micro-Magnet Arrays," *IEEE Transactions on Magnetics*, vol. 58, no. 2, pp. 1-5, 2022.
[26] N. Wang, B. J. Bowers, and D. P. Arnold, "Wax-bonded NdFeB micromagnets for microelectromechanical systems applications," *Journal of Applied Physics*, vol. 103, no. 7, p. 07E109, 2008/04/01 2008.
[27] M. T. Bodduluri *et al.*, "Fully Integrated High-Performance MEMS Energy Harvester for Mechanical and Contactless Magnetic excitation in Resonance and at low Frequencies," *Micromachines*, vol. 13, no. 6, p. 863, 2022.
[28] H. Wang, M. Matsuura, S. Yamada, S. Sugimoto, and S. Tanaka, "Temperature stable rare earth magnetic powder Sm-Fe-N based micro magnets with remanence enhanced by easy axis alignment and its application in MEMS actuator," *Journal of Micromechanics and Microengineering*, vol. 31, no. 7, p. 075002, 2021/05/24 2021.
[29] L. Li *et al.*, "Fabrication of highly dense isotropic Nd-Fe-B nylon bonded magnets via extrusion-based additive manufacturing," *Additive Manufacturing*, vol. 21, pp. 495-500, 2018/05/01/ 2018.
[30] K. Gandha, I. C. Nlebedim, V. Kunc, E. Lara-Curzio, R. Fredette, and M. P. Paranthaman, "Additive manufacturing of highly dense anisotropic Nd–Fe–B bonded magnets," *Scripta Materialia*, vol. 183, pp. 91-95, 2020/07/01/ 2020.
[31] V. Neu, S. Sawatzki, M. Kopte, C. Mickel, and L. Schultz, "Fully Epitaxial, Exchange Coupled SmCo $ _ {5} $/Fe Multilayers With Energy Densities above 400 kJ/m $^{3} $," *IEEE transactions on magnetics*, vol. 48, no. 11, pp. 3599-3602, 2012.
[32] N. Lupu, P. Pascariu, C. Gherasim, and H. Chiriac, "Magnetic properties of electrodeposited FeGa/CoFeB multilayered films and nanowire arrays," *IEEE Transactions on Magnetics*, vol. 44, no. 11, pp. 3005-3008, 2008.
[33] F. Wang, X. Xu, Y. Liang, J. Zhang, and H. Wu, "FeAu/FePt exchange-spring media fabricated by magnetron sputtering and postannealing," *Applied Physics Letters*, vol. 95, no. 2, p. 022516, 2009.
[34] Q. Zhang, Y. Wang, L. Zhao, and E. S. Kim, "Integration of microfabricated low resistance and thousand-turn coils for vibration energy harvesting," *Journal of Micromechanics and Microengineering*, vol. 26, no. 2, p. 025019, 2016/01/13 2016.
[35] C. Ruffert and H. Gatzen, "Fabrication and test of multilayer microcoils with a high packaging density," *Microsystem technologies*, vol. 14, no. 9, pp. 1589-1592, 2008.

[36] F. Herrault, S. Yorish, T. M. Crittenden, C.-H. Ji, and M. G. Allen, "Parylene-insulated ultradense microfabricated coils," *Journal of microelectromechanical systems*, vol. 19, no. 6, pp. 1277-1283, 2010.
[37] J. Leicht, D. Maurath, and Y. Manoli, "Autonomous and self-starting efficient micro energy harvesting interface with adaptive MPPT, buffer monitoring, and voltage stabilization," in *2012 Proceedings of the ESSCIRC (ESSCIRC)*, 2012, pp. 101-104.
[38] U. Radhakrishna *et al.*, "A low-power integrated power converter for an electromagnetic vibration energy harvester with 150 mV-AC cold startup, frequency tuning, and 50 Hz AC-to-DC conversion," in *2018 IEEE Custom Integrated Circuits Conference (CICC)*, 2018, pp. 1-4.
[39] C. Ó. Mathúna, N. Wang, S. Kulkarni, and S. Roy, "Review of integrated magnetics for power supply on chip (PwrSoC)," *IEEE Transactions on Power Electronics*, vol. 27, no. 11, pp. 4799-4816, 2012.